

# Northumbria Research Link

Citation: Angelis, Dimitrios (2023) Wide angle reflection and refraction methods for ground penetrating radar. Doctoral thesis, Northumbria University.

This version was downloaded from Northumbria Research Link:  
<https://nrl.northumbria.ac.uk/id/eprint/51516/>

Northumbria University has developed Northumbria Research Link (NRL) to enable users to access the University's research output. Copyright © and moral rights for items on NRL are retained by the individual author(s) and/or other copyright owners. Single copies of full items can be reproduced, displayed or performed, and given to third parties in any format or medium for personal research or study, educational, or not-for-profit purposes without prior permission or charge, provided the authors, title and full bibliographic details are given, as well as a hyperlink and/or URL to the original metadata page. The content must not be changed in any way. Full items must not be sold commercially in any format or medium without formal permission of the copyright holder. The full policy is available online: <http://nrl.northumbria.ac.uk/policies.html>



**WIDE ANGLE  
REFLECTION AND REFRACTION  
METHODS FOR  
GROUND PENETRATING RADAR**

**D ANGELIS**



Northumbria University

PhD

2023

**WIDE ANGLE  
REFLECTION AND REFRACTION  
METHODS FOR  
GROUND PENETRATING RADAR**

**DIMITRIOS ANGELIS**

A thesis submitted in partial fulfilment of  
the requirements of the  
University of Northumbria at Newcastle  
for the degree of  
Doctor of philosophy

Research undertaken in the  
Faculty of Engineering and Environment

January 2023

# Abstract

Multi-offset ground-penetrating radar (GPR) data acquisition modes such as the common midpoint (CMP) and wide-angle reflection and refraction (WARR) have many benefits over the traditional single-offset common offset (CO) mode, as they allow for each subsurface point to be sensed by multiple transmitter-receiver pairs, and thus by multiple wavefronts. However, despite their benefits, CMP and WARR data acquisition modes have seen limited adoption in recent decades for several reasons, primarily because they require multiple offsets and they were being performed with a single transmitter-receiver pair, thus making them extremely time-consuming and expensive.

Recent advancements in GPR technology have led to the development of new GPR systems with multiple concurrent data acquisition receivers. These newly developed GPRs allow for the fast and dense acquisition of CMP/WARR data with the same speed as the traditional CO mode, and thus offer the potential to provide, rapidly and therefore with low survey cost, all the benefits of the multi-offset modes. However, both the character and the large volume of data generated by these GPR systems, as well as the large number of transducers required for their operation, necessitates the development and automation of new processing methods, workflows, and tools, as well as the investigation of new configurations with reduced transducers.

A novel MATLAB-based software with a user-friendly graphical user interface (GUI) has been developed to enable the visualisation and processing of multi-concurrent receiver GPR data, as well as the testing and evaluation of new processing methods and workflows for such data. The software supports GPR file formats from various manufacturers, but most importantly, it supports the ability to manage both single- and multi-offset GPR data, including simulated data and multi-concurrent receiver GPR data. The software provides a large number of processing methods, both simple and advanced, as well as novel processing methods developed exclusively for multi-concurrent receiver GPR data.

Three specific processing methods have been developed to address challenges associated with the character and the large volume of data generated by multi-concurrent

receiver GPR systems. The first is a time-zero alignment method for correcting and managing the time misalignments from multi-concurrent receivers; the second is a CMP trace balancing method for compensating for the large amplitude versus offset (AVO) differences in the data; and the third is an automatic velocity spectrum picking method for facilitating velocity analysis of large volumes of data. All three methods have been evaluated and validated using both synthetic and real field data, demonstrating their efficiency and performance.

The aforementioned software and specific processing methods have enabled a robust and comprehensive processing workflow for multi-concurrent receiver GPR data to be created, which is capable of producing detailed velocity models, further enhancing data quality, and thus GPR interpretations. The workflow has been evaluated and validated with both synthetic and real field data acquired by different GPR systems from various environments. It is shown for the first time that seven multi-concurrent receivers are sufficient to provide both manually as well as automatically detailed stacking velocity fields and enhanced zero offset stacked time sections, thus also demonstrating the true potential of multi-concurrent receiver GPR systems.

Finally, the system/survey design of multi-concurrent receiver GPR systems has been explored with the primary objective being of making them more practicable and cost-effective. Utilising both simulated data and real field data it is shown that reducing the number of receivers from a configuration with seven equally spaced receivers to a sparse four-receiver configuration can sustain acceptable velocity resolution in velocity spectra panels. It is also demonstrated for the first time that not only seven but also four receivers can provide detailed stacking velocity fields and enhanced zero-offset stacked time sections.

With a robust and comprehensive data processing workflow for multi-concurrent receiver GPR data now established, there will be opportunities to further automate velocity analysis and add processing steps such as depth imaging and migration. Furthermore, apart from moveout-based velocity spectra analysis, other advanced velocity analysis methods such as prestack depth migration velocity analysis or reflection tomography can be explored.

# Publications

**Angelis, D.,** Warren, C., & Diamanti, N. (2019). Preliminary development of a workflow for processing multi-concurrent receiver GPR data. *10th International Workshop on Advanced Ground Penetrating Radar, 1*, 1–7.  
<https://doi.org/10.3997/2214-4609.201902572>

**Angelis, D.,** Warren, C., & Diamanti, N. (2020). A software toolset for processing and visualization of single and multi-offset GPR data. *18th International Conference on Ground Penetrating Radar, Golden, Colorado, 14–19 June 2020*, 320–323.  
<https://doi.org/10.1190/gpr2020-084.1>

**Angelis, D.,** Warren, C., Diamanti, N., James, M., & Annan, A. P. (2021). Challenges and opportunities from large volume, multi-offset Ground Penetrating Radar data. *EGU General Assembly 2021, Online, 19–30 Apr 2021*, EGU21-13138.  
<https://doi.org/10.5194/egusphere-egu21-13138>

**Angelis, D.,** Warren, C., Diamanti, N., Martin, J., & Annan, A. P. (2022a). Development of a workflow for processing ground-penetrating radar data from multiconcurrent receivers. *Geophysics*, 87(4), WB9–WB18.  
<https://doi.org/10.1190/geo2021-0376.1>

**Angelis, D.,** Warren, C., Diamanti, N., Martin, J., & Annan, A. P. (2022b). The effects of receiver arrangement on velocity analysis with multi-concurrent receiver GPR data. *Near Surface Geophysics*, 20(5), 519–530.  
<https://doi.org/10.1002/nsg.12235>

# Contents

Abstract .....	i
Publications .....	iii
Contents .....	iv
List of abbreviations.....	vii
List of figures .....	ix
List of tables .....	xxiv
Acknowledgements .....	xxv
Declaration .....	xxvi
1 Introduction .....	1
1.1 Motivation for the thesis.....	2
1.2 Aims of the thesis .....	3
1.3 Structure of the thesis .....	4
2 Ground-penetrating radar principles .....	7
2.1 History of GPR.....	8
2.2 GPR applications .....	9
2.3 GPR wave propagation.....	10
2.3.1 Wave paths.....	10
2.3.2 Material types and properties.....	13
2.3.3 Wave velocity and losses.....	18
2.4 GPR systems.....	22
2.4.1 System types .....	23
2.4.2 System centre frequency and depth penetration .....	24
2.4.3 System centre frequency and resolution .....	25
2.5 GPR data collection.....	28
2.5.1 Data acquisition modes.....	28
2.5.2 Antenna orientation .....	29
2.6 GPR data visualisation .....	31
2.7 GPR data processing .....	33
3 Review of multi-offset GPR methods .....	47
3.1 Multi-offset GPR data collection .....	48
3.2 Multi-offset GPR data processing .....	50

---

3.3 Multi-concurrent receiver GPR systems .....	60
3.3.1 Previous studies .....	62
3.4 Summary .....	64
4 Tools for obtaining and processing multi-concurrent receiver GPR data.....	65
4.1 Numerical modelling .....	66
4.1.1 GPR forward problem.....	66
4.1.2 FDTD method .....	68
4.1.3 The gprMax FDTD solver .....	70
4.2 The “WARR Machine” GPR .....	76
4.2.1 A typical multi-concurrent receiver GPR data set.....	78
4.3 GPR data visualisation and processing software.....	80
4.3.1 2D module .....	82
4.3.2 CMP/WARR module.....	87
4.3.3 3D module .....	90
5 Addressing the challenges of processing multi-concurrent receiver GPR data .....	92
5.1 Time-zero alignment .....	93
5.1.1 Synthetic data example .....	98
5.1.2 Field data example .....	103
5.2 CMP trace balancing .....	105
5.2.1 Synthetic data example .....	107
5.2.2 Field data example .....	111
5.3 Automated velocity spectra picking .....	114
5.3.1 Synthetic data example .....	117
5.3.2 Field data example .....	119
6 A processing workflow for multi-concurrent receiver GPR data .....	122
6.1 Processing workflow .....	123
6.2 Synthetic data case study 1 .....	125
6.2.1 Model and data description.....	125
6.2.2 Stacking velocity field and stacked section .....	128
6.3 Synthetic data case study 2.....	133
6.3.1 Model and data description.....	133
6.3.2 Stacking velocity field and stacked section .....	135
6.4 Field data case study 1 .....	140
6.4.1 Data description .....	140

6.4.2 Stacking velocity field and stacked section .....	142
6.5 Field data case study 2.....	146
6.5.1 Data description .....	146
6.5.2 Stacking velocity field and stacked section .....	148
7 The effect of multi-concurrent receiver arrangement on velocity analysis.....	152
7.1 Decrease in the number of receivers .....	153
7.1.1 Synthetic data example .....	154
7.1.2 Field data example .....	160
7.2 Increase in the number of receivers.....	172
7.2.1 Synthetic data example .....	174
8 Conclusions and recommendations.....	180
8.1 Conclusions .....	181
8.1.1 Development of processing tools.....	181
8.1.2 Development of processing methods.....	182
8.1.3 Development of a processing workflow .....	184
8.1.4 System/survey design investigation.....	186
8.2 Recommendations for future research.....	188
A MATLAB scripts for converting Vox format to HDF5 format .....	190
References .....	201

# List of abbreviations

1D	One-dimensional
2D	Two-dimensional
3D	Three-dimensional
ABC	Absorbing boundary condition
ADC	Analogue-to-digital converter
AGC	Automatic gain control
ASCII	American standard code for information interchange
AVO	Amplitude versus offset
CC	Unnormalised cross-correlation sum
CDP	Common depth point
CLF	Courant-Freidrichs-Lewy
CMP	Common midpoint
CO	Common offset
CPU	Central processing unit
CRP	Common reflection point
CSG	Common shot gather
CVP	Constant velocity panels
CVS	Constant velocity stacks
CW	Continuous wave
DNAPL	Dense non-aqueous phase liquid
DSP	Digital signal processing
EM	Electromagnetic
FDTD	Finite-difference time-domain
FFT	Fast Fourier transform
FK	Frequency-wavenumber
GPR	Ground-penetrating radar
GPS	Global positioning system
GPU	Graphics processing unit
GSSI	Geophysical Survey Systems Inc.
GUI	Graphical user interface
HMO	Hyperbolic moveout

HPC	High-performance computing
I/O	Input/Output
IAD	Inverse amplitude decay
LMO	Linear moveout
MF	Multi-fold
NE	Normalised output-to-input energy ratio/Semblance
NMO	Normal moveout
INMO	Inverse normal moveout
PML	Perfectly matched layer
PRF	Pulse repetition frequency
R/r	Correlation coefficient
RADAR	Radio Detection And Ranging
RAM	Random-access memory
RMS	Root mean square
RMSE	Root mean square error
Rx	Receiver/receiving antenna
S	Stacked amplitude
SEC	Spreading/Spherical and exponential compensation/correction
SF	Single-fold
SNR	Signal-to-noise ratio
STD	Standard deviation
TDR	Time-domain-reflectometry
TWT	Two-way travel time
Tx	Transmitter/transmitting antenna
UDG	User-defined gain
VTK	Visualisation Toolkit
WARR	Wide angle reflection refraction

# List of figures

Figure 2.1: a) The signal ray path for the direct air wave (black), the direct ground wave (orange), the reflected wave (green), and the critically refracted wave (red). b) The arrival time of the signals of (a) versus the offset.....	11
Figure 2.2: Attenuation mechanisms of the GPR signal. The largest contributors are depicted in red colour. Figure adapted from Cassidy (2008a).....	21
Figure 2.3: Typical GPR system (pulseEKKO – Sensors & Software Inc. (2021b)).....	22
Figure 2.4: The pulse width (W), bandwidth (B) and centre frequency (fc).....	24
Figure 2.5: a) Depth and lateral resolution of a GPR system. b) Depth and lateral resolution concept for two circular targets. Figure(s) adapted from Annan (2005)...	26
Figure 2.6: GPR data acquisition modes.....	29
Figure 2.7: Tx and Rx antenna orientations. The electric field is assumed to be aligned along the long axis of the antenna.....	30
Figure 2.8: GPR data visualisation modes. A-scan, B-scan, C-scan, and time/depth slice. ....	32
Figure 2.9: SNR improvement through vertical stacking on a GPR trace. ....	34
Figure 2.10: Dewow on a raw GPR trace. ....	35
Figure 2.11: The five most-used positions for the time-zero correction according to Yelf (2004).....	36
Figure 2.12: a) GPR data before time-zero correction. b) GPR data after time-zero correction.....	36
Figure 2.13: a) GPR data before the application of time gain. b) GPR data after the application of time gain (SEC gain).....	37
Figure 2.14: a) GPR data before the application of the background removal filter. b) GPR data after the application of the background removal filter. ....	38
Figure 2.15: a) GPR data before the application of bandpass frequency filtering. b) GPR data after the application of bandpass frequency filtering. ....	40

Figure 2.16: a) GPR data before the application of bandpass wavenumber filtering. b) GPR data after the application of bandpass wavenumber filtering.....	40
Figure 2.17: a) GPR data before the application of predictive deconvolution. b) GPR data after the application of predictive deconvolution. ....	41
Figure 2.18: Hyperbolic fitting of GPR data ( $v = 0.09$ m/ns).....	43
Figure 2.19: a) GPR data before the application of migration b) GPR data after the application of migration (FK migration – $v = 0.09$ m/ns).....	44
Figure 2.20: a) GPR data before the Hilbert transform. b) GPR data after the Hilbert transform – instantaneous amplitude. c) GPR data after the Hilbert transform – instantaneous phase. d) GPR data after the Hilbert transform – instantaneous frequency.....	46
Figure 3.1: a) The SF CO mode of operation, and a typical single-offset GPR system. b) The MF CMP and WARR modes of operation, and a typical multi-offset GPR system. Figure adapted from Sensors & Software Inc. (2021b). ....	50
Figure 3.2: 3D two-layered model used to generate synthetic data for demonstrating basic MF GPR data processing steps. ....	51
Figure 3.3: WARR data acquisition mode and CMP gather formulation. ....	52
Figure 3.4: a) Synthetic CMP gather contaminated with white Gaussian noise and noise bursts (white rectangles), showing the direct air wave (black line), direct ground wave (orange line), reflected wave (green line), and critically refracted wave (red line). b) NMO over-corrected CMP gather of (a). c) NMO under-corrected CMP gather of (a). d) NMO corrected with proper velocity CMP gather of (a). ....	54
Figure 3.5: a) Synthetic CMP gather contaminated with white Gaussian noise and noise bursts. b) Combined LMO NMO velocity spectrum panel/S panel of (a). c) Combined LMO NMO velocity spectrum panel/CC panel of (a). d) Combined LMO NMO velocity spectrum panel/NE panel of (a). e) NMO corrected CMP gather of (a) using velocity picked from NE panel (d). In (b) – (d) orange arrows highlight the maxima corresponding to the direct ground wave, while green arrows highlight the maxima that correspond to the reflected wave.....	58
Figure 3.6: a) Synthetic CMP gather contaminated with white Gaussian noise and noise bursts. b) NMO corrected CMP gather of (a). c) NMO corrected CMP gather of	

(a) after the application of stretch mute. In (b) the triangle highlights the high-stretch zone, while in (c) the muted zone. ....	59
Figure 3.7: a) NMO corrected synthetic CMP gather contaminated with white Gaussian noise and noise bursts after the application of stretch mute. b) Stacked trace of (a).....	60
Figure 3.8: a) The SF CO and MF WARR mode of operation. b) Multi-concurrent receiver GPR system that combines the two modes of (a). The “WARR Machine” by Sensors & Software Inc.....	62
Figure 4.1: Single 3D FDTD Yee cell showing electric (red arrows) and magnetic (green arrows) field components. Figure adapted from Giannopoulos (2005).....	69
Figure 4.2: a) 3D two-layered model showing also the FDTD grid, Yee cells, and PML region. b) Synthetic WARR gather (WARR 50) generated from the model of (a). At the top, the transducer configuration can be seen, with the Tx depicted in red, and the Rx's in yellow. ....	73
Figure 4.3: a) Development stages for creating an antenna model similar to a Geophysical Survey Systems Inc. (GSSI) 1.5 GHz centre frequency antenna in MagicaVoxel. b) Development stages for creating a Sensors & Software Inc. 500 MHz centre frequency like antenna model. c) Antenna models of (a) and (b) imported to gprMax and used with a heterogeneous soil model. ....	75
Figure 4.4: Dome-like and rectangular-like complex objects/targets created using MagicaVoxel.....	75
Figure 4.5: Two forms of the seven-channel “WARR Machine with 500 MHz centre frequency transducers. Figure adapted from Diamanti et al. (2018). a) SmartTow transducer configuration. b) SmartCart transducer configuration.....	77
Figure 4.6: Seven-channel “WARR Machine” with 1000 MHz centre frequency transducers.....	77
Figure 4.7: a) Field data WARR gather (WARR 50) after the application of dc shift removal. b) CO profile of the first receiver, $Tx - Rx_1 = 0.25$ m. c) CO profile of the fourth receiver, $Tx - Rx_4 = 1.0$ m. d) CO profile of the seventh receiver, $Tx - Rx_7 = 1.75$ m. DC shift removal and IAD gain have been applied to the CO profiles. The black dotted lines highlight the direct air wave responses and the white arrow the pipe	

response. The transducer configuration is shown at the top of each sub-figure, with the Tx in red and the Rxs in yellow. ....	79
Figure 4.8: GUI showing the main elements of the 2D module for SF CO GPR data: 1. menu bar, 2. raw or previous processing step data visualisation panel, 3. info/header panel, 4. current/chosen processing step data visualisation panel, 5. workflow list panel. ....	83
Figure 4.9: Various analysis methods of the 2D module, used in different stages of data processing. a) Frequency spectrum analysis. b) FK spectrum analysis. c) Signal attenuation analysis. d) Velocity hyperbolic fitting analysis. ....	84
Figure 4.10: GUI showing the main elements of the CMP/WARR module: 1. menu bar, 2. velocity spectrum panel, 3. 1D stacking velocity panel, 4. CMP gather panel, 5. stacked trace panel, 6. NMO corrected zero-offset stacked section and interpolated stacking velocity cross-section panel. ....	88
Figure 4.11: Fold graph generated using fold analysis function. ....	89
Figure 4.12: GUI showing the main elements of the 3D module: 1. file menu, 2. gridding panel, 3. 3D visualisation options panel. ....	91
Figure 5.1: Field data CMP gather, semblance plot of the CMP gather, CMP gather after NMO correction using velocities picked automatically from the semblance plot (white line), and resultant stacked trace of the NMO corrected CMP gather. The transducer configuration is shown at the top of each sub-figure, with the Tx in red and the Rxs in yellow. a) Non-implementation of the time-zero alignment. b) Improper implementation of the time-zero alignment (error 1 – 2 time samples per trace). c) Proper implementation of the time-zero alignment. ....	95
Figure 5.2: a) Air-launched field data WARR gather before and after time-zero alignment. The time shift required for each trace has been calculated using equation (5.1). b) Ground-coupled field data WARR gather before and after time-zero alignment. The time shift required for each trace has been calculated from the air-launched data of (a). To aid visualisation, the first 10 ns are also shown after trace balancing. In (a) the blue line highlights the first large deflections (i.e., first peaks), and the red dot the first break of the first/near-offset receiver. In (a) and (b) green line highlights the theoretical direct air-wave response which is given by equation (2.1).	

The transducer configuration is shown at the top of each sub-figure, with the Tx in red and the Rx's in yellow.....	97
Figure 5.3: a) Antenna model (Tx-Rx pair) similar to a Sensors & Software Inc. 500 MHz centre frequency antenna. b) Sensors & Software Inc. 500 MHz centre frequency antenna (Tx-Rx pair) collecting air-launched data inside the anechoic chamber of Northumbria University. c) A comparison between a field air-launched trace collected using the aforementioned antenna in the anechoic chamber (blue), a synthetic air-launched trace generated using a Hertzian dipole source fed with a 500 MHz centre frequency ricker waveform (green), and a synthetic air-launched trace generated using the antenna model with a voltage source at the transmitting dipole feed point with a 500 MHz centre frequency Gaussian waveform (red). .....	99
Figure 5.4: a) Sensors & Software 500 MHz centre frequency modelled transducers developed to generate the synthetic data to demonstrate the proposed time-zero alignment method. The Tx is depicted in red and the Rx's in yellow. b) Synthetic air-launched traces. c) Synthetic air-launched traces after the application of randomised time shifts and white Gaussian noise. In (b) and (c) green lines highlight the theoretical direct air wave response which is given by equation (2.1). In (c) red lines highlight the first break positions chosen using a threshold equal to 5 % of the peak amplitude of each trace – Diamanti et al. (2018) method, and blue lines indicate the first large deflections, i.e., the first peaks – proposed method. ....	101
Figure 5.5: a – e) Field data CMP gather, semblance plot of the CMP gather, CMP gather after NMO correction using velocities picked automatically from the semblance plot (white dotted line), and resultant stacked trace of the NMO corrected CMP gather. The transducer configuration is shown at the top of each sub-figure, with the Tx in red and the Rx's in yellow. a – d) Time-zero alignment using the first break positions chosen using a threshold equal to 5 % (a), 10 % (b), 15 % (c), and 20 % (d) of the peak amplitude of each trace – Diamanti et al. (2018) method. e) Time-zero alignment using the first peaks – proposed method. f) Combined plot of the stacking velocities picked automatically from the semblance plots of (a) – (e), and combined plot of the stacked traces of (a) – (e). ....	104
Figure 5.6: Field data CMP gather showing the stages (left to right) of the proposed trace balancing method. The green line highlights the direct air wave responses, whilst	

the green arrows indicate the time shift to either negative (left-hand side) or positive (right-hand side) times, which is given by equation (2.1). The red and blue rectangle highlight the sliding window (10 ns window) for the first (i.e., reference trace) and second (i.e., trace to be balanced) trace, respectively, whereas the black rectangle and arrow represent the computed balance factors and their application to the second trace. .....	107
Figure 5.7: 3D four-layered model developed to generate synthetic data for demonstrating CMP trace balancing. ....	108
Figure 5.8: a – d) Synthetic CMP gather contaminated with white Gaussian noise and noise bursts, respective combined LMO NMO velocity spectrum panel, and coherency curves from the time windows centred on the four different events present in the gather, namely the ground wave and the three reflected waves. a) Unbalanced CMP gather and the respective semblance plot and semblance curves. b) Unbalanced CMP gather and the respective AB semblance plot and AB semblance curves. c) Balanced CMP gather using the typical single-window RMS balancing method and the respective semblance plot and semblance curves. d) Balanced CMP gather using the proposed sliding window RMS balancing method (8 ns window) and the respective semblance plot and semblance curves.....	110
Figure 5.9: a – d) Field data CMP gathers, respective NMO velocity spectrum panels, and coherency curves from the time window centred on the main reflected event of the data set, namely the pipe response/event. a) Unbalanced CMP gathers along with their respective semblance plots and semblance curves. b) Unbalanced CMP gathers along with their respective AB semblance plots and AB semblance curves. c) Balanced CMP gathers using the typical single-window RMS balancing method along with their respective semblance plots and semblance curves. d) Balanced CMP gathers using the proposed sliding window RMS balancing method (10 ns window) along with their respective semblance plots and semblance curves. ....	113
Figure 5.10: a) Field data CMP gather. b) Semblance plot of (a) showing the automatic velocity picks at the first iteration. The red line indicates the initial automatic velocity picks chosen based on the semblance maxima at each time sample, the blue line shows the weighted with the weight ( $w_s$ ) of equation (5.3) linear fitted curve of the initial picks, and the white line highlights the smoothed velocity picks. c) Semblance plot of	

(a) showing the automatic velocity picks at the second iteration. The red line indicates the smoothed velocity picks of the previous iteration (i.e., white line in (b)) which are now used as pre-set picks for the current iteration, the blue line shows the new weighted linear fitted curve of those picks, and the white line highlights the new smoothed velocity picks. d) Semblance plot of (a) showing the automatic velocity picks at the final iteration. The white line highlights the smoothed velocity picks, whereas the white arrows the spurious peaks that were avoided and not picked by the algorithm. The transparency of the semblance plot has been modified to aid visualisation in (b) and (c)..... 117

Figure 5.11: a) Synthetic CMP gather contaminated with white Gaussian noise. b – e) Semblance plots of (a) showing the true velocities used to create the synthetic CMP gather via INMO correction (black solid line), the velocities obtained manually by hand-picking (red dotted line), and the velocities picked automatically by the algorithm (white dotted line) using different thresholds (ths) and (thv) for the weights (ws) and (wv) of equations (5.3) and (5.4), respectively. In (c) – (e) white arrows highlight the supposedly spurious semblance peaks. .... 119

Figure 5.12: a) 1000 MHz centre frequency field data CMP gather, combined LMO NMO semblance plot of the CMP gather, CMP gather after NMO correction using the hand-picked velocities (red line), and CMP gather after NMO correction using the velocities picked automatically (white line). b) 500 MHz centre frequency field data CMP gather, NMO semblance plot of the CMP gather, CMP gather after NMO correction using the hand-picked velocities (red line), and CMP gather after NMO correction using the velocities picked automatically (white line)..... 121

Figure 6.1: Proposed processing workflow for multi-concurrent receiver GPR data. Highlighted in red is a section that includes standard GPR data processing steps. Marked in blue is a section that incorporates standard seismic reflection data processing steps, adapted for GPR. Highlighted in green is a section that contains steps used to address multi-concurrent receiver GPR data challenges as well as to improve the efficiency of other processing steps. The “\*” symbol denotes the optional processing steps of the workflow..... 124

Figure 6.2: a) 2D four-layered model with both vertical and lateral velocity variations developed to generate the synthetic data to test and demonstrate the proposed

processing methods/processing workflow. b) Processed CO profile of the first ( $Tx - Rx_1 = 0.25$  m), fourth ( $Tx - Rx_4 = 1.0$  m), and seventh receiver ( $Tx - Rx_7 = 1.75$  m). c) Processed CO profile of the first, fourth, and seventh receiver, after the application of white Gaussian noise and artificial AVO attenuation. The transducer configuration is shown at the top of each sub-figure, with the Tx in red and the Rx's in yellow. ... 127

Figure 6.3: 2D four-layered model synthetic data set. a) Interpolated stacking velocity field derived from manual hand-picked combined LMO NMO velocity analysis on every 20 CMP gathers, i.e., every 0.5 m. b) Smoothed stacking velocity field of (a). c) Stacking velocity field derived from automated combined LMO NMO velocity analysis on all high-fold CMP gathers. d) Filtered and smoothed stacking velocity field of (c). The white arrows indicate some of the areas in which the automated velocity field outperforms the manual hand-picked one and captures much better the layer boundaries. The low-fold areas, as well as the muted area of the direct air wave, are also highlighted in the sub-figures. .... 131

Figure 6.4: 2D four-layered model synthetic data set. a) Processed CO profile of the first receiver ( $Tx - Rx_1 = 0.25$  m). b) Processed and contaminated with white Gaussian noise CO profile of (a). c) Stacked section, derived using the smoothed velocity field obtained via manual hand-picked velocity analysis shown in Figure 6.3b. d) Stacked section, derived using the filtered/smoothed velocity field obtained via automated velocity analysis shown in Figure 6.3d. In (a) – (d) the blue arrow highlights an area of reduced high-frequency noise and an enhanced micro-reflector, and the green arrow marks a reflector with improved continuity. In (c), and (d), the white arrow shows a reflector with a slight difference in vertical width indicating an NMO stretch difference. The low-fold areas, as well as the muted area of the direct air wave, are also highlighted in the sub-figures. .... 132

Figure 6.5: a) 2D three-layered model with both vertical and lateral velocity variations developed to generate the synthetic data to test and demonstrate the proposed processing methods/processing workflow. The white arrows highlight three different targets also contained in this model. b) Processed CO profile of the first ( $Tx - Rx_1 = 0.25$  m), fourth ( $Tx - Rx_4 = 1.0$  m), and seventh receiver ( $Tx - Rx_7 = 1.75$  m). c) Processed CO profile of the first, fourth, and seventh receiver, after the application of white Gaussian noise and artificial AVO attenuation. The transducer configuration is shown at the top of each sub-figure, with the Tx in red and the Rx's in yellow. .... 134

Figure 6.6: 2D three-layered model synthetic data set. a) Interpolated stacking velocity field derived from manual hand-picked combined LMO NMO velocity analysis on every 20 CMP gathers, i.e., every 0.5 m. b) Smoothed stacking velocity field of (a). c) Stacking velocity field derived from automated combined LMO NMO velocity analysis on all high-fold CMP gathers. d) Filtered and smoothed stacking velocity field of (c). The white arrows indicate some of the areas in which the automated velocity field outperforms the manual hand-picked one and captures much better the layer boundaries and the left-hand side of the hyperbola. The low-fold areas, as well as the muted area of the direct air wave, are also highlighted in the sub-figures..... 138

Figure 6.7: 2D three-layered model synthetic data set. a) Processed CO profile of the first receiver ( $Tx - Rx_1 = 0.25$  m). b) Processed and contaminated with white Gaussian noise CO profile of (a). c) Stacked section, derived using the smoothed velocity field obtained via manual hand-picked velocity analysis shown in Figure 6.6b. d) Stacked section, derived using the filtered/smoothed velocity field obtained via automated velocity analysis shown in Figure 6.6d. In (a) – (d) the red arrow highlights an area with a reduced ringing noise, the green arrow marks a reflector with improved continuity, and the blue arrow indicates an area of reduced high-frequency noise and an enhanced micro-reflector. In (c), and (d), the white arrows show two areas with slightly different stacking results. The low-fold areas, as well as the muted area of the direct air wave, are also highlighted in the sub-figures. .... 139

Figure 6.8: 500 MHz centre frequency field data set used to demonstrate the proposed processing methods/processing workflow. a) Field data WARR gather (WARR 45) after the application of dc shift removal. b) CO profile of the first receiver,  $Tx - Rx_1 = 0.25$  m. c) CO profile of the fourth receiver,  $Tx - Rx_4 = 1.0$  m. d) CO profile of the seventh receiver,  $Tx - Rx_7 = 1.75$  m. DC shift removal and IAD gain have been applied to the CO profiles. The black dotted lines highlight the direct air wave responses and the white arrows the linear pipe response. The transducer configuration is shown at the top of each sub-figure, with the Tx in red and the Rx's in yellow..... 141

Figure 6.9: 500 MHz centre frequency field data set. a) Interpolated stacking velocity field derived from manual hand-picked NMO velocity analysis on every 8 CMP gathers, i.e., every 0.5 m. b) Smoothed stacking velocity field of (a). c) Stacking velocity field derived from automated NMO velocity analysis on all high-fold CMP gathers. d) Filtered and smoothed stacking velocity field of (c). The white arrows

indicate an area (0 – 10 m and 10 – 30 ns) in which the automated velocity field outperforms the manual hand-picked one and captures much better the subsurface reflectors. The low-fold areas, as well as the muted area of the direct air wave and direct ground wave, are also highlighted in each sub-figure. .... 144

Figure 6.10: 500 MHz centre frequency field data set. a) Processed CO profile of the first receiver ( $T_x - R_{x_1} = 0.25$  m). b) Stacked section, derived using the smoothed velocity field obtained via manual hand-picked velocity analysis shown in Figure 6.9b. c) Stacked section, derived using the filtered/smoothed velocity field obtained via automated velocity analysis shown in Figure 6.9d. In (a) – (c) the red arrow highlights an area with a reduced ringing noise, the green arrow marks a reflector with improved continuity, and the blue arrow indicates an enhanced reflector. The low-fold areas, as well as the muted area of the direct air wave and direct ground wave, are also highlighted in each sub-figure..... 145

Figure 6.11: 1000 MHz centre frequency field data set used to demonstrate the proposed processing methods/processing workflow. a) Field data WARR gather (WARR 500) after the application of dc shift removal. b) CO profile of the first receiver,  $T_x - R_{x_1} = 0.165$  m. c) CO profile of the fourth receiver,  $T_x - R_{x_4} = 0.66$  m. d) CO profile of the seventh receiver,  $T_x - R_{x_7} = 1.155$  m. DC shift removal and IAD gain have been applied to the CO profiles. The black dotted lines highlight the direct air wave responses and the white arrows the different layers. The transducer configuration is shown at the top of each sub-figure, with the Tx in red and the Rx's in yellow..... 147

Figure 6.12: 1000 MHz centre frequency field data set. a) Interpolated stacking velocity field derived from manual hand-picked combined LMO NMO velocity analysis on every 12 CMP gathers, i.e., every 0.495 m. b) Smoothed stacking velocity field of (a). c) Stacking velocity field derived from automated combined LMO NMO velocity analysis on all high-fold CMP gathers. d) Filtered and smoothed stacking velocity field of (c). The white arrows indicate an area (35 – 50 m and 8 – 12 ns) in which the automated velocity field outperforms the manual hand-picked one and captures much better the layer boundary. The low-fold areas, as well as the muted area of the direct air wave, are also highlighted in each sub-figure. .... 150

Figure 6.13: 1000 MHz centre frequency field data set. a) Processed CO profile of the first receiver ( $Tx - Rx_1 = 0.165$ m). b) Stacked section, derived using the smoothed velocity field obtained via manual hand-picked velocity analysis shown in Figure 6.12b. c) Stacked section, derived using the filtered/smoothed velocity field obtained via automated velocity analysis shown in Figure 6.12d. In (a) – (c) the red arrow highlights an area with a reduced ringing noise, the green arrow marks a reflector with improved continuity, and the blue arrow and blue boxes indicate some enhanced reflectors. The low-fold areas, as well as the muted area of the direct air wave, are also highlighted in each sub-figure.....	151
Figure 7.1: Initial plan for decreasing the number of receivers. ....	153
Figure 7.2: a) 3D six-layered model, with both vertical and lateral velocity variations, developed to generate synthetic data for demonstrating the effect of reducing the number of receivers on velocity spectrum semblance analysis. b) 7Rx synthetic data CMP gather contaminated with white Gaussian noise and resultant semblance plot of the CMP gather. The transducer configuration is shown at the top of each sub-figure, with the Tx in red and the Rx's in yellow. ....	158
Figure 7.3: Near-offset receiver configuration scenarios/lack of far-offset receivers scenarios, using synthetic data CMP gather of Figure 7.2b. a) 7Rx semblance plot, $Tx - Rx_1 = 0.25$ m, $Tx - Rx_7 = 1.75$ m, Rx separation = 0.25 m. b) 6Rx semblance plot, $Tx - Rx_1 = 0.25$ m, $Tx - Rx_6 = 1.50$ m, Rx separation = 0.25 m. c) 5Rx semblance plot, $Tx - Rx_1 = 0.25$ m, $Tx - Rx_5 = 1.25$ m, Rx separation = 0.25 m. d) 4Rx semblance plot, $Tx - Rx_1 = 0.25$ m, $Tx - Rx_4 = 1.00$ m, Rx separation = 0.25 m. e) 3Rx semblance plot, $Tx - Rx_1 = 0.25$ m, $Tx - Rx_3 = 0.75$ m, Rx separation = 0.25 m. The transducer configuration is shown at the top of each sub-figure, with the Tx in red and the Rx's in yellow.....	158
Figure 7.4: Far-offset receiver configuration scenarios/lack of near-offset receivers scenarios, using synthetic data CMP gather of Figure 7.2b. a) 7Rx semblance plot, $Tx - Rx_1 = 0.25$ m, $Tx - Rx_7 = 1.75$ m, Rx separation = 0.25 m. b) 6Rx semblance plot, $Tx - Rx_1 = 0.50$ m, $Tx - Rx_6 = 1.75$ m, Rx separation = 0.25 m. c) 5Rx semblance plot, $Tx - Rx_1 = 0.75$ m, $Tx - Rx_5 = 1.75$ m, Rx separation = 0.25 m. d) 4Rx semblance plot, $Tx - Rx_1 = 1.00$ m, $Tx - Rx_4 = 1.75$ m, Rx separation = 0.25 m. e) 3Rx semblance plot, $Tx - Rx_1 = 1.25$ m, $Tx - Rx_3 = 1.75$ m, Rx separation = 0.25 m. The transducer	

configuration is shown at the top of each sub-figure, with the Tx in red and the Rxs in yellow..... 159

Figure 7.5: Sparse receiver configuration scenarios/lack of intermediate receivers scenarios, using synthetic data CMP gather of Figure 7.2b. a) 7Rx semblance plot,  $T_x - R_{x1} = 0.25$  m,  $T_x - R_{x7} = 1.75$  m, Rx separation = 0.25 m. b) 4Rx semblance plot,  $T_x - R_{x1} = 0.25$  m,  $T_x - R_{x4} = 1.75$  m, Rx separation = 0.5 m. c) 3Rx semblance plot,  $T_x - R_{x1} = 0.25$  m,  $T_x - R_{x3} = 1.75$  m, Rx separation = 1.00 m. The transducer configuration is shown at the top of each sub-figure, with the Tx in red and the Rxs in yellow..... 159

Figure 7.6: a) Processed CO profile of the first/near-offset receiver ( $T_x - R_{x1} = 0.25$  m). The white arrows indicate some of the subsurface features, and the black line indicates the location of the investigated CMP gather (CMP 272). b) 7Rx field data CMP gather 272 and resultant semblance plot of the CMP gather. The transducer configuration is shown at the top of each sub-figure, with the Tx in red and the Rxs in yellow..... 163

Figure 7.7: Near-offset receiver configuration scenarios/lack of far-offset receivers scenarios, using field data CMP gather 272 of Figure 7.6b. a) 7Rx semblance plot,  $T_x - R_{x1} = 0.25$  m,  $T_x - R_{x7} = 1.75$  m, Rx separation = 0.25 m. b) 6Rx semblance plot,  $T_x - R_{x1} = 0.25$  m,  $T_x - R_{x6} = 1.50$  m, Rx separation = 0.25 m. c) 5Rx semblance plot,  $T_x - R_{x1} = 0.25$  m,  $T_x - R_{x5} = 1.25$  m, Rx separation = 0.25 m. d) 4Rx semblance plot,  $T_x - R_{x1} = 0.25$  m,  $T_x - R_{x4} = 1.00$  m, Rx separation = 0.25 m. e) 3Rx semblance plot,  $T_x - R_{x1} = 0.25$  m,  $T_x - R_{x3} = 0.75$  m, Rx separation = 0.25 m. The white arrows mark some of the spurious semblance peaks. The transducer configuration is shown at the top of each sub-figure, with the Tx in red and the Rxs in yellow..... 163

Figure 7.8: Far-offset receiver configuration scenarios/lack of near-offset receivers scenarios, using synthetic data CMP gather 272 of Figure 7.6b. a) 7Rx semblance plot,  $T_x - R_{x1} = 0.25$  m,  $T_x - R_{x7} = 1.75$  m, Rx separation = 0.25 m. b) 6Rx semblance plot,  $T_x - R_{x1} = 0.50$  m,  $T_x - R_{x6} = 1.75$  m, Rx separation = 0.25 m. c) 5Rx semblance plot,  $T_x - R_{x1} = 0.75$  m,  $T_x - R_{x5} = 1.75$  m, Rx separation = 0.25 m. d) 4Rx semblance plot,  $T_x - R_{x1} = 1.00$  m,  $T_x - R_{x4} = 1.75$  m, Rx separation = 0.25 m. e) 3Rx semblance plot,  $T_x - R_{x1} = 1.25$  m,  $T_x - R_{x3} = 1.75$  m, Rx separation = 0.25 m. The white arrows

mark some of the spurious semblance peaks. The transducer configuration is shown at the top of each sub-figure, with the Tx in red and the Rx's in yellow. .... 164

Figure 7.9: Sparse receiver configuration scenarios/lack of intermediate receivers scenarios, using synthetic data CMP gather 272 of Figure 7.6b. a) 7Rx semblance plot,  $Tx - Rx_1 = 0.25$  m,  $Tx - Rx_7 = 1.75$  m, Rx separation = 0.25 m. b) 4Rx semblance plot,  $Tx - Rx_1 = 0.25$  m,  $Tx - Rx_4 = 1.75$  m, Rx separation = 0.5 m. c) 3Rx semblance plot,  $Tx - Rx_1 = 0.25$  m,  $Tx - Rx_3 = 1.75$  m, Rx separation = 1.00 m. The white arrows mark some of the spurious semblance peaks. The transducer configuration is shown at the top of each sub-figure, with the Tx in red and the Rx's in yellow. .... 164

Figure 7.10: 500 MHz centre frequency field data set. a) Processed CO profile of the first receiver ( $Tx - Rx_1 = 0.25$  m). b) Filtered/smoothed stacking velocity field of the seven-receiver configuration derived from automated NMO velocity analysis on all high-fold/seven-fold CMP gathers. c) Filtered/smoothed stacking velocity field of the four-receiver sparse configuration derived from automated NMO velocity analysis on all high-fold/four-fold CMP gathers. d) Seven-fold stacked section obtained using the respective velocity field of (b). e) Four-fold stacked section obtained using the corresponding velocity field of (c). In (a), (d), and (e) the red arrow highlights an area with reduced horizontal ringing noise, the green arrow marks a reflector with improved continuity, and the blue arrow indicates an enhanced reflector. In (b) and (c) the white arrow indicates an area with different stacking velocities, whilst in (a), (d), and (e) the left-hand side of the hyperbola/pipe response. The transducer configuration is shown at the top of each sub-figure, with the Tx in red and the Rx's in yellow. The low-fold areas, as well as the muted area of the direct air wave and direct ground wave, are also highlighted in each sub-figure. .... 167

Figure 7.11: 500 MHz centre frequency field data set also previously presented in Ch. 6.4. a) Processed CO profile of the first receiver ( $Tx - Rx_1 = 0.25$  m). b) Filtered/smoothed stacking velocity field of the seven-receiver configuration derived from automated NMO velocity analysis on all high-fold/seven-fold CMP gathers. c) Filtered/smoothed stacking velocity field of the four-receiver sparse configuration derived from automated NMO velocity analysis on all high-fold/four-fold CMP gathers. d) Seven-fold stacked section obtained using the respective velocity field of (b). e) Four-fold stacked section obtained using the corresponding velocity field of (c). In (a), (d), and (e) the red arrow highlights an area with reduced ringing noise, the

- green arrow marks a reflector with improved continuity, and the blue arrow indicates an enhanced reflector. The transducer configuration is shown at the top of each sub-figure, with the Tx in red and the Rx's in yellow. The low-fold areas, as well as the muted area of the direct air wave and direct ground wave, are also highlighted in each sub-figure. .... 170
- Figure 7.12: 1000 MHz centre frequency field data set also previously presented in Ch. 6.5. a) Processed CO profile of the first receiver ( $Tx - Rx_1 = 0.165$  m). b) Filtered/smoothed stacking velocity field of the seven-receiver configuration derived from automated combined LMO NMO velocity analysis on all high-fold/seven-fold CMP gathers. c) Filtered/smoothed stacking velocity field of the four-receiver sparse configuration derived from automated combined LMO NMO velocity analysis on all high-fold/four-fold CMP gathers. d) Seven-fold stacked section obtained using the respective velocity field of (b). e) Four-fold stacked section obtained using the corresponding velocity field of (c). In (a), (d), and (e) the red arrow highlights an area with reduced ringing noise, the green arrow marks a reflector with improved continuity, and the blue arrow and blue boxes indicate some enhanced reflectors. The transducer configuration is shown at the top of each sub-figure, with the Tx in red and the Rx's in yellow. The low-fold areas, as well as the muted area of the direct air wave, are also highlighted in each sub-figure. .... 171
- Figure 7.13: Plan for increasing the number of receivers. .... 173
- Figure 7.14: a) 3D model with two horizontal layers developed to generate synthetic data for demonstrating the effect of increasing the number of receivers on velocity spectrum semblance analysis. b) 7Rx synthetic data CMP gather, obtained from the standard seven-receiver configuration, contaminated with white Gaussian noise and resultant semblance plot of the CMP gather. c) 13Rx synthetic data CMP gather, obtained from the diagonal thirteen-receiver configuration, contaminated with white Gaussian noise and resultant semblance plot of the CMP gather. The transducer configuration is shown at the top of each sub-figure, with the Tx in red and the Rx's in yellow. .... 177
- Figure 7.15: a) 3D two-layered model with the second layer dipping parallel to the survey line at a 45-degree angle developed to generate synthetic data for demonstrating the effect of increasing the number of receivers on velocity spectrum semblance

---

analysis. b) 7Rx synthetic data CMP gather, obtained from the standard seven-receiver configuration, contaminated with white Gaussian noise and resultant semblance plot of the CMP gather. c) 13Rx synthetic data CMP gather, obtained from the diagonal thirteen-receiver configuration, contaminated with white Gaussian and resultant semblance plot of the CMP gather. The transducer configuration is shown at the top of each sub-figure, with the Tx in red and the Rx's in yellow. .... 178

Figure 7.16: a) 3D two-layered model with the second layer dipping perpendicular to the survey line at a 45-degree angle developed to generate synthetic data for demonstrating the effect of increasing the number of receivers on velocity spectrum semblance analysis. b) 7Rx synthetic data CMP gather, obtained from the standard seven-receiver configuration, contaminated with white Gaussian noise and resultant semblance plot of the CMP gather. c) 13Rx synthetic data CMP gather, obtained from the diagonal thirteen-receiver configuration, contaminated with white Gaussian and resultant semblance plot of the CMP gather. The transducer configuration is shown at the top of each sub-figure, with the Tx in red and the Rx's in yellow. .... 179

# List of tables

Table 2.1: Materials that are typically encountered with GPR and their properties (relative permittivity, velocity, conductivity, attenuation), measured at 1 GHz frequency (Cassidy, 2008a).....	20
Table 2.2: Sensors & Software Inc. pulseEKKO range. Suitable frequencies for different applications (Sensors & Software Inc., 2021b).....	27
Table 4.1: Software supported file formats.....	86
Table 4.2: Processing methods of the 2D module of the software for SF CO GPR data. ....	86
Table 5.1: Estimated, relative to the first receiver, time errors between the applied time shifts and the detected time shifts calculated using the first break method used by Diamanti et al. (2018) for different thresholds. For clarity, the time errors have been rounded to the first decimal place so that they translate more easily as a number of samples. It is noted that the sampling interval of the data is equal to 0.1 ns. ....	102
Table 5.2: Estimated, relative to the first receiver, time errors between the applied time shifts and the detected time shifts calculated using the proposed method. For clarity, the time errors have been rounded to the first decimal place so that they translate more easily as a number of samples. It is noted that the sampling interval of the data is equal to 0.1 ns. ....	102

# Acknowledgements

First and foremost, I would like to express my sincere gratitude to my supervisor, Dr Craig Warren, for believing in me and providing me with the opportunity to further my studies, as well as for his continuous guidance, support, and patience. I could not have asked for a better advisor and mentor.

I would also like to thank my second supervisor, Prof James Martin, for supervising this project, as well as for his interest, enthusiastic support, and many useful suggestions.

My sincere gratitude to my third supervisor, Dr Nectaria Diamanti, from the Aristotle University of Thessaloniki, for supervising this project, as well as for her invaluable guidance, support, and patience.

Special thanks to Dr Peter Annan, from Sensors & Software Inc., for all the technical discussions and useful suggestions, as well as Sensors & Software Inc. for providing the necessary data for this project.

I thank my former office mates and especially Hisham for all the memorable times we had.

I would also like to thank my family and particularly my grandmother Efi and brother Argyris for all the motivating discussions and continuous support.

Finally, I owe sincere thanks to Eleftheria without who I would not have been able to complete this journey.

# Declaration

I declare that the work contained in this thesis has not been submitted for any other award and that it is all my own work. I also confirm that this work fully acknowledges opinions, ideas, and contributions from the work of others.

Any ethical clearance for the research presented in this thesis has been approved. Approval has been sought and granted through the Researcher's submission to Northumbria University's Ethics Online System on 6 January 2019.

I declare that the word count of this thesis is 52213 words.

Name: Dimitrios Angelis

Date: 15/01/2023

# 1

## **Introduction**

This introductory chapter presents the background and motivation for the research, the main as well as the specific objectives of the research project, and finally the structure of the thesis.

## 1.1 Motivation for the thesis

Ground-penetrating radar (GPR), also often referred to as ground-probing radar, subsurface radar, or simply georadar, is an active high-frequency (typically 2 MHz – 2 GHz) electromagnetic (EM) geophysical technique that exploits the wave character of EM fields in order to sense dielectric discontinuities in the shallow subsurface (typically < 50 m) (Neal, 2004). GPR is fully non-destructive/non-invasive and can generally provide rapidly, high-resolution surveys, as well as real-time data display, and therefore on-site feedback (Annan, 2005). For these reasons, it has gained immense popularity in recent years and is used either as a standalone technique or in combination with other geophysical methods for a wide variety of near-surface applications such as archaeological, engineering, environmental, geological, and military applications, among others.

GPR data can be collected using a variety of different survey methods. The most frequently used data acquisition mode is the common offset (CO), which is a single transmitter-receiver antenna offset mode, that allows for very fast and dense data acquisition, and hence, low-cost large-scale surveys to be conducted with relative ease (Annan, 2003). However, there are other, multi transmitter-receiver antenna offset acquisition modes, such as the common midpoint (CMP) and the wide-angle reflection and refraction (WARR), which can be considered as the EM equivalent to the seismic refraction and wide-angle reflection (Annan & Cosway, 1992). These modes have many benefits over the CO including the ability to process multi-offset GPR data similarly to seismic reflection data owing to their similarities, and thus the potential to exploit existing well-established processing schemes and tools of the latter, as well as the ability to provide subsurface EM wave velocity cross-sections and enhanced reflection cross-sections (Jol, 2009).

Despite their usefulness, multi-offset GPR data acquisition modes have seen limited adoption, since as their name implies, they require multiple offsets. This understandably translates into much more effort in data collection, especially when utilising a single transmitter-receiver pair, as well as in processing, and therefore, additional survey time and overall cost. However, recent advances in GPR timing and control

technology, have allowed the development of new multi-channel GPR systems with multiple concurrent data acquisition receivers (Annan & Jackson, 2017). These newly developed systems can conduct a simultaneous sampling from all receivers, and therefore can acquire very fast, i.e., with the same speed as the traditional CO mode of operation, multi-offset GPR data. Thus, they offer the potential to provide all the above-mentioned benefits with significantly reduced survey time and costs.

Nevertheless, despite their potential, these new GPRs come with many challenges. For instance, they can generate exceptionally large volumes of multi-offset GPR data (i.e., thousands of WARR/CMP gathers per hour), which not only makes them much more difficult to handle, but also significantly increases their overall analysis/processing time, and consequently the total cost of the survey itself. Furthermore, despite the similarities, there are also significant character differences between seismic reflection and GPR data, such as in timing alignment, signal attenuation, and velocity, which generally makes the adoption of well-established seismic schemes/tools problematic for high-volume multi-offset GPR data acquired by these systems. In addition, these systems can require many transducers to operate (e.g., eight transducers compared to the standard GPRs operating with only two transducers), which significantly increases their overall size, weight, and power requirements. This in turn also impacts the field environments and field conditions under which they can be deployed, but most importantly their cost, which is increased significantly compared to a typical single-channel CO GPR system.

## **1.2 Aims of the thesis**

The primary aim of this thesis is to investigate and develop new methods, workflows, as well as tools required for processing data acquired exclusively from newly developed GPR systems with multi-concurrent sampling receivers. A secondary aim is to investigate and evaluate different system configurations and survey parameters for these GPRs. These aims seek to address the key research question of whether highly accurate and detailed velocity models can be efficiently produced from large-volume multi-concurrent receiver GPR data, to improve GPR interpretations in a variety of geophysical and engineering problems.

The following specific objectives will enable the aforementioned project aims to be met:

- Develop a software framework and tool to enable large-volume, multi-offset GPR data to be visualised and processed, and a framework to test new algorithms/methods and workflows for multi-concurrent receiver GPR data.
- Develop new processing algorithms/methods to address specific challenges associated with processing multi-concurrent receiver GPR data, e.g., time misalignments, signal attenuation, and high-volume data analysis.
- Develop a processing workflow for multi-concurrent receiver GPR data, by incorporating in addition to any new necessary processing methods, any other suitable standard GPR and seismic reflection data processing methods, to create detailed velocity models and improve the quality of the data.
- Investigate and evaluate the system and survey design of the multi-concurrent receiver GPR systems, i.e., receiver density, position, and spatial sampling interval, to improve data quality and make them more practicable and cost-effective.

## **1.3 Structure of the thesis**

This thesis is organised into a further seven chapters as follows:

### **Chapter 2: Ground-penetrating radar principles**

In this chapter, a brief introduction to the concept of GPR is given. The history and applications of GPR as well as the basic theoretical background of the method, are discussed. The main types of GPR systems are described as well as the different GPR data collection and visualisation methods. Special emphasis is given in the chapter to the basic single-offset GPR data processing techniques, which are thoroughly discussed.

### **Chapter 3: Review of multi-offset GPR methods**

In this chapter, a short overview of the multi-offset GPR methods is given. The multi-offset GPR data acquisition modes are presented, and their advantages/disadvantages

compared to the single-offset mode are described. The basic multi-offset GPR data processing steps are detailed, with particular emphasis given to the moveout-based processing techniques and horizontal stacking. In addition, a review of the newly developed multi-concurrent receiver GPR systems is provided with an extensive discussion of the work that has been done with these systems to date.

#### **Chapter 4: Tools for obtaining and processing multi-concurrent receiver GPR data**

In this chapter, the tools that were used and developed to obtain and process multi-concurrent receiver GPR data are presented. A brief review of numerical modelling is provided, and the numerical solver used to generate synthetic data is presented. The GPR system(s) used to collect field data are described, and an example of a typical multi-concurrent receiver field data set is provided. Finally, special emphasis is given to the software that was developed for both visualising and processing GPR data, including data acquired by GPR systems with multi-concurrent receivers.

Research in this chapter has been published in Angelis et al. (2019) and Angelis et al. (2020).

#### **Chapter 5: Addressing the challenges of processing multi-concurrent receiver GPR data**

In this chapter, novel methods developed to address the main challenges of processing multi-concurrent receiver GPR data are presented. The chapter is divided into three different parts/sections, one for each method. In the first section, a method for managing the time misalignments from multi-concurrent receivers is introduced. In the second section, a CMP trace balancing method for compensating for the large amplitude differences in the data is described. Finally, in the third section, an automatic velocity analysis method is presented.

Research in this chapter has been published in Angelis et al. (2022a).

## **Chapter 6: A processing workflow for multi-concurrent receiver GPR data**

In this chapter, a processing workflow for multi-concurrent receiver GPR data is presented. This chapter is organised into five different sections. In the first section, the actual processing workflow is introduced. Then, in the following four sections, the processing workflow is evaluated in four different data case studies.

Research in this chapter has been published in Angelis et al. (2021) and Angelis et al. (2022a).

## **Chapter 7: The effect of multi-concurrent receiver arrangement on velocity analysis**

In this chapter, the effects of multi-concurrent receiver arrangement on velocity analysis are presented. The chapter is divided into two different sections. In the first section, the effects of reducing the number of receivers are presented and in the second section the effects of increasing the number of receivers.

Research in this chapter has been published in Angelis et al. (2022b).

## **Chapter 8: Conclusions and recommendations**

In this chapter, a summary of the thesis outputs is given along with some recommendations for future research.

# 2

## **Ground-penetrating radar principles**

This chapter provides a brief introduction to the concept of GPR. The chapter begins with a short overview of the history and applications of GPR. Then, the basic principle of GPR operation and wave propagation is discussed, as well as the material properties and their relationship to EM wave velocity and losses. Next, the types of GPR systems are described, including the relationship between the centre frequency of a system and EM wave depth penetration and resolution. Finally, following a brief discussion on the different GPR data collection modes and data visualisation methods, the basic single-offset data processing techniques are discussed in detail.

## 2.1 History of GPR

GPR is an EM geophysical technique that utilises high-frequency radio waves, typically in the range of 2 MHz to 2 GHz, to probe “the ground” (Annan, 2009), namely to map the distribution of its dielectric properties. It operates by the same fundamental rules as a conventional navigational RADAR – an acronym for Radio Detection And Ranging – but is applied primarily to subsurface investigations.

Historically, the basic principle of radar detection goes back almost to the beginning of the subject of electromagnetism itself. In 1886, Heinrich Hertz by testing Maxwell’s theories demonstrated that light and radio waves have similar behaviour, and verified experimentally the reflection and refraction of the latter by metallic objects and dielectric prisms, respectively (Skolnik, 2001). About two decades later, in the early 1900s, Hülsmeyer assembled and subsequently patented (Hülsmeyer, 1904) a device that would nowadays be known as a monostatic pulse radar. Hülsmeyer became the first person to utilise radar waves to detect remote terrestrial objects, and more specifically, to detect ships (Skolnik, 2001).

Nevertheless, the first description of the use of radio waves for the detection of buried objects, which is also probably the first report of a true GPR system, appeared in 1910 in two German patents by Leimbach & Löwy (1910a, 1910b). A few years later, in 1926, Hülsenbeck & Co (1926) used pulsed excitation techniques to determine the structure of buried features, while in 1930 Stern (1929, 1930) used radio waves to determine the ice thickness on the lower part of the Vernagtferner glacier in Austria (Clarke, 1987). Shortly afterwards, during World War II, radar development was accelerated rapidly as the military realised its capabilities, and in particular that it could be used for both defensive and offensive purposes (Skolnik, 2001).

After the war and until the 1970s radar technology remained relatively static. However, during this period, El-Said (1956) used radio waves to locate water tables in the Egyptian desert, while Waite & Schmidt (1962) and Bailey et al. (1964) used low-frequency radio waves to detect ice sheets. Then in the early 1970s, the interest in GPR boomed due to the Apollo Lunar missions (Annan, 1973), and more specifically, the Apollo 17

exploration mission, which also carried a GPR to generate a continuous Lunar profile (Porcello et al., 1974).

Since then, the general advancements in technology, such as the development and utilisation of analogue-to-digital converters (ADCs), fibre-optic cables, Bluetooth links, and improved shielding materials, have enabled the development of both single- and multi-channel array commercial GPR systems. This, in turn, has led to the expansion of the method in several different fields. A comprehensive breakdown of the general history of radar and GPR in particular, both from a commercial and research perspective, has been compiled by Skolnik (2001), Annan (2002), and Daniels (2004).

## 2.2 GPR applications

GPR is a popular geophysical method with a wide range of diverse applications. This is mainly due to its non-invasive nature and its ability to provide very fast, high-resolution data as well as on-site feedback. An overview of these applications is presented below, whilst more detailed information can be found in Peters et al. (1994), Daniels (2004), Reynolds (2011), and Wai-Lok Lai et al. (2018).

- **Archaeological applications**

- Subsurface mapping for excavation planning (e.g., Conyers et al., 2002).
- Location and identification of buried structures, and graves (e.g., Yalçiner et al., 2009).
- Investigation of ancient monuments, and statues (e.g., Angelis et al., 2018).

- **Geological and environmental applications**

- Stratigraphy mapping (e.g., Davis & Annan, 1989).
- Natural void and cavities detection (e.g., Chamberlain et al., 2000).
- Groundwater table investigation/mapping (e.g., Endres et al., 2000).
- Contamination assessment (e.g., Daniels et al., 1995).

- **Glaciological applications**

- Glacier bodies mapping (e.g., Bernard et al., 2014).
- Ice thickness mapping (e.g., Kämäri et al., 2017).

- **Engineering and construction applications**
  - Railway inspection (e.g., Hugenschmidt, 2000).
  - Concrete and rebar inspection (e.g., Gehrig et al., 2004).
  - Road and bridge inspection (e.g., Benedetto et al., 2012).
  - Underground utility detection such as pipes and cables (e.g., Porsani et al., 2012).
- **Military and security applications**
  - Land mine detection (e.g., Metwaly, 2007).
  - Human body detection (e.g., Instanes et al., 2004).
  - Location of hidden tunnels (e.g., Diamanti & Annan, 2019).

## 2.3 GPR wave propagation

The basic principle of GPR operation is quite simple and is based on transmitting and receiving EM waves into and from the subsurface respectively, utilising antennas. Antennas are devices that radiate energy as EM waves by transforming electrical currents flowing on their structures (Balanis, 2016).

More specifically, a typical GPR system works by emitting a short-duration (i.e., order of a few nanoseconds) high-voltage pulse of EM energy, in a frequency range around a centre frequency, from a transmitting antenna (Tx) into the investigated medium. The energy is then reflected and/or scattered due to the discontinuities of the electrical properties of the materials inside the medium (Annan, 2003). Finally, part of the reflected energy is sensed by a receiving antenna (Rx) which records the amplitude of the signal, i.e., the signal strength, as well as the two-way travel time (TWT), i.e., the time duration from when the pulse was emitted to when reflected forms of it are received.

### 2.3.1 Wave paths

Nevertheless, the reflections caused by the subsurface discontinuities are not the only signals sensed and recorded by the receiving antenna. Figure 2.1 illustrates the four main wave/ray paths that transmitted GPR signals could follow, along with their

arrival times versus the transmitter-receiver separation distance/offset (Annan, 2005; Neal, 2004).

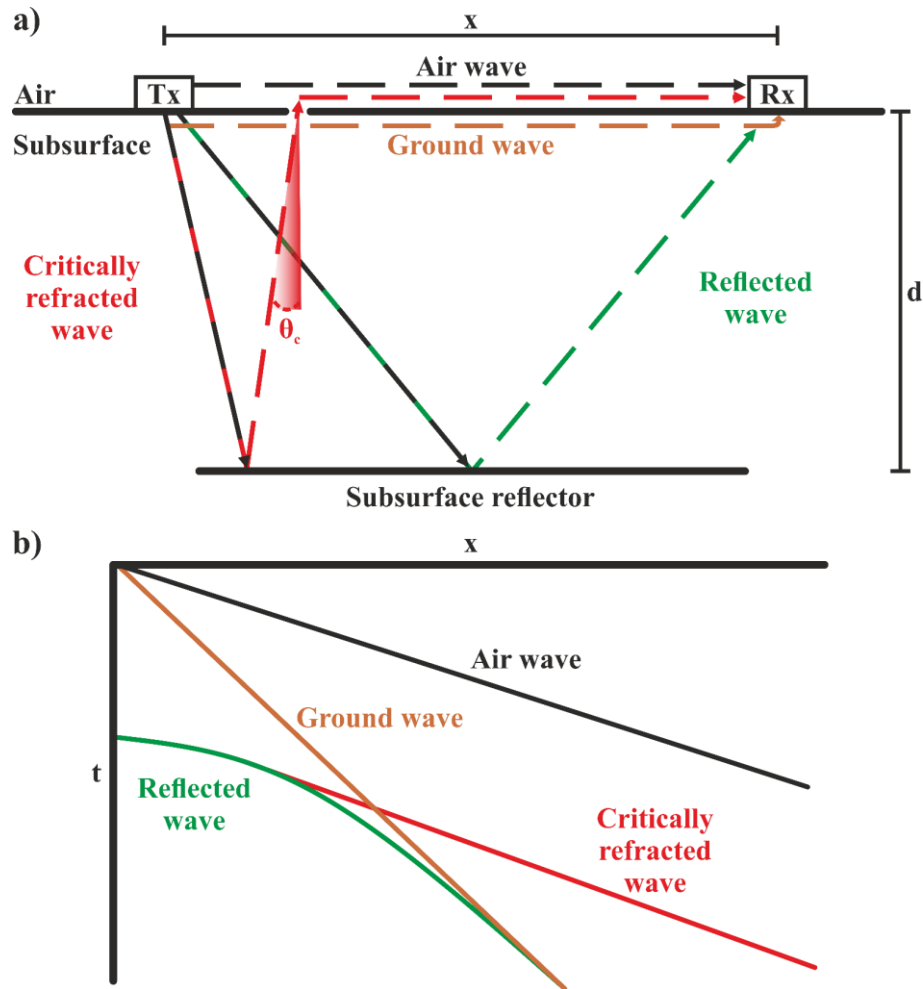


Figure 2.1: a) The signal ray path for the direct air wave (black), the direct ground wave (orange), the reflected wave (green), and the critically refracted wave (red). b) The arrival time of the signals of (a) versus the offset.

**Direct air wave:** This is the first signal/wave sensed and recorded by the receiver, and as its name implies, it follows a direct path. It travels through the air with the velocity of light ( $c$ ) and very often appears to have the largest amplitude, as it is usually subject to the lowest attenuation and scattering. The travel time of the direct air wave ( $t_a$ ) is linear and is given by (2.1).

$$t_a = \frac{x}{c} \quad (2.1)$$

where:

- $t_a$  The travel time of the direct air wave (s).
- $x$  The transmitter and receiver separation distance (m).
- $c$  The velocity of light in free space ( $\sim 3 \times 10^8$  m/s).

**Direct ground wave:** This is usually (see Figure 2.1b) the second wave recorded by the receiver, and like the air wave, it follows a direct path. However, rather than travelling through the air with the velocity of light, it travels along the surface interface with a velocity ( $v$ ). Both the air wave and the ground wave mask any primary reflections coming from shallow features (Neal, 2004). The travel time of the direct ground wave ( $t_g$ ) is also linear and is given by (2.2).

$$t_g = \frac{x}{v} \quad (2.2)$$

where:

- $t_g$  The travel time of the direct ground wave (s).
- $x$  The transmitter and receiver separation distance (m).
- $v$  The velocity of EM waves in the medium (m/s).

**Reflected wave:** This wave travels through the subsurface layer with a velocity ( $v$ ). Since it takes a longer path than the aforementioned waves, it arrives later in time. The travel time of the reflected wave ( $t_r$ ) is hyperbolic and is given by (2.3).

$$t_r = \frac{\sqrt{x^2 + 4d^2}}{v} \quad (2.3)$$

where:

- $t_r$  The travel time of the reflected wave (s).
- $x$  The transmitter and receiver separation distance (m).
- $d$  The distance/depth to the subsurface reflector (m).
- $v$  The velocity of EM waves in the medium (m/s).

**Critically refracted wave:** This wave, which is also often referred to as a lateral wave, is a result of a shallow reflected wave that approaches the surface at the appropriate critical angle ( $\theta_c$ ) and is then, as Snell's law states, refracted along the surface interface (Clough, 1976; Neal, 2004). The travel time of the critically refracted wave ( $t_c$ ) is linear and is given by (2.4) (Bohidar & Hermance, 2002).

$$t_c = \frac{x}{c} + \frac{2d\cos\theta_c}{v} \quad (2.4)$$

where:

- $t_c$  The travel time of the critically refracted wave (s).
- $c$  The velocity of light in free space ( $\sim 3 \times 10^8$  m/s).
- $x$  The transmitter and receiver separation distance (m).
- $v$  The velocity of EM waves in the medium (m/s).
- $\theta_c$  The critical angle between the reflected wave and the surface interface ( $^\circ$ ).

### 2.3.2 Material types and properties

The propagation of the EM waves in the subsurface depends to a significant extent on the materials and their properties. Generally, materials, depending on whether the predominant phenomenon is polarisation (i.e., electric displacement current density), magnetisation (i.e., magnetic displacement current density), or conduction (i.e., electric conduction current density), can be categorised as **dielectrics**, **magnetics**, or **conductors**, respectively (Balanis, 2012).

#### Dielectrics, permittivity, and relative permittivity

A dielectric material is a material whose internal dominant electric charges, i.e., positive and negative charges, are bounded by atomic and molecular forces, and are consequently, not free to flow. When an external electric field is applied to such material the charged particles within the material shift slightly in positions relative to each other and therefore cause electric polarisation.

There are three different mechanisms of electric polarisation: dipole or orientational polarisation, ionic or molecular polarisation, and electronic polarisation. For the frequency range where GPR mainly operates, the primary mechanism is that of dipole polarisation in which the electric dipoles of the material tend to align with the externally applied field (Warren, 2009).

The free space relationship between the electric flux density ( $\vec{D}$ ) and the applied electric field ( $\vec{E}$ ) is given by (2.5), while the electric polarisation ( $\vec{P}$ ) is given by (2.6).

$$\vec{D} = \epsilon_0 \vec{E} \quad (2.5)$$

$$\vec{P} = \epsilon_0 \chi_e \vec{E} \quad (2.6)$$

where:

$\vec{D}$  The electric flux density (C/m<sup>2</sup>).

$\vec{P}$  The electric polarisation (C/m<sup>2</sup>).

$\vec{E}$  The electric field intensity (V/m).

$\epsilon_0$  The electric permittivity of free space (8.854 x 10<sup>-12</sup> F/m).

$\chi_e$  The electric susceptibility (dimensionless quantity).

In case dipole polarisation occurs, then the electric polarisation vector which is defined by (2.6) is added to equation (2.5), and the new equations are given by (2.7) and (2.8).

$$\begin{aligned} \vec{D} &= \epsilon_0 \vec{E} + \vec{P} \\ \Leftrightarrow \vec{D} &= \epsilon_0 \vec{E} + \epsilon_0 \chi_e \vec{E} \\ \Leftrightarrow \vec{D} &= \epsilon_0 (1 + \chi_e) \vec{E} \end{aligned} \quad (2.7)$$

$$\Leftrightarrow \vec{D} = \epsilon \vec{E} \quad (2.8)$$

where:

$\vec{D}$  The electric flux density (C/m<sup>2</sup>).

$\vec{E}$  The electric field intensity (V/m).

$\epsilon$  The electric permittivity (F/m).

$\epsilon_0$  The electric permittivity of free space (8.854 x 10<sup>-12</sup> F/m).

$\chi_e$  The electric susceptibility (dimensionless quantity).

Lastly, by equating (2.7) and (2.8), equation (2.9) occurs, which describes the material property known as relative electric permittivity or simply dielectric constant. The **relative electric permittivity** ( $\epsilon_r$ ) is the ratio of the **electric permittivity** ( $\epsilon$ ), which indicates the charge storage capacity of the material, to the electric permittivity of free space ( $\epsilon_0$ ).

$$\epsilon_r = \frac{\epsilon}{\epsilon_0} = 1 + \chi_e \quad (2.9)$$

where:

- $\epsilon_r$  The relative electric permittivity/dielectric constant (dimensionless quantity).
- $\epsilon$  The electric permittivity (F/m).
- $\epsilon_0$  The electric permittivity of free space ( $8.854 \times 10^{-12}$  F/m).
- $\chi_e$  The electric susceptibility (dimensionless quantity).

### **Magnetics, permeability, and relative permeability**

Magnetic material is a material that exhibits magnetic polarisation when subjected to an external magnetic field. Like dielectrics whose electric dipoles align with the applied electric field, the magnetic dipoles of this type of material tend to align with the externally applied magnetic field.

The free space relationship between the magnetic flux density ( $\vec{B}$ ) and the applied magnetic field ( $\vec{H}$ ) is given by (2.10), and the magnetic polarisation ( $\vec{M}$ ) is given by (2.11).

$$\vec{B} = \mu_0 \vec{H} \quad (2.10)$$

$$\vec{M} = \mu_0 \chi_\mu \vec{H} \quad (2.11)$$

where:

- $\vec{B}$  The magnetic flux density (W/m<sup>2</sup>).
- $\vec{M}$  The magnetic polarisation (W/m<sup>2</sup>).
- $\vec{H}$  The magnetic field intensity (A/m).
- $\mu_0$  The magnetic permeability of free space ( $4\pi \times 10^{-7}$  H/m).
- $\chi_\mu$  The magnetic susceptibility (dimensionless quantity).

In case magnetic polarisation occurs, then the magnetic polarisation vector which is defined by (2.11) is added to equation (2.10), and the new equations are given by (2.12) and (2.13).

$$\begin{aligned}\vec{B} &= \mu_0 \vec{E} + \vec{M} \\ \Leftrightarrow \vec{B} &= \mu_0 \vec{E} + \mu_0 \chi_\mu \vec{H} \\ \Leftrightarrow \vec{B} &= \mu_0 (1 + \chi_\mu) \vec{H} \end{aligned} \tag{2.12}$$

$$\Leftrightarrow \vec{B} = \mu \vec{H} \tag{2.13}$$

where:

$\vec{B}$  The magnetic flux density (W/m<sup>2</sup>).

$\vec{H}$  The magnetic field intensity (A/m).

$\mu$  The magnetic permeability (H/m).

$\mu_0$  The magnetic permeability of free space ( $4\pi \times 10^{-7}$  H/m).

$\chi_\mu$  The magnetic susceptibility (dimensionless quantity).

Lastly, by equating (2.12) and (2.13), equation (2.14) occurs, which describes the material property known as relative magnetic permeability. The **relative magnetic permeability** ( $\mu_r$ ) is the ratio of the **magnetic permeability** ( $\mu$ ), which indicates the ability of the material to support the formation of a magnetic field, to the magnetic permeability of free space ( $\mu_0$ ).

$$\mu_r = \frac{\mu}{\mu_0} = 1 + \chi_\mu \tag{2.14}$$

where:

$\mu_r$  The relative magnetic permeability (dimensionless quantity).

$\mu$  The magnetic permeability (H/m).

$\mu_0$  The magnetic permeability of free space ( $4\pi \times 10^{-7}$  H/m).

$\chi_\mu$  The magnetic susceptibility (dimensionless quantity).

In general, the magnetic effect of materials has a negligible influence on the propagation of the GPR waves (Olhoeft, 1998). Therefore, in most cases, the magnetic permeability of materials is considered to be equal to that of free space, and consequently, the relative magnetic permeability is equal to one (i.e.,  $\mu_r = 1$ ) (Telford et al., 1990). In a few words, materials are usually assumed to be non-magnetic (Cassidy, 2009a). Nonetheless, the relative magnetic permeability of a material must be taken under consideration in cases where the volume of its magnetic minerals (e.g., magnetite, hematite, maghemite) is more than 10 – 20 %, for instance in igneous rocks, iron-rich soils, and rusting steel rebars (Cassidy, 2008b; Olhoeft & Capron, 1993).

### **Conductors, and conductivity**

A conductor is a material whose predominant feature is the continuous random migration of negative electric charges, known as free electrons, and the generation of current flow. In general, free electrons move randomly and produce a net zero current through the surface of the material. However, when an external electric field is applied, then they drift in the negative direction of that field, and as a result, they generate a conduction current.

The material property that characterises the conductive properties of the free electrons, i.e., the property that measures the ability of the material to conduct an electric current, is called **conductivity** ( $\sigma$ ), and relates the electric field intensity ( $\vec{E}$ ) to the electric conduction current density ( $\vec{J}$ ). The equation that describes this relation is known as Ohm's Law and is given by (2.15).

$$\vec{J} = \sigma \vec{E} \tag{2.15}$$

where:

$\vec{J}$  The electric conduction current density ( $A/m^2$ ).

$\vec{E}$  The electric field intensity ( $V/m$ ).

$\sigma$  The electric conductivity ( $S/m$ ).

### 2.3.3 Wave velocity and losses

Permittivity, permeability, and conductivity are known as constitutive parameters and govern the propagation velocity as well as the attenuation of the EM waves in a medium.

The velocity ( $v$ ) of EM waves in a material is generally given by (2.16), which is developed from the solution for a uniform plane wave propagating in an unbounded lossy medium (Balanis, 2012). For a material that is a good conductor (i.e., when the loss factor  $(\sigma/(\omega\epsilon_0\epsilon_r))^2 \gg 1$ ), equation (2.16) simplifies and the velocity of EM waves can be approximated by (2.17). Similarly, for a material that is a poor conductor/low-loss material (i.e., when the loss factor  $(\sigma/(\omega\epsilon_0\epsilon_r))^2 \ll 1$ ), equation (2.16) also simplifies and the velocity of EM waves can be approximated by (2.18).

$$v = \frac{c}{\sqrt{\frac{\epsilon_r \mu_r}{2} \left( \sqrt{1 + \left( \frac{\sigma}{\omega \epsilon_0 \epsilon_r} \right)^2} + 1 \right)}} \quad (2.16)$$

$$v \approx \sqrt{\frac{2\omega}{\mu_0 \mu_r \sigma}} \quad (2.17)$$

$$v \approx \frac{c}{\sqrt{\epsilon_r \mu_r}} \quad (2.18)$$

where:

- $v$  The velocity of EM waves in the medium (m/s).
- $c$  The velocity of light in free space ( $\sim 3 \times 10^8$  m/s).
- $\epsilon_r$  The relative electric permittivity/dielectric constant (dimensionless quantity).
- $\epsilon_0$  The electric permittivity of free space ( $8.854 \times 10^{-12}$  F/m).
- $\mu_r$  The relative magnetic permeability (dimensionless quantity).
- $\mu_0$  The magnetic permeability of free space ( $4\pi \times 10^{-7}$  H/m).
- $\sigma$  The electric conductivity (S/m).
- $\omega$  The angular frequency (rad/s).

The attenuation ( $\alpha$ ) of EM waves in a material is generally given by (2.19), which is also developed from the solution for a uniform plane wave propagating in an unbounded lossy medium (Balanis, 2012). From the equation (2.19), it is evident that attenuation is frequency-dependent, with high-frequency EM waves attenuating faster than low-frequency ones, as it is proportional to the angular frequency ( $\omega$ ) of the waves, and thus, to their frequency ( $f$ ) (i.e.,  $\omega = 2\pi f$ ). For a good conductor, equation (2.19) simplifies and the attenuation of EM waves can be approximated by (2.20). Similarly, for a poor conductor equation (2.19) also simplifies and the attenuation of EM waves can be approximated by (2.21). Notice that in the case of a good conductor, attenuation is frequency-dependent, whilst in the case of a poor conductor attenuation is frequency-independent.

$$\alpha = 8.686\omega \sqrt{\frac{\epsilon_0\epsilon_r\mu_0\mu_r}{2} \left( \sqrt{1 + \left(\frac{\sigma}{\omega\epsilon_0\epsilon_r}\right)^2} - 1 \right)} \quad (2.19)$$

$$\alpha \simeq 8.686 \sqrt{\frac{\omega\mu_0\mu_r\sigma}{2}} \quad (2.20)$$

$$\alpha \simeq 8.686 \frac{\sigma}{2} \sqrt{\frac{\mu_0\mu_r}{\epsilon_0\epsilon_r}} \quad (2.21)$$

where:

- $\alpha$  The attenuation of EM waves in the medium (dB).
- $\epsilon_r$  The relative electric permittivity/dielectric constant (dimensionless quantity).
- $\epsilon_0$  The electric permittivity of free space ( $8.854 \times 10^{-12}$  F/m).
- $\mu_r$  The relative magnetic permeability (dimensionless quantity).
- $\mu_0$  The magnetic permeability of free space ( $4\pi \times 10^{-7}$  H/m).
- $\sigma$  The electric conductivity (S/m).
- $\omega$  The angular frequency (rad/s).

Having described the constitutive parameters and their significant effect on velocity as well as the attenuation of EM waves in a medium, Table 2.1 shows some materials commonly encountered with GPR. Along with these materials are also shown the corresponding values of the relative permittivity, velocity, conductivity, and attenuation, all measured at 1 GHz frequency.

Table 2.1: Materials that are typically encountered with GPR and their properties (relative permittivity, velocity, conductivity, attenuation), measured at 1 GHz frequency (Cassidy, 2008a).

<b>Material</b>	$\epsilon_r$	$v$ (m/ns)	$\sigma$ ( $\mu\text{S/m}$ )	$\alpha$ (dB/m)
<b>Air</b>	1	0.3	0	0
<b>Clay (dry)</b>	2 – 20	0.07 – 0.21	1 – 100	1 – 36
<b>Clay (wet)</b>	15 – 40	0.05 – 0.08	100 – 1000	42 – 252
<b>Concrete (dry)</b>	4 – 10	0.09 – 0.15	1 – 10	< 1 – 5
<b>Concrete (wet)</b>	10 – 20	0.07 – 0.09	10 – 100	5 – 36
<b>Fresh water</b>	81	0.03	0.1 – 10	< 1
<b>Fresh water ice</b>	3 – 4	0.15 – 0.17	1	< 1
<b>Granite (dry)</b>	5 – 8	0.11 – 0.13	0.001 – 0.00001	< 1 – 5
<b>Granite (wet)</b>	5 – 15	0.08 – 0.13	1 – 10	< 1 – 4
<b>Limestone (dry)</b>	4 – 8	0.11 – 0.15	0.001 – 0.0000001	< 1
<b>Limestone (wet)</b>	6 – 15	0.08 – 0.12	10 – 100	6 – 42
<b>Sand (dry)</b>	4 – 6	0.12 – 0.15	0.001 – 1	< 1
<b>Sand (wet)</b>	10 – 30	0.05 – 0.09	0.1 – 10	< 1 – 3
<b>Sea water</b>	81	0.03	4000	> 600
<b>Sea water ice</b>	4 – 8	0.11 – 0.15	10 – 100	8 – 57
<b>Soil (average)</b>	16	0.08	5	2

Nevertheless, the total losses of the GPR EM waves do not depend solely on the attenuation caused by the materials of the subsurface. The EM wave losses, and hence, their penetration depth is primarily governed by the total path loss ( $L_T$ ), which is given by (2.22) and the mechanism of which is shown in Figure 2.2. Material attenuation loss ( $L_a$  or  $\alpha$ ), which was previously discussed, along with the antenna spreading loss ( $L_s$ ), and the target scattering loss ( $L_{sc}$ ), are the largest contributors (red colour in Figure 2.2). More detailed information about these mechanisms can be found in Daniels (2004) and Reynolds (2011).

$$L_T = L_e + L_m + L_{t1} + L_{t2} + L_s + L_a + L_{sc} \quad (2.22)$$

where:

- $L_T$  The total path loss (dB).
- $L_e$  The antenna radiation efficiency loss (dB).
- $L_m$  The antenna mismatch efficiency loss (dB).
- $L_{t1}$  The transmission loss from the air to the material (dB).
- $L_{t2}$  The transmission loss from the material to the air (dB).
- $L_s$  The antenna spreading loss (dB).
- $L_a$  The material attenuation loss (dB).
- $L_{sc}$  The target scattering loss (dB).

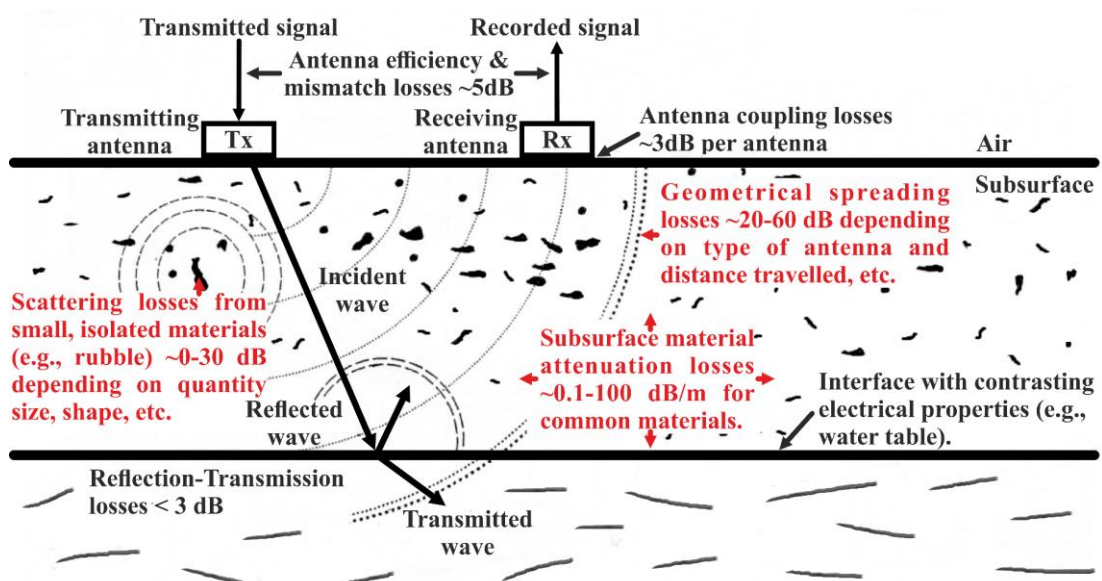


Figure 2.2: Attenuation mechanisms of the GPR signal. The largest contributors are depicted in red colour. Figure adapted from Cassidy (2008a).

## 2.4 GPR systems

A typical commercial GPR system, an example of which is shown in Figure 2.3, consists mainly of four different parts:

- The **transmitting antenna**, which transforms the electrical voltage signals into EM pulses and radiates them into the investigated medium
- The **receiving antenna**, which detects the EM waves returning from the investigated medium (i.e., the scattered, refracted, and reflected waves) and transforms them into recordable electrical voltage signals.
- The **control/computer unit**, which handles the functions of the transducers as well as of other useful survey parameters, records the detected signals, and has visualisation, processing and data storage capabilities.
- The **battery pack** (usually a 12 V battery), which is used to power the system.

Most of the time, however, GPR systems also include additional parts such as a **sledge** or a **survey cart** with an odometer, which allows the system to be pulled and/or pushed across the surface of the ground, and a **global positioning system (GPS)**. Both the survey cart and the GPS assist in the accurate lateral and vertical positioning of the collected data.

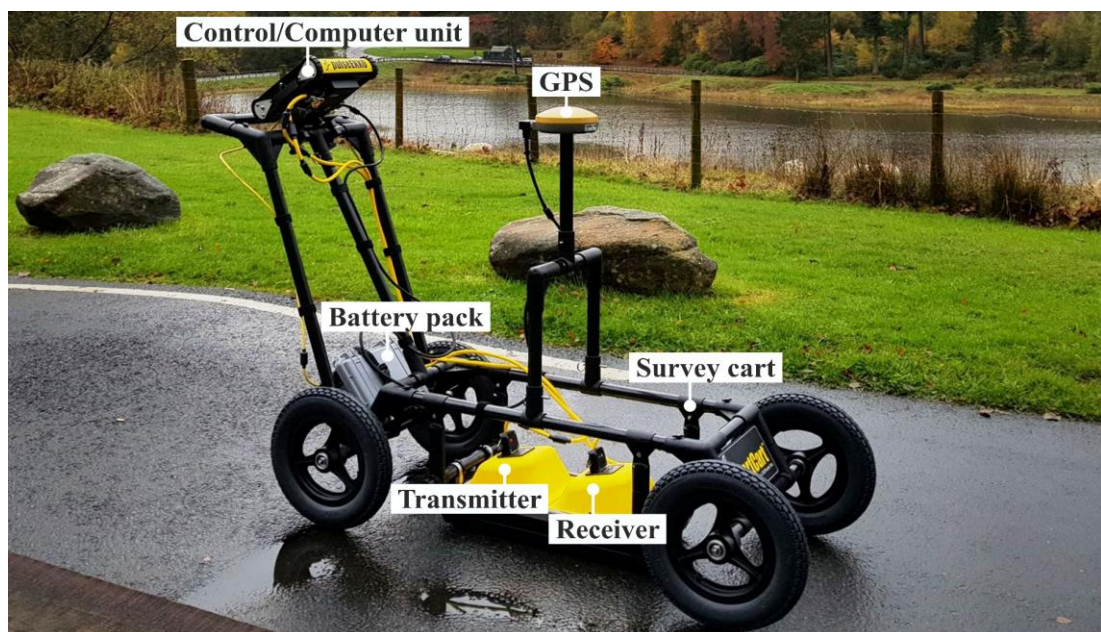


Figure 2.3: Typical GPR system (pulseEKKO – Sensors & Software Inc. (2021b)).

### 2.4.1 System types

GPR systems, depending on the domain that they operate, namely the time or the frequency domain, can be classified into two different categories: **impulse** and **continuous wave (CW)** systems (Koppenjan, 2009).

The majority of the GPR systems today belong to the first category, i.e., impulse. Their principle of operation is based on the transmission of a discrete short-duration pulse at a given pulse repetition frequency (PRF) into the investigated medium and recording the reflected signals as a function of time. The main advantages of impulse GPRs are the low-cost parts and the fact that generating an impulse waveform is generally simple. Their disadvantages are the undesirable ringing and limitations in resolution owing to the pulse width (Koppenjan, 2009).

The CW and stepped frequency GPR systems, as their name implies, transmit the signal as a continuous waveform whose carrier frequency changes either continuously or in frequency steps. Since they produce a frequency and not a time-domain response, an inverse Fourier transform is required. The main advantages of the CW and stepped frequency GPR systems are the controlled transmission of frequencies, as well as their power efficiency. Their disadvantages are the complex electronics and the requirement of a digital signal processing (DSP) board to perform the aforementioned transform (Koppenjan, 2009).

Finally, GPR systems can also be categorised based on the arrangement of the transmitting and receiving antennas into **monostatic** and **bistatic** systems. Monostatic GPRs have only one antenna that can be used both as a transmitter and receiver, whereas bistatic have two separate antennas that serve as a transmitter and receiver, respectively. Bistatic antennas can be contained in separate (see Figure 2.3) or in the same housing that usually makes their separation distance fixed (Annan, 2005; Reynolds, 2011).

## 2.4.2 System centre frequency and depth penetration

GPR systems are generally identified by their operating frequency, which is one of their most important factors, and usually indicates the centre frequency ( $f_c$ ) as well as bandwidth (B) of the system. The bandwidth which is normally related to the centre frequency (Annan, 2003), is the range of frequencies present in the waveform, and for impulse GPRs, is defined as the inverse of the duration of the generated pulse, i.e., the inverse of the pulse width (W) (2.23). A graphical representation of the pulse width, bandwidth, and centre frequency is presented in Figure 2.4.

As has been shown in a previous section (Ch. 2.3.3), material attenuation, which is one of the primary contributors to the total path loss, is frequency-dependent, and more specifically is proportional to the frequency. Consequently, this means that the EM wave penetration is greatly affected and is inversely proportional to the centre frequency of the GPR system.

$$B = \frac{1}{W} = f_c \quad (2.23)$$

where:

B The bandwidth (Hz).

W The pulse width (s).

$f_c$  The centre frequency (Hz).

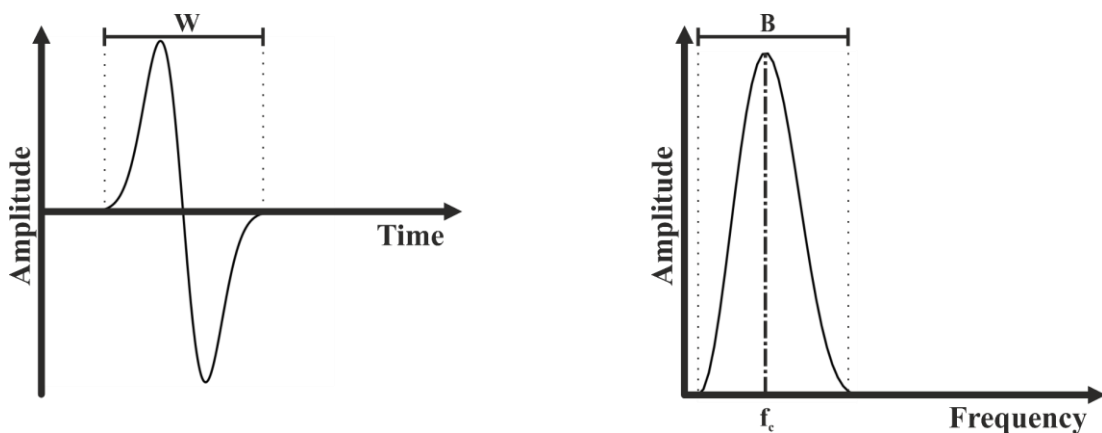


Figure 2.4: The pulse width (W), bandwidth (B) and centre frequency ( $f_c$ ).

### 2.4.3 System centre frequency and resolution

Another important factor of a GPR system is its resolution/resolving power, as it determines whether the target(s) can be detected, and if so, with how much precision and geometrical detail (i.e., size, shape, thickness, etc.) (Annan, 2003). The overall resolution of a GPR system is divided into **vertical or depth resolution** and **horizontal or lateral resolution** as depicted in Figure 2.5a.

Figure 2.5b illustrates the resolution concept for two localised circular targets. As can be seen, the depth resolution is defined as the minimum vertical separation distance ( $\Delta r$ ) between the two targets so that they are detectable, whereas the lateral resolution is defined as the minimum horizontal separation distance ( $\Delta l$ ). According to Annan (2005), these two distances are given by (2.24) and (2.25), respectively. Equation (2.24) shows that depth resolution is a function of the pulse width and the velocity of EM waves in the medium, whereas equation (2.25) shows that lateral resolution is a function not only of the aforementioned but also of the distance of the targets from the antennas, with the greater this distance the lower the lateral resolution.

Finally, given these two equations, as well as the relationship between pulse width and centre frequency (2.23), it becomes obvious that the resolution, either vertical or horizontal, is also greatly affected by the centre frequency of the system. More specifically, it is proportional to it.

$$\Delta r \geq \frac{vW}{4} \quad (2.24)$$

$$\Delta l \geq \sqrt{\frac{vdW}{2}} \quad (2.25)$$

where:

- $\Delta r$  The vertical distance between two targets (m).
- $\Delta l$  The horizontal distance between two targets (m).
- $W$  The pulse width (s).
- $d$  The distance/depth to the targets (m).
- $v$  The velocity of EM waves in the medium (m/s).

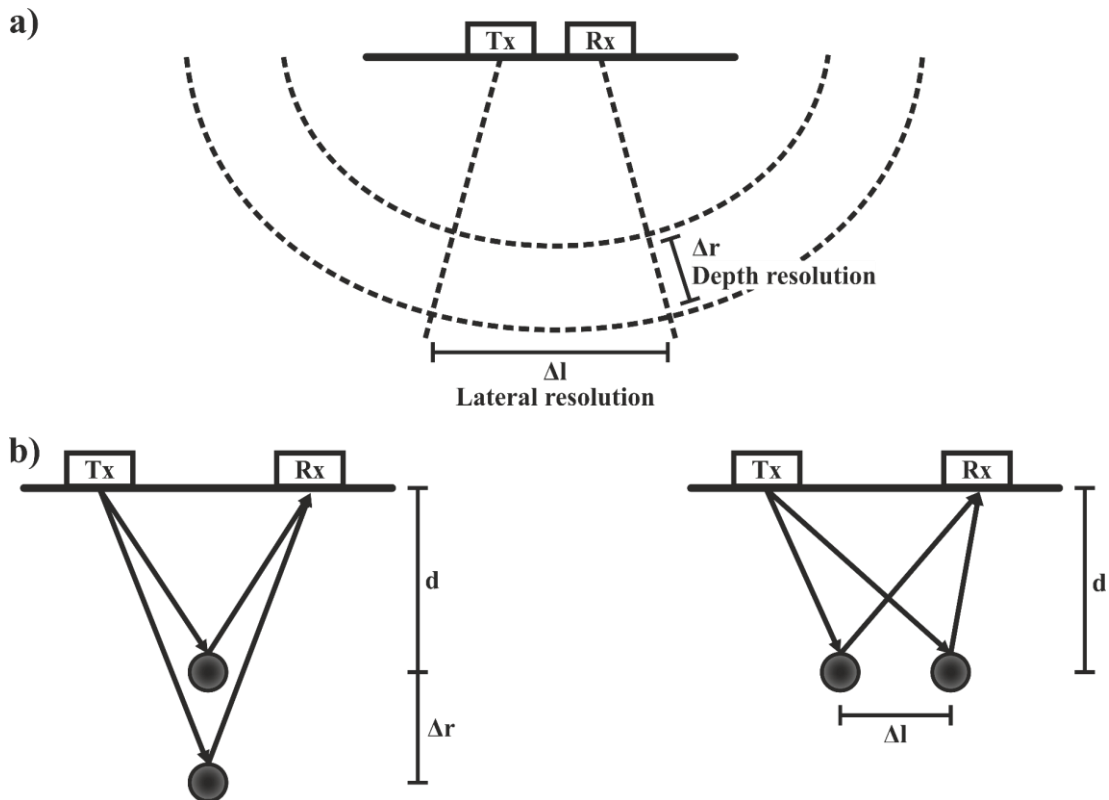


Figure 2.5: a) Depth and lateral resolution of a GPR system. b) Depth and lateral resolution concept for two circular targets. Figure(s) adapted from Annan (2005).

From the above (i.e., Ch. 2.4.2 and Ch. 2.4.3), it also becomes understandable that the choice of the antenna, i.e., of the centre frequency, is crucial for a GPR investigation, and that very often a compromise between penetration and resolution is necessary. That being said, Table 2.2 illustrates each GPR system in the Sensors & Software Inc. pulseEKKO range by a centre frequency and their intended application.

Table 2.2: Sensors & Software Inc. pulseEKKO range. Suitable frequencies for different applications (Sensors & Software Inc., 2021b).

Centre frequency (MHz)	Deep geology, glaciology	Geology	Utilities, geotechnical	Archaeology	Forensics/snow and ice	Mining quarrying	Concrete, roads, bridges
12.5	▪						
25	▪						
50	▪	▪					
100		▪	▪				
200		▪	▪				
250			▪	▪	▪		
500				▪	▪		
1000						▪	▪

## 2.5 GPR data collection

GPR data can be collected using a wide variety of different methods, where the total number of transducers or even the physical relationship between them, such as their separation distance and/or orientation, may be different. These methods, depending on the purpose of the survey, can either be deployed separately or together to provide additional subsurface information or to enhance certain responses.

### 2.5.1 Data acquisition modes

The primary GPR data acquisition mode is the **CO** illustrated in Figure 2.6. This is a single-offset mode that deploys a single transmitter and receiver which always maintain a constant separation distance and are moved together along the survey line. The main advantage of this mode of operation is that allows fast high-resolution surveys to be conducted. However, it can only provide constant subsurface EM wave velocity models and requires data to be collected at uniform spacings in order to be visualised and processed using advanced techniques (Annan, 2009).

In addition to the CO mode, there are other, multi-offset acquisition modes such as the **CMP** and **WARR**, which are the EM equivalent of the seismic refraction and wide-angle reflection (Annan & Cosway, 1992) and are also depicted in Figure 2.6. In the first one, both the transmitter and the receiver are moved simultaneously away from a fixed location, whilst in the second one the transmitter or the receiver remains stationary, and the other transducer moves along the survey line at regular intervals. Both modes have many benefits over the CO, such as providing detailed subsurface EM wave velocity models. However, compared to the CO mode, they are very time-consuming, as they not only require multiple offsets, instead of a common/single offset, but also different and/or additional signal processing steps (Daniels, 2004). The multi-offset GPR methods will be discussed in detail in the next chapter of this thesis (Ch. 3), which is dedicated to them.

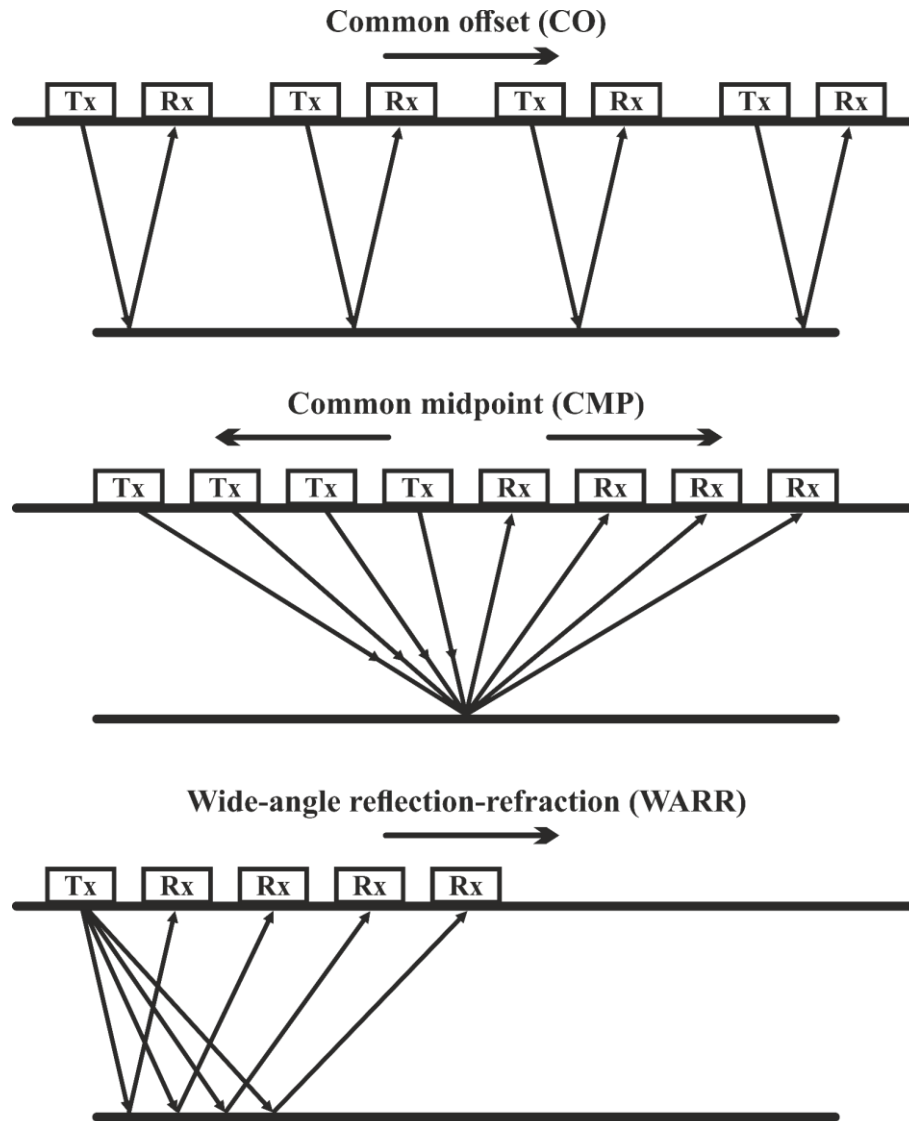


Figure 2.6: GPR data acquisition modes.

## 2.5.2 Antenna orientation

Another important factor that is seldom discussed, yet can play a significant role in a GPR investigation, is the orientation of the transmitting and receiving antennas with respect to each other as well as to the survey line (Diamanti, 2008). This factor is particularly critical, as most commercial GPR systems today use polarised antennas (Annan, 2003) and antenna polarisation is known to affect the quality of the collected data (Lutz et al., 2003). Figure 2.7 shows the possible different configurations of antenna orientations.

The most commonly used orientation in shallow geophysical investigations (Sassed & Everett, 2005), in sedimentary environments (Bristow & Jol, 2003), and in WARR soundings (Annan & Cosway, 1992), is the **perpendicular broadside mode**, as it provides the widest angular coverage of the subsurface reflectors (Annan, 2005; Bristow & Jol, 2003; Schubert, 2015). Nevertheless, many times different orientations can also be used to enhance the responses from different types of targets.

For instance, Guy et al. (1999) and Tsoflias et al. (2015) demonstrated the importance of cross-pole data for site and fracture characterisation, respectively, while Porsani et al. (2010) illustrated the benefits of using different antenna orientations by comparing the target detection and location performance of the parallel broadside and perpendicular broadside modes. In general, many researchers (e.g., Bradford, 2003, 2004; Lualdi & Lombardi, 2014; Radzevicius & Daniels, 2000; Sassen & Everett, 2009; van der Kruk et al., 2003) have shown that a multi-polarisation GPR survey, even though requires a considerably greater effort, and therefore time, compared to a single-polarisation one, can, in fact, provide much more information regarding the size, shape, and orientations of the subsurface targets.

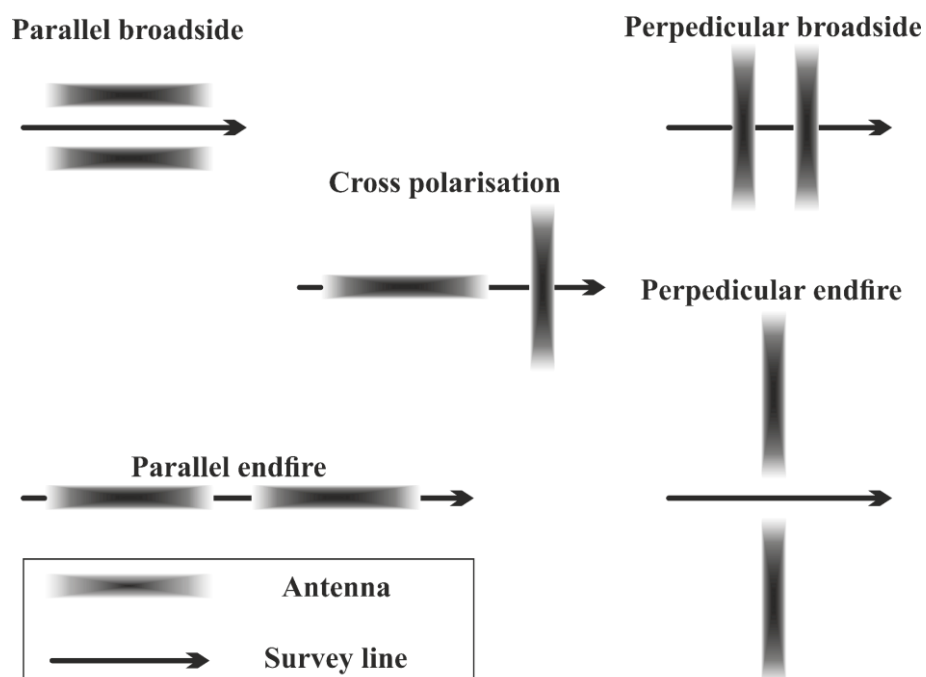


Figure 2.7: Tx and Rx antenna orientations. The electric field is assumed to be aligned along the long axis of the antenna.

## 2.6 GPR data visualisation

Image reconstruction techniques can play an important role in both the interpretation as well as presentation of data. In general, GPR data are recorded in the form of **one-dimensional (1D) signals, known as traces**. The collected traces can undergo various coordinate transformations and be visualised in different ways to provide subsurface information both horizontally and laterally. In addition to the 1D traces, other standard visualisation methods include **two-dimensional (2D) reflection sections/cross-sections**, and **three-dimensional (3D) volumes**, which based on acoustic terminology are also known as **A-scans** (amplitude), **B-scans** (brightness), and **C-scans** (contrast), respectively (Figure 2.8) (Scheers, 2001).

Overall, according to Benedetto et al. (2017), the collected signal can be defined by (2.26),

$$f(x, y, z) = A(x_i, y_j, z_k) \quad (2.26)$$

with  $i, j$ , and  $k$  ranging from 1 to  $N, M$ , and  $P$ , respectively.

As it was previously mentioned, GPR records the amplitude of the subsurface responses versus the TWT. This recorded waveform/trace is called A-scan and can be expressed by (2.27),

$$f(z) = A(x_i, y_j, z_k) \quad (2.27)$$

with  $i, j$  equal to a constant value and  $k$  ranging from 1 to  $P$ .

Multiple A-scans, resulting from continuous recording at regular intervals during the GPR movement, can be placed side by side giving a GPR cross-section. This section is called B-scan and can be defined by (2.28),

$$f(x, z) = A(x_i, y_j, z_k) \quad (2.28)$$

with  $j$  equal to a constant value, and  $i$  and  $k$  ranging from 1 to  $N$  and  $P$ , respectively. Usually, in B-scans, the signal amplitude is represented by a colour scale (e.g., grey-scale) in which each colour is matched to a specific power of the signal.

Lastly, multiple B-scans resulting from recording over a regular grid in  $XY$ -plane can also be placed side by side and interpolated to give a 3D volume or C-scan. From a C-scan one can obtain amplitude maps at a specific time or depth which are known as **time or depth slices**, respectively. A time or depth slice can be expressed by (2.29),

$$f(x, y, z) = A(x_i, y_j, z_k) \quad (2.29)$$

with  $k$  equal to a constant value and  $i$  and  $j$  ranging from 1 to  $N$  and  $M$ , respectively.

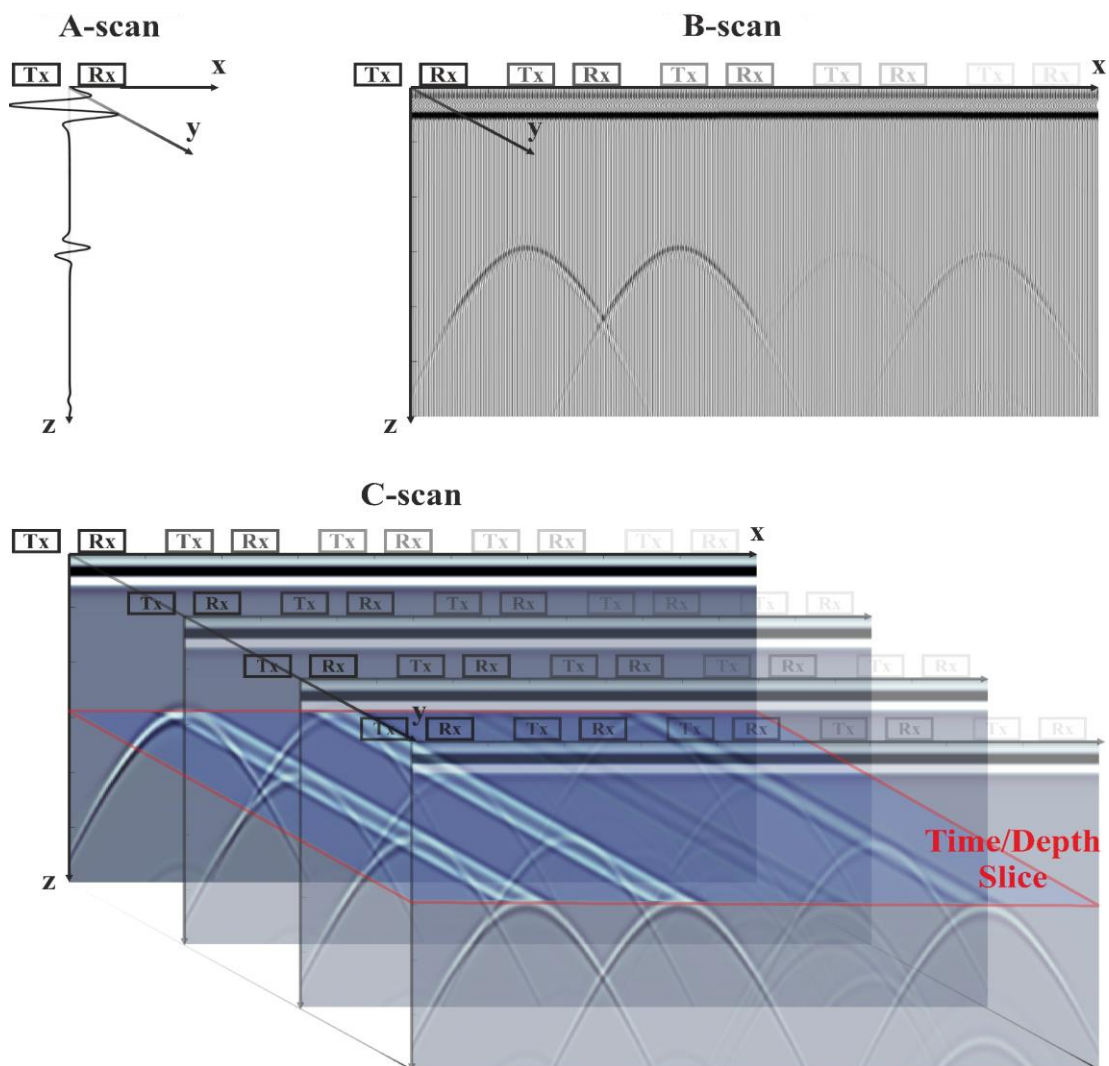


Figure 2.8: GPR data visualisation modes. A-scan, B-scan, C-scan, and time/depth slice.

## 2.7 GPR data processing

Processing GPR data is essential, as it can generally highlight the information related to the purpose of the GPR survey. In many cases, the subsurface features of interest are detectable or interpretable even from the raw GPR data. However, processing, can amplify and enhance the recorded signals, reduce or even eliminate the unwanted noise, and therefore, produce a final image that is not only easier to interpret by the survey operator but is also more understandable and presentable to the end-user or client (Angelis et al., 2020). Nevertheless, it is crucial that processing is always applied carefully, as there is a serious risk of removing important features from the data or even introducing non-existing features (i.e., artefacts) into the data.

In the following, the basic processing steps are discussed in the order that they would be typically applied in a GPR CO mode data set. For this demonstration field data from a pipe investigation are being used.

### **Stacking or vertical stacking**

Stacking is the process of averaging several traces coming from a certain location to reduce the random background noise, and thus improve the signal-to-noise ratio (SNR), and consequently the depth of exploration. This type of stacking, which is also referred to as vertical stacking, to be distinguished from horizontal CMP stacking (Mayne, 1962), is usually performed automatically by the GPR system during the data acquisition. Therefore, it can also be considered a pre-processing step (Diamanti, 2008). An example of the effect of vertical stacking is shown in Figure 2.9.

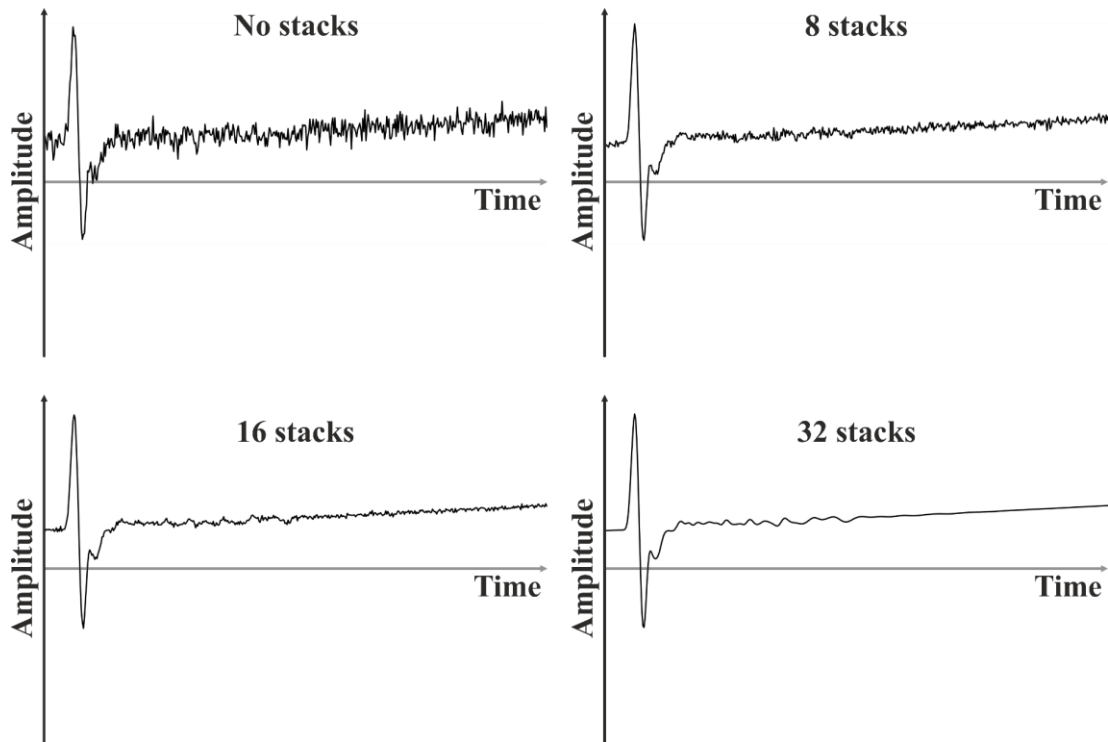


Figure 2.9: SNR improvement through vertical stacking on a GPR trace.

### Dewow

Dewow is usually the first processing step applied to the data after their acquisition. Most modern GPR systems and processing software perform this step automatically. The objective of dewowing the data is to remove the initial DC signal component, also known as DC bias, as well as the low-frequency trend, also known as “wow” noise (Dojack, 2012; Dougherty et al., 1994), which is caused either by inductive phenomena or by possible instrumentation dynamic range limitations (Annan, 2003). This processing step/filter is very important, as it reduces the data to a mean zero level, and hence, enables them to be visualised with positive-negative colour filling (Cassidy, 2009b). It should be noted, however, that depending on the data set as well as the choice of the filter and its parameters, dewow may occasionally introduce artefacts to the data such as a pre-cursor shortly before the first break (see Time-zero correction below), which operators should be aware of. An example of a dewowed trace with and without the pre-cursor artefact is illustrated in Figure 2.10.

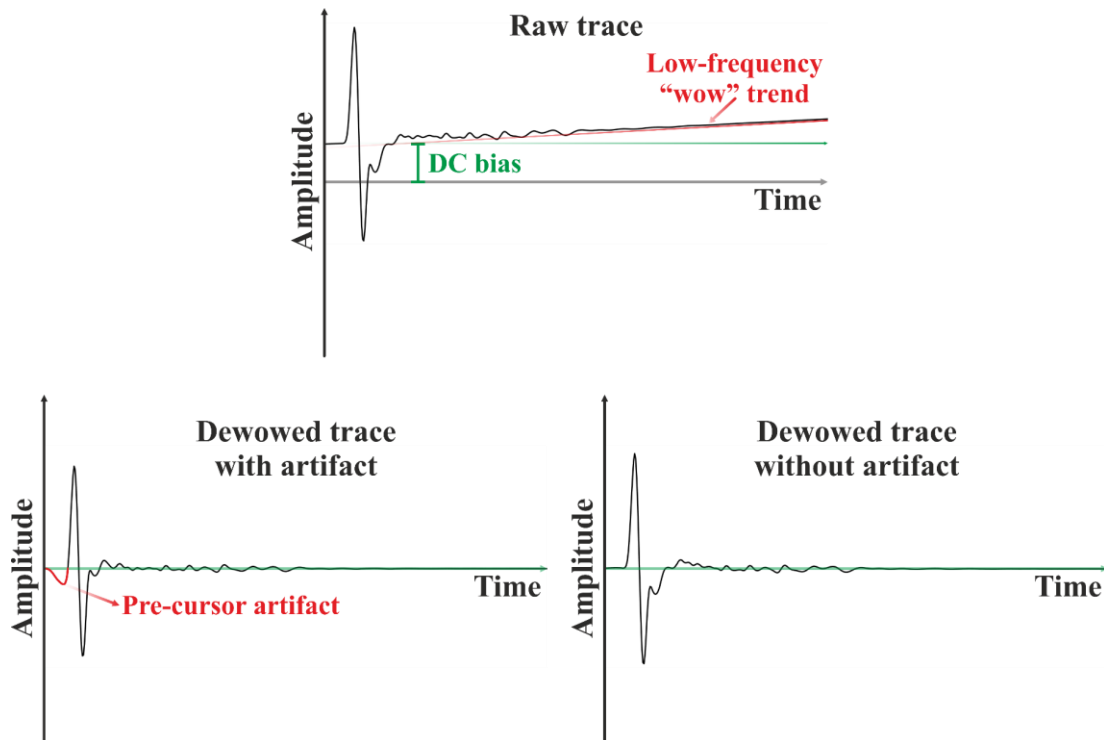


Figure 2.10: Dewow on a raw GPR trace.

### Time-zero correction

Differences in temperature, supply voltage, or even cable lengths, can very often cause “jumps” in the GPR signal, and as a result, time misalignments (Cassidy, 2009b). The time-zero correction is the process of readjusting the GPR response so that the first arrival, i.e., direct air wave response, corresponds to the zero time. This processing step is particularly important, as it ensures not only the realignment of the subsurface reflections but also the accurate determination of their time/depth. According to Yelf (2004) the five most-used positions by GPR practitioners for the time-zero correction are the following (Figure 2.11):

1. The first break point.
2. The first positive peak.
3. The mid-amplitude point between the positive and negative peaks.
4. The zero-amplitude point between the positive and negative peaks.
5. The first negative peak.

For the example presented in Figure 2.12, the first break (1) point has been used.

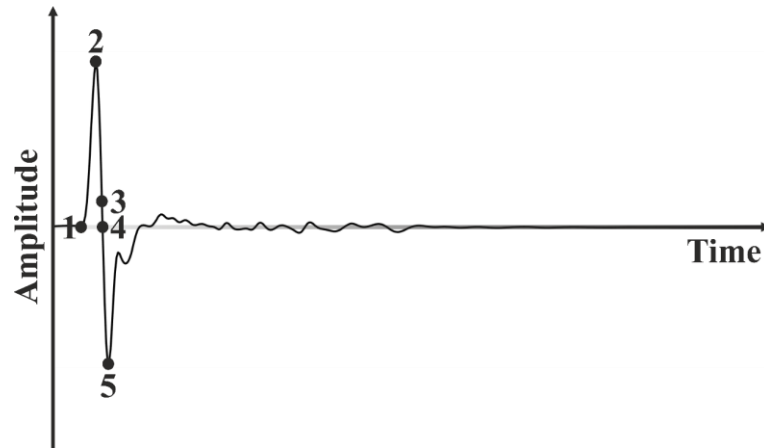


Figure 2.11: The five most-used positions for the time-zero correction according to Yelf (2004).

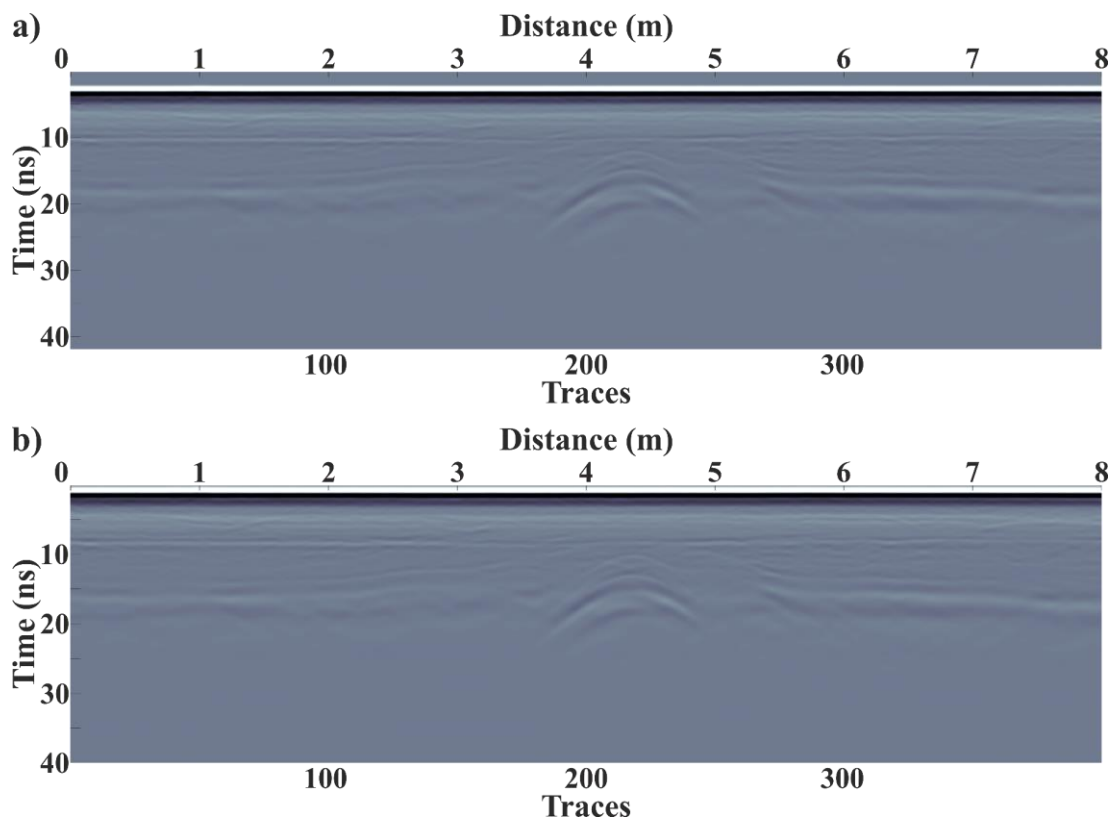


Figure 2.12: a) GPR data before time-zero correction. b) GPR data after time-zero correction.

### Time-varying gain

As explained in a previous section (Ch. 2.3.3), the radar signal attenuates as it propagates into the subsurface. This often, rapid attenuation of EM waves makes it difficult to detect and therefore interpret reflections at later times, i.e., reflections caused by deeper targets. Time gain is used to boost signal strength, and therefore, to enhance

the low amplitude indistinguishable reflections. However, this processing step should always be performed with caution, as along with the desired signals the noise is also amplified. According to Annan (2003), Cassidy (2009b), and Ciampoli et al. (2019) the most commonly used gain functions are the following:

- Automatic gain control (AGC).
- Inverse amplitude decay (IAD) gain.
- Spreading/spherical and exponential compensation/correction (SEC) gain.
- User-defined gain (UDG). Such as linear or exponential gain functions based on specific mathematical expressions.

Figure 2.13 shows GPR data before and after the application of time gain. For this example, a SEC gain has been used.

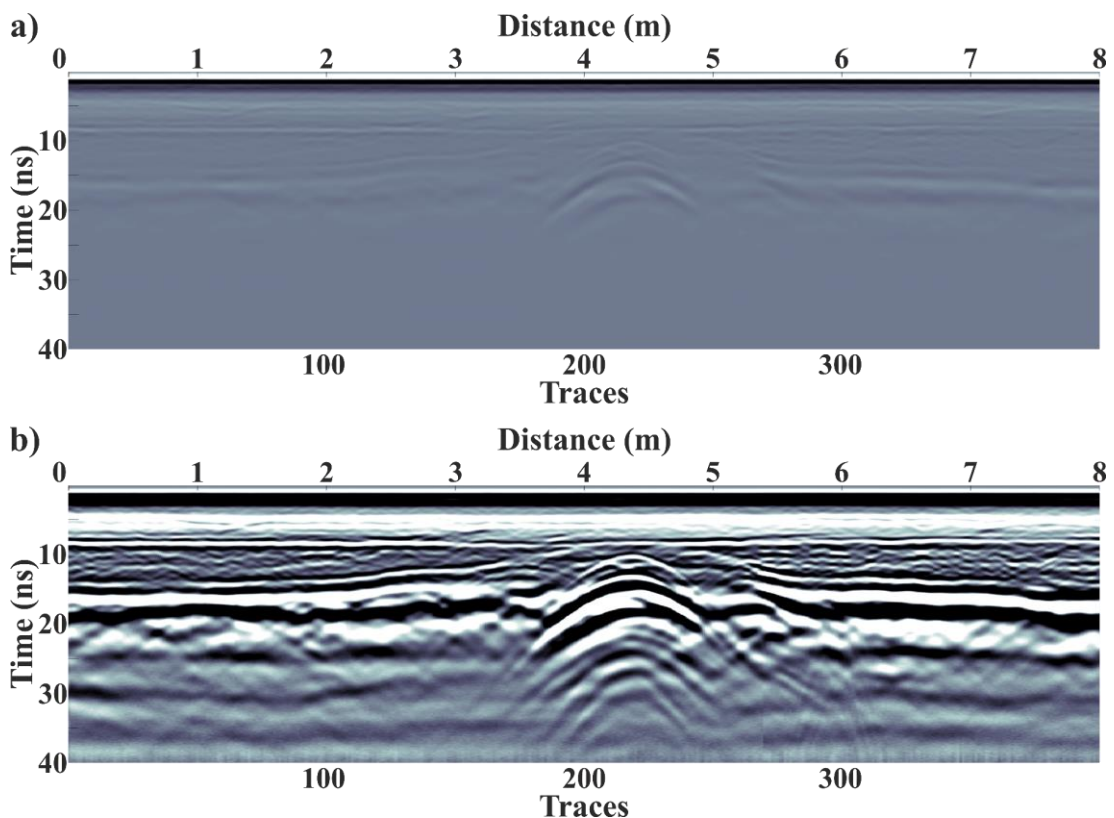


Figure 2.13: a) GPR data before the application of time gain. b) GPR data after the application of time gain (SEC gain).

### Background removal

Background removal is a routine step in GPR data processing that is used to reduce GPR clutter (i.e., signals unrelated to scattering characteristics) (Daniels, 2004), as well as to remove the direct air and direct ground wave responses. Background removal is a spatial filter that in its most simplistic form works by subtracting from each individual trace the mean trace of the GPR cross-section. Therefore, background removal can also be particularly useful for suppressing or even completely removing horizontal ringing events, and consequently, for enhancing dipping events (Kim et al., 2007; Szymczyk & Szymczyk, 2013). Nevertheless, it should be avoided or at least used with caution when the targets of interest are planar interfaces (Daniels, 2004). Figure 2.14 illustrates the application of background removal in GPR data.

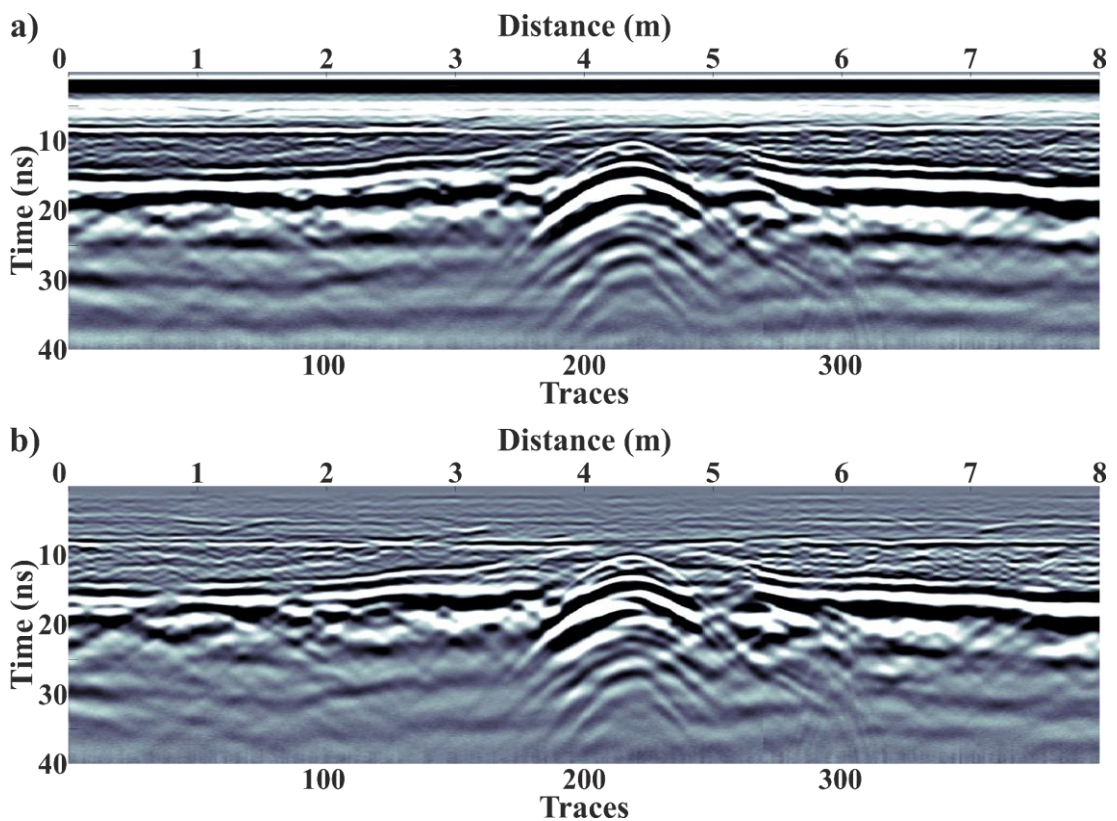


Figure 2.14: a) GPR data before the application of the background removal filter. b) GPR data after the application of the background removal filter.

### **Frequency and wavenumber filtering**

To improve the visual quality and aid interpretation, it is necessary to remove as much noise as possible from the data. To achieve that, temporal as well as spatial filters are commonly used. Temporal filtering acts on individual traces (e.g., dewow), i.e., on the time axis, whilst spatial filtering across a number of traces (e.g., background removal), i.e., on the distance axis (Annan, 2003). Very often, these filtering techniques are also combined to create advanced 2D filters that operate in the time and space domain simultaneously (Cassidy, 2009b). The most “powerful” of these techniques are based on the fast Fourier transform (FFT) and are frequency filtering (temporal), wavenumber filtering (spatial), and frequency-wavenumber (FK) filtering (temporal-spatial), which is their corresponding 2D combination.

Unwanted frequencies can be easily removed from the data using frequency filtering. High pass filtering increases the SNR and reduces low-frequency noise (e.g., horizontal banding system noise), while low pass filtering decreases the high-frequency noise or “snow” (Diamanti, 2008; Szymczyk & Szymczyk, 2013). An example of bandpass frequency filtering in GPR data, which is a combination of low and high pass filtering, is shown in Figure 2.15.

In a similar manner, unwanted wavenumbers can be removed using wavenumber filtering in the spatial wavenumber domain. High pass filtering is particularly useful in removing/suppressing unwanted horizontal events, and hence, ringing phenomena, which generally correspond to low wavenumbers, whereas low pass filtering can be used to suppress dipping events (Kim et al., 2007). An example of bandpass (i.e., the combination of low and high pass) wavenumber filtering is illustrated in Figure 2.16.

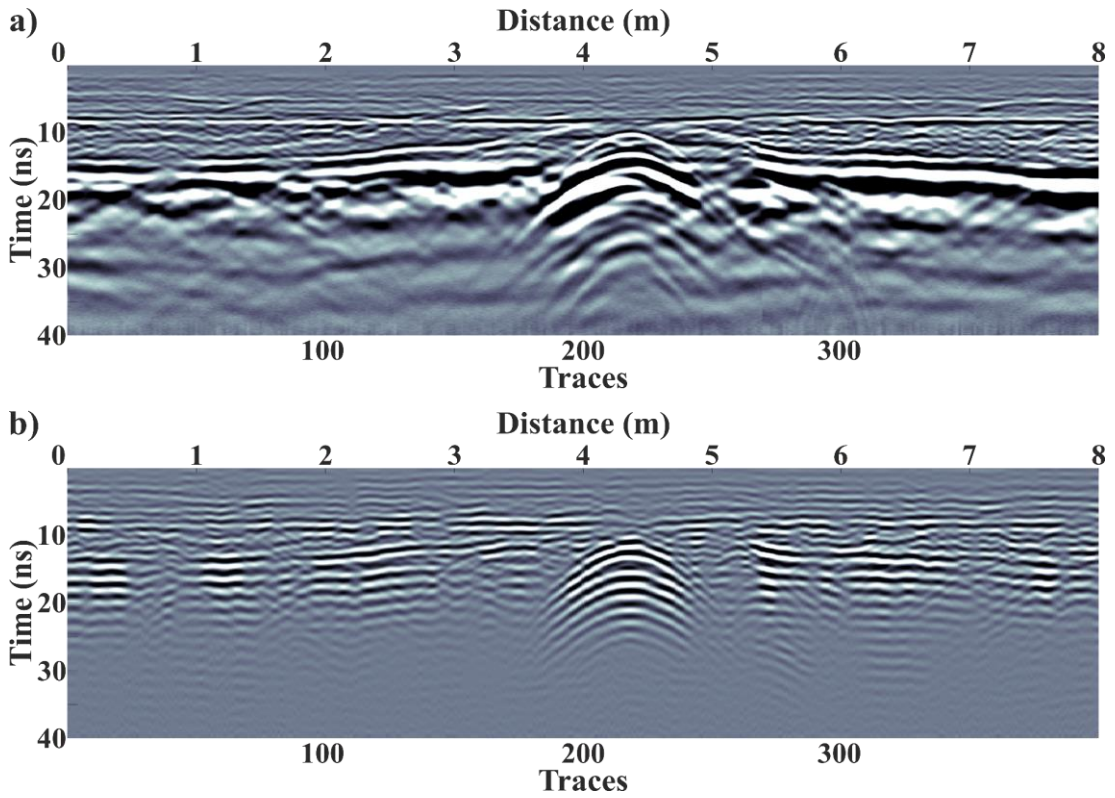


Figure 2.15: a) GPR data before the application of bandpass frequency filtering. b) GPR data after the application of bandpass frequency filtering.

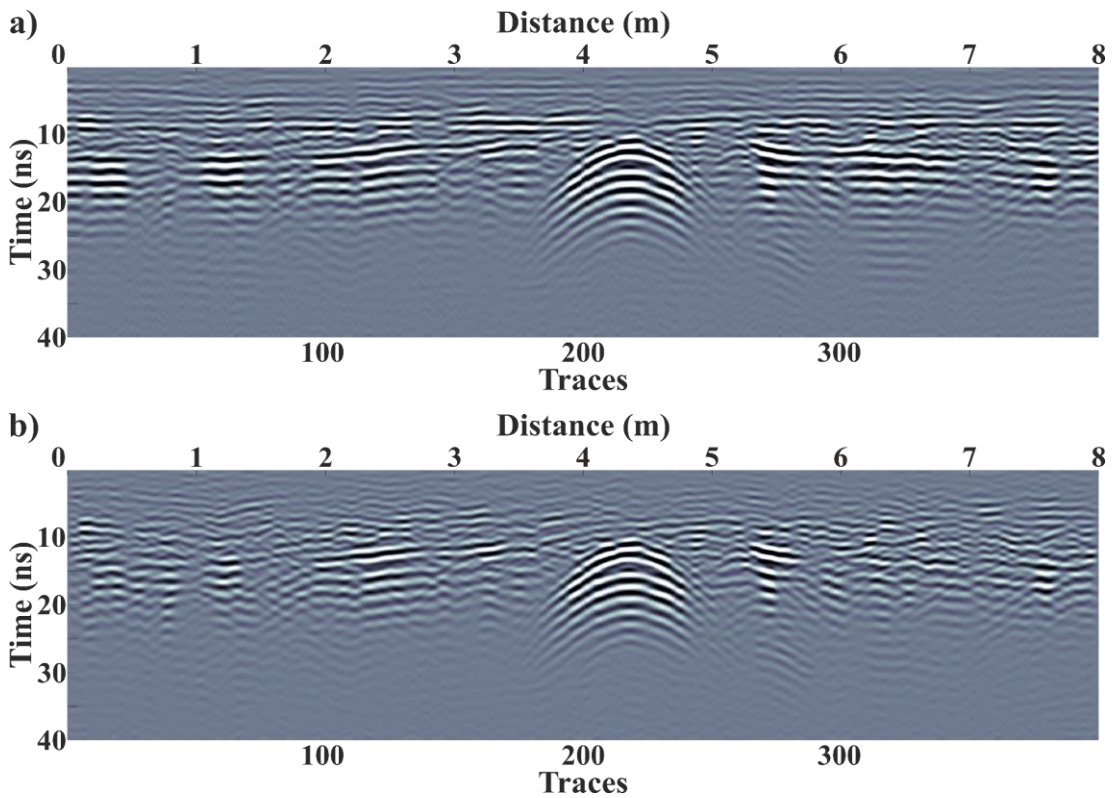


Figure 2.16: a) GPR data before the application of bandpass wavenumber filtering. b) GPR data after the application of bandpass wavenumber filtering.

### Predictive deconvolution

According to Yilmaz (2001), “deconvolution compresses the basic wavelet in the recorded seismogram, attenuates reverberations and short-period multiples, thus increases temporal resolution and yields a representation of subsurface reflectivity”.

In general, deconvolution techniques are very limited in GPR data due to the required assumptions for wavelet estimation which are not always appropriate for non-seismic data (Annan, 2003), and consequently tend to be successful only in well-defined subsurface environments (Cassidy, 2009b). However, predictive filtering techniques, such as predictive deconvolution (Peacock & Treitel, 1969), which is the most common type of deconvolution, can sometimes be used with great success in GPR in conjunction with other advanced processing steps. This type of filtering attempts to estimate and then suppress/remove predictable parts of the data, namely multiple reflections. An example of the use of predictive deconvolution (1D trace-by-trace filter) is shown in Figure 2.17.

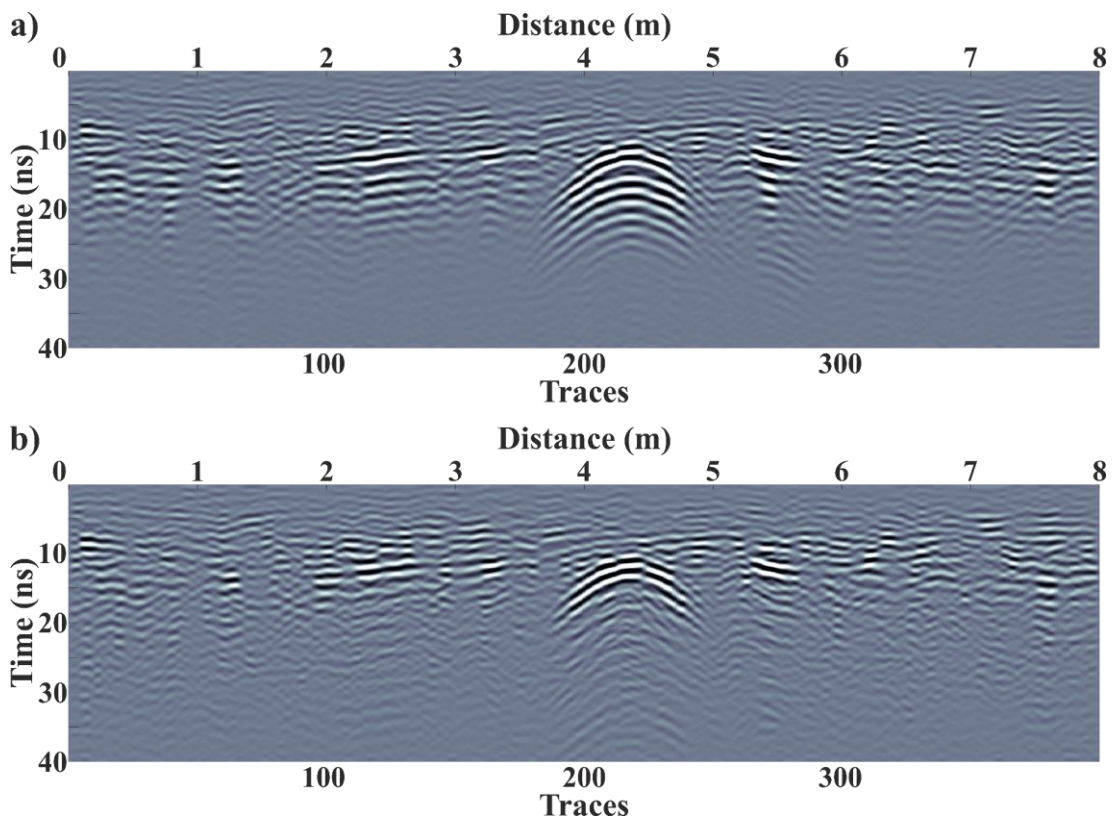


Figure 2.17: a) GPR data before the application of predictive deconvolution. b) GPR data after the application of predictive deconvolution.

### **Velocity analysis and depth conversion**

In order to make realistic interpretations, it is necessary to convert the TWT into depth. To achieve this, a good subsurface EM wave velocity model is required. Subsurface EM wave velocity, which is important not only for the depth conversion but also for further processing steps/corrections such as migration (see migration below), can be estimated in many different ways (Cassidy, 2009b; Goodman et al., 2009; Neal, 2004; Reynolds, 2011):

- By guesswork, which may give a depth accuracy ranging from -20 to 20 %.
- By field samples and direct laboratory experiments.
- By associating the TWT with a horizon or buried target of known depth.
- By travel time measurements using borehole radar between two or more adjacent logs.
- By using time-domain-reflectometry (TDR) probes in the field.
- By hyperbolic fitting/matching.
- By using the moveout principles similarly as in the seismic method.

The last two methods are the most frequently used in GPR. However, the latter, which is also the most accurate method, requires the use of the multi-offset data acquisition modes, namely CMP and WARR. Therefore, this method will be explored in detail in the next chapter (Ch. 3.2).

Hyperbolic fitting is based on hyperbolic reflections produced by subsurface point scatterers such as pipes or cables, whose shape/time is given as a function to distance to the antenna by (2.30) (Daniels, 2004; Goodman & Piro, 2013; Xie et al., 2018). This hyperbolic shape is produced because the radiated antenna beam is in reality a complex 3D cone (Neal, 2004), and hence, the radar detects the target, which is denoted by the apex of the hyperbola, several traces before and after its true location. Therefore, by exploiting equation (2.30) different hyperbolas with assumed velocities can be calculated until they match/fit the hyperbolic pattern(s) of the data, as shown in Figure 2.18. It is also apparent from (2.30) that this method should only be performed on targets of known orientations or with an orientation perpendicular to the scan, otherwise the assumed velocity will not correspond to the true subsurface velocity of the EM waves.

$$t_h = \frac{2\sqrt{x^2 \sin^2 \theta + d^2}}{v} \quad (2.30)$$

where:

- $t_h$  The travel time of the hyperbola (s).
- $x$  The horizontal distance to the subsurface target (m).
- $\theta$  The angle between the GPR traverse and the target orientation ( $^\circ$ ).
- $d$  The distance/depth to the subsurface reflector (m).
- $v$  The velocity of EM waves in the medium (m/s).

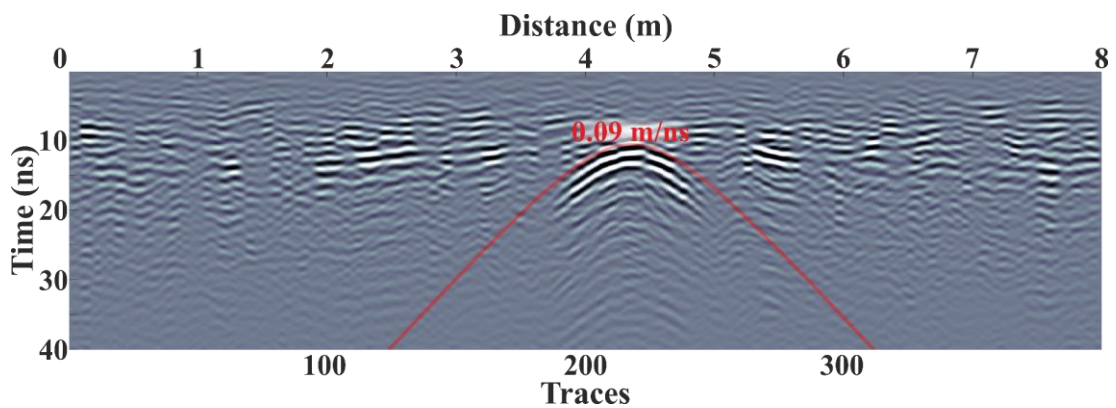


Figure 2.18: Hyperbolic fitting of GPR data ( $v = 0.09$  m/ns).

## Migration

The process that describes the reconstruction of the geometrically correct radar reflectivity distribution of the subsurface is called migration (Annan, 2009). The main purpose of this technique is to remove distortions, collapse the hyperbolic diffractions, and move the dipping reflectors back to their true subsurface positions, namely to improve lateral resolution and produce a better representation of the subsurface (Fisher et al., 1992). Although migration is a particularly useful and powerful technique it has one major drawback, it requires a very good knowledge of the subsurface velocity to work properly.

Nowadays, there are many different migration types/algorithms (Özdemir et al., 2014). The most commonly used in GPR data are the FK migration, which is also often referred to as Stolt's migration (Stolt, 1978) and is based on the FFT, Kirchhoff

migration (Schneider, 1978), and Reverse time migration (Baysal et al., 1983). Figure 2.19 illustrates the result of FK migration in GPR data.

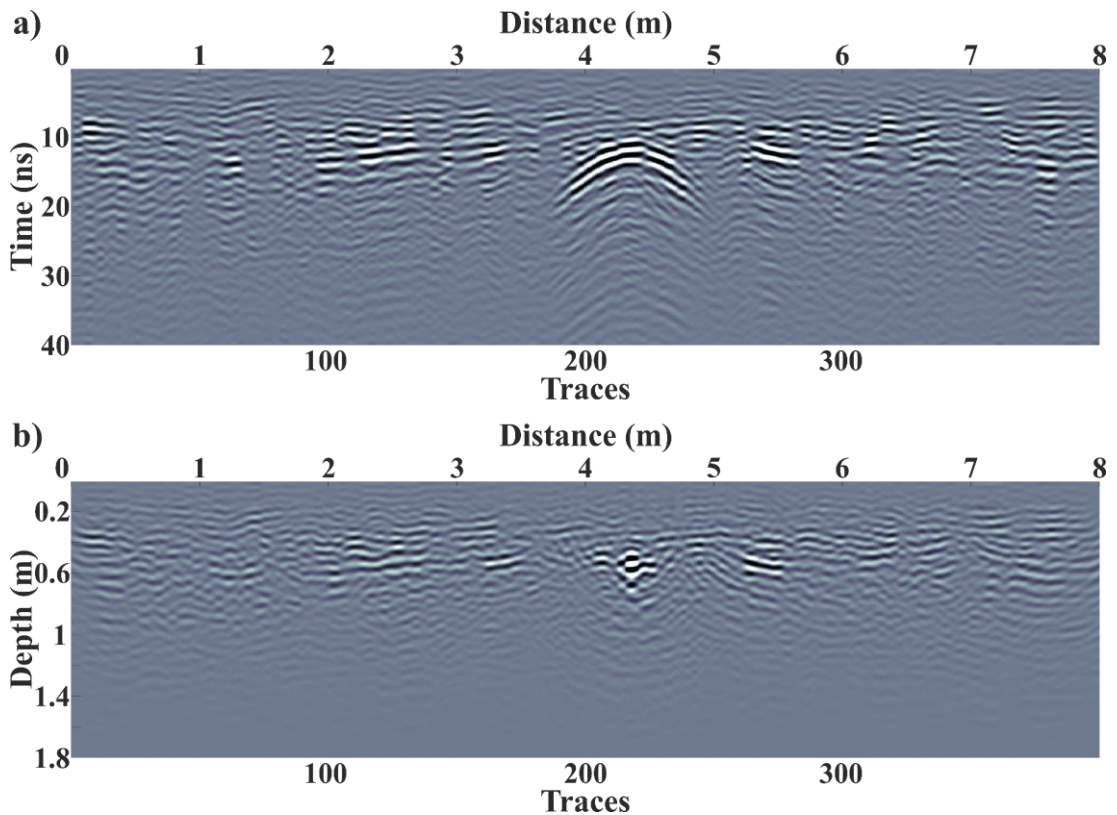


Figure 2.19: a) GPR data before the application of migration b) GPR data after the application of migration (FK migration –  $v = 0.09$  m/ns).

### Hilbert transform – instantaneous attributes

Another process that is very often applied to the GPR data/traces ( $s(t)$ ), and usually after migration, is the Hilbert transform (HT) (2.31) (King, 2009a). Through this transformation, one can obtain the instantaneous attributes, namely the instantaneous amplitude ( $a(t)$ ) (2.32), phase ( $\theta(t)$ ) (2.33), and frequency ( $\omega(t)$ ) (2.34) (King, 2009b; Taner et al., 1979).

The most commonly used attribute by GPR practitioners is the instantaneous amplitude, also often referred to as envelope, and is a unipolar signal very useful in imaging regions of weak/dim or strong/bright reflections (Goodman et al., 2009). The instantaneous phase is particularly useful for identifying thin layers and emphasising the continuity of reflectors, while the instantaneous frequency is very useful for separating

reflections that arrive at roughly the same time (Reynolds, 2011). Figure 2.20 shows the GPR data before and after the Hilbert transform (amplitude, phase, and frequency).

$$\hat{s}(t) = \frac{1}{\pi} P \int_{-\infty}^{+\infty} \frac{s(\tau)}{t-\tau} d\tau = \text{HT}[s(t)] \quad (2.31)$$

$$a(t) = \sqrt{s^2(t) + \hat{s}^2(t)} \quad (2.32)$$

$$\theta(t) = \tan^{-1} \left( \frac{\hat{s}(t)}{s(t)} \right) \quad (2.33)$$

$$\omega(t) = \frac{d\theta(t)}{dt} \quad (2.34)$$

where:

HT The Hilbert transform.

P The Cauchy principal value of the integral.

$s(t)$  The real GPR trace.

$\hat{s}(t)$  The imaginary/quadrature GPR trace.

$a(t)$  The instantaneous amplitude.

$\theta(t)$  The instantaneous phase.

$\omega(t)$  The instantaneous frequency.

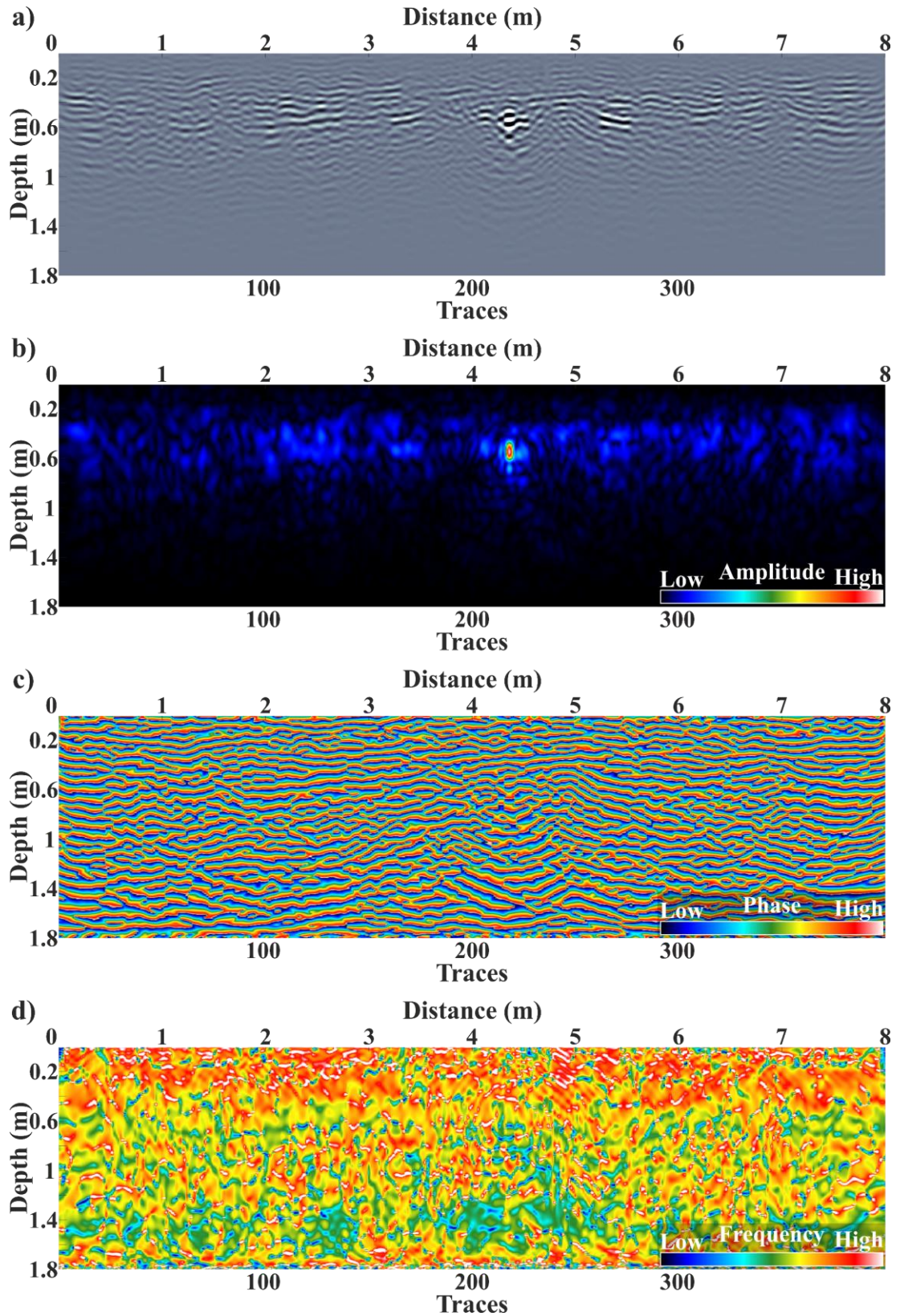


Figure 2.20: a) GPR data before the Hilbert transform. b) GPR data after the Hilbert transform – instantaneous amplitude. c) GPR data after the Hilbert transform – instantaneous phase. d) GPR data after the Hilbert transform – instantaneous frequency.

# 3

## **Review of multi-offset GPR methods**

This chapter provides a concise overview of the multi-offset GPR methods. The chapter begins with a discussion of the multi-offset GPR data acquisition modes and their advantages and disadvantages over the traditional single-offset mode. Then, the basic multi-offset GPR data processing steps are detailed, with special emphasis given to the moveout correction, velocity spectrum analysis, and horizontal stacking. Finally, the chapter concludes with a review of the newly developed GPR systems with multi-concurrent receivers, in which the work that was done so far with these systems is thoroughly discussed.

### 3.1 Multi-offset GPR data collection

GPR data can be collected by different survey methods. The most popular data acquisition mode is the single-offset, also often referred to as **single-fold (SF)**, CO, which utilises a single transmitter and receiver pair that moves along the survey line while maintaining a fixed separation distance (Figure 3.1a). The main advantage of this mode of operation is that enables fast and dense data acquisition, and thus, high-resolution, large-scale investigations to be carried out with relative ease, and at a relatively low cost (Annan, 2003). CO mode, however, has one major drawback, it can only provide constant subsurface EM wave velocity models.

There are also multi-offset, also often referred to as **multi-fold (MF)**, acquisition modes such as the CMP and the WARR. For WARR, the transmitter or receiver remains at a fixed position while the other transducer is moved along the survey line at regular intervals, whilst in CMP mode, both the transmitter and the receiver are moved simultaneously away from a fixed position. MF GPR modes have many benefits over the SF CO mode (Annan, 2009), as contrasted to the latter they enable each point of the subsurface to be sensed, and therefore mapped, not only by a single, but by multiple transmitter-receiver pairs, and as a result by multiple wavefronts (Forte & Pipan, 2017).

The benefits of MF GPR modes have been described and demonstrated over the years by many researchers in many studies (e.g., Annan & Davis, 1976; Arcone, 1984; Becht et al., 2006; Berard & Maillol, 2007; Booth et al., 2008; Booth, Clark, Hamilton, et al., 2010; Bradford, 2006; Bradford & Deeds, 2006; Causse & Sénéchal, 2006; Delaney et al., 1990; Fisher et al., 1992; Forte & Pipan, 2017; Greaves et al., 1996; Jacob & Urban, 2016; Nakashima et al., 2001; Pipan et al., 1999, 2003), with most important being:

- The ability to provide detailed subsurface EM wave velocity models (including both vertical and lateral variations), and hence, additional models of other subsurface properties (e.g., dielectric constant, water content, porosity).

- The ability to provide enhanced reflection sections with a higher SNR, and therefore, improved exploration depth, reflection continuity, as well as dip imaging.
- The ability to process GPR data in a similar way to seismic data, and thus, the possibility to exploit many of the well-established advanced processing schemes and tools of the latter that already exist.

Despite these advantages, MF GPR acquisition modes had limited use in recent decades, mainly for the following reasons (Annan, 2009; Daniels, 2004; Forte & Pipan, 2017; Neal, 2004):

- Only a few commercial GPR systems support separate transmitter and receiver transducers, as most of them are designed with both transducers in the same housing to reduce costs as well as improve portability and manoeuvrability.
- Data collection is extremely time-consuming since they require multiple offsets and each measurement (i.e., the collection of a single trace) requires manual movement of the transducers (Figure 3.1b).
- The collected data requires not only many additional, but also much more advanced processing steps than those used for CO data, and therefore, very often, specialised data processing software as well. In particular, usually seismic data processing software, as most GPR data processing software are primarily designed for handling SF CO GPR data.

All the above are understandably translated into additional survey and data analysis time, and consequently, increased costs.

Ideally, the use of GPR systems that can support multiple concurrent data acquisition receivers could have addressed some of these issues but their development, until recently, was very challenging (Annan & Jackson, 2017).

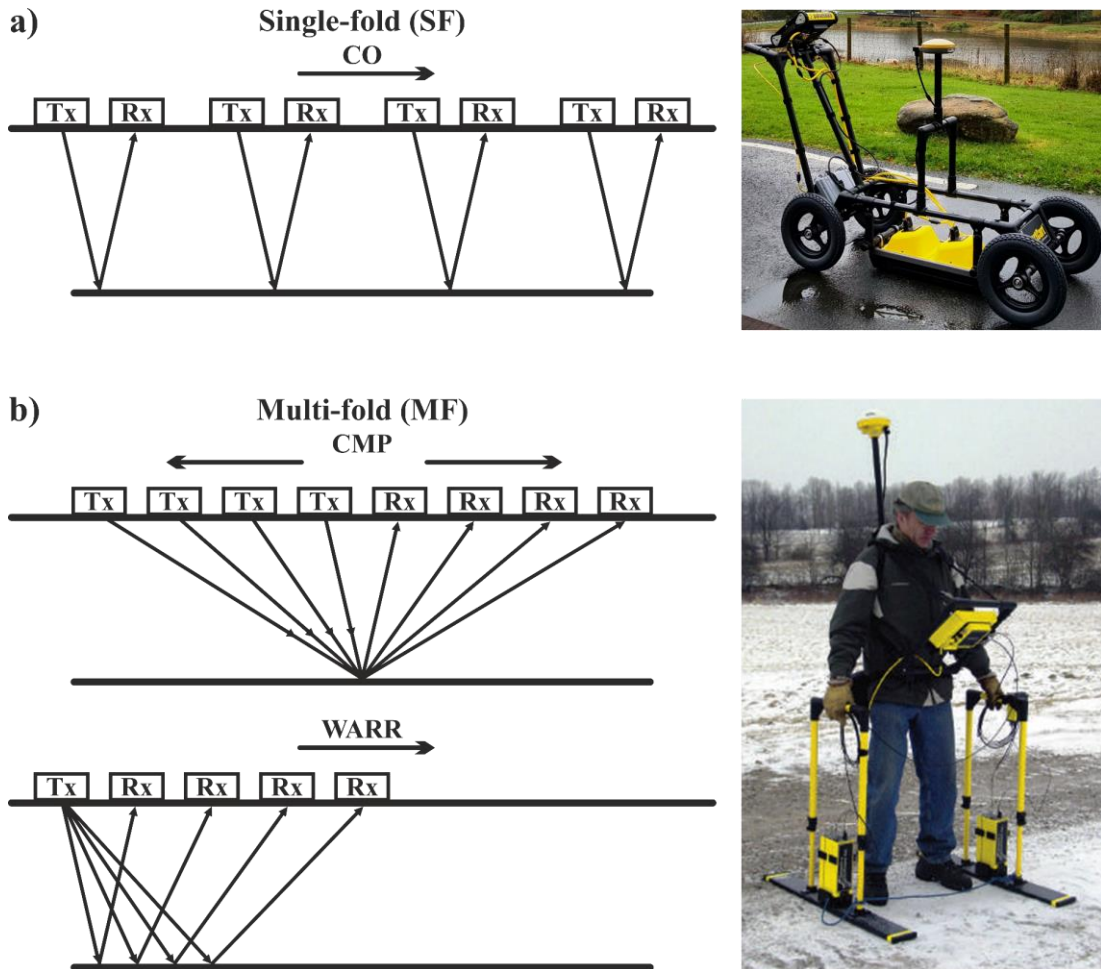


Figure 3.1: a) The SF CO mode of operation, and a typical single-offset GPR system. b) The MF CMP and WARR modes of operation, and a typical multi-offset GPR system. Figure adapted from Sensors & Software Inc. (2021b).

## 3.2 Multi-offset GPR data processing

Processing MF GPR data requires special steps, such as the application of the moveout principles, in order to extract detailed velocity models and boost the SNR. Due to the correlations between the kinematics of the seismic and EM wave field methods (Carcione, 2015; Carcione & Cavallini, 1995; Ursin, 1983), most of the processing techniques used today for MF GPR data came/evolved from well-established seismic data processing methods.

However, despite the similarities, there are also important differences between EM and acoustic phenomena, with the most significant being the vectorial character of EM

waves compared to the scalar nature of acoustic waves (Forte & Pipan, 2017; van der Kruk et al., 2003). In addition, there are also differences in frequency, velocity, impedance, amplitude attenuation, timing alignment, and scaling factors (Davis & Annan, 1989; Diamanti et al., 2018; Forte & Pipan, 2017). This means that some MF seismic data processing schemes are suitable for use with GPR data but can require modification and careful consideration to provide optimal results.

In the following, the basic and most used MF GPR data processing steps are discussed. To demonstrate these steps, a synthetic GPR data set has been generated. It uses a WARR mode of acquisition from a 3D two-layered model, as shown in Figure 3.2. A single source (Hertzian dipole) and ten receivers, all separated by 0.25 m, were used, and the trace step and time window were set to 0.025 m and 45 ns, respectively. Finally, time-zero correction, SEC gain, trace balancing, and Gaussian white noise (including artificial noise bursts) were applied and added to the synthetic data.

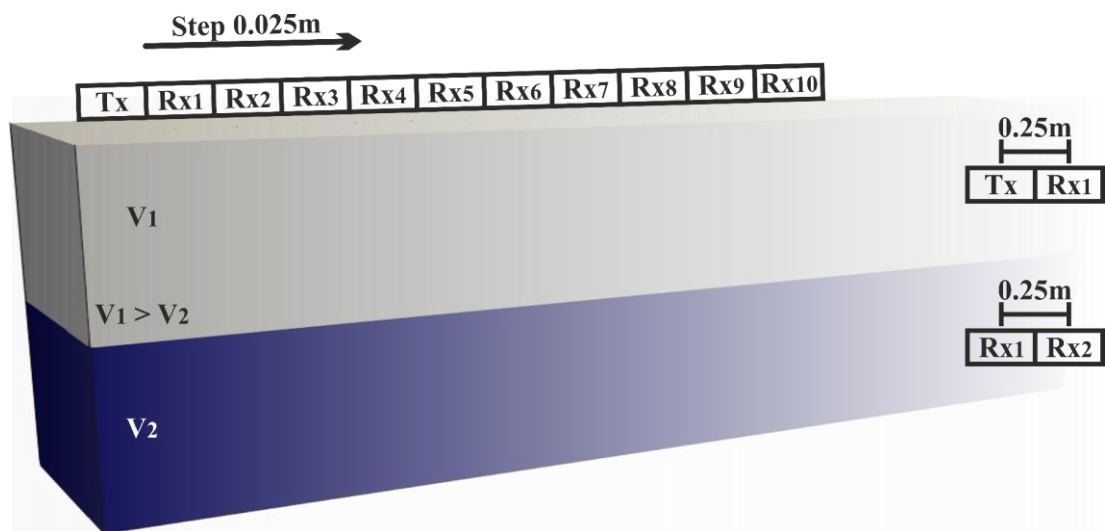


Figure 3.2: 3D two-layered model used to generate synthetic data for demonstrating basic MF GPR data processing steps.

### **CMP sorting**

CMP sorting is typically the first processing step applied to the data. This is necessary for the next processing phase, as like in seismic, most MF GPR data processing takes place in the CMP domain. CMP sorting is required for data collected using the WARR mode of operation and is the process of rearranging the traces of the WARR gathers –

often referred to in the seismic literature as common shot gathers (CSG) – through a coordinate transform, into CMP gathers (Figure 3.3).

A CMP gather, as its name implies, is a gather/group of traces that correspond to the same midpoint located between different transmitter-receiver pairs. Many times, instead of CMP, the terms common reflection point (CRP) or common depth point (CDP) are found in the literature. However, the use of these terms is quite often incorrect, as they are only valid in the case of a flat reflector and when there are no lateral velocity variations (Reynolds, 2011; Yilmaz, 2001).

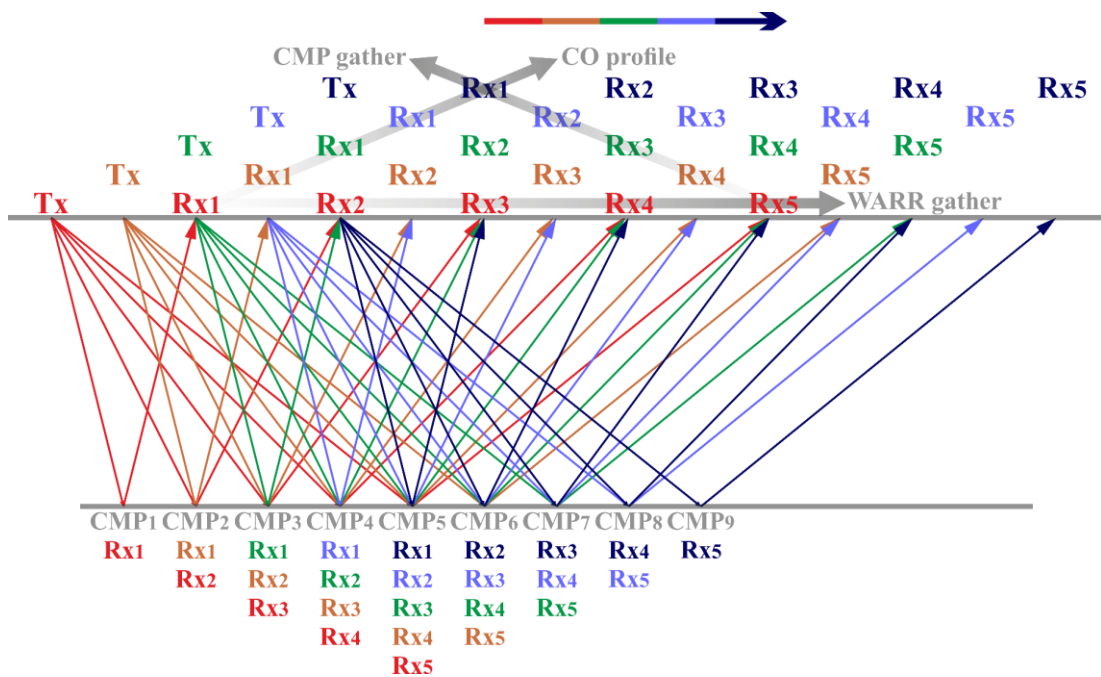


Figure 3.3: WARR data acquisition mode and CMP gather formulation.

### Moveout correction

The moveout correction is the process of eliminating the effect of transmitter-receiver offset and transforming the data of the CMP gather into zero-offset data. The moveout correction is referred to as linear moveout (LMO) correction when applied to linear events and to as hyperbolic or normal moveout (HMO or NMO) correction when applied to hyperbolic events. The NMO correction is typically performed after velocity analysis and before horizontal stacking (see horizontal stacking below). However,

since it is also, along with the LMO correction, the basis for the moveout-based velocity analysis using velocity spectra panels, it will be discussed in this part of the chapter.

In a CMP gather, the travel times ( $t(x)$ ) of the direct ground wave follow a linear trajectory (orange line in Figure 3.4a) and are given as a function of offset ( $x$ ) by (3.1) (Zhou, 2014). LMO correction attempts to remove the transmitter-receiver moveout effect ( $\Delta t_{LMO}(x)$ ) (3.2) and flatten the event by moving in time the data of the CMP gather.

Similarly, in a CMP gather, the reflection travel times ( $t(x)$ ) of a subsurface reflector follow a hyperbolic trajectory (green line in Figure 3.4a), which in their simplest form, based on the Pythagorean theorem, are given as a function of offset ( $x$ ) by (3.3) (Uieda, 2017; Yilmaz, 2001). NMO correction, the process of which is illustrated in Figure 3.4, attempts to remove the transmitter-receiver moveout effect ( $\Delta t_{NMO}(x)$ ) (3.4) and flatten the reflection by stretching in time the data of the CMP gather (Figure 3.4d).

$$t(x) = t_0 + \frac{x}{v_{LMO}} \quad (3.1)$$

$$\Delta t_{LMO}(x) = t(x) - t_0 \quad (3.2)$$

$$t(x) = \sqrt{t_0^2 + \frac{x^2}{v_{NMO}^2}} \quad (3.3)$$

$$\Delta t_{NMO}(x) = t(x) - t_0 \quad (3.4)$$

where:

$t(x)$  The travel time at an offset not equal to zero (s).

$t_0$  The travel time at zero-offset (s).

$x$  The transmitter and receiver separation distance (m).

$v_{LMO}$  The LMO velocity (m/s).

$v_{NMO}$  The NMO velocity (m/s).

$\Delta t_{LMO}(x)$  The difference between the travel time at an offset not equal to zero and the travel time at zero-offset for linear events (s).

$\Delta t_{NMO}(x)$  The difference between the travel time at an offset not equal to zero and the travel time at zero-offset for hyperbolic events (s).

From both equation (3.1) and (3.3) it is understood that to completely remove the moveout (either linear or hyperbolic), and therefore, to flatten an event, a correct velocity is required as shown with the NMO correction example in Figure 3.4d. Low-velocity estimates can lead to over-corrected events (i.e., upward curves) (Figure 3.4b), whereas high-velocity estimates can result in under-corrected events (i.e., downward curves) (Figure 3.4c).

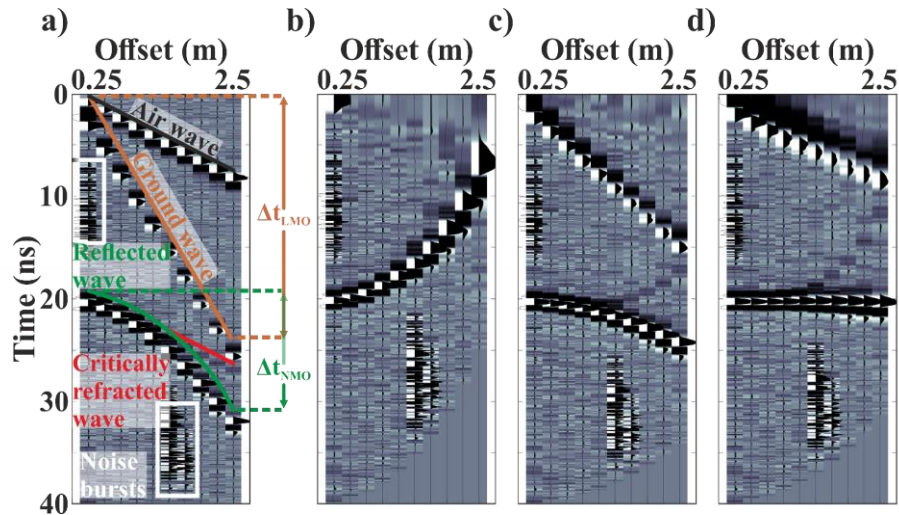


Figure 3.4: a) Synthetic CMP gather contaminated with white Gaussian noise and noise bursts (white rectangles), showing the direct air wave (black line), direct ground wave (orange line), reflected wave (green line), and critically refracted wave (red line). b) NMO over-corrected CMP gather of (a). c) NMO under-corrected CMP gather of (a). d) NMO corrected with proper velocity CMP gather of (a).

### Velocity analysis

As shown in the previous chapter (Ch. 2.7), subsurface EM wave velocity models are critical for the analysis as well as the interpretation of GPR data. Velocity is not only used to convert the TWT of GPR pulses into depth, but also for a series of processing and imaging steps such as gain (e.g., SEC gain), static (e.g., elevation static correction) as well as dynamic corrections (e.g., NMO correction), and migration (e.g., FK migration) (Forte et al., 2014; Mousa & Al-Shuhail, 2011). Moreover, velocity information, assuming low-loss (i.e.,  $(\sigma/(\omega\epsilon_0\epsilon_r))^2 \ll 1$ ) and non-magnetic (i.e.,  $\mu_r = 1$ ) materials, can be coupled with equation (2.18) or other more complex, mixing equations (e.g., Endres et al., 2009; Looyenga, 1965; Paren, 1970; Topp et al., 1980; Wharton et al., 1980) to allow for the estimation of different subsurface properties including dielectric

constant (e.g., Annan & Davis, 1976; Arcone, 1984; Arcone et al., 1998; Bohidar & Hermance, 2002; Deeds & Bradford, 2002; Delaney et al., 1990; Van Overmeeren et al., 1997), water content (e.g., Bradford, 2008; Bradford, Nichols, et al., 2009; Greaves et al., 1996; Hamann et al., 2013; Huisman et al., 2003; Klotzsche et al., 2018; H. Liu & Sato, 2012; Macheret et al., 1993; Murray et al., 2000, 2007), and porosity (e.g., Bradford, 2004; Bradford et al., 2009; Causse & Sénéchal, 2006; Igel et al., 2013; Turesson, 2006).

Unlike other methods, for example, hyperbolic fitting (see Ch. 2.7), MF GPR data velocity analysis techniques have one major advantage. They can provide detailed velocity cross-sections, and thus, information about both vertical and lateral velocity variations, as they are executed in the CMP domain, and more specifically, in each CMP gather separately. Nevertheless, they are usually performed on a selected number of CMP gathers (van der Kruk, 2001), with high SNR, and the velocity data are then interpolated to produce the desired velocity cross-sections. There are many methods to determine velocity through the CMP domain such as  $t^2$ - $x^2$  analysis, constant velocity panels (CVP), constant velocity stacks (CVS), and velocity spectrum panels (Hatton et al., 1986; Onajite, 2014; van der Kruk, 2001; Yilmaz, 2001). The latter method is the most popular and used with GPR data, as it is generally the most robust.

The velocity spectrum is shown as a plane/panel of velocity (on the horizontal axis) versus TWT (on the vertical axis), in which the stacking results of an LMO and/or NMO corrected CMP gather (i.e., the results can also be combined into a single LMO NMO velocity spectrum panel), for a range of trial constant velocities using equation (3.1) and/or (3.3), are plotted side by side (Taner & Koehler, 1969) (Figure 3.5b to Figure 3.5d). The velocity spectrum panel indicates the optimum stacking velocities ( $v_{STK}$ ), i.e., the velocities that will best flatten the events of the CMP gather and will enable the optimal horizontal stacking of its traces (see horizontal stacking below). The desired stacking velocities are obtained by selecting the peaks/maxima of the spectrum panel that correspond to linear (LMO panel) and/or hyperbolic (NMO panel) events of the CMP gather (orange and green arrows in Figure 3.5b to Figure 3.5d). Although stacking velocities do not directly correspond to the true material velocities, they can often be translated, assuming small transmitter-receiver offsets compared to the reflector depth and horizontal isotropic subsurface layers (3.5) (Reynolds, 2011;

Yilmaz, 2001; Zhou, 2014), into true subsurface EM wave velocities ( $v_{INT}$ ) using Dix's analysis approach (3.6) (Dix, 1955) (e.g., Becht et al., 2006; Booth et al., 2010; Bradford, 2003, 2004; Causse & Sénéchal, 2006; Fisher et al., 1992; Greaves et al., 1996; Huisman et al., 2003; Igel et al., 2013; H. Liu & Sato, 2012; S. Liu et al., 2020; Murray et al., 2000, 2007; Nakashima et al., 2001; Turesson, 2006).

$$v_{RMS} \approx v_{LMO/NMO} \approx v_{STK} \quad (3.5)$$

$$v_{INT} = \sqrt{\frac{v_{RMS_n}^2 t_n - v_{RMS_{n-1}}^2 t_{n-1}}{t_n - t_{n-1}}} \quad (3.6)$$

where:

- $v_{RMS}$       The RMS velocity (m/s).
- $v_{STK}$       The stacking velocity (m/s).
- $v_{LMO/NMO}$     The LMO/NMO velocity (m/s).
- $v_{INT}$       The interval velocity (m/s).
- $t$           The travel time (s).
- $n$           The number of subsurface layers.

In general, velocity spectra resolution can be affected by several factors, which are well described by van der Kruk (2001) and Yilmaz (2001). The most important and relevant to this research work, as demonstrated in later chapters, are the following:

- The SNR of the CMP gather data.
- The spread length (i.e., the maximum offset).
- The stacking fold (i.e., the number of traces in the CMP gather).
- The choice of coherency measure.

Velocity spectra can be generated/calculated using a variety of different coherency measures (Yilmaz, 2001), each of which expresses in a slightly different way the similarity between the traces of the CMP gather, such as:

- The stacked amplitude (S) (3.7), which is a measure particularly sensitive to trace polarity (Figure 3.5b) (e.g., Causse & Sénéchal, 2006; Fisher et al., 1992; Van Overmeeren et al., 1997).

- The unnormalised cross-correlation sum (CC) (3.8), which highlights better the strong/high-amplitude events of the CMP gather (Figure 3.5c) (e.g., Feng et al., 2009; Feng & Sato, 2004; Hamann et al., 2013).
- The normalised output-to-input energy ratio (NE) (3.9), which is a biased measure that always returns a value between 0 and 1 (Figure 3.5d). The NE, which is commonly referred to in the literature as semblance (Neidell & Taner, 1971), and offers a better standout of the different events than the other two measures, while it is also, as a process, straightforward, computationally efficient, and robust against noise (Zhou, 2014). Therefore, semblance, for these reasons is nowadays the most widely used measure for generating velocity spectra in both the seismic reflection method and the GPR method (e.g., Becht et al., 2006; Berard & Maillol, 2007; Booth et al., 2008; Booth, Clark, & Murray, 2010; Bradford, 2003; Church et al., 2020; Dal Bo et al., 2019; De Domenico et al., 2013; Forte & Pipan, 2017; Greaves et al., 1996; Huisman et al., 2003; Igel et al., 2013; Jacob & Urban, 2016; H. Liu & Sato, 2012; Murray et al., 2007; Pipan et al., 2003; Rashed et al., 2003; Turesson, 2006).

However, despite the advantages, conventional semblance has a major drawback, it does not handle strong amplitude versus offset (AVO) variations properly, as it assumes a constant amplitude model (i.e., requires the CMP gather event(s) to have a constant amplitude) (Sarkar et al., 2001). Consequently, it can perform poorly for data that are characterised by such variations. Even though there is a measure of coherency known as AB semblance (Sarkar et al., 2002) which was developed for such variations, it is more computationally expensive, twice as sensitive to noise, and has half the resolution of its conventional counterpart (Fomel, 2009).

$$S_i = \sum_{j=1}^F a(i, j) \quad (3.7)$$

$$CC = \frac{1}{2} \sum_{i=k-N/2}^{k+N/2} \left\{ \left[ \sum_{j=1}^F a(i, j) \right]^2 - \sum_{j=1}^F a^2(i, j) \right\} \quad (3.8)$$

$$NE = \frac{1}{F} \frac{\sum_{i=k-N/2}^{k+N/2} (\sum_{j=1}^F a(i, j))^2}{\sum_{i=k-N/2}^{k+N/2} \sum_{j=1}^F a^2(i, j)} \quad (3.9)$$

where:

- S The stacked amplitude.  
 CC The unnormalised cross-correlation sum.  
 NE The normalised output-to-input energy ratio/semblance.  
 F The fold of the gather.  
 N The window length.  
 k The centre of the window.  
 $a(i, j)$  The amplitude of  $i^{\text{th}}$  sample of the  $j^{\text{th}}$  trace.

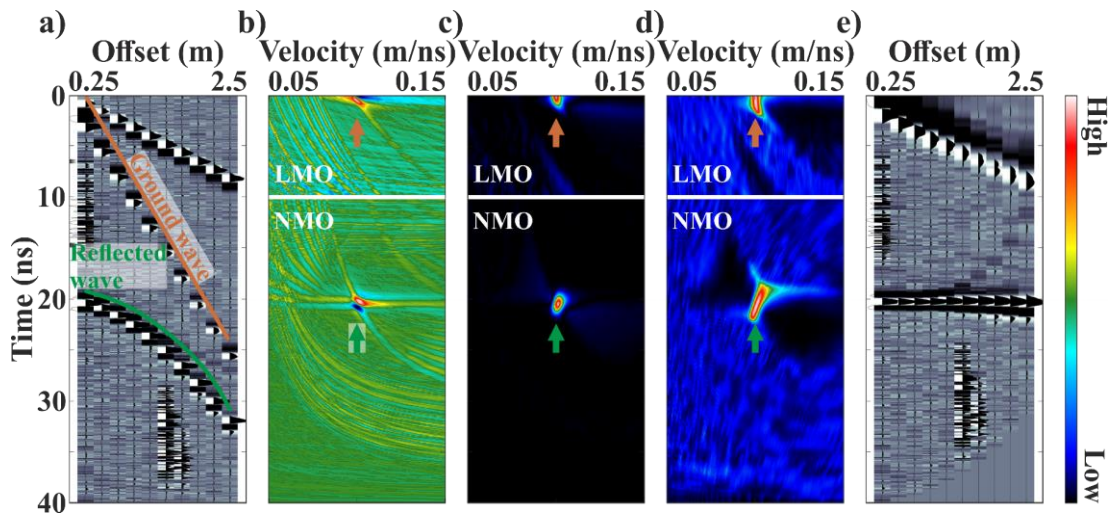


Figure 3.5: a) Synthetic CMP gather contaminated with white Gaussian noise and noise bursts. b) Combined LMO NMO velocity spectrum panel/S panel of (a). c) Combined LMO NMO velocity spectrum panel/CC panel of (a). d) Combined LMO NMO velocity spectrum panel/NE panel of (a). e) NMO corrected CMP gather of (a) using velocity picked from NE panel (d). In (b) – (d) orange arrows highlight the maxima corresponding to the direct ground wave, while green arrows highlight the maxima that correspond to the reflected wave.

### NMO stretch and mute

As it was mentioned above, NMO correction stretches the data in time and does so in a non-constant manner, i.e., the values of a trace are shifted with a different amount, hence it is a dynamic correction (van der Kruk, 2001). The NMO stretch ( $S_{\text{NMO}}(x)$ ) is given by (3.10) (Mousa & Al-Shuhail, 2011; Yilmaz, 2001) and is a frequency distortion ( $\Delta f$ ) in which the data of the CMP gather are shifted to lower frequencies (Onajite, 2014). The NMO stretch is also particularly high for shallow times and larger offsets (Figure 3.6b).

Therefore, since stacking NMO corrected traces (i.e., stretched traces) will damage the shallow events, very often before stacking, a mute based on a threshold is applied to the high-stretch zones of the NMO corrected CMP gather (Figure 3.6c).

$$S_{\text{NMO}}(x) = \frac{\Delta t_{\text{NMO}}}{t_0} = \frac{\Delta f}{f_c} \quad (3.10)$$

where:

$S_{\text{NMO}}(x)$  The NMO stretch at an offset.

$t_0$  The travel time at zero-offset (s).

$\Delta t_{\text{NMO}}(x)$  The difference between the travel time at an offset not equal to zero and the travel time at zero-offset for hyperbolic events (s).

$\Delta f$  The change in frequency (Hz).

$f_c$  The dominant frequency (Hz).

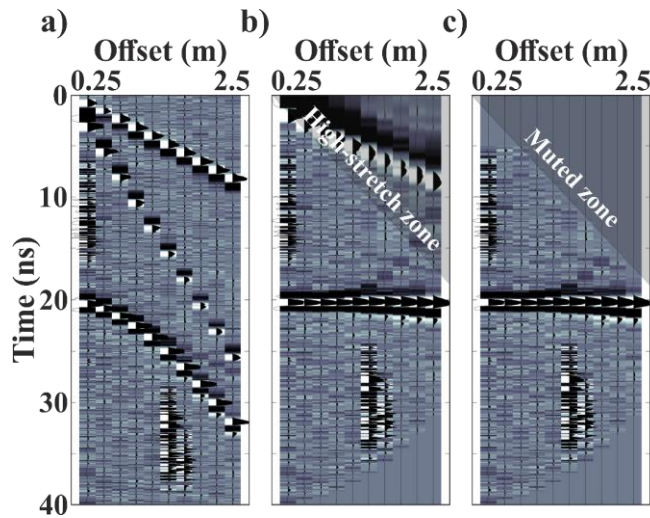


Figure 3.6: a) Synthetic CMP gather contaminated with white Gaussian noise and noise bursts. b) NMO corrected CMP gather of (a). c) NMO corrected CMP gather of (a) after the application of stretch mute. In (b) the triangle highlights the high-stretch zone, while in (c) the muted zone.

### Stacking or horizontal stacking

CMP stacking, which is also often referred to as horizontal stacking, was first introduced by William Harry Mayne in 1962 (Mayne, 1962), and has since then been one of the most important seismic reflection and MF GPR data processing steps (Rashed, 2014). Same as vertical stacking previously discussed (Ch. 2.7), is the process of

averaging several traces coming from the same location, and in this case, the traces of an NMO corrected CMP gather (Figure 3.7). The purpose of this step is to reduce the background noise, and hence, to improve SNR, which can be increased by  $\sqrt{F}$  where  $F$  is the CMP gather fold (Hatton et al., 1986; Yilmaz, 2001).

Optimum results from CMP horizontal stacking can only be obtained if a proper NMO correction has been previously performed to the gather, as misaligned, over-corrected or under-corrected events will lead to poor stacking results. However, exactly due to this fact, CMP stacking itself can also be used as a method of attenuating multiple reflections. This is because multiples correspond to lower velocities than primaries, and therefore, after a proper NMO correction with primary velocities, they will be slightly under-corrected (Yilmaz, 2001).

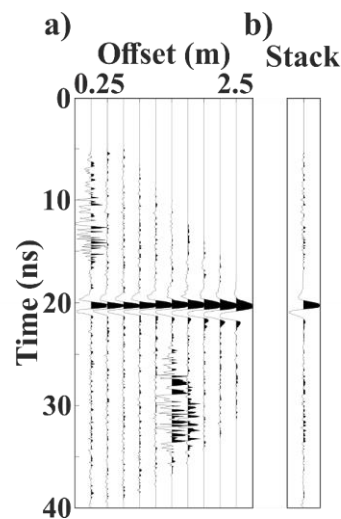


Figure 3.7: a) NMO corrected synthetic CMP gather contaminated with white Gaussian noise and noise bursts after the application of stretch mute. b) Stacked trace of (a).

### 3.3 Multi-concurrent receiver GPR systems

Until the late 1980s, GPR data processing, and hence interpretation, was very limited, as data were collected in analogue form on audiotapes and digitised at later times. This has changed with the advent of new technology, namely the digitally recording GPR systems. These systems not only improved the quality of the collected data (e.g., Davis & Annan, 1989) but also made it possible to adapt seismic processing workflows to the GPR data (e.g., Fisher et al., 1992). At the same time, and mainly due to those

reasons, the need for multi-channel GPR systems that could allow for the acquisition of simultaneous and continuous multi-offset soundings began to become apparent and has since then been highlighted over the years by many researchers (e.g., Bangbing et al., 2006; Becht et al., 2006; Booth et al., 2008; Fisher et al., 1992; Forte et al., 2014; Greaves et al., 1996). Nevertheless, the development of such highly advanced instruments has until recently been particularly challenging.

With the advances in ADCs (Pelgrom, 2013), new high-speed chips have become available that allow for increased sampling speeds, and therefore higher data SNR, whilst requiring the same or even less acquisition time (Annan, 2009; Johnsson & Björklund, 2005; Koppenjan, 2009). Furthermore, undesired signals arising from the GPR system cables, well-known issues for the past three decades (e.g., Ebihara et al., 1998; E. Guy & Radzevicius, 2001; Sato & Thierbach, 1991; Wright et al., 1984), are now trackable and can therefore be significantly reduced (e.g., with the use of fibre-optic cables, Bluetooth links, better shielding materials, etc.) (Babcock et al., 2016). Moreover, the drifting time delays resulting from various other hardware-related factors (e.g., differences in temperature, supply voltage, etc.) (Sensors & Software Inc., 2001), which can cause time uncertainties in the GPR transducers, are now possible to be reduced to tens of picoseconds or less, thus allowing concurrent receiver operation (Annan & Jackson, 2017).

All these improvements have finally led to the development of new multi-channel GPR systems with multiple concurrent data acquisition receivers, such as the “WARR Machine” manufactured by Sensors & Software Inc. and shown in Figure 3.8. These newly developed GPRs offer the potential to provide all the benefits of the MF modes (see Ch. 3.1), with significantly less effort, and therefore, reduced survey time and cost, as they enable the rapid acquisition of multi-offset WARR soundings with the same speed as the traditional CO mode of operation. For instance, the so-called “WARR Machine” GPR allows for the acquisition of up to seven CO profiles, simultaneously, which can then be sorted into WARR and/or CMP gathers. Nevertheless, despite their potential, these systems as well as the data that they produce come with a lot of challenges, some of which have been identified by Annan & Jackson (2017), Diamanti et al. (2018), and Kaufmann et al. (2020), currently the only published works on the use of such systems.

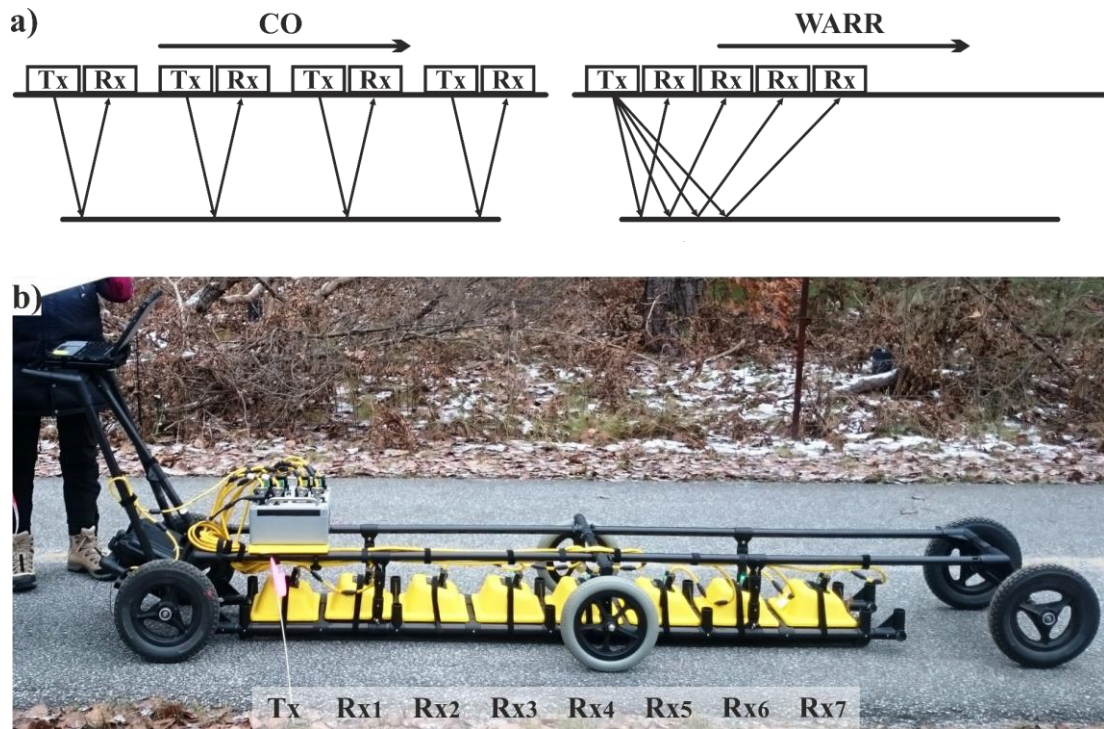


Figure 3.8: a) The SF CO and MF WARR mode of operation. b) Multi-concurrent receiver GPR system that combines the two modes of (a). The “WARR Machine” by Sensors & Software Inc.

### 3.3.1 Previous studies

#### The WARR Machine (Annan & Jackson, 2017)

In 2017, Annan & Jackson introduced the first embodiment of a fully flexible multi-channel GPR WARR system with multi-concurrent sampling receivers. Their system, the so-called “WARR Machine”, consisted of one transmitter and seven receivers, all with 500 MHz centre frequency, placed sequentially and separated by 0.25 m. Annan & Jackson described, in their relatively short study, the general limitations of developing a GPR system of this type (e.g., physical limitations on receiver spacing and limitations on the number of receivers due to cost and mobility), the challenges that they had to overcome to successfully develop it (e.g., stabilising timing controls and minimising electronic delays), as well as other challenges related to the large volume of WARR data that it can generate and need to be explored further (e.g., improving data handling and automating the processing sequence). In addition, they deployed the system in the field on a controlled test line and performed a simplified analysis of the collected MF data. Specifically, they used standard seismic data processing routines,

including automated velocity analysis to create NMO corrected stacked cross-sections. Their results, however, were not the expected. Nevertheless, they demonstrated that the goal is generally viable.

**The WARR Machine: System Design, Implementation and Data (Diamanti et al., 2018)**

Almost a year after the preliminary work of Annan & Jackson (2017), Diamanti et al. (2018) presented a much more extended and in-depth study on the same multi-channel GPR, namely the “WARR Machine”. They described in detail the basic instrumentation challenges, while also focusing on the handling and processing aspects of the high volume of WARR data that can be generated by this newly developed system. Diamanti et al. highlighted the need for automation and better data handling, as well as the necessity to adapt the standard seismic concepts to address the different character of GPR data, particularly the timing alignment and strong AVO variations. Furthermore, they presented a processing workflow, including a step to manage the time misalignments from the different receivers, and applied it to field data collected from two different sites to produce NMO corrected stacked cross-sections. However, their results, including the stacking velocity cross-sections and the stacked cross-sections, were not as expected, and proved problematic. Diamanti et al. also tested the concept of stacking the data using constant velocities rather than velocity cross-sections, as well as that of spatial semblance filtering to improve velocity picking from the spectra panels. Although the results were not optimal, they looked very promising, and therefore, the need for further investigation was stressed by the research group. Diamanti et al. concluded their study by providing numerous topics that could be further explored, which are related both to the design of the system (e.g., number of receivers required for reliable results) as well as to the management (e.g., optimal use of the high-volume of MF data generated) and processing (e.g., automation of velocity analysis) of the data.

**Simultaneous multichannel multi-offset ground-penetrating radar measurements for soil characterization (Kaufmann et al., 2020)**

Finally, a very good study using multi-concurrent receiver GPR data for soil characterisation was published by Kaufmann et al. in 2020. Kaufmann et al. deployed Sensors & Software Inc. “WARR Machine” on an agricultural test site to investigate the potential of estimating, with such a GPR system, the subsurface EM wave velocity and soil water content. Similarly, as Diamanti et al. (2018), they presented a processing workflow for multi-concurrent receiver GPR data, including a method for managing the time misalignments between the different receivers as well as an automated semblance analysis approach with filtering. However, while their method for managing the time misalignments is accurate, it is also very time-consuming because it requires additional controlled data collected in a specific way, and while their semblance analysis approach is automatic, it has only been developed for ground wave velocity picking. Furthermore, Kaufmann et al. successfully estimated subsurface EM wave velocity using a semi-automated semblance analysis approach (i.e., automatic ground wave velocity picking and manual reflected wave velocity picking) and compared the results obtained from the “WARR Machine” with respective results from a single-channel GPR system. Nonetheless, despite estimating subsurface EM wave velocity, they have not attempted to create NMO corrected stacked cross-sections. Finally, it is worth noting that they also conducted a time-lapse permittivity and soil water content analysis and their findings agreed with soil truth as well as EM induction data. The analysis, however, was based solely on ground wave velocities.

### **3.4 Summary**

The above brief review outlined the plethora of benefits that multi-offset GPR data can provide while explaining the reason behind their limited acquisition and use in recent decades. Furthermore, it underlined the similarities between seismic and EM wave fields but also highlighted their differences as well as the necessity to develop processing tools and adapt seismic processing for multi-offset GPR data. Finally, it revealed the potential of newly developed multi-concurrent receiver GPR systems while showcasing the need for further research, in particular, in the area of system design, data handling, and data processing.

# 4

## **Tools for obtaining and processing multi-concurrent receiver GPR data**

This chapter focuses on the tools that were used as well as developed to obtain and process multi-concurrent receiver GPR data. The chapter begins with a brief review of numerical modelling and a short presentation of the numerical solver used to generate the synthetic data. Then, the multi-concurrent receiver GPR system(s) used to collect the field data are discussed in detail, and a typical field data set is presented to demonstrate their character. Finally, a novel MATLAB-based software/software toolset is presented, which was developed for the visualisation and processing of both single-offset and multi-offset GPR data, including multi-concurrent receiver GPR data.

Research in this chapter has been published in Angelis et al. (2019) and Angelis et al. (2020).

## 4.1 Numerical modelling

The continuous evolution of technology, and in particular, the significant increase in computing power (e.g., central processing units (CPUs) and graphics processing units (GPUs) chips with multiple cores, faster random-access memory (RAM) chips, etc.) over the last two decades has allowed the rapid development of numerical modelling/simulation. As a result, numerical modelling has grown immensely and has become today a valuable and powerful tool for understanding and analysing almost any scientific problem (Inan & Marshall, 2011). Numerical modelling could not, of course, be absent from the field of near-surface geophysics and the GPR method itself, which nowadays has become more or less a standard approach for the following reasons (Angelis et al., 2018; Giannakis, 2016; Giannopoulos, 2005):

- It can be used for educational purposes.
- It can be applied to test data processing algorithms, workflows, and interpretation software.
- It can provide a better understanding of the scattering mechanisms within a medium, and therefore guide the interpretation of real data.

Numerical modelling has been used extensively in recent years for a variety of GPR-related problems such as mineral exploration (e.g., S. Liu et al., 2011), detection of dense non-aqueous phase liquids (DNAPLs) (e.g., Wilson et al., 2009), detection of landmines (e.g., Giannakis et al., 2016), detection of geological targets (e.g., Rao Hu et al., 2012), detection of moisture in monuments (e.g., Angelis et al., 2018), detection/assessment of pipes (e.g., Cassidy & Millington, 2009), assessment of bridges (e.g., Diamanti & Giannopoulos, 2011), tunnel inspection (e.g., He et al., 2009), and planetary exploration (e.g., Hamran et al., 2020), among others.

### 4.1.1 GPR forward problem

All EM phenomena, on a macroscopic scale, and therefore the EM wave propagation in a medium can be described by a set of equations which are known as **Maxwell's** equations (Maxwell, 1865). These are first-order partial differential equations that

express and describe mathematically the behaviour of electric and magnetic fields as well as their interactions with matter. Maxwell's equations are derived as a generalisation from the laws of **Faraday** (4.1), **Ampere** (4.2), and **Gauss** for both electric (4.3) and magnetic fields (4.4) (Balanis, 2012).

**Faraday's law**

$$\nabla \times \vec{E} = -\vec{M}_i - \frac{\partial \vec{B}}{\partial t} = -\vec{M}_i - \vec{M}_d \quad (4.1)$$

**Ampere's law**

$$\nabla \times \vec{H} = \vec{J}_i + \vec{J}_c + \frac{\partial \vec{D}}{\partial t} = \vec{J}_i + \vec{J}_c + \vec{J}_d \quad (4.2)$$

**Gauss's law for electric fields**

$$\nabla \cdot \vec{D} = \rho \quad (4.3)$$

**Gauss's law for magnetic fields**

$$\nabla \cdot \vec{B} = 0 \quad (4.4)$$

where:

- $\vec{E}$  The electric field intensity (V/m).
- $\vec{M}_i$  The impressed (source) magnetic current density (V/m<sup>2</sup>).
- $\vec{M}_d$  The magnetic displacement current density (V/m<sup>2</sup>).
- $\vec{H}$  The magnetic field intensity (A/m).
- $\vec{J}_i$  The impressed (source) electric current density (A/m<sup>2</sup>).
- $\vec{J}_c$  The electric conduction current density (A/m<sup>2</sup>).
- $\vec{J}_d$  The electric displacement current density (A/m<sup>2</sup>).
- $\vec{D}$  The electric flux density (C/m<sup>2</sup>).
- $\vec{B}$  The magnetic flux density (W/m<sup>2</sup>).
- $\rho$  The electric charge density (C/m<sup>3</sup>).
- $t$  The time (s).

The solution to the GPR forward problem is realised by solving/approximating the above equations using appropriate initial and boundary conditions since the nature of the problem itself classifies it as an initial value – open boundary problem (Giannopoulos, 2005). This can be achieved with the use of numerical methods, of which the **finite-difference time-domain (FDTD)** stands out for several reasons, the most important of which are mentioned below.

### 4.1.2 FDTD method

The FDTD method is nowadays one of the most popular and well-established methods used for GPR modelling, as it is robust, flexible and accurate, easy to understand, and has a short development time and explicit nature (Cassidy & Millington, 2009; Inan & Marshall, 2011; Taflove & Hagness, 2005). With the FDTD approach, both space and time are discretised into discrete counterparts, and as a result, the FDTD model represents a discretised reduced-size version of the real problem. The grid created by the discretisation is commonly referred to as the **FDTD grid**, and its building block is the **FDTD Yee cell** illustrated in Figure 4.1, which is named after Kane Yee who first introduced the FDTD method in 1966 (Taflove & Hagness, 2005; Yee, 1966). The spatial ( $\Delta x$ ,  $\Delta y$ ,  $\Delta z$ ) and temporal ( $\Delta t$ ) discretisation steps are particularly important, as the smaller they are, the more accurate the FDTD model is to the real problem, but at the same time, the more computing resources are required (i.e., processing power, memory, etc.). Therefore, most often a compromise between the accuracy of the model and the available computing resources is made, as the latter are, for obvious reasons, finite.

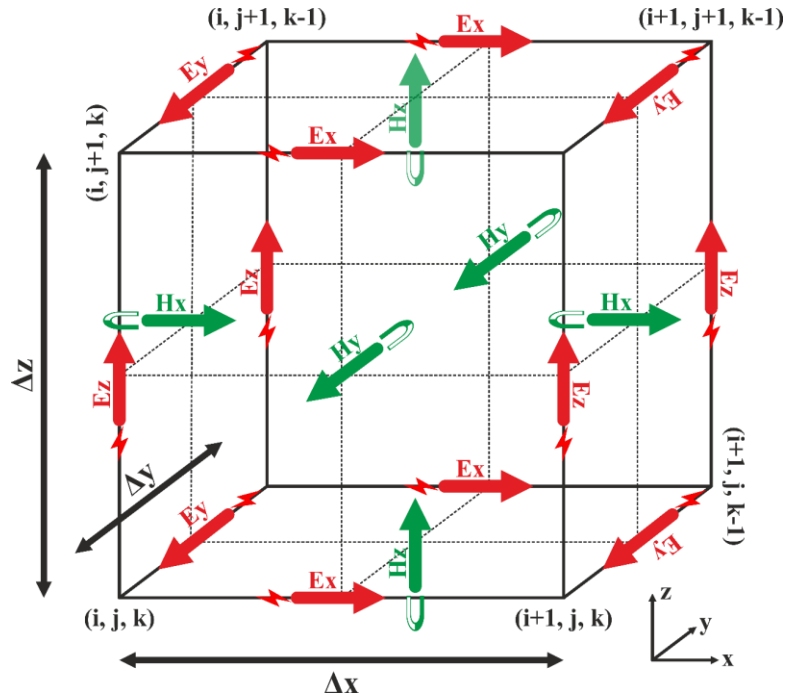


Figure 4.1: Single 3D FDTD Yee cell showing electric (red arrows) and magnetic (green arrows) field components. Figure adapted from Giannopoulos (2005).

### Stability condition

The FDTD numerical solution is obtained directly in the time domain by applying a discretised version of Maxwell's equations to each cell separately, whereas the simulation of time is done by solving the problem iteratively using a time step ( $\Delta t$ ). However, obtaining the solution directly in the time domain comes at a price, as the temporal ( $\Delta t$ ) and spatial ( $\Delta x$ ,  $\Delta y$ ,  $\Delta z$ ) discretisation steps cannot be assigned independently, and are bound to each other by the condition given by (4.5). This condition is known as the **CLF condition**, named after the initials of Courant, Freidrichs and Lewy, and ensures the stability of the FDTD method (Taflove & Hagness, 2005). The CLF condition for the 2D case can be easily obtained by letting ( $\Delta y \rightarrow \infty$ ) and is given by (4.6).

$$\Delta t \leq \frac{1}{c \sqrt{\frac{1}{(\Delta x)^2} + \frac{1}{(\Delta y)^2} + \frac{1}{(\Delta z)^2}}} \quad (4.5)$$

$$\Delta t \leq \frac{1}{c \sqrt{\frac{1}{(\Delta x)^2} + \frac{1}{(\Delta z)^2}}} \quad (4.6)$$

where:

$\Delta t$  The time step.

$\Delta x$  The cell size on the X-axis.

$\Delta y$  The cell size on the Y-axis.

$\Delta z$  The cell size on the Z-axis.

$c$  The velocity of light in free space ( $\sim 3 \times 10^8$  m/s).

### **Absorbing boundary condition**

As previously mentioned, the GPR forward problem is an open boundary problem. This, in other words, means that to obtain the desired numerical solution, the simulated EM waves must be calculated until their energy becomes equal to zero, i.e., they must propagate until infinity. Since this is practically impossible to accurately simulate on a computer, owing to finite computing resources, the computational domain is truncated, and therefore limited, by introducing boundaries at the edges of the FDTD grid. This is being done with the application of an **absorbing boundary condition (ABC)**, the role of which is to absorb the impinging EM waves, and thus simulate an unbounded space (Giannopoulos, 2005). One such type of ABC is the well-known **perfectly matched layer (PML)**. The PML was first introduced in 1994 by Berenger (1994) and has since then become the most commonly used ABC in the FDTD method, as in contrast to other previous methods is more accurate, more stable, and very effective in complex media (e.g., non-linear, anisotropic, dispersive, etc.) (Bérenger, 2007; Gedney, 2011; Taflove & Hagness, 2005).

### **4.1.3 The gprMax FDTD solver**

To perform the numerical simulations and generate the synthetic MF GPR data needed to conduct this research gprMax numerical solver was used. gprMax is open-source software (<https://www.gprmax.com/>) that simulates EM wave propagation by solving Maxwell's equations (4.1) – (4.4), either in 2D or 3D space, using the FDTD method. The software was originally developed in the C programming language in 1995 (Giannopoulos, 2005) when numerical modelling was still in its infancy. It was then rewritten in Python and Cython in 2016 (Warren et al., 2016), and has since been continually developed to the point where it nowadays allows simulations to run not only

on multi-core CPUs but also on multiple GPUs (Warren et al., 2019). `gprMax` incorporates a variety of advanced modelling features (Warren et al., 2016) such as:

- higher-order multi-pole PMLs (Giannopoulos, 2012, 2018)
- diagonally anisotropic as well as dispersive material modelling (Giannakis & Giannopoulos, 2014)
- soil modelling with heterogeneous objects and rough surface generation (Giannakis, Giannopoulos, & Warren, 2016)
- built-in libraries of antenna models (Giannakis et al., 2019; Warren & Giannopoulos, 2011)

and has become the de facto simulation tool for GPR, having been used successfully over many years by many researchers for a diverse range of applications in both academia and industry (e.g., Angelis et al., 2018; Diamanti & Annan, 2013; Galagedara et al., 2005; Giannakis et al., 2021; Giannakis, Giannopoulos, & Yarovoy, 2016; Hamran et al., 2020; Lopera & Milisavljevic, 2007; Miorali et al., 2011; Wilson et al., 2009).

### **Modelling with `gprMax`**

`gprMax` is a command-line-driven software that does not currently have a graphical user interface (GUI) and works via text-based input files and/or scripting. The input file is an American standard code for information interchange (ASCII) text file that is supplied to the software and contains all the necessary information to create the model and run the simulation (e.g., size of the domain, spatial discretisation size, time window, type of excitation waveform, etc.). The information is given to the input file in the form of various commands, which in order to be detected by the software code must begin with the hash character (#). An example of such commands is shown in the listing below, which is actually the input file used to create the 3D two-layered model used to generate the synthetic data for demonstrating the MF GPR data processing steps in the previous chapter (Ch. 3.2).

1. #title: Two layered model
2. #domain: 5 1 2.2
3. #dx\_dy\_dz: 0.005 0.005 0.005
4. #pml\_cells: 20
5. #waveform: gaussiandot 1 0.5e9 waveform
6. #hertzian\_dipole: y 0.5 0.5 2 waveform
7. #rx\_array: 0.75 0.5 2 3 0.5 2 0.25 0 0
8. #src\_steps: 0.025 0 0
9. #rx\_steps: 0.025 0 0
10. #time\_window: 45e-9
11. #material: 09 0.005 1 0 layer1
12. #material: 14 0.010 1 0 layer2
13. #box: 0 0 1 5 1 2 layer1
14. #box: 0 0 0 5 1 1 layer2
15. #geometry\_view: 0 0 0 5 1 2.2 0.005 0.005 0.005 two\_layered n

The command shown in line 15 allows outputting information about the geometry of the model. gprMax uses the open-source Visualisation Toolkit (VTK) file format (<https://vtk.org/>) (Schroeder et al., 2006), which can be viewed by several free VTK readers such as ParaView (<https://www.paraview.org/>) (Ahrens et al., 2005). Figure 4.2a depicts the modelled geometry resulting from the above listing/input file, rendered in ParaView. The model domain is 5 x 1 x 2.2 m (x, y, and z axes, respectively), with a spatial discretisation of  $\Delta x = \Delta y = \Delta z = 0.005$  m and a time step  $\Delta t = \sim 9.63$  ps, as calculated by the CLF condition (4.5), as well as 20 PML cells/layers on each side. The objects in the model are two boxes, representing two different layers, with properties defined in lines 11 and 12, respectively (i.e., relative permittivity, electric conductivity (S/m), relative permeability, magnetic loss ( $\Omega$ /m), material id). There is also a Hertzian dipole source (red square) fed with a waveform shaped as the first derivative of a Gaussian with an amplitude equal to 1 and 500 MHz centre frequency, representing the transmitter antenna, as well as ten receiver points (yellow squares), representing the receiver antennas. The source and receivers are all separated by 0.25 m and moved, using the WARR mode of operation, along the centre-line of the model in increments of 0.025 m (i.e.,  $T_x - R_{x_1} / 10$ ). The analysis steps are set to 50 to allow the creation of maximum-fold CMP gathers (i.e., 10-fold CMP gathers), and the time

window is set to 45 ns. Figure 4.2b shows one of the synthetic WARR gathers (WARR 50) that were generated from the 3D two-layered model.

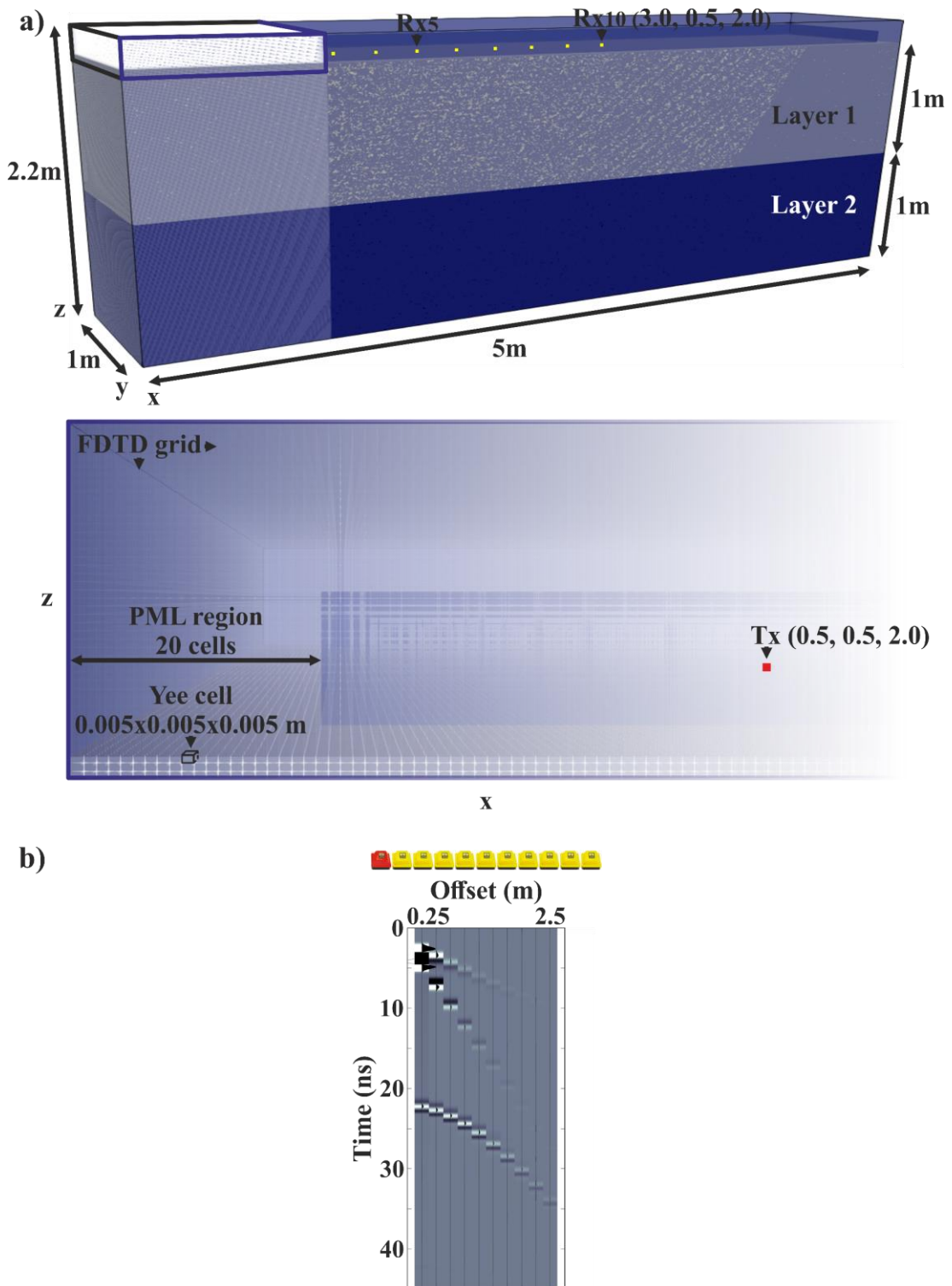


Figure 4.2: a) 3D two-layered model showing also the FDTD grid, Yee cells, and PML region. b) Synthetic WARR gather (WARR 50) generated from the model of (a). At the top, the transducer configuration can be seen, with the Tx depicted in red, and the Rx's in yellow.

### **Toolset for creating complex model geometries with gprMax**

As mentioned above, gprMax does not currently feature a GUI and operates using text-based input files and/or scripting. While this makes it very flexible and offers many benefits, such as allowing it to run easily on high-performance computing (HPC) environments (i.e., supercomputers) (Warren et al., 2016), it does make modelling objects with complex geometries very time-consuming. gprMax uses the FDTD method, namely a method based on Yee cells, which are essentially voxels. Therefore, a toolset (i.e., MATLAB-based scripts) has been developed to couple the software with a voxel editor to enable the creation of models with complex geometries quickly and easily using a GUI.

Nowadays, voxel editors are mainly used for two purposes: art design, which is also known as pixel art; and modelling and/or rendering for voxel-based games. For this work, MagicaVoxel (<https://ephtracy.github.io/>) has been used, which is a free lightweight 8-bit voxel editor and interactive path tracing renderer. This editor features a very user-friendly interface that allows for simple voxel editing, painting, and movement in a cubic grid.

MATLAB-based scripts have been developed that associate each individual voxel of MagicaVoxel to a Yee cell in the FDTD grid of gprMax, thus allowing voxels of different colours to correspond to different materials, and hence to different EM properties. The scripts, which are also given in Appendix A, convert the output of the voxel editor (i.e., vox format, <https://github.com/ephtracy/voxel-model>) to a suitable geometry file (i.e., HDF5 format <https://github.com/gprMax/gprMax>) that can be imported into gprMax. In addition, the scripts allow for the created geometry to be resized, and for multiple voxel models with different objects to be combined into a single geometry file.

Using this toolset, antenna models which require significant details to be modelled, and therefore typically hundreds of lines of code using scripting, can now be developed very fast using voxel drawing and editing and can be easily imported into GPR simulations as illustrated in Figure 4.3. The same process can also be used to model any other object and target with complex geometries as shown in Figure 4.4.

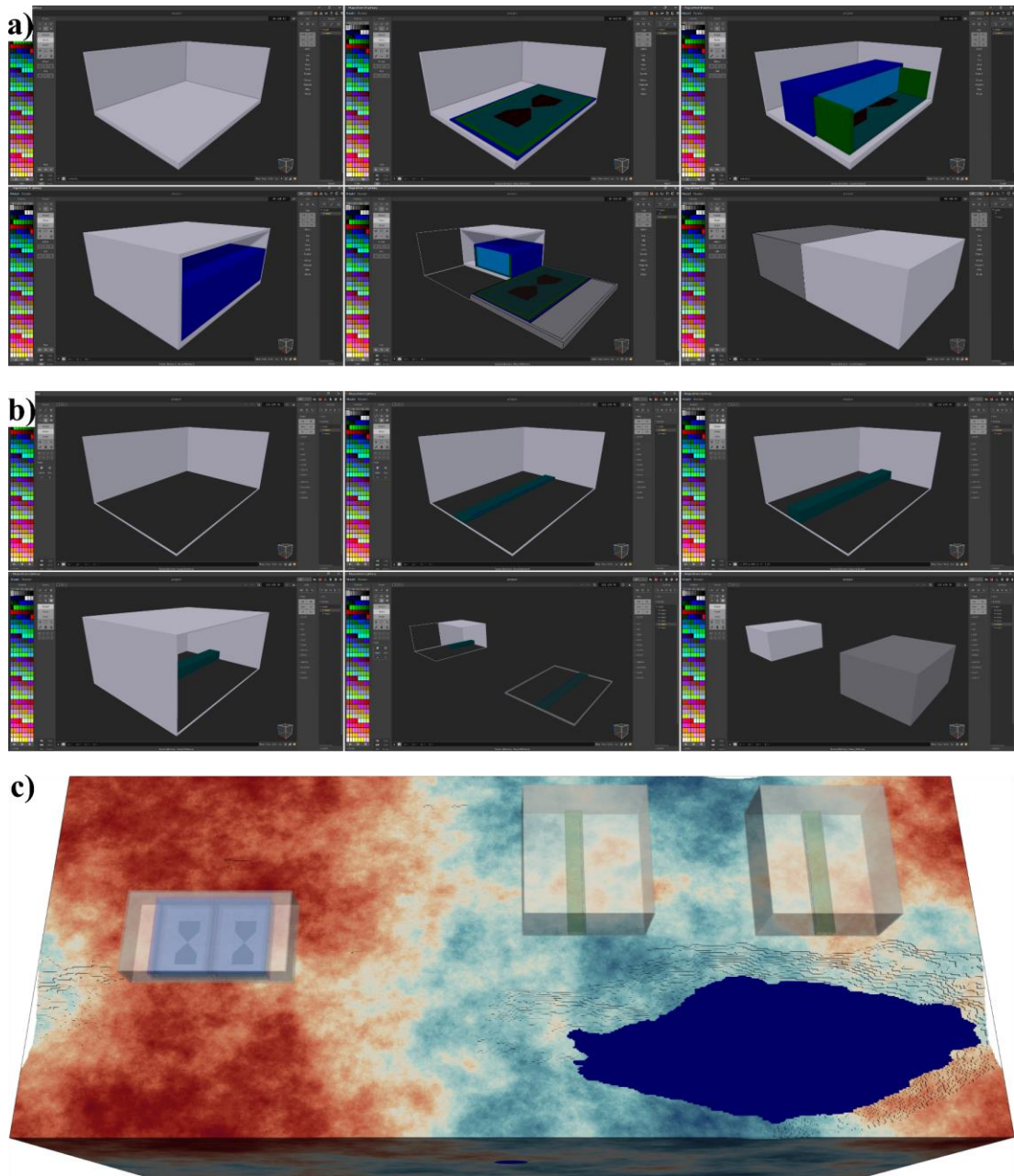


Figure 4.3: a) Development stages for creating an antenna model similar to a Geophysical Survey Systems Inc. (GSSI) 1.5 GHz centre frequency antenna in MagicaVoxel. b) Development stages for creating a Sensors & Software Inc. 500 MHz centre frequency like antenna model. c) Antenna models of (a) and (b) imported to gprMax and used with a heterogeneous soil model.

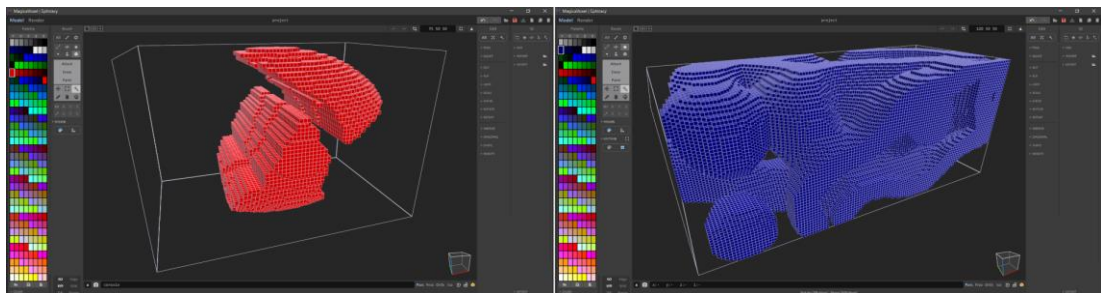


Figure 4.4: Dome-like and rectangular-like complex objects/targets created using MagicaVoxel.

## 4.2 The “WARR Machine” GPR

In order to carry out this research, in addition to generating synthetic MF GPR data, it was also necessary to perform field tests and collect field data with an actual multi-concurrent receiver GPR system. For this purpose, a visit had been planned to the headquarters of the industrial partner/sponsor – Sensors & Software Inc. – in Canada, as they have, both developed and possess many GPR systems of this particular type. However, unfortunately, this visit had to be cancelled twice due to the coronavirus pandemic (COVID-19) travel restrictions. Therefore Sensors & Software Inc. were asked to collect and provide the necessary data directly.

All field data sets used in this thesis were collected by Sensors & Software Inc. using the “WARR Machine” (Annan & Jackson, 2017; Diamanti et al., 2018), which is their newly developed multi-channel GPR WARR system featuring eight transducers, namely one transmitter and seven multi-concurrent sampling receivers (see also Ch. 3.3.1). The system enables the simultaneous acquisition of up to seven CO profiles at different offsets along the same line, resulting in the acquisition of hundreds of thousands of WARR and/or CMP gathers per hour. Data were collected in different time periods ranging from 2017 to 2021, from various environments, using different types of transducers and configurations for the system.

The two forms of the “WARR Machine” used to collect the data can be seen below. The first one, shown in Figure 4.5a, is the so-called SmartTow transducer configuration in which the receivers trail the moving transmitter, and the second one, shown in Figure 4.5b, is the so-called SmartCart which is a typical push configuration. Both the SmartTow and the SmartCart configurations use odometer wheel triggering for the transmitter. Regarding the GPR sensors, two different types of transducers were used, 500 MHz (Figure 4.5) and 1000 MHz (Figure 4.6) centre frequency transducers, which were all separated by 0.25 m and 0.165 m, respectively.

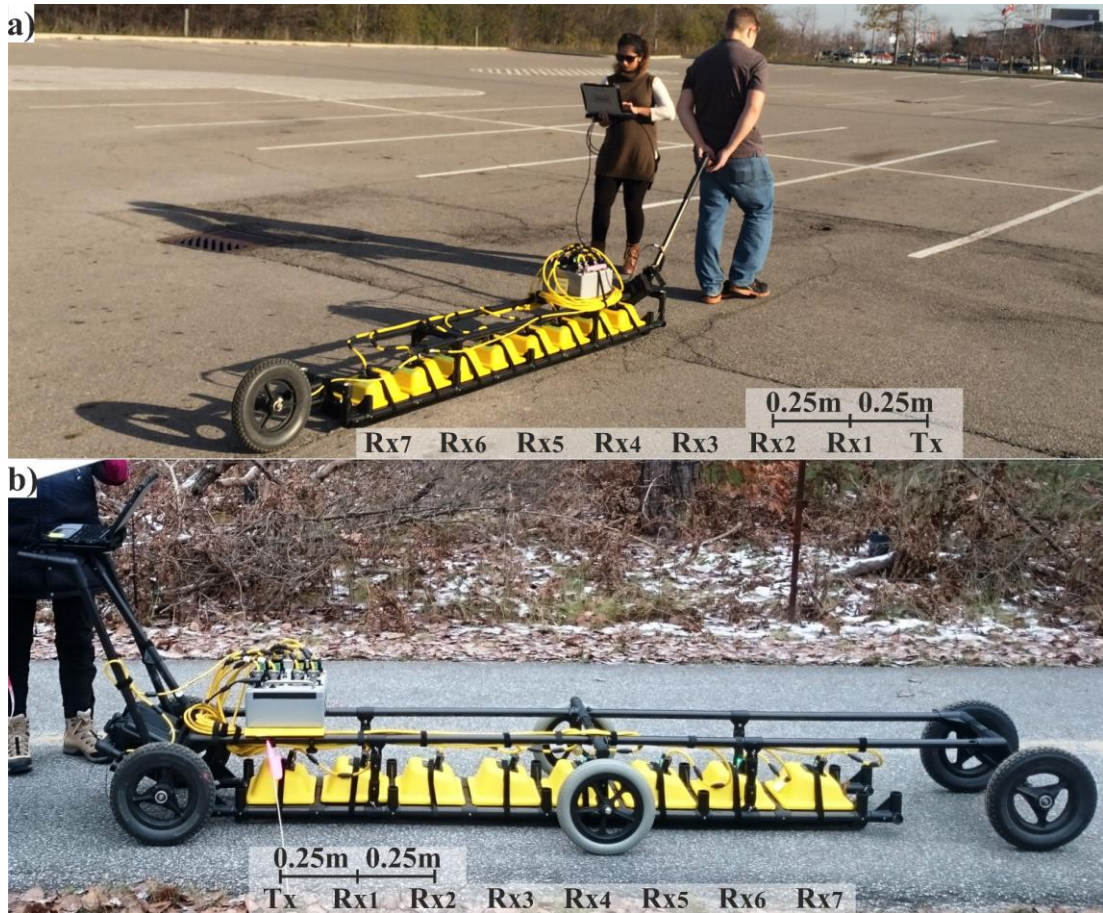


Figure 4.5: Two forms of the seven-channel “WARR Machine with 500 MHz centre frequency transducers. Figure adapted from Diamanti et al. (2018). a) SmartTow transducer configuration. b) SmartCart transducer configuration.



Figure 4.6: Seven-channel “WARR Machine” with 1000 MHz centre frequency transducers.

### 4.2.1 A typical multi-concurrent receiver GPR data set

An example of a typical multi-concurrent receiver GPR data set, which was provided by Sensors & Software Inc., is shown below. The data set was acquired from an asphalt-covered parking lot where the target of interest was a pipe. Data were collected at normal walking speed using the SmartTow configuration with 500 MHz centre frequency transducers all separated by 0.25 m (see Figure 4.5a). Measurements were performed using 16 vertical stacks per trace per receiver and with a spatial trace step of 0.0625 m (i.e.,  $Tx - Rx_1 / 4$ ), whilst the time window and sampling interval were 40 ns and 0.2 ns, respectively. Using these system/survey parameters, for a ~ 12 m long transect, seven CO profiles, equivalent to a total of approximately 200 WARR soundings, were acquired simultaneously in less than a minute.

The quality of the collected data can be seen in Figure 4.7a to Figure 4.7d which illustrate one of the WARR gathers (WARR 50), and the CO profile of the first (i.e.,  $Tx - Rx_1 = 0.25$  m), fourth (i.e.,  $Tx - Rx_4 = 1.0$  m), and seventh receiver (i.e.,  $Tx - Rx_7 = 1.75$  m), respectively. For visualisation purposes, i.e., to highlight the different sub-surface features, a dc shift removal has been applied to the WARR gather, and both dc shift removal and IAD gain to the CO profiles. The colour scale/greyscale of the CO profiles has also been adjusted accordingly. Notice the character of the collected data, and in particular:

- the time misalignments (e.g., the direct air wave responses of  $Rx_7$  and  $Rx_4$  are earlier in time than  $Rx_1$ , despite the increase of the offset – black dotted lines),
- the very strong AVO attenuation (e.g., see the amplitude values in the colour scales),
- and the increase of the high-frequency noise content (e.g., see the area/signal before the direct air wave/black dotted lines).

Thus, it is revealed that multi-concurrent receiver GPR data are in fact large-volume low-fold multi-offset GPR data, suffering from time misalignments, strong AVO attenuation, and reduced SNR versus offset.

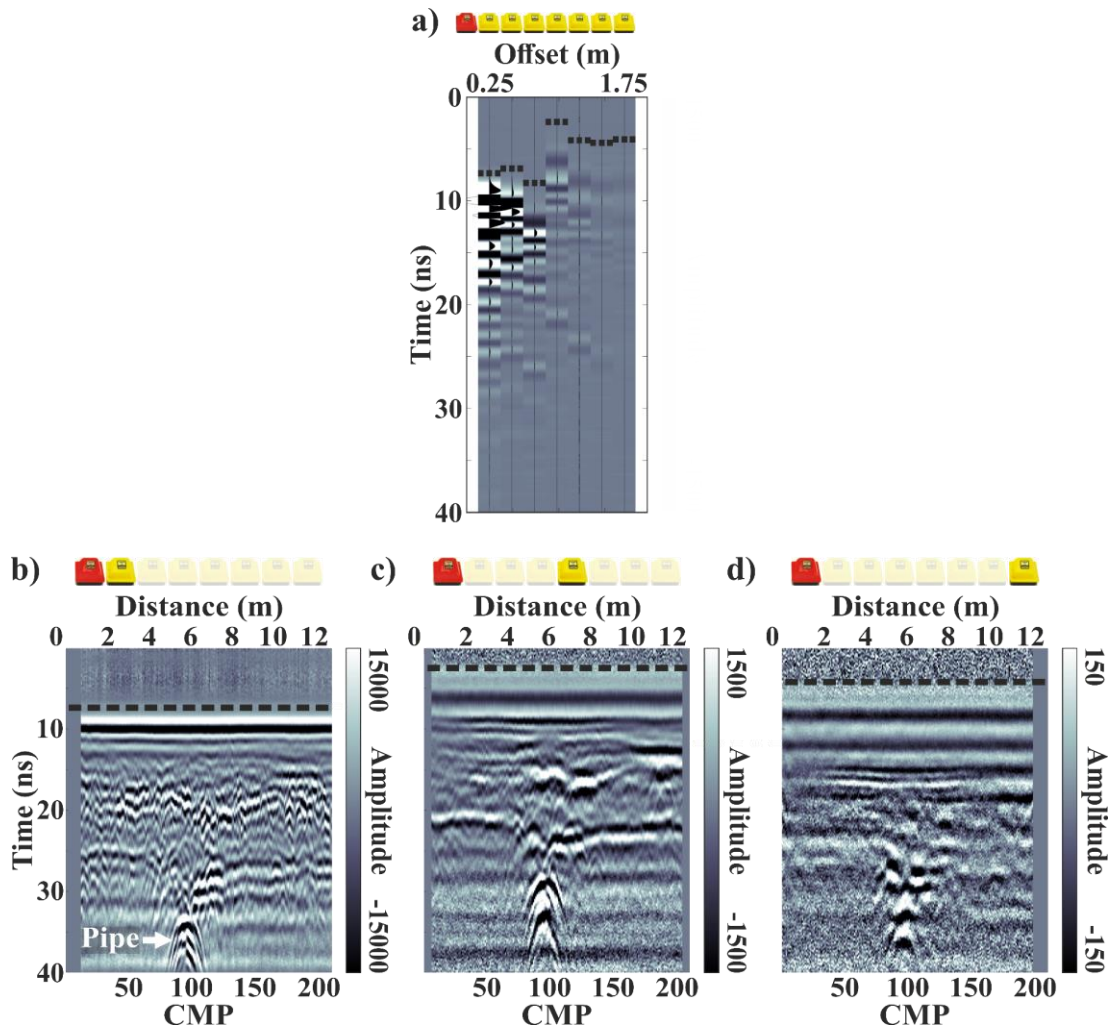


Figure 4.7: a) Field data WARR gather (WARR 50) after the application of dc shift removal. b) CO profile of the first receiver,  $T_x - R_{x_1} = 0.25$  m. c) CO profile of the fourth receiver,  $T_x - R_{x_4} = 1.0$  m. d) CO profile of the seventh receiver,  $T_x - R_{x_7} = 1.75$  m. DC shift removal and IAD gain have been applied to the CO profiles. The black dotted lines highlight the direct air wave responses and the white arrow the pipe response. The transducer configuration is shown at the top of each sub-figure, with the Tx in red and the Rx's in yellow.

## 4.3 GPR data visualisation and processing software

As mentioned and shown with various examples in previous chapters of this thesis, the visualisation and processing of GPR data is essential. GPR data visualisation techniques are particularly important, as they can aid in both the interpretation as well as presentation of the data. GPR data can be subjected to various coordinate transformations and be visualised in many ways providing subsurface information both horizontally and laterally (see Ch. 2.6). Likewise, processing GPR data is also particularly important, as it can be used to amplify and enhance the recorded signals, reduce or even eliminate the undesired signals, and therefore aid in the interpretation by highlighting the information relevant to the purpose of the survey (see Ch. 2.7). Processing is also necessary in the case of MF GPR data, as advanced specialised steps are required to further boost their SNR as well as to extract desired subsurface information such as EM wave propagation velocity (see Ch. 3.2).

Most GPR data visualisation and processing software nowadays are dedicated proprietary closed-source software provided (i.e., purchased or leased) either with the GPR system itself from the same manufacturer (e.g., EKKO Project<sup>TM</sup> – Sensors & Software Inc. (2021a); RADAN<sup>®</sup> – GSSI (2021)) or as independent standalone packages from other vendors (e.g., Geolitix – Geolitix Technologies Inc. (2021); GPR-Slice<sup>®</sup> – GPR-SLICE (2021)) (Cassidy, 2009b). The former cannot be used to visualise and/or process data collected by GPR systems of different manufacturers, whilst both the former and the latter generally incorporate simplified and/or a limited range of processing tools, especially for MF data. This is because these software packages have been mainly/also developed for users who are not fully experienced with the GPR and/or seismic reflection method from which several GPR processing techniques have been adopted. While there are some open-source software such as matGPR (MATLAB-based) (Tzanis, 2010), RGPR (R-based) (Huber & Hans, 2018), and GPRPy (Python-based) (Plattner, 2020), that can visualise and/or process GPR data from a variety of manufacturers and which incorporate many advanced processing tools, these have been developed either only or primarily for handling SF and not MF GPR data.

MATLAB<sup>®</sup> (The MathWorks Inc., 2021) is a programming and numeric computing platform and a high-level matrix-based scripting/programming language. MATLAB<sup>®</sup> is widely used both in academia and industry for visualising, analysing, and processing various types of engineering and scientific data. This is due to its many benefits the most important of which are listed below:

- The MATLAB language itself is quite easy to learn, understand, and use, owing to its very simple syntax.
- Has a user-driven highly active community (e.g., MATLAB answers forum, MATLAB file exchange, etc.).
- Has a rich set of toolboxes with numerous built-in functions (e.g., signal processing toolbox, image processing toolbox, etc.).
- Allows the development, testing, and debugging of algorithms very easily (e.g., live editor, code analyser, etc.).
- Allows the development of GUI applications in a variety of ways such as programmatically or using visual design environments (e.g., GUIDE, App Designer).

That said, to successfully fulfil the aims of the research project a MATLAB-based software with a user-friendly GUI for visualising and processing GPR data has been developed. The software supports file formats from various GPR manufacturers as well as the ability to handle data generated from gprMax (i.e., synthetic data) and the “WARR Machine” (i.e., multi-concurrent receiver GPR data). It consists of three different modules, each one developed with its own GUI and processing functions, which can work either independently or together:

- The **2D module** (Ch. 4.3.1), that can handle both SF and MF GPR data and allows for easy and fast control of the processing workflow, as well as batch processing (Figure 4.8).
- The **CMP/WARR module** (Ch. 4.3.2), that incorporates an interactive GUI tool used for velocity spectrum picking, as well as many advanced processing steps for MF GPR data (Figure 4.10).
- The **3D module** (Ch. 4.3.3), that supports most of the standard 3D data visualisation methods, as well as data export in formats suitable for visualisation and processing with third-party software (Figure 4.12).

### 4.3.1 2D module

The 2D module could easily be considered the heart of the software, since, under certain conditions, such for example the total number and extension of the files loaded or the type of the data, can also allow access to the two other modules, namely the CMP/WARR module and the 3D module. Moreover, depending on the above-mentioned conditions, additional menu options, as well as panels and buttons, can also be enabled and/or disabled on the GUI in order to facilitate the handling, visualisation, and processing of the imported data. Figure 4.8 depicts the GUI of the 2D module in its simplest form for a SF CO GPR data set. As can be seen consists of five different elements which are detailed below:

1. The menu bar, from which the user can access the file input/output (I/O), data analysis, editing, processing, and imaging options.
2. A data visualisation panel, which is used to visualise either the raw data or the data from the previous processing step (both an A-scan and the B-scan).
3. The info/header panel, which is a simple text panel that displays the data acquisition parameters (e.g., number of samples and traces, sampling intervals, etc.), as well as other computed information (e.g., number of WARRs/CMPs, maximum fold, etc.)
4. An additional data visualisation panel, which is used to visualise only the data from the current/chosen (see workflow panel below) processing step (both an A-scan and the B-scan).
5. The workflow panel, which is an interactive text list panel from which the user can access the data from any processing step (i.e., by double-clicking a step), undo or restore the data to a previous processing step (i.e., by pressing the left-hand side button), and save the processing workflow to a text file (.prc – file extension) (i.e., by pressing the right-hand side button) that can be used at any other time for batch processing.

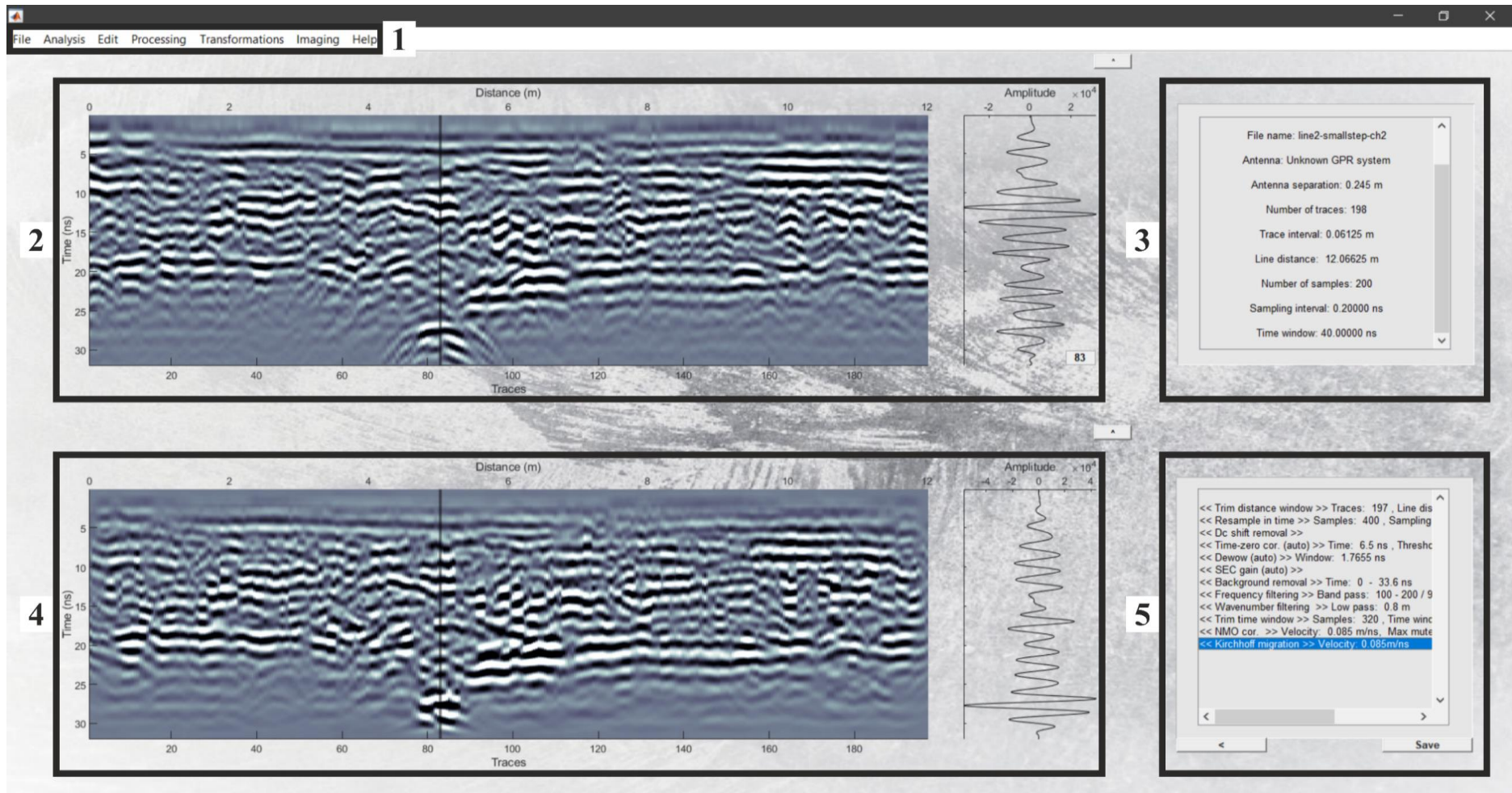


Figure 4.8: GUI showing the main elements of the 2D module for SF CO GPR data: 1. menu bar, 2. raw or previous processing step data visualisation panel, 3. info/header panel, 4. current/chosen processing step data visualisation panel, 5. workflow list panel.

The file menu provides all the standard file I/O operations. Different data file formats generated by a variety of GPR systems/manufacturers or via numerical modelling can be imported, exported, converted, or even combined under certain conditions (i.e., when the data acquisition parameters are the same) into a single file. The file formats supported by the software can be seen in Table 4.1. In addition, this menu allows for the batch processing of multiple data sets utilising the aforementioned processing workflow text file (i.e., .prc), which can be generated from the workflow panel.

The analysis menu offers a variety of functions for analysing GPR data. These functions are categorised as frequency spectrum analysis, FK spectrum analysis, signal attenuation analysis, fold analysis, and velocity hyperbolic fitting analysis (Figure 4.9). In addition, if certain conditions are met, related to the number of files or the type of data imported to the module, then this menu can also enable access to the other two modules of the software, namely the CMP/WARR and the 3D module.

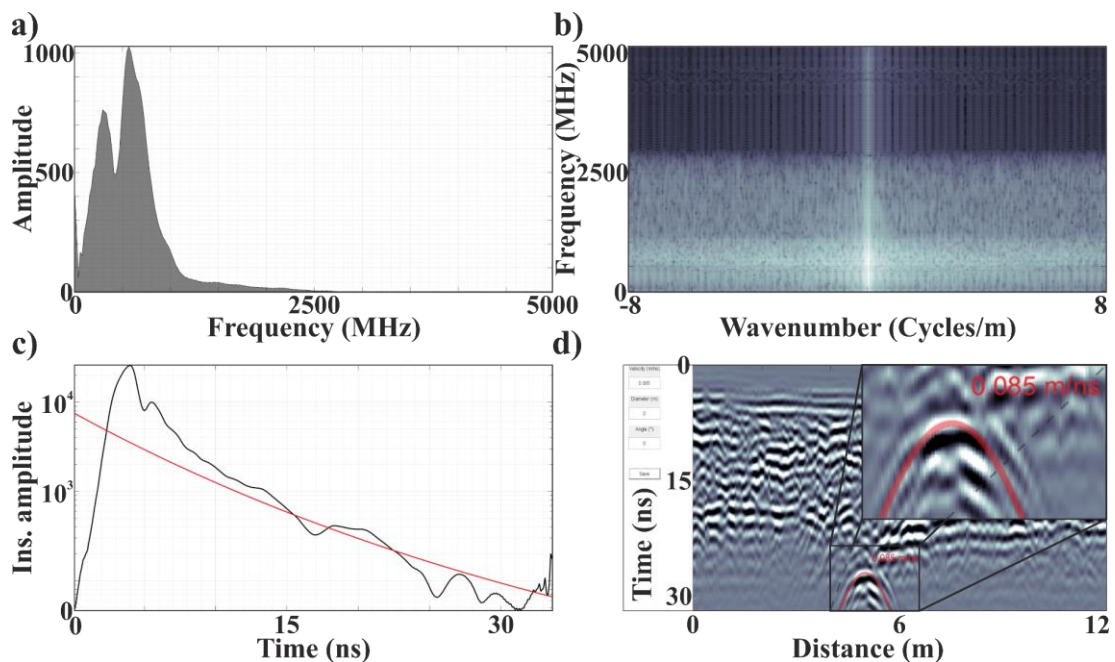


Figure 4.9: Various analysis methods of the 2D module, used in different stages of data processing. a) Frequency spectrum analysis. b) FK spectrum analysis. c) Signal attenuation analysis. d) Velocity hyperbolic fitting analysis.

The edit, processing, and transformation menus provide a wide variety of functions for many simplified and advanced processing methods, as well as other specialised techniques developed exclusively for multi-concurrent receiver GPR data. The latter will

be discussed in detail in the next chapter of this thesis (Ch. 5). Table 4.2 shows the available processing methods of the 2D module for SF CO GPR data. Several of these techniques, for example, time-zero correction, dewow, or even some types of time gain, can also be performed automatically, whilst most of them, for instance, background removal, frequency filtering, or AGC, provide additional options (e.g., window size, filter type, AGC type, etc.) via pop-up windows.

Last but not least, the imaging menu offers all the standard data visualisation tools such as display interpolation, different colourmaps, colour contrast/saturation, and wiggle trace plot.

Table 4.1: Software supported file formats.

<b>Developer</b>	<b>File extension</b>
gprMax	.out
GSSI	.dzt, .dzt
Impulse Radar	.iprb, iprh, .cor
Måla	.rd3, .rd7, .rad, .cor
MATLAB	.mat
Sensors & Software Inc.	.dt1, .hd, .gp2
Society of Exploration Geophysics	.sgy

Table 4.2: Processing methods of the 2D module of the software for SF CO GPR data.

<b>Edit</b>	<b>Processing</b>	<b>Transformations</b>
<ul style="list-style-type: none"> <li>▪ Time-zero correction</li> <li>▪ Residual statics</li> <li>▪ Reverse X-axis</li> <li>▪ Declip</li> <li>▪ Resample                             <ul style="list-style-type: none"> <li>□ Time</li> <li>□ Distance</li> </ul> </li> <li>▪ Downsample                             <ul style="list-style-type: none"> <li>□ Time</li> <li>□ Distance</li> </ul> </li> <li>▪ Mute                             <ul style="list-style-type: none"> <li>□ Area</li> <li>□ Traces</li> <li>□ Direct air wave</li> </ul> </li> <li>▪ Trim                             <ul style="list-style-type: none"> <li>□ Time window</li> <li>□ Distance window</li> </ul> </li> <li>▪ GSSI gain removal</li> </ul>	<ul style="list-style-type: none"> <li>▪ DC shift removal</li> <li>▪ Dewow</li> <li>▪ Time gain                             <ul style="list-style-type: none"> <li>□ AGC</li> <li>□ IAD</li> <li>□ SEC</li> <li>□ Power</li> <li>□ Custom</li> </ul> </li> <li>▪ Normalise traces</li> <li>▪ Background removal</li> <li>▪ Horizontal filtering</li> <li>▪ Frequency filtering</li> <li>▪ Wavenumber filtering</li> <li>▪ Karhunen-Loève filtering</li> <li>▪ Deconvolution</li> <li>▪ NMO correction</li> <li>▪ Migration                             <ul style="list-style-type: none"> <li>□ Stolt (time)</li> <li>□ Kirchhoff (time)</li> <li>□ Reverse time (depth)</li> </ul> </li> </ul>	<ul style="list-style-type: none"> <li>▪ Depth</li> <li>▪ Topography</li> <li>▪ Phase shift</li> <li>▪ Mathematical                             <ul style="list-style-type: none"> <li>□ Absolute</li> <li>□ Derivative</li> <li>□ Logarithm</li> <li>□ Power</li> <li>□ Root</li> </ul> </li> <li>▪ Hilbert transform                             <ul style="list-style-type: none"> <li>□ Amplitude</li> <li>□ Phase</li> <li>□ Frequency</li> </ul> </li> <li>▪ Sobel transform                             <ul style="list-style-type: none"> <li>□ Horizontal</li> <li>□ Vertical</li> </ul> </li> </ul>

### 4.3.2 CMP/WARR module

The CMP/WARR module was developed specifically for MF GPR data moveout-based processing (i.e., moveout-based velocity analysis, LMO/NMO correction, etc.). The CMP/WARR module can operate either independently or in conjunction with the 2D module as they are interconnected, which essentially means that the processing applied to the latter can also be passed internally to the former. Since moveout-based velocity analysis is a highly interactive procedure (e.g., velocity picking trials, etc.) that often also requires frequent parameter changes (e.g., velocity spectrum algorithms try-outs, etc.), a different approach was taken to design and develop the GUI of this module. More specifically, unlike the 2D module, all data visualisation and processing functions are in the main window rather than in menus, whereas any change in any parameter is directly reflected on all panels of the GUI. Figure 4.10 depicts the GUI of the CMP/WARR module. As it can be seen consists of six different elements which are detailed below:

1. The menu bar, from which the file I/O, as well as the data analysis options, can be accessed.
2. The velocity spectrum panel, which comes with an interactive tool that allows for manual velocity picking.
3. A panel for visualising the 1D stacking velocity function derived from velocity picking (black line), along with another computed velocity function such for example the instantaneous interval velocity or the average velocity (default option – instantaneous interval velocity – red line).
4. A panel for the visualisation of the investigated CMP gather.
5. A panel for displaying the near-offset trace of the CMP gather (black trace) versus the resultant stacked trace (red trace).
6. A panel for the visualisation of the resultant NMO corrected zero-offset stacked section (greyscale colourmap) overlaid by an interpolated velocity cross-section such for instance the stacking velocity or the interval velocity cross-section (default option – stacking velocity cross-section – rainbow colourmap).

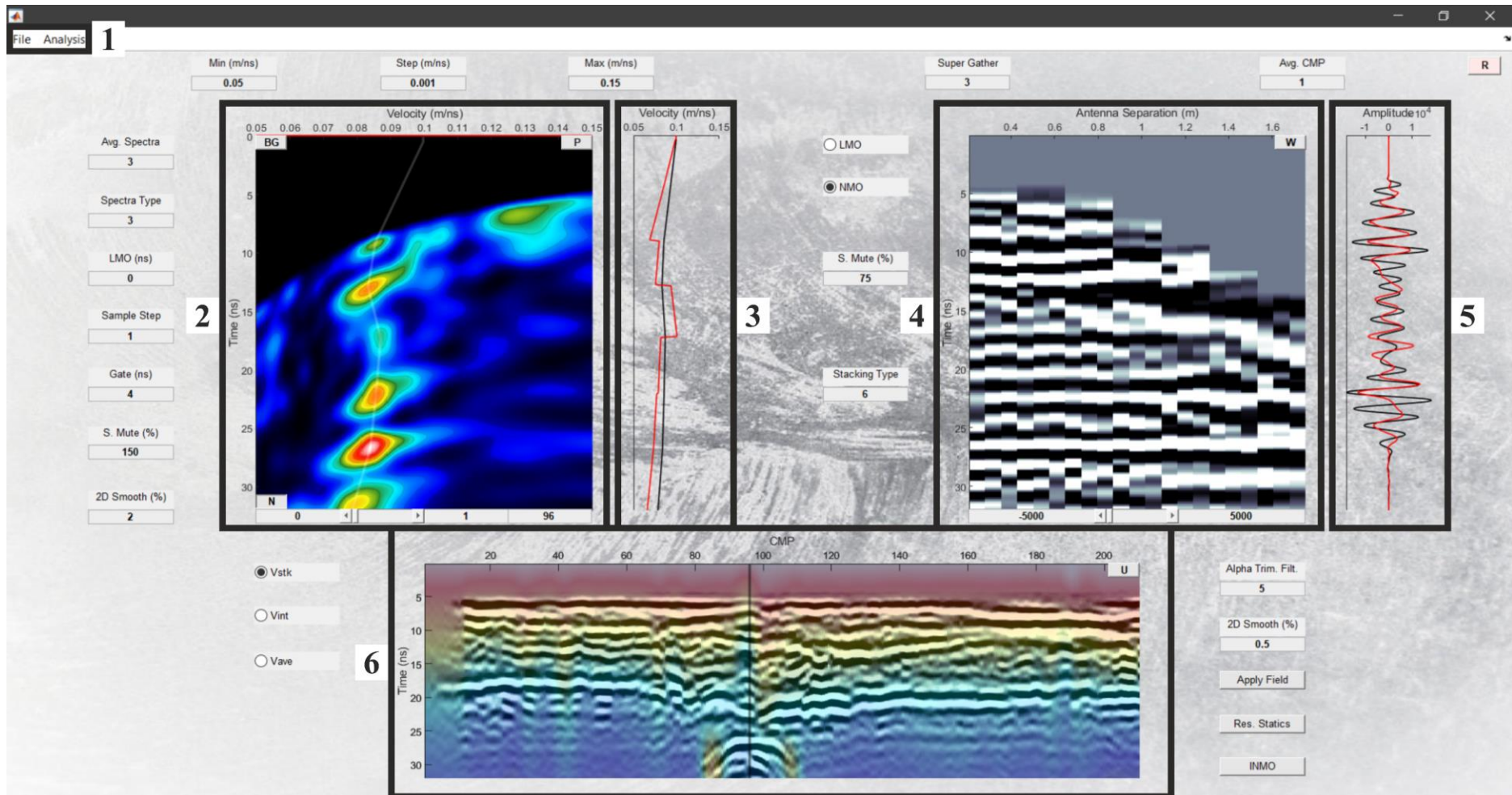


Figure 4.10: GUI showing the main elements of the CMP/WARR module: 1. menu bar, 2. velocity spectrum panel, 3. 1D stacking velocity panel, 4. CMP gather panel, 5. stacked trace panel, 6. NMO corrected zero-offset stacked section and interpolated stacking velocity cross-section panel.

The file menu, as in the 2D module, provides all the standard file I/O operations, as well as the ability to export the resultant interpolated velocity fields and the NMO corrected zero-offset stacked section.

The analysis menu offers three different functions for data analysis. The first is the same fold analysis function of the 2D module, which is also accessible from this module (Figure 4.11). The second is an interactive tool for picking the layer boundaries, if any, to allow the calculation of the interval velocities rather than the instantaneous interval velocities. Finally, the third is an automated velocity analysis picking tool, the algorithm of which will be discussed in detail in the following chapter of this thesis.

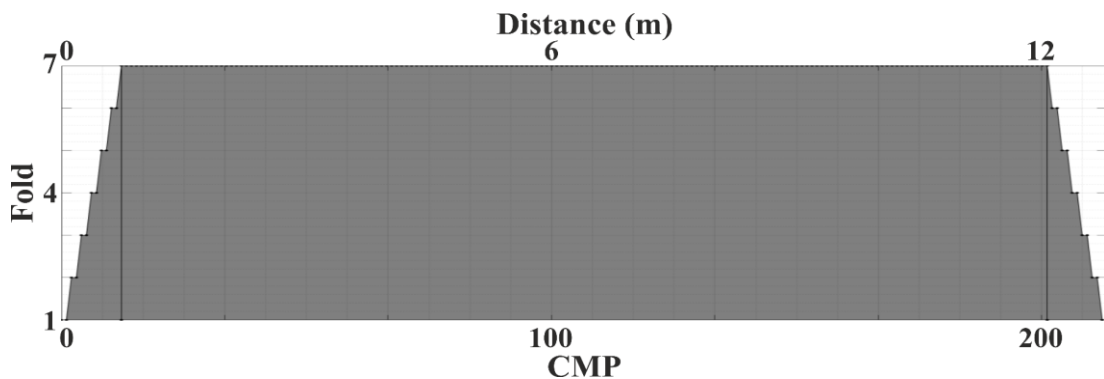


Figure 4.11: Fold graph generated using fold analysis function.

In terms of processing, this module incorporates a wide range of functions for many processing steps, some of which are more advanced and have been adopted from seismic reflection data processing methods. WARR and CMP gather sorting, CMP gather averaging, super CMP gather formulation, CMP trace balancing, LMO and NMO correction, NMO stretch mute, and residual statics correction, are some of these processing steps. Furthermore, the module provides different measures of coherency for computing the velocity spectrum, such as the stacked amplitude, unnormalised cross-correlation sum, semblance, AB semblance, high-resolution weighted semblance and AB semblance (Ebrahimi, Kahoo, Chen, et al., 2017; Ebrahimi, Kahoo, Porsani, et al., 2017; Fomel, 2009; Sarkar et al., 2001; Yilmaz, 2001), whilst also allowing for the computation of combined LMO NMO spectra, as well as spatial averaging/filtering of the spectra. Finally, the module incorporates several stacking methods for producing the final NMO corrected zero-offset stacked section including mean, median, alpha-trimmed mean, and smart stack (Rashed, 2008, 2014).

### 4.3.3 3D module

The 3D module was developed specifically for creating, manipulating, and visualising 3D GPR data. It is currently limited to GPR data collected in XY rectangular grids; however, further, development is planned to improve its functionality to also allow utilising data collected in semi-random paths with GPS. The 3D module can work either independently or in combination with the 2D module as they are interconnected, meaning that the processing applied to the latter is also applied to the former. Figure 4.12 depicts the GUI of the 3D module. As can be seen consists of three different elements which are detailed below:

1. The file menu, which provides all the standard file I/O operations, as well as the ability to export the data in different formats, including CSV, for visualisation and processing with other third-party software (e.g., Surfer and Voxler – Golden Software LLC., 2021).
2. A panel that contains the necessary gridding options for creating the 3D data set.
3. A panel that contains various buttons and sliders for all supported visualisation options, including 2D time and depth slices, isosurfaces, and 3D volumes.

Finally, something that is worth mentioning is that rather than incorporating an additional panel with various buttons and/or sliders for zooming and rotating options into its GUI, the results are visualised using a simple standard separate MATLAB figure.

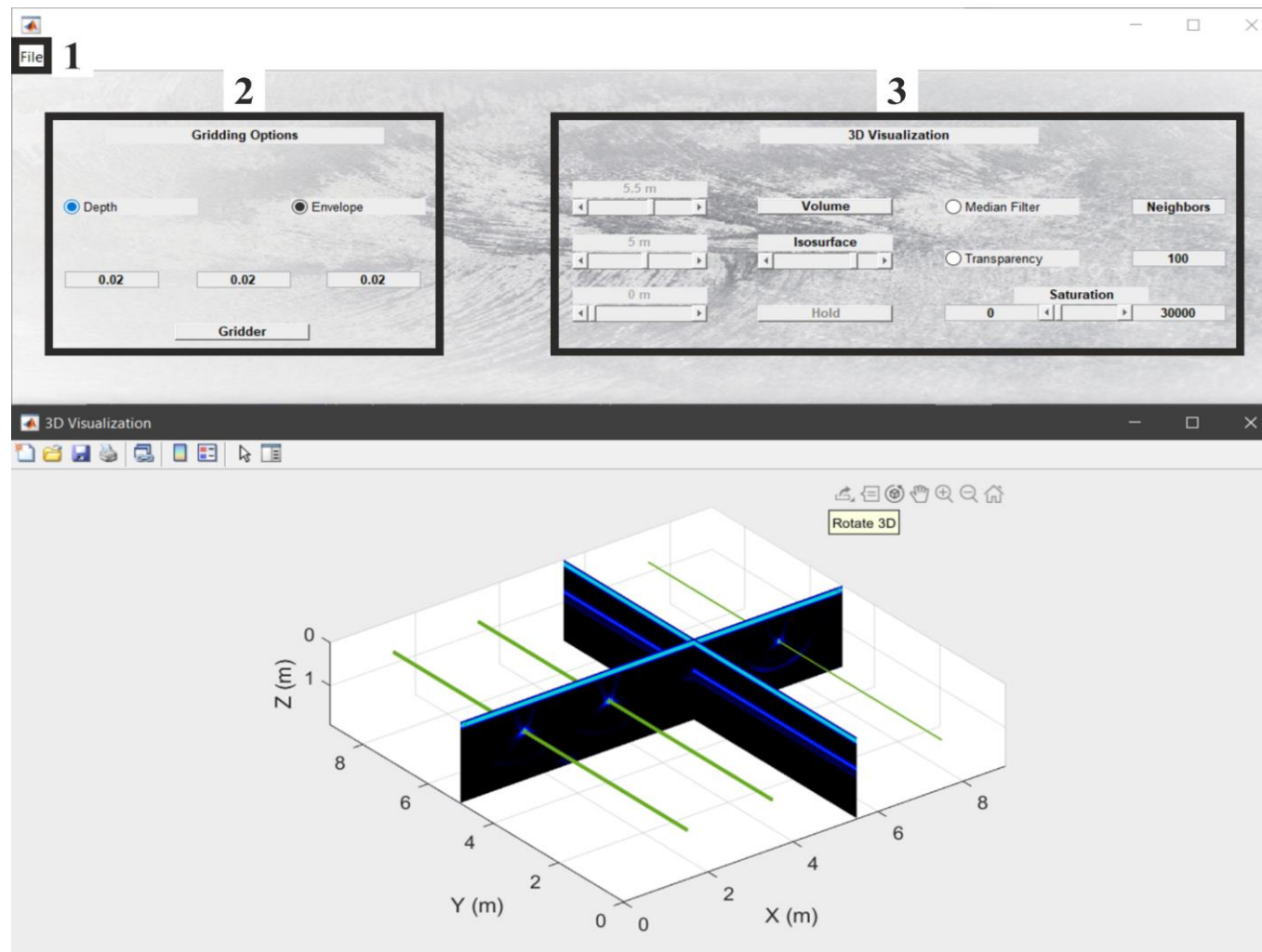


Figure 4.12: GUI showing the main elements of the 3D module: 1. file menu, 2. gridding panel, 3. 3D visualisation options panel.

# 5

## **Addressing the challenges of processing multi-concurrent receiver GPR data**

This chapter focuses on addressing the main challenges of processing multi-concurrent receiver GPR data and is divided into three different parts/sections. The chapter begins, with a presentation of a novel method developed for dealing with time misalignments from multi-concurrent receivers. Next, a new CMP trace balancing method is described that was developed to compensate for the large AVO differences in the data and thus improve semblance analysis and horizontal stacking. Finally, the chapter concludes with a presentation of a novel automatic velocity spectrum picking method designed to facilitate the analysis of large volumes of data generated by newly developed multi-concurrent receiver GPR systems.

Research in this chapter has been published in Angelis et al. (2022a).

## 5.1 Time-zero alignment

Recent advancements in GPR technology, and in particular, developments related to both the hardware and the interior design of GPR systems, such as the use of new high-speed ADCs, Bluetooth wireless connections, fibre-optic cables, stable well-positioned properly-aligned conductive cables, improved well-researched shielding materials, etc., have resulted in not only a significant reduction of unwanted noise but also in a sufficient minimisation of drifting time delays (Annan & Jackson, 2017; Babcock et al., 2016). Nevertheless, despite these advancements, the GPR signal is still affected by a variety of factors, such as differences in operating temperature, supply voltage variabilities, cable length differences, mechanical cable bending, component ageing, etc. (Diamanti et al., 2018; Sensors & Software Inc., 2001), and as a result, can exhibit noise, especially at a large offset, but most importantly can exhibit a slight time drift, and consequently be incorrectly aligned in time.

With a traditional single-channel GPR system comprised of a single transmitter-receiver pair, the latter issue is manageable and addressed with a single time-zero correction, as explained and shown in a previous chapter of this thesis (see Time-zero correction – Figure 2.12). Nevertheless, as the number of interlinked receivers increases in a system, as in the case of the newly developed multi-concurrent sampling receiver GPR systems, and thus of the “WARR Machine”, so does the number of required time-zero corrections. This is because the receivers exhibit not only different, but also inconsistent with their offset time drifts, due to the aforementioned factors, possible interferences between them, and small dissimilarities in their hardware (e.g., very small differences in cable lengths, cable placement and orientation, material properties, etc.). In addition, these corrections can become particularly challenging and exceedingly difficult to consistently apply to far-offset receivers/traces, owing to their barely discernible direct air wave responses, because of pulse dispersion, SNR versus offset reduction, and strong AVO attenuation.

That being said, the time-zero alignment can be defined as the process/correction whereby each CO profile or each trace in a WARR gather generated by the corresponding receiver is readjusted so that its first break coincides with the theoretically expected

travel time of the direct air wave response (i.e., to be consistent with the corresponding transmitter-receiver offset), which is given by equation (2.1).

The time-zero alignment of the traces is critical before any of the moveout-based processing step(s) is applied to the data and should always be performed with the utmost precision. Failure to do so will almost certainly lead to misaligned linear and hyperbolic events in both the WARR and CMP domain, and consequently to false stacking velocity estimates with all the consequences that this entails (i.e., false estimates of interval velocities, material properties, depth, etc.), as well as poor stacking results. This is demonstrated very well in Figure 5.1 which shows the results and the consequences of a non-implementation, improper implementation (error of 1 – 2 time samples per receiver/trace), and proper implementation of the time-zero alignment to a field data CMP gather. To aid visualisation the CMP gather has been treated with some basic GPR data processing steps (i.e., dewow, time gain, and frequency filtering) as well as trace balancing.

Currently, two different methods have been proposed for performing the process of the time-zero alignment. Both methods were presented using data collected with the “WARR Machine” GPR and are briefly described below.

- Diamanti et al. (2018) used air-launched/air-controlled data instead of ground-coupled data in order to estimate in a somewhat more reliable way the first breaks using a relative threshold value (i.e., percentage) of the peak amplitude of the traces of the corresponding receivers.
- Kaufmann et al. (2020) estimated the relative to the first receiver time misalignments. To do so they compared the same controlled data set collected at one specific location for all seven receivers of the “WARR Machine” each one placed in all seven positions of the sledge. That is, they compared seven WARR gathers, each of which was obtained from each receiver. Interestingly, after performing the same process several times and in different locations they observed that the relative time misalignments remained consistent.

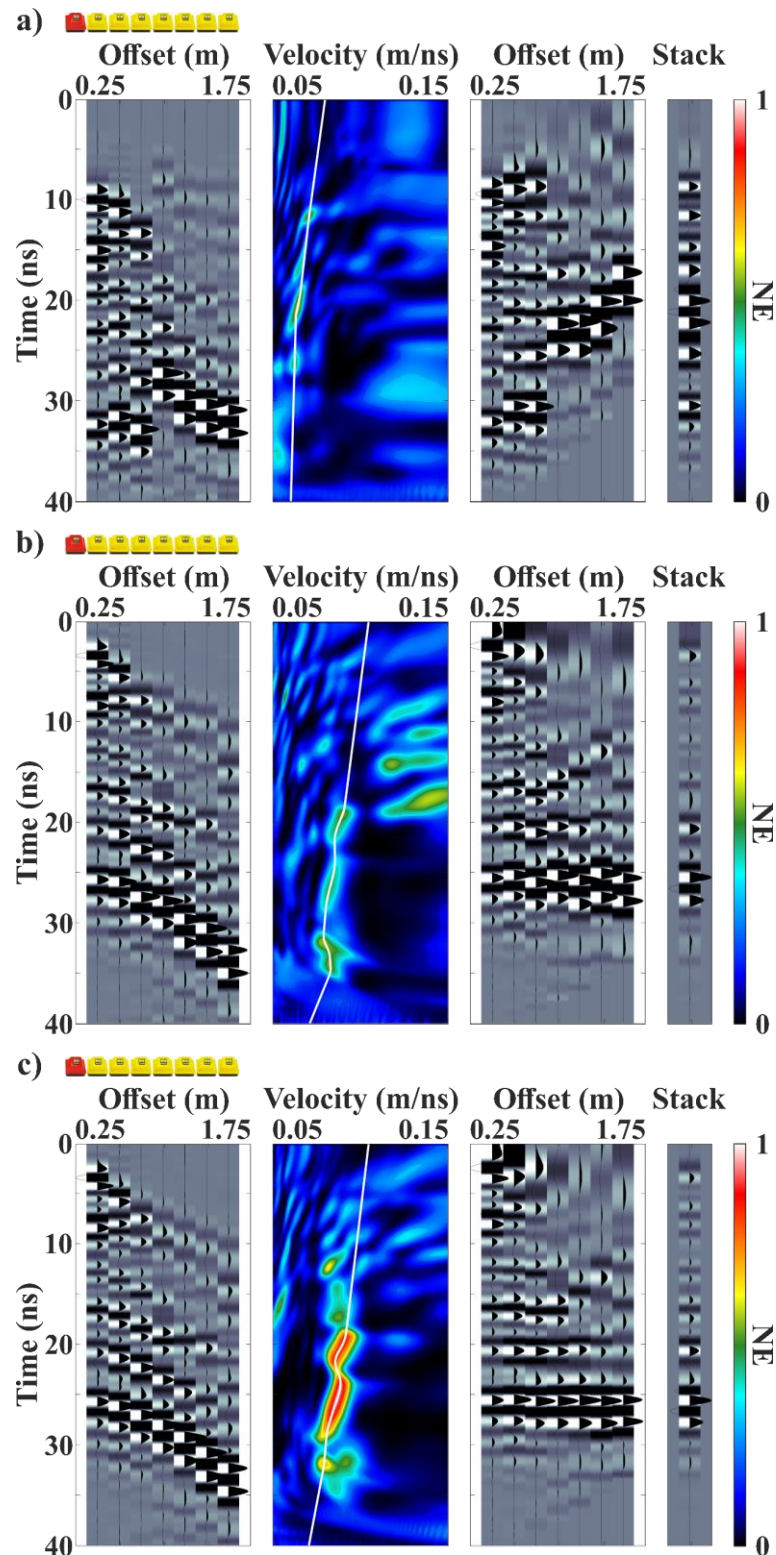


Figure 5.1: Field data CMP gather, semblance plot of the CMP gather, CMP gather after NMO correction using velocities picked automatically from the semblance plot (white line), and resultant stacked trace of the NMO corrected CMP gather. The transducer configuration is shown at the top of each sub-figure, with the Tx in red and the Rx's in yellow. a) Non-implementation of the time-zero alignment. b) Improper implementation of the time-zero alignment (error 1 – 2 time samples per trace). c) Proper implementation of the time-zero alignment.

The first method used by Diamanti et al. is disadvantageous, as the exact actual positions of the first breaks of all the traces (especially the far-offset low-SNR traces) are difficult to pinpoint and reliably pick using threshold techniques. The second method used by Kaufmann et al. is very time-consuming, i.e., ~ 40 minutes for only collecting the necessary controlled data set, and will most likely have to be repeated regularly, as the relative time misalignments are expected to change throughout the lifespan of the system for the aforementioned reasons (e.g., cable stability, component replacement and/or ageing, etc.). Therefore, in this thesis, a new method is proposed for dealing with the time misalignments of multi-concurrent receiver GPR data.

The proposed method is similar to that presented by Diamanti et al., since it is also based on the use of air-launched data, as shown in Figure 5.2a. This is because the direct air wave responses of such data are free from any interference from the direct ground wave, and more specifically, from the medium itself, the coupling with which can alter their frequency, phase, and amplitude (Diamanti & Annan, 2017; Lambot et al., 2012; Sato et al., 1984; Yelf, 2004). Furthermore, the air-launched data have the benefit of having higher SNR than ground-coupled data, as well as the advantage of being very easy and fast to collect i.e., lift and/or turn over the GPR system and collect traces in the air. Nevertheless, instead of realigning the traces based on estimated positions of first breaks deriving by a percentage-based threshold technique, the first large deflections, either positive peaks or negative troughs, are used (first peaks – blue line in Figure 5.2a). This is because they are easily detectable, either manually or automatically, as well as very stable for the reason outlined above. After the elimination of the relative time misalignments is performed, a common-to-all traces, positive static time shift based on only the first break of the high-SNR near-offset trace (red dot in Figure 5.2a) is applied. Although this process may seem quite complex at first glance, it can be easily realised that the overall time shift/time correction ( $t_{\text{shift}(\text{Rx}_n)}$ ) necessary for each CO profile or each trace in a WARR gather is given by (5.1). The same time shifts calculated from the air-launched data can subsequently be applied to the ground-coupled data, as indicated in Figure 5.2b.

In the following sections, the proposed method is evaluated and compared to that reported by Diamanti et al., which for convenience will also be referred to as the first break method, using both synthetic and field air-launched data. The lack of comparison

between the proposed method and that of Kaufmann et al. is due to the latter's necessary and extremely time-consuming measurements, which could not be performed owing to the COVID-19 pandemic.

$$t_{\text{shift}(\text{Rx}_n)} = t_{\text{a}(\text{Rx}_n)} - t_{\text{fpeak}(\text{Rx}_n)} + t_{\text{fpeak}(\text{Rx}_1)} - t_{\text{fbreak}(\text{Rx}_1)} \quad (5.1)$$

where:

$t_{\text{shift}(\text{Rx}_n)}$  The total time shift required for each CO profile or each trace in the WARR gather of the corresponding receiver  $n$ .

$t_{\text{a}(\text{Rx}_n)}$  The theoretical travel time of the direct air wave for receiver  $n$ , which is given by equation (2.1).

$t_{\text{fpeak}(\text{Rx}_n)}$  The TWT of the first peak of receiver  $n$ .

$t_{\text{fpeak}(\text{Rx}_1)}$  The TWT of the first peak of the first receiver.

$t_{\text{fbreak}(\text{Rx}_1)}$  The TWT of the first break of the first receiver.

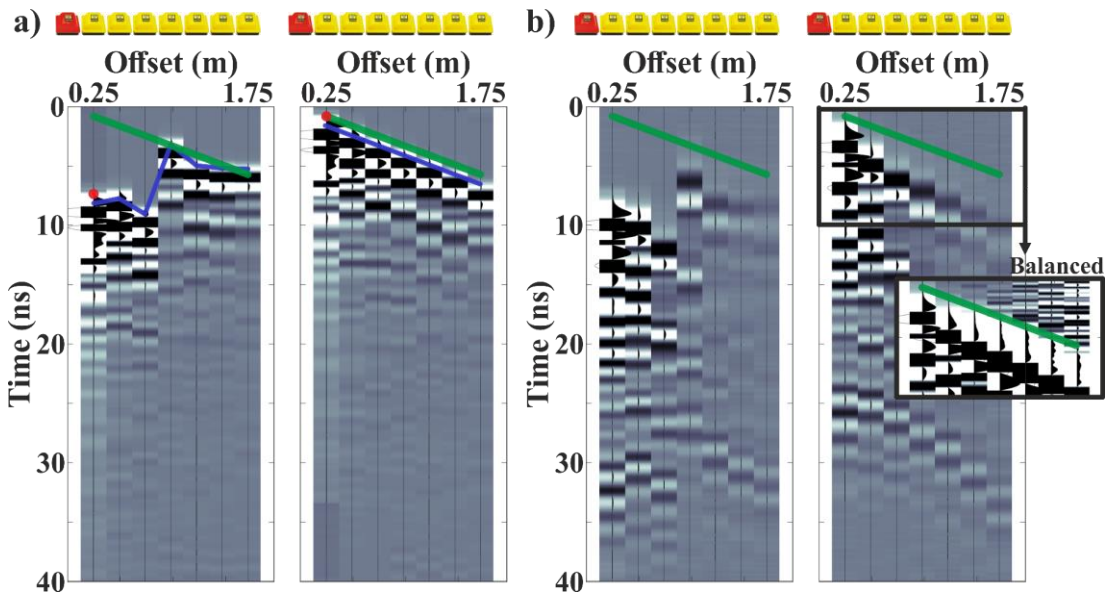


Figure 5.2: a) Air-launched field data WARR gather before and after time-zero alignment. The time shift required for each trace has been calculated using equation (5.1). b) Ground-coupled field data WARR gather before and after time-zero alignment. The time shift required for each trace has been calculated from the air-launched data of (a). To aid visualisation, the first 10 ns are also shown after trace balancing. In (a) the blue line highlights the first large deflections (i.e., first peaks), and the red dot the first break of the first/near-offset receiver. In (a) and (b) green line highlights the theoretical direct air-wave response which is given by equation (2.1). The transducer configuration is shown at the top of each sub-figure, with the Tx in red and the Rx's in yellow.

### 5.1.1 Synthetic data example

Most GPR FDTD numerical simulations nowadays utilise simple excitation models to represent the antenna, such as an infinitesimal dipole source (e.g., Hertzian dipole source), rather than a physical model of the actual antenna, even though the latter can reproduce much more accurately the amplitude and the shape of the real GPR signal. This is mainly because developing and simulating such a model requires not only a thorough knowledge of the geometry and material properties of the real antenna, but also significantly more computational resources and simulation time, as a fine FDTD grid is required to capture all the details of the real structure (e.g., Diamanti & Annan, 2013; Giannakis, 2016; Giannakis, Giannopoulos, & Warren, 2016; Warren, 2009; Warren & Giannopoulos, 2011, 2017). The latter is in fact the reason why simulations with 3D antenna model(s) have been only performed once in this thesis, and in particular only in the present chapter.

In order to adequately evaluate and compare the above-mentioned time-zero alignment methods via synthetic data, it was crucial to replicate the real GPR signal as much as possible (Figure 5.3). Therefore, to achieve this, a 3D antenna model (transmitter-receiver pair) (Figure 5.3a) as a digital equivalent of the 500 MHz centre frequency Sensors & Software Inc. antenna (transmitter-receiver pair) (Figure 5.3b) was developed to be used as a sub-model for generating the necessary for this work synthetic air-launched data. The antenna model was developed using both a voxel editor (see Ch. 4.1.3) as well as scripting using commercially sensitive information, such as geometry and material properties, provided directly by the industrial partner – Sensors & Software Inc.

Figure 5.3c shows a field data air-launched trace (blue) that was collected in the anechoic chamber at Northumbria University using the aforementioned antenna. In the same figure, there are also two synthetic air-launched traces, one generated using a Hertzian dipole source fed with a ricker waveform of 500 MHz centre frequency (green) and another one generated using the antenna model with a voltage source at the transmitting dipole feed point with a Gaussian waveform of the same centre frequency (red). As observed, the synthetic and real data are generally in good agreement. Nonetheless, it is clear that the synthetic trace generated by the antenna model captures

both the amplitude and phase of the real trace better than the synthetic trace generated by the Hertzian dipole source. This is also corroborated by the respective root mean square error (RMSE) and correlation coefficient ( $r$ ) values.

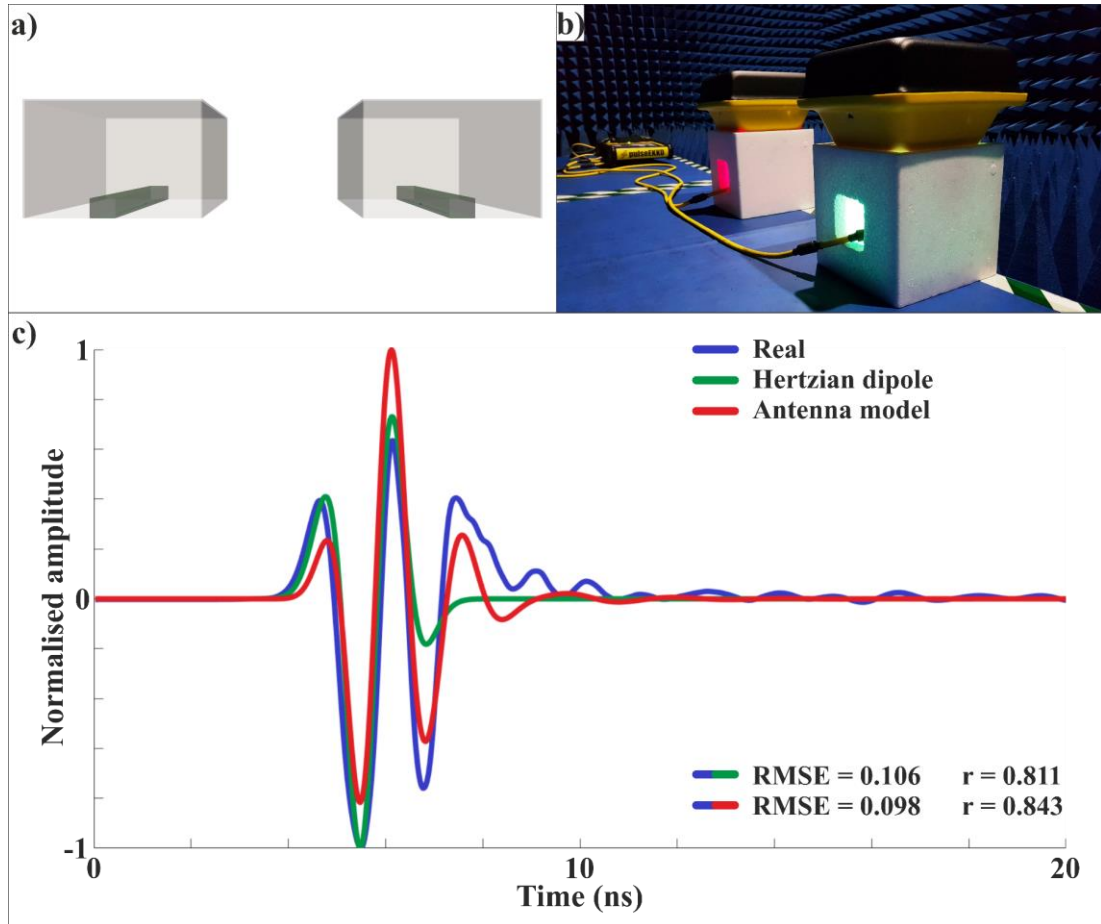


Figure 5.3: a) Antenna model (Tx-Rx pair) similar to a Sensors & Software Inc. 500 MHz centre frequency antenna. b) Sensors & Software Inc. 500 MHz centre frequency antenna (Tx-Rx pair) collecting air-launched data inside the anechoic chamber of Northumbria University. c) A comparison between a field air-launched trace collected using the aforementioned antenna in the anechoic chamber (blue), a synthetic air-launched trace generated using a Hertzian dipole source fed with a 500 MHz centre frequency ricker waveform (green), and a synthetic air-launched trace generated using the antenna model with a voltage source at the transmitting dipole feed point with a 500 MHz centre frequency Gaussian waveform (red).

To generate the synthetic data needed, a simple free-space modelling scenario (i.e.,  $\epsilon_r = 1$  and  $\sigma = 0$ ) was considered. The model domain used was  $2 \times 0.3 \times 0.2$  m ( $x$ ,  $y$ , and  $z$  axes), with a very small spatial discretisation of  $\Delta x = \Delta y = \Delta z = 0.001$  m and a time step  $\Delta t = \sim 1.93$  ps (CLF condition (4.5)) to allow capturing all the details of the antenna sub-model(s). Moreover, there were 50 PML layers on each side of the

model to minimise as much as possible the reflections caused by the surrounding boundaries. Regarding the time window, that was set to 20 ns resulting in that way in 10386 time steps/samples. Finally, there were eight modelled transducers (i.e., eight sub-models), namely one transmitter and seven receivers, all separated by 0.25 m, i.e., considering a transducer geometry similar to that of the “WARR Machine” GPR (500 MHz transducers – Figure 4.5), as illustrated in Figure 5.4a.

The synthetic data produced, shown in Figure 5.4b, were normalised to the maximum absolute value and resampled to a more realistic sampling interval such as that of the field data, namely 0.1 ns, resulting in 200 time samples. In addition, randomised time shifts and random white Gaussian noise were applied to the data, as can be seen in Figure 5.4c. Both the time shifts and random noise were applied to simulate a scenario with time misalignments and SNR versus receiver offset reduction. Although not all noise in real GPR data is random, the purpose of implementing this scheme was to ensure that the synthetic data more closely resembled the real data, in which noise may be troublesome, particularly at large offsets (see also Ch. 4.2.1 – Figure 4.7).

Subsequently, the contaminated with noise time misaligned data were used to evaluate the effectiveness and potential drawbacks of the aforementioned methods by performing the following simple experiment. Using each method, the relative to the first receiver for all receivers time shifts were calculated and subtracted by the true time shifts, i.e., those previously applied to the data for the purpose of this experiment, in order to calculate the time difference/error for each method. The same experiment was repeated in a loop for one million iterations in each of which both the time shifts and Gaussian noise were slightly different. In addition, especially for the first break method, a wide variety of thresholds ranging from 1 – 20 % of the peak amplitude value of each trace for detecting the corresponding first breaks were also used.

The estimated relative to the first receiver/trace mean time errors for all receivers/traces and each method are shown in Table 5.1 and Table 5.2, respectively. For clarity, the errors have been rounded to the first decimal place so that they also translate much more easily as a number of samples. As can be seen in Table 5.1 the first break method exhibits significant time errors for every threshold and in at least two of the traces, ranging from 0.1 ns to 10.1 ns (i.e., 1 – 101 samples). Although there is a

threshold for each receiver that does not return an error, it is clear that predicting the proper combination of thresholds for all receivers and data sets is nearly impossible. On the other hand, by observing Table 5.2 it can be clearly seen that the performance of the proposed method is nearly perfect, since not only does only one receiver exhibit an error, but also this error is very small, namely 0.1 ns corresponding to only one time sample.

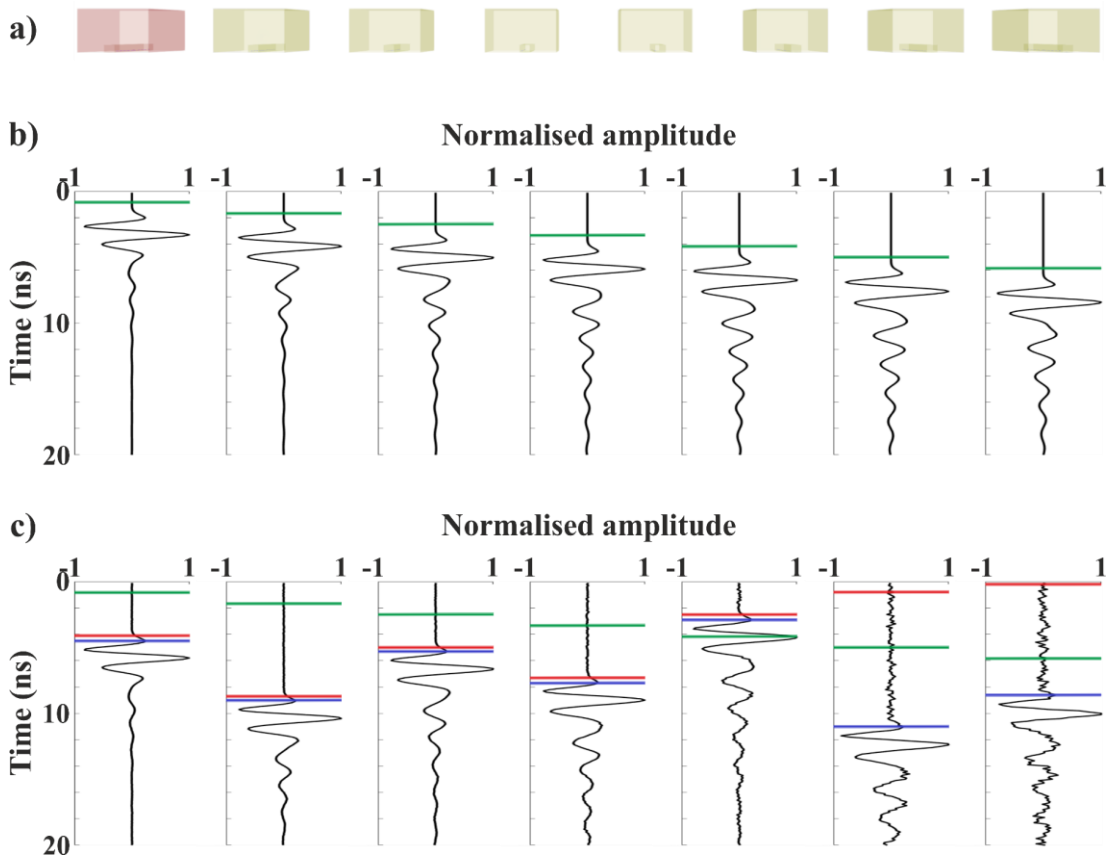


Figure 5.4: a) Sensors & Software 500 MHz centre frequency modelled transducers developed to generate the synthetic data to demonstrate the proposed time-zero alignment method. The Tx is depicted in red and the Rx's in yellow. b) Synthetic air-launched traces. c) Synthetic air-launched traces after the application of randomised time shifts and white Gaussian noise. In (b) and (c) green lines highlight the theoretical direct air wave response which is given by equation (2.1). In (c) red lines highlight the first break positions chosen using a threshold equal to 5 % of the peak amplitude of each trace – Diamanti et al. (2018) method, and blue lines indicate the first large deflections, i.e., the first peaks – proposed method.

Table 5.1: Estimated, relative to the first receiver, time errors between the applied time shifts and the detected time shifts calculated using the first break method used by Diamanti et al. (2018) for different thresholds. For clarity, the time errors have been rounded to the first decimal place so that they translate more easily as a number of samples. It is noted that the sampling interval of the data is equal to 0.1 ns.

Threshold (%)	Time error (ns)					
	Rx1-Rx2	Rx1-Rx3	Rx1-Rx4	Rx1-Rx5	Rx1-Rx6	Rx1-Rx7
1	-0.2	-1.5	-6	-1.8	-10.1	-7.8
2	0	0	-2.2	-1.4	-10	-7.8
3	0	0.1	-0.3	-0.7	-9.7	-7.8
4	0.1	0	0	-0.2	-8.8	-7.6
5	0.1	0.1	0.1	0	-7.1	-7.4
6	0	0	0	0	-5.2	-7
7	0.1	0	0.1	0.1	-3.4	-6.4
8	0.1	0.1	0.1	0.1	-2	-5.5
9	0.1	0.1	0.1	0.1	-1	-4.6
10	0	0	0	0	-0.6	-3.7
11	0.1	0	0.1	0.1	-0.3	-2.8
12	0.1	0	0.1	0.1	-0.1	-2.1
13	0.1	0.1	0.1	0.1	0	-1.5
14	0.1	0.1	0.1	0.1	0.1	-1
15	0	0.1	0.1	0.1	0.1	-0.7
16	0.1	0	0.1	0.1	0.1	-0.4
17	0.1	0.1	0.1	0.1	0.2	-0.2
18	0.1	0.2	0.3	0.3	0.3	0
19	0.2	0.7	0.9	0.6	0.4	0.1
20	1.1	1.2	1.1	0.8	0.6	0.3

Table 5.2: Estimated, relative to the first receiver, time errors between the applied time shifts and the detected time shifts calculated using the proposed method. For clarity, the time errors have been rounded to the first decimal place so that they translate more easily as a number of samples. It is noted that the sampling interval of the data is equal to 0.1 ns.

Threshold	Time error (ns)					
	Rx1-Rx2	Rx1-Rx3	Rx1-Rx4	Rx1-Rx5	Rx1-Rx6	Rx1-Rx7
1 <sup>st</sup> peak/trough	0	0	0	0	0.1	0

### 5.1.2 Field data example

To evaluate and compare the aforementioned time-zero alignment methods via real field data, a different approach was required contrasted to that used with the synthetic data, as the true time errors between the receivers are in reality unknown. The field data were first time-zero aligned using both methods, then processed with standard GPR data steps (i.e., dewow, time gain, and frequency filtering), next sorted into CMP gathers, and then subjected to velocity spectrum semblance analysis, NMO correction, as well as horizontal stacking. Finally, the obtained results were evaluated and compared by visual inspection. In general, it is expected that with a proper time-zero alignment a CMP gather will have clear hyperbolic events, which should be ideally perfectly flat following an NMO correction with the correct stacking velocities. In addition, strong semblance responses, as well as good stacking results are also to be expected.

Figure 5.5a to Figure 5.5d show the obtained results using the first break method for thresholds equal to 5 %, 10 %, 15 %, and 20 %, respectively, whereas Figure 5.5e shows those from the proposed method. To aid visualisation trace balancing was also applied to the CMP gathers. Looking at the first four figures (Figure 5.5a – Figure 5.5d), and in particular, the two main events in the NMO corrected gathers (i.e., the two events at  $\sim 20$  ns and  $\sim 25$  ns), it is evident that there are generally significant time misalignments. These misalignments, have an effect on both the semblance responses (i.e., on their strength and shape) and thus stacking velocities, as well as on the stacked traces, which as observed are slightly different in each case (see also Figure 5.5f). On the other hand, by looking at the same events in the NMO corrected CMP gather obtained using the proposed method (Figure 5.5e) no considerable time misalignments are observed. This is also supported by the corresponding semblance panel and stacked trace shown in Figure 5.5e, which exhibit stronger responses and slightly higher amplitudes, respectively, than those shown in Figure 5.5a to Figure 5.5d.

The above findings not only validate the proposed method but also highlight the importance of time-zero alignment in general. Since, as shown, even the slightest time error(s) in the GPR signals can have an impact on semblance analysis, i.e., velocity

picking and/or velocity function itself, as well as on horizontal stacking results (Figure 5.5f).

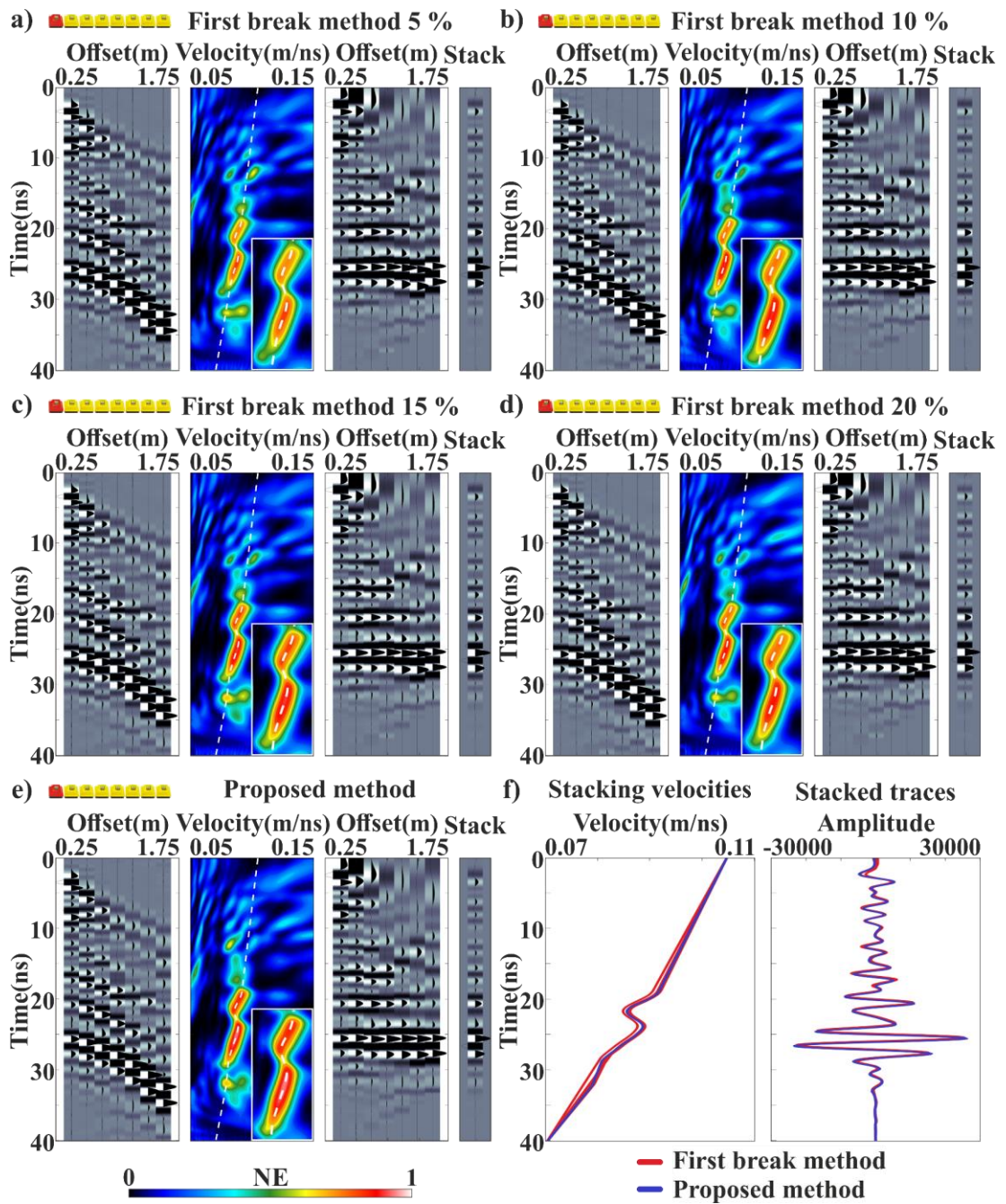


Figure 5.5: a – e) Field data CMP gather, semblance plot of the CMP gather, CMP gather after NMO correction using velocities picked automatically from the semblance plot (white dotted line), and resultant stacked trace of the NMO corrected CMP gather. The transducer configuration is shown at the top of each sub-figure, with the Tx in red and the Rx in yellow. a – d) Time-zero alignment using the first break positions chosen using a threshold equal to 5 % (a), 10 % (b), 15 % (c), and 20 % (d) of the peak amplitude of each trace – Diamanti et al. (2018) method. e) Time-zero alignment using the first peaks – proposed method. f) Combined plot of the stacking velocities picked automatically from the semblance plots of (a) – (e), and combined plot of the stacked traces of (a) – (e).

## 5.2 CMP trace balancing

As discussed and shown in a previous chapter (Ch. 4.2.1 – Figure 4.7) multi-concurrent receiver GPR data can suffer from very strong AVO attenuation. Consequently, in addition to the standard time-variant amplitude scaling (i.e., the use of time gain function), some supplementary time-invariant scaling is necessary for the CMP gathers in order to compensate for the significant, and in some cases severe, AVO differences. Such scaling is essential for an optimal velocity spectrum analysis with the semblance measure, as the latter due to its simplicity, namely its assumption of constant amplitude models, cannot handle AVO variations properly (Sarkar et al., 2001). Although there is a special variant of the semblance known as AB semblance (Sarkar et al., 2002), which was developed to handle such variations, it also has drawbacks such as increased computational time, higher sensitivity to noise, and lower resolution than its conventional counterpart (Fomel, 2009). Therefore, the additional scaling has the potential to improve the velocity resolution of the semblance panel/plot, i.e., to improve the sharpness/width/broadness and boost the strength of the peaks corresponding to the CMP gather events, and hence the velocity information obtained. In addition, it could also improve horizontal stacking results, as with such strong AVO variations as those exhibited in multi-concurrent receiver GPR data and combined with their low fold, the contribution of the far offset traces to the stack can be negligible to non-existent.

A trace balancing scheme, also often referred to as trace equalisation, can be used for such a purpose. Trace balancing, according to Yilmaz (2001), is a time-invariant amplitude scaling of the traces to a common level, typically that of the root mean square (RMS) amplitude level. More precisely, for each trace in a group of traces, such as a WARR or a CMP gather, a single time-invariant scaling/balance factor is determined and applied. The balance factor, in the most simplistic form, is defined as the ratio of the desired RMS amplitude, which in a CMP gather can be that of the near-offset trace, which is also usually the highest SNR trace, to the RMS amplitude of the trace to be balanced. Nevertheless, in typical trace balancing only a single balance factor is calculated for and applied to each trace (i.e., the procedure is akin to a single-window AGC). This essentially means that not all events in a CMP gather will be properly balanced (i.e., resulting in non-constant amplitude models not optimal for semblance),

especially if there are noise bursts present in the traces. As a result, not all corresponding to the CMP gather events semblance responses will be sharp and strong, which in turn could lead to inaccurate stacking velocity estimates (especially if velocity picking is done manually) with all the consequences this entails. Therefore, a modified trace balancing with a sliding window is proposed in this thesis, which allows the determination of not just one, but multiple balance factors for each trace, and hence for improved balancing.

Figure 5.6 illustrates the steps (from left to right) of the proposed trace balancing approach using a processed (i.e., time-zero alignment, dewow, time gain, and frequency filtering) field data CMP gather. As can be seen, the traces are first shifted upwards in time (negative time shift – green arrows on the left-hand side) using equation (2.1) so that their first breaks, and therefore, their direct air wave responses be at the same time position and appear horizontal (green line in the middle). This step seeks to shorten the time window in which a hyperbolic reflected event appears in the gather, and thus enable the use of a shorter length sliding window for the balancing process that follows. The desired RMS amplitudes are then computed from the first trace, which currently serves as the reference trace, using a sliding tapered window whose length is user-defined and should be at least equal to or larger than the time window in which the reflected event appears in the time-shifted gather (10 ns window in this example – red rectangle in the middle). Similarly, the RMS amplitudes of the second trace, which is currently the trace to be balanced, are also computed (blue rectangle in the middle). The ratio between the above RMS amplitudes yields the balance factors for the second trace (black rectangle) to which they are subsequently applied. Next, the balance factors for the third trace are calculated in the same way, but this time using the second and already balanced trace as a reference trace. The same process is repeated for the remaining traces in the CMP gather. Tapering the sliding window produces smoother balance factors/function, whilst the moving reference trace scheme reduces horizontal overbalancing and allows for a smoother adjacent balancing. Finally, as the last step, the traces are shifted forward in time (positive time shift – green arrows on the right-hand side) to their original position, again using equation (2.1).

To demonstrate the importance of CMP trace balancing for the semblance analysis, as well as to evaluate and compare the proposed sliding window method with the single-

window one, both methods were applied to both synthetic and field data CMP gathers. The resultant semblance panels of the proposed method were then compared with the respective semblance and AB semblance panels obtained from the unbalanced gathers as well as from balanced gathers computed using the typical single-window trace balancing method. In addition, the semblance and/or AB semblance curves computed for each case from the time windows centred on the corresponding CMP gather events were also compared.

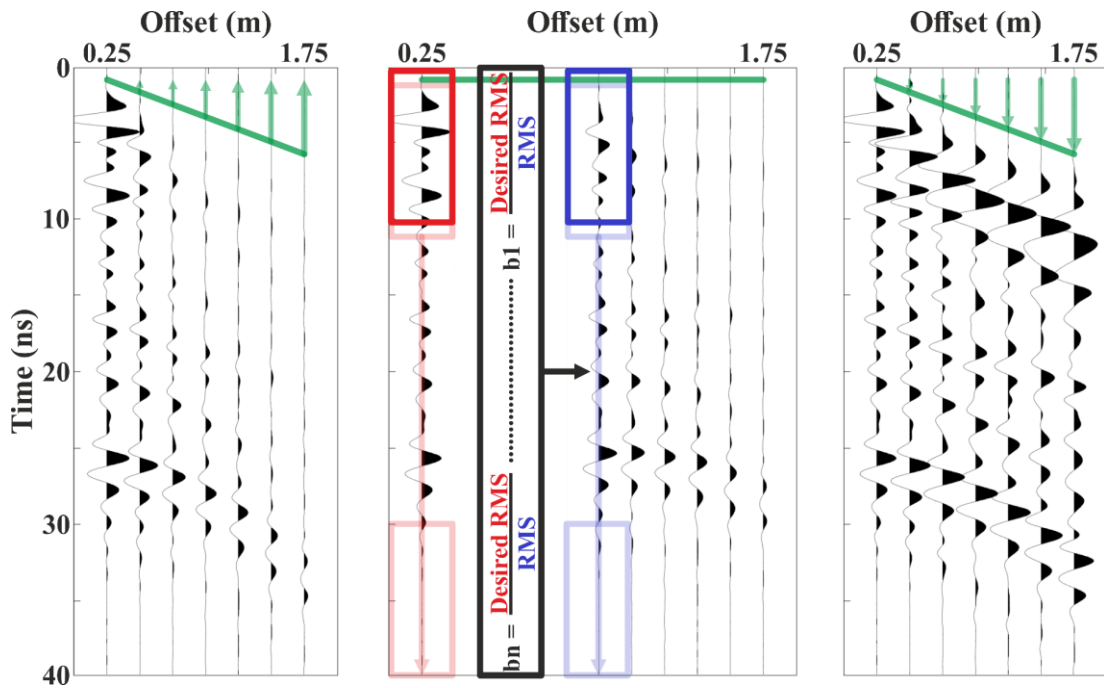


Figure 5.6: Field data CMP gather showing the stages (left to right) of the proposed trace balancing method. The green line highlights the direct air wave responses, whilst the green arrows indicate the time shift to either negative (left-hand side) or positive (right-hand side) times, which is given by equation (2.1). The red and blue rectangle highlight the sliding window (10 ns window) for the first (i.e., reference trace) and second (i.e., trace to be balanced) trace, respectively, whereas the black rectangle and arrow represent the computed balance factors and their application to the second trace.

### 5.2.1 Synthetic data example

To generate the synthetic data needed, a layered cake modelling scenario was considered. The model, which is shown in Figure 5.7, is a 3D four-layered model in which the velocity decreases with depth. Each layer of the model consists of inhomogeneous soil that was created using a soil mixing approach (Peplinski et al., 1995) resulting in additional lateral velocity variations. The model domain is equal to 5 x 1 x 2.2 m (x,

y, and z axes, respectively), with a spatial discretisation of  $\Delta x = \Delta y = \Delta z = 0.005$  m, and hence a time step of  $\Delta t = \sim 9.63$  ps (CLF condition (4.5)), as well as with 20 PML cells on each side. A single Hertzian dipole source, fed with a waveform shaped as the first derivative of a Gaussian with an amplitude equal to 1 and 500 MHz centre frequency, was used, as were seven receiver points, all separated by 0.25 m. Finally, the time window was set to 45 ns and the spatial trace step to 0.025 m.

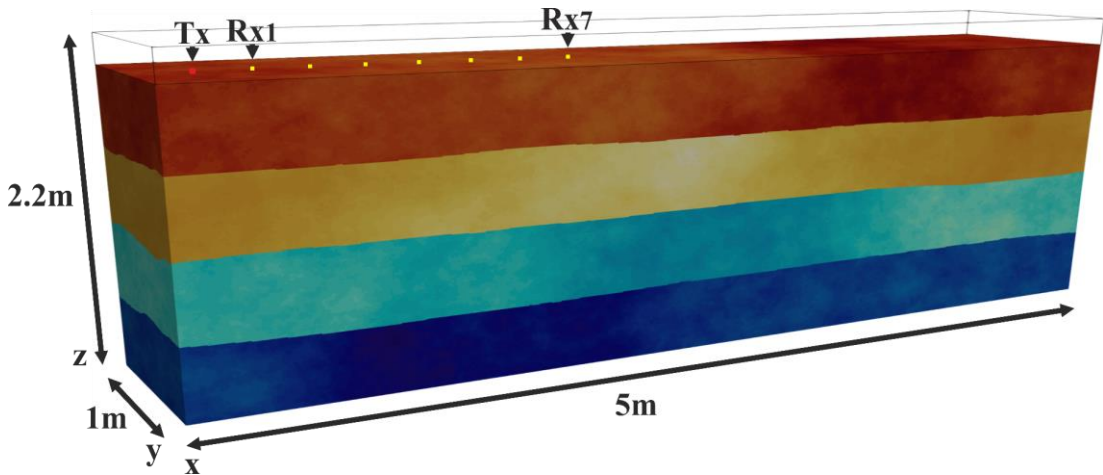


Figure 5.7: 3D four-layered model developed to generate synthetic data for demonstrating CMP trace balancing.

Figure 5.8a depicts a time gained synthetic unbalanced CMP gather generated by the above-mentioned model along with the computed combined LMO NMO semblance plot. The semblance curves for the four different events of interest in the gather, namely the ground wave and the three reflected waves, are also depicted in the same figure. Random white Gaussian noise, including artificial noise bursts, was added to the CMP gather to mimic the effects of a worst-case scenario where the SNR decreases rapidly with receiver offset as well as the presence of very noisy and/or corrupted traces. Moreover, because it is generally difficult to directly reproduce strong AVO attenuation phenomena when not modelling with physical sub-models of the actual antennas, an additional artificial AVO reduction was applied to the gather to mimic the AVO attenuation that occurs in real field data as much as possible. As observed in the figure, the CMP the gather suffers from significant AVO attenuation (modelled plus additional manual AVO) and as a result, produces very weak semblance responses, as the contribution of the far offset traces to the semblance summation is minimal. The same unbalanced CMP gather is shown along with the computed AB

semblance plot and AB semblance curves for the four events in Figure 5.8b. Unsurprisingly, AB semblance returns strong responses for all events in the gather, as it is developed to handle AVO variations. Nevertheless, when comparing the AB semblance plot (Figure 5.8b) to the conventional semblance plot (Figure 5.8a), it is evident that the width of the responses (both on the time and velocity axes) has significantly increased, indicating that there is, as expected (e.g., Fomel, 2009; Sarkar et al., 2002), a loss of velocity resolution, which could lead to inaccurate velocity estimates, especially when manual picking is used. This is also clearly illustrated in the accompanying curves. Notice the increase in strength, but also the increase in the width of the peaks in the AB semblance curves (Figure 5.8b) compared to the conventional semblance ones (Figure 5.8a).

Finally, Figure 5.8c and Figure 5.8d depict the balanced CMP gathers resulting from the typical single-window and proposed sliding window trace balancing method (8 ns window in this example), respectively. The corresponding semblance plots and semblance curves are also depicted in the same figures. Looking at the figures two observations can be made. The first observation is that the balanced gathers obtained using both methods result in stronger semblance responses than those of the unbalanced gather (Figure 5.8a) and much sharper than those shown in the AB semblance plot (Figure 5.8b). The second observation, which is also the most important, is that the resultant CMP gather of the proposed sliding window method (Figure 5.8d) is significantly better balanced than the gather obtained using the single-window method (Figure 5.8c). Notice the AVO similarity of the events in the CMP gather in Figure 5.8d, as well as the decimation of the noise bursts which is due to the fact that the balancing process was initiated using the near-offset high-SNR trace as the first reference trace. The improved balancing shown in Figure 5.8d has the potential to boost stacking results, which is also reflected in the corresponding semblance panel and semblance curves that have much stronger and slightly sharper peaks than those shown in Figure 5.8c.

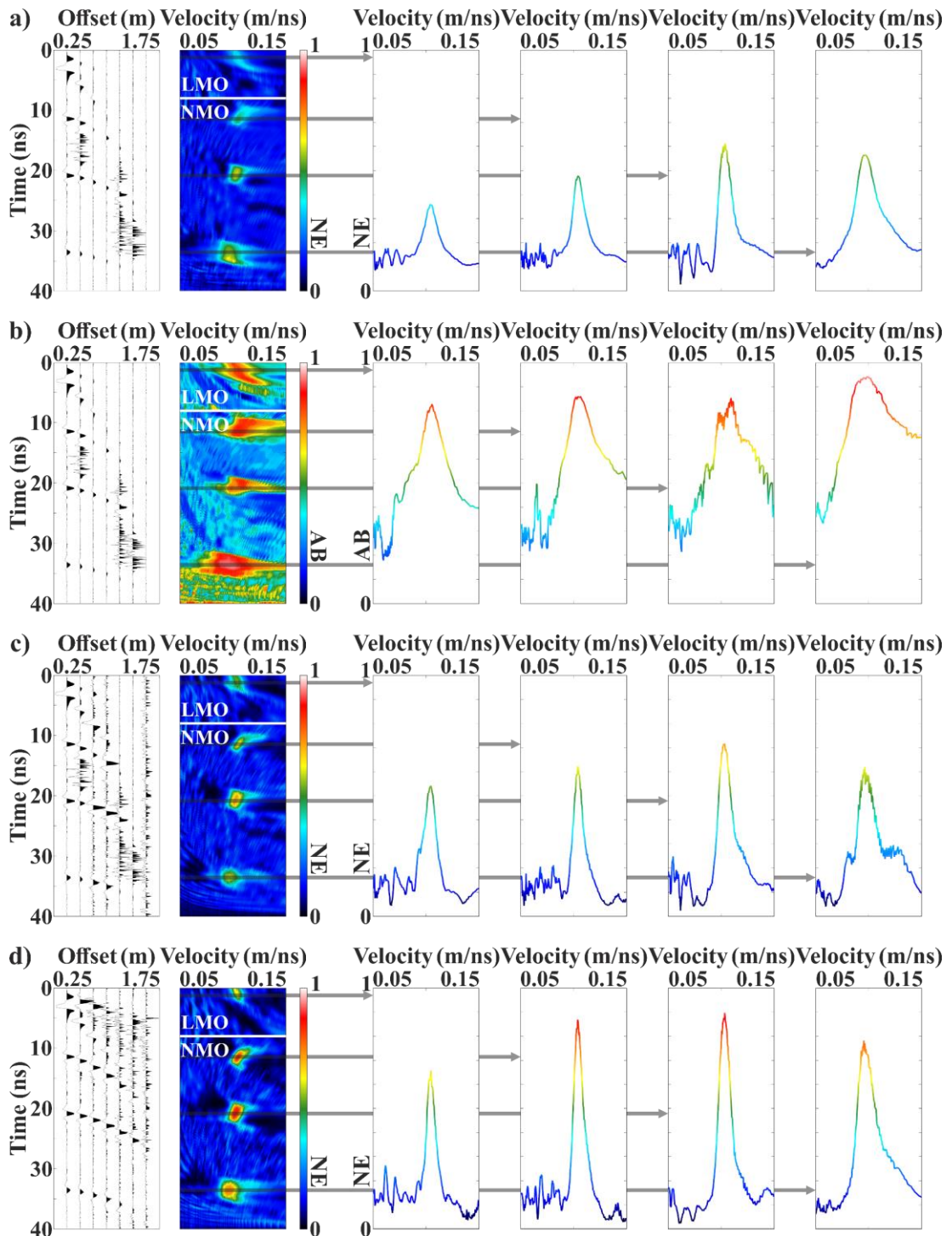


Figure 5.8: a – d) Synthetic CMP gather contaminated with white Gaussian noise and noise bursts, respective combined LMO NMO velocity spectrum panel, and coherency curves from the time windows centred on the four different events present in the gather, namely the ground wave and the three reflected waves. a) Unbalanced CMP gather and the respective semblance plot and semblance curves. b) Unbalanced CMP gather and the respective AB semblance plot and AB semblance curves. c) Balanced CMP gather using the typical single-window RMS balancing method and the respective semblance plot and semblance curves. d) Balanced CMP gather using the proposed sliding window RMS balancing method (8 ns window) and the respective semblance plot and semblance curves.

### 5.2.2 Field data example

Figure 5.9a depicts two real field data unbalanced CMP gathers (CMP I and CMP II), that have been processed with some basic processing steps (i.e., time-zero alignment, dewow, time gain, and frequency filtering), along with their computed NMO semblance plots. A combined LMO NMO semblance approach was not used in this example, as the direct ground wave was not very coherent in the gathers. The semblance curves for the main event of the data set, which is a response from a pipe, are also depicted in the same figure (time windows centred on 25.8 ns and 20.5 ns, respectively). As shown in Figure 5.9a, both gathers suffer from significant AVO attenuation, and consequently, produce weak semblance responses, apart from the one corresponding to the pipe event in the CMP gather I. The same unbalanced CMP gathers are shown together with their computed AB semblance plots and AB semblance curves in Figure 5.9b. As expected, like the synthetic data example, the AB semblance plots show very strong responses for all hyperbolic events of the gathers, but at the same time much wider than those of the conventional semblance plots, indicating a loss velocity resolution, which as previously mentioned could lead to inaccurate velocity estimates. This is also very well illustrated in the corresponding semblance (Figure 5.9a) and AB semblance curves (Figure 5.9b) of the unbalanced CMP gathers.

Finally, Figure 5.9c and Figure 5.9d depict the balanced gathers produced using the typical single-window and proposed sliding window trace balancing method, respectively. The same figures also depict the corresponding semblance plots and semblance curves for the pipe event. Looking at the figures two observations can be made, which are similar to those of the synthetic data example. The first observation is that the resultant gathers balanced by both methods exhibit stronger semblance responses than those of the unbalanced gathers (Figure 5.9a) and sharper than those shown in the AB semblance plots (Figure 5.9b). There is however an exception in Figure 5.9c, where the single-window balancing method unbalanced the CMP gather I even more. This exception, which is also illustrated very well in the corresponding semblance curve, shows that typical single-window balancing can sometimes even lead to the opposite of the desired results, and therefore be detrimental to the semblance analysis. The second observation is similar to the synthetic data example, and is that both resultant CMP gathers produced by the proposed sliding window method (Figure 5.9d) are much

better balanced than those produced by the single-window method, as evidenced by the stronger and slightly sharper peaks on their corresponding semblance plots and semblance curves.

The above findings demonstrate the significance of CMP trace balancing in velocity spectrum semblance analysis, but most importantly the performance of the proposed sliding window method. Nevertheless, it should be also noted that the relative amplitude information is lost when using any such trace balancing method. Therefore, such type of time-invariant scaling should be performed only for velocity analysis in case the objective of the research survey is to interpret AVO variations.

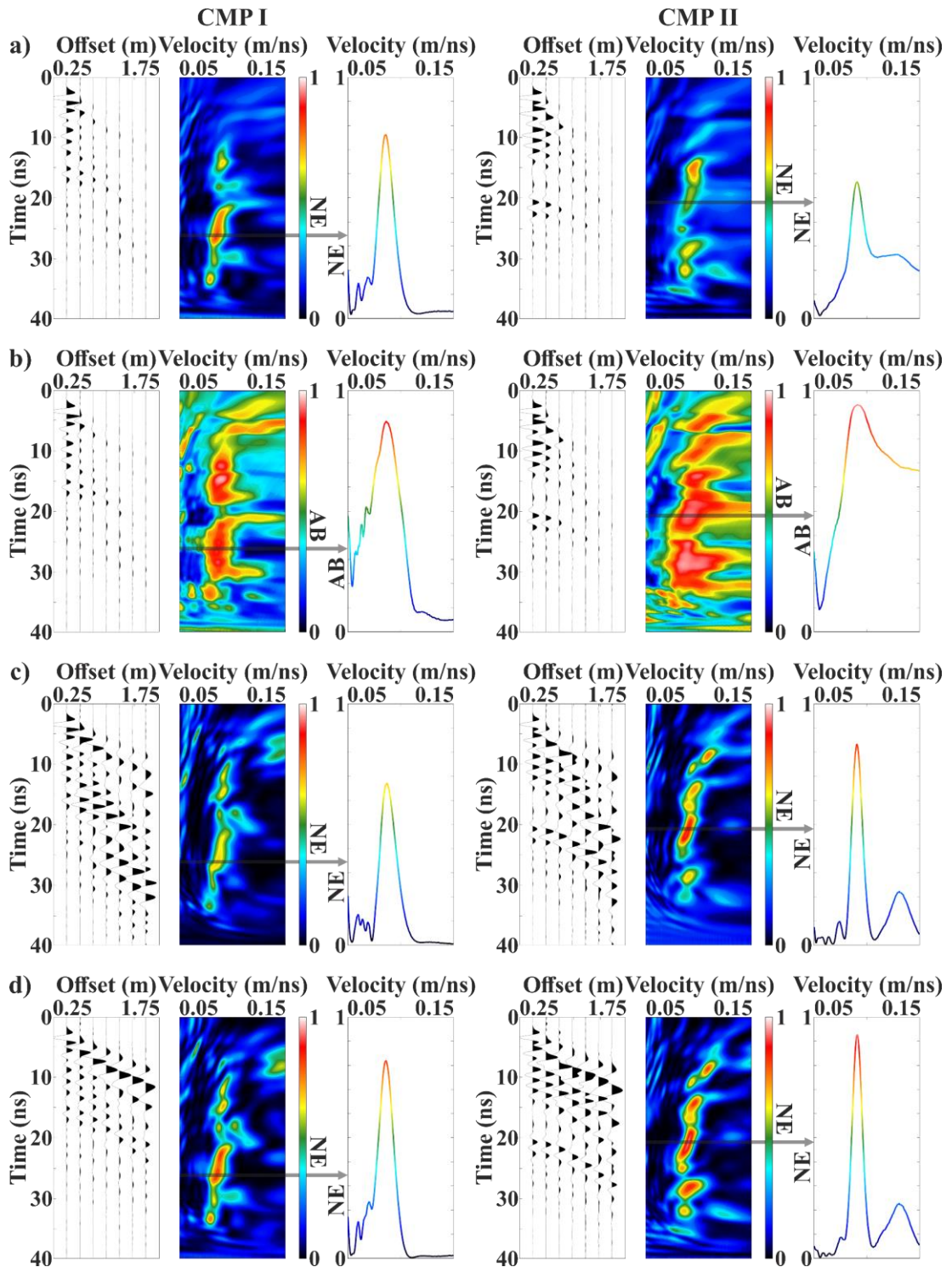


Figure 5.9: a – d) Field data CMP gathers, respective NMO velocity spectrum panels, and coherency curves from the time window centred on the main reflected event of the data set, namely the pipe response/event. a) Unbalanced CMP gathers along with their respective semblance plots and semblance curves. b) Unbalanced CMP gathers along with their respective AB semblance plots and AB semblance curves. c) Balanced CMP gathers using the typical single-window RMS balancing method along with their respective semblance plots and semblance curves. d) Balanced CMP gathers using the proposed sliding window RMS balancing method (10 ns window) along with their respective semblance plots and semblance curves.

## 5.3 Automated velocity spectra picking

As explained and shown in previous chapters (e.g., Ch. 3.3.1 and Ch. 4.2), newly developed GPRs with multiple concurrent data acquisition receivers, such as the “WARR Machine”, can generate hundreds of thousands of WARR and/or CMP gathers in a timely manner. All these gathers can potentially be analysed, allowing the production of detailed velocity fields, and consequently, the improvement of subsurface information. As it is understandable, manual velocity picking of thousands or even hundreds of velocity spectra panels can be a tedious and extremely time-consuming task, therefore some form of automation is required.

Whilst there are several automatic velocity picking methods/algorithms available, the vast majority of them are computationally intensive and have been developed primarily for handling seismic reflection data velocity spectra panels. These panels are generally free of irregularities because seismic data usually tend to deal with horizontal slowly varying events, but most importantly, because they are computed by high stacking fold CMP gathers (i.e., gathers containing dozens or sometimes even hundreds of traces), which is a factor known to have a direct and positive effect on velocity spectrum quality (Yilmaz, 2001). As a result, these algorithms are not ideal for dealing with multi-concurrent receiver GPR velocity spectra panels, as contrasted to seismic, they can be quite irregular and often contain false/spurious peaks. This is mostly owing to the significantly smaller stacking fold, which in their case, is exclusively dictated by the total number of receivers in the GPR system (i.e., equal to seven receivers for the “WARR Machine”), as well as due to the overall character of GPR data, which tend to have steep high angle dips and many localised diffraction events.

Therefore, efficiently to analyse the large volume of data generated by multi-concurrent receiver GPRs, a new method/algorithm has been developed, that overcomes the above-mentioned irregularities issues. The proposed algorithm which is based on work first published by Fomel (2003) is automated and conducts iteratively a reweighted regularisation of velocity picks. The operation of the algorithm is discussed in detail below using a processed (i.e., time-zero alignment, dewow, time gain, frequency filtering, and trace balancing) field data CMP gather (Figure 5.10a).

At first, the velocity spectrum panel is scanned at each time sample and the velocity where the semblance is maximum is picked (red line in Figure 5.10b). Then, the velocity picks are regularised/smoothed (Fomel, 2003) using a small regularisation parameter and a weight ( $w$ ), which is the product of two components/weights and is given by (5.2).

$$w = w_s * w_v \quad (5.2)$$

The first weight ( $w_s$ ) is given by equation (5.3), and is simply the corresponding semblance values ( $s$ ) of the chosen picks, ranging between 0 and 1 (Neidell & Taner, 1971), with a user-defined threshold value ( $th_s$ ) ( $th_s = 0.5$  in the example below). This weight is associated with the semblance value of a pick and guarantees that a high semblance velocity pick will not be smoothed as much. The threshold on the other hand ensures that any velocity pick corresponding to a semblance value lower than its value will be instantly completely smoothed.

$$\begin{cases} w_s = s \\ w_s < th_s = 0 \end{cases} \quad (5.3)$$

The second weight ( $w_v$ ) is given by equation (5.4), and it is the normalised, with a user-defined threshold value ( $th_v$ ) ( $th_v = 0.05$  in the example below), absolute velocity difference ( $v_d$ ) of the chosen picks (red line in Figure 5.10b) and the weighted with the ( $w_s$ ) (5.3) linear fitted curve of the picks (blue line in Figure 5.10b). This weight is associated with the velocity difference of a pick from the linear trend and guarantees that even a high semblance value velocity pick that is far away from the linear trend and could potentially be spurious, will be smoothed as much as possible (white arrows in Figure 5.10d). The threshold on the other hand normalises the velocity difference and ensures that any velocity pick corresponding to a velocity difference higher than its value will be instantly completely smoothed.

$$\begin{cases} w_v = 1 - \left( \frac{|v_d|}{th_v} \right) \\ w_v < 0 = 0 \end{cases} \quad (5.4)$$

Finally, the smoothed velocity picks of the first iteration (white line in Figure 5.10b) are used as pre-set picks for the next iteration (red line in Figure 5.10c). The same process is iterated for user-defined iterations or else until the RMS percentage difference between the current and smoothed velocity picks becomes too small (Figure 5.10d).

In addition to the above, an initial starting/surface and/or an ending/floor velocity, with a fixed for all iterations non-zero weight ( $w(1) \neq 0$  and/or  $w(n) \neq 0$ , where  $n$  is the number of samples) so that they are not instantly smoothed, can be optionally provided to the algorithm. This can be done to further improve the linear trend and produce more realistic velocity functions and velocity fields. This option is also particularly useful when the direct ground wave is not very coherent in a data set for a combined LMO NMO approach to be used, as well as when there are insufficient primary and/or many spurious near-surface and/or deep semblance peaks for a good velocity field to be generated.

In the following sections, the proposed automatic velocity analysis algorithm is evaluated and compared with manual hand-picked velocity analysis using both synthetic and field data CMP gathers.

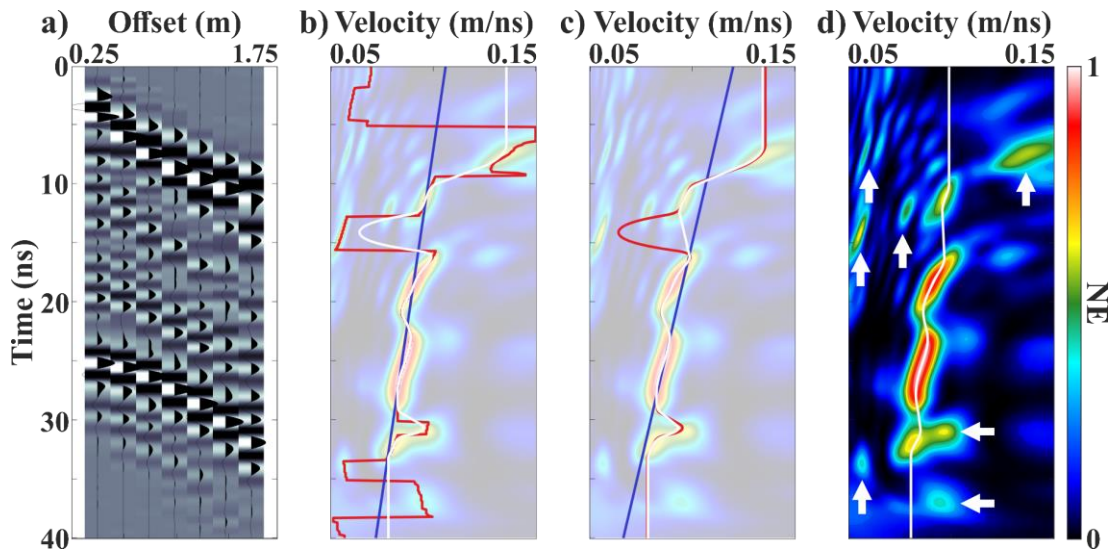


Figure 5.10: a) Field data CMP gather. b) Semblance plot of (a) showing the automatic velocity picks at the first iteration. The red line indicates the initial automatic velocity picks chosen based on the semblance maxima at each time sample, the blue line shows the weighted with the weight ( $w_s$ ) of equation (5.3) linear fitted curve of the initial picks, and the white line highlights the smoothed velocity picks. c) Semblance plot of (a) showing the automatic velocity picks at the second iteration. The red line indicates the smoothed velocity picks of the previous iteration (i.e., white line in (b)) which are now used as pre-set picks for the current iteration, the blue line shows the new weighted linear fitted curve of those picks, and the white line highlights the new smoothed velocity picks. d) Semblance plot of (a) showing the automatic velocity picks at the final iteration. The white line highlights the smoothed velocity picks, whereas the white arrows the spurious peaks that were avoided and not picked by the algorithm. The transparency of the semblance plot has been modified to aid visualisation in (b) and (c).

### 5.3.1 Synthetic data example

Figure 5.11a shows a synthetic CMP gather, consisting of seven traces, with seven clear hyperbolic events, which was generated in MATLAB by applying inverse normal moveout (INMO) correction with a variable moveout velocity (black solid lines in Figure 5.11). Random white Gaussian noise was also added to the gather to simulate the effects of very low and rapidly decreasing SNR with receiver offset. Figure 5.11b to Figure 5.11e depict the corresponding semblance plot of the gather, for different scenarios/cases, superimposed by the true velocities (black solid lines), the manually hand-picked velocities (red dotted lines), and the velocities picked automatically by the algorithm (white dotted lines) using different thresholds ( $(th_s)$  and  $(th_v)$ ) for each scenario.

Looking at Figure 5.11b, it is immediately observed that both the hand-picked, as expected, and the automatically picked velocities are in very good agreement with the true velocities used to generate the synthetic CMP gather, as they nearly perfectly coincide. In addition, it can be also observed that in this scenario the automatic velocities are slightly better matched to the true velocities than the hand-picked ones. The latter is also supported by the corresponding RMSE values, thus indicating in that way the effectiveness and accuracy of the proposed algorithm.

To demonstrate the usage of the two thresholds of the algorithm, let us assume that two of the seven semblance peaks are somehow spurious, and thus do not correspond to real events. The first one, centred at 15 ns, is a low to medium strength peak very close to the linear trend (marked with a white arrow in Figure 5.11c and Figure 5.11e), whereas the second, centred at 25 ns, is a high strength peak far away from the trend (marked with a white arrow in Figure 5.11d and Figure 5.11e). In the first case in Figure 5.11c, we want the algorithm to avoid picking the low to medium strength close to the trend semblance peak (white arrow), therefore  $(th_s)$  is increased so that peaks of such strength correspond to a zero weight ( $w_s$ ). Next, in the second case in Figure 5.11d, we want the algorithm to avoid picking the high strength far from the trend semblance peak (white arrow), hence  $(th_v)$  is decreased so that peaks of such velocity difference from the trend correspond to a zero weight ( $w_v$ ). Finally, in the third case in Figure 5.11e, we want the algorithm to avoid picking both the aforementioned semblance peaks (white arrows), therefore  $(th_s)$  is increased, whilst  $(th_v)$  is decreased.

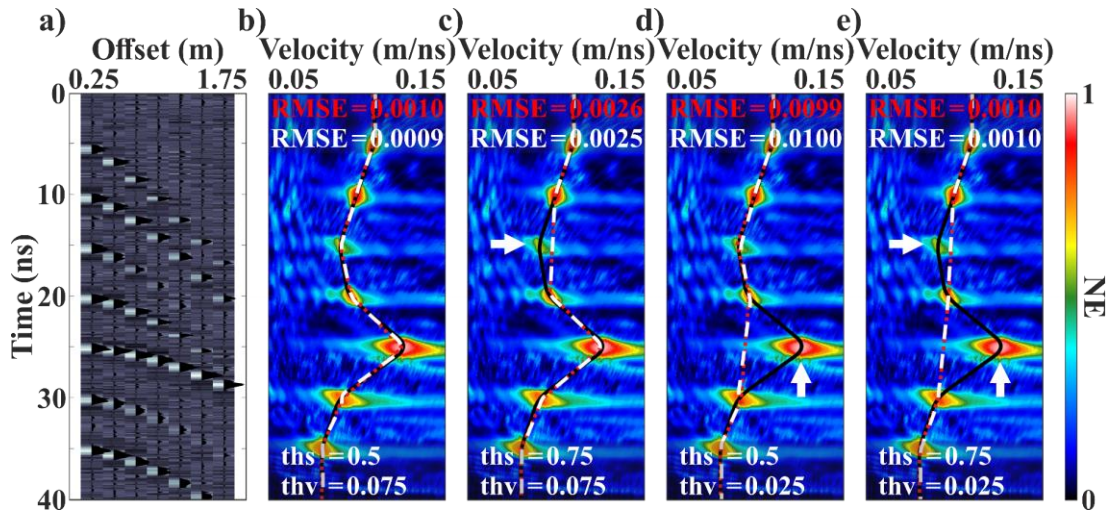


Figure 5.11: a) Synthetic CMP gather contaminated with white Gaussian noise. b – e) Semblance plots of (a) showing the true velocities used to create the synthetic CMP gather via INMO correction (black solid line), the velocities obtained manually by hand-picking (red dotted line), and the velocities picked automatically by the algorithm (white dotted line) using different thresholds ( $th_s$ ) and ( $th_v$ ) for the weights ( $w_s$ ) and ( $w_v$ ) of equations (5.3) and (5.4), respectively. In (c) – (e) white arrows highlight the supposedly spurious semblance peaks.

### 5.3.2 Field data example

To evaluate and compare the automatic velocity analysis algorithm with manual hand-picked velocity analysis via real field data CMP gathers, a different approach was followed than the one used with the synthetic gather above. This was necessary, as the stacking velocities are the unknown variables and they can only be verified indirectly. The CMP gathers were first processed with standard steps (i.e., time-zero alignment, dewow, time gain, frequency filtering, and trace balancing) and then subjected to hand-picked as well as automated semblance analysis. The resultant velocity functions from both methods were subsequently used to NMO correct the gathers. Finally, the obtained results were evaluated and compared by visual inspection. In general, as has been mentioned many times above, it is expected that optimal stacking velocities will produce NMO corrected CMP gathers with perfectly flat events.

Figure 5.12 illustrates the obtained results from two field CMP gathers. The first one shown in Figure 5.12a is a 1000 MHz centre frequency gather with a relatively coherent direct ground wave, and with several reflected events across multiple time intervals. Therefore, for this gather, a combined LMO NMO semblance approach was

used, while in addition no surface and/or floor velocity was provided to the automatic algorithm for the analysis of the corresponding semblance panel. The second one shown in Figure 5.12b is a 500 MHz centre frequency gather without a coherent direct ground wave and few reflected events. Therefore, for this gather, a simple NMO semblance approach was used, while in addition both a surface and a floor velocity were provided to the algorithm to assist the analysis of the corresponding semblance panel. The initial surface and floor velocity were chosen based on the resultant semblance panels of multiple adjacent CMP gathers from the same data set.

Looking at the semblance plots of both gathers in Figure 5.12 it can be clearly seen that there is a very good agreement between the hand-picked velocities and the velocities picked automatically by the algorithm, as they coincide almost perfectly. This is also corroborated by the NMO corrected CMP gathers obtained using both velocity functions (i.e., hand-picked – red line, and automatic – white line), which are nearly indistinguishable and have flat events. Nevertheless, it should be noted that the NMO corrected gathers resulting from using the automatic velocities show less stretching and a slightly improved flatness. This is due to the higher smoothness and likely higher accuracy of the automatic velocity function, thus indicating the effectiveness of the proposed algorithm.

The above findings validate the proposed automatic velocity analysis algorithm which can significantly aid the analysis of the large volumes of multi-offset GPR data that can be generated by the newly developed GPR systems with multiple concurrent acquisition receivers.

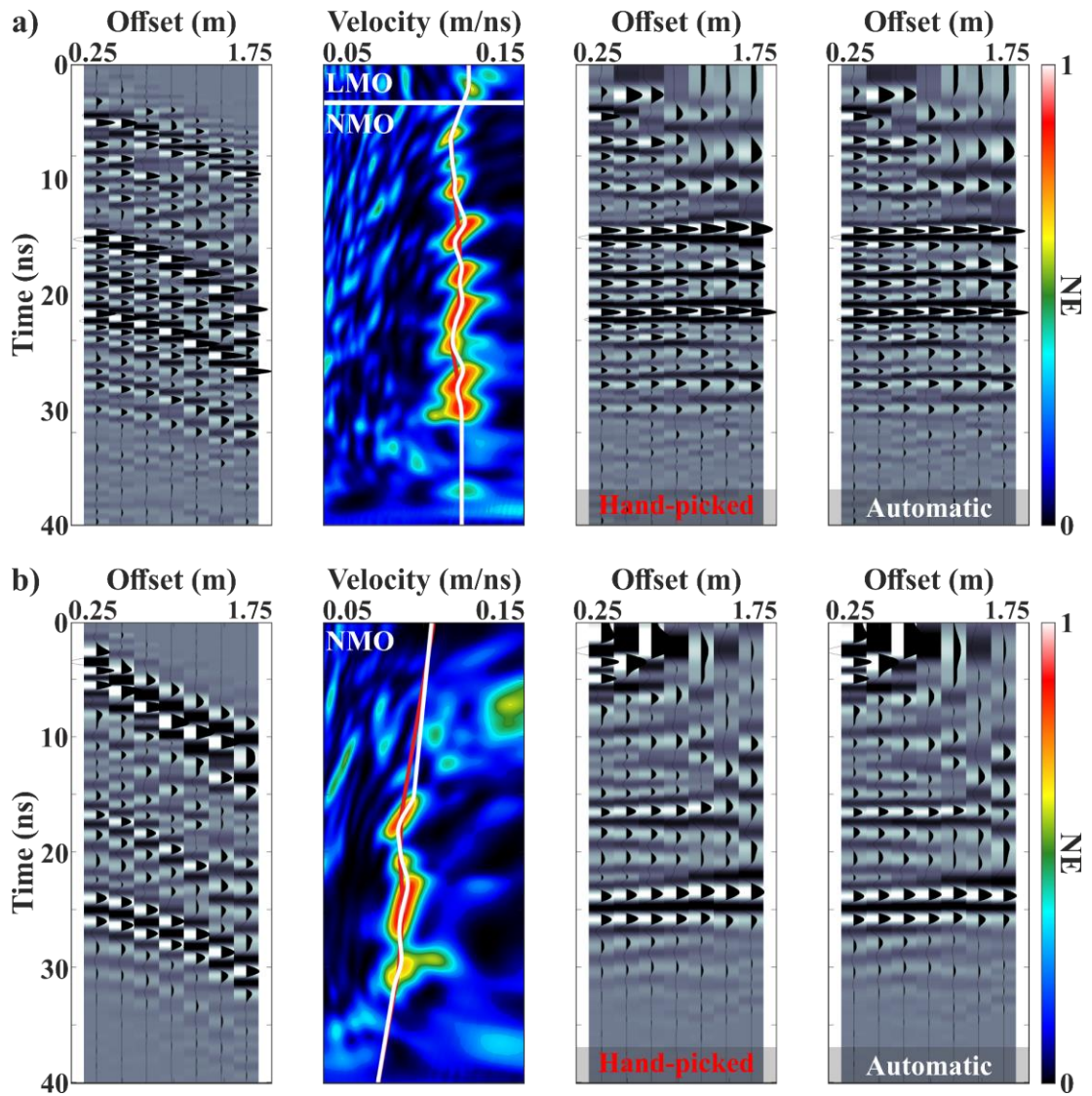


Figure 5.12: a) 1000 MHz centre frequency field data CMP gather, combined LMO NMO semblance plot of the CMP gather, CMP gather after NMO correction using the hand-picked velocities (red line), and CMP gather after NMO correction using the velocities picked automatically (white line). b) 500 MHz centre frequency field data CMP gather, NMO semblance plot of the CMP gather, CMP gather after NMO correction using the hand-picked velocities (red line), and CMP gather after NMO correction using the velocities picked automatically (white line).

# 6

## **A processing workflow for multi-concurrent receiver GPR data**

This chapter focuses on the development of a processing workflow for multi-concurrent receiver GPR data and is organised into five different sections. The chapter begins by introducing the actual processing workflow, which also incorporates the processing methods presented in the previous chapter. Next, the processing methods/processing workflow are/is evaluated with two synthetic data sets as well as two field data sets collected from different locations and with different multi-concurrent receiver GPR systems.

Research in this chapter has been published in Angelis et al. (2021) and Angelis et al. (2022a).

## 6.1 Processing workflow

As has been shown with several detailed examples in this thesis, MF GPR data require, in addition to standard GPR data processing (e.g., Ch. 2.7), more advanced specialised processing (e.g., Ch. 3.2) to provide detailed velocity models (i.e., velocity models with both vertical and lateral velocity variations) as well as to improve SNR. Most, if not all, of those additional advanced processing steps, were adapted gradually over the years from well-established seismic reflection data processing methods, owing, of course, to the similarities of the seismic and EM wavefields.

Therefore, following the successful development of new processing methods/algorithms in the previous chapter (Ch. 5) for addressing challenges associated with multi-concurrent receiver GPR data, a complete bespoke processing workflow is required. This workflow would allow for the production of detailed stacking velocity models capable of further improving the quality of the data, and hence, qualitative and quantitative GPR interpretations. The workflow that is proposed in this thesis for processing multi-concurrent receiver GPR data and producing detailed stacking velocity fields and enhanced zero-offset stacked reflection time sections is illustrated in Figure 6.1. It consists of three different sections:

- A section, which is highlighted in red and includes standard GPR data processing steps, i.e., steps typically used for CO SF GPR data (e.g., see Ch. 2.7 and Annan, 2003).
- A section, which is marked in blue and incorporates standard seismic data processing steps, i.e., steps typically used for seismic reflection data that have been adapted for GPR (e.g., see Ch. 3.2 and Yilmaz, 2001).
- A section, which is highlighted in green and contains the necessary steps:
  - To allow the transition of the data from the CO domain to the CMP domain, i.e., CMP gather sort, and if required, trace/distance resampling to fix the spatial step to enable CMP gather sort.
  - To boost semblance vertical resolution, as well as to improve static corrections and thus horizontal stacking efficiency, i.e., trace/time resampling to increase the number of time samples, and mute.

- To address some of the main multi-concurrent receiver GPR data challenges, i.e., time-zero alignment and CMP trace balancing (see Ch. 5).

In the following sub-chapters, the proposed processing workflow, which also includes the processing methods presented in chapter 5, is evaluated with synthetic data sets generated by complex 2D models using gprMax as well as field data sets collected from two different “WARR Machine” GPRs. It should be noted that all processing was performed exclusively in MATLAB using the software presented in chapter 4, whilst 2D modelling was chosen over 3D modelling, as it was a necessary compromise between the size and accuracy of the models and the available computational resources. Finally, it should be also pointed out that, while each data set is treated as a standalone case study, and thus analysed and presented separately in a different sub-chapter, only the first one is presented in full detail. This is primarily to avoid excessive repetition, as the same processing methods and processing workflow were used with all data sets. Of course, important differences and features are discussed for each dataset.

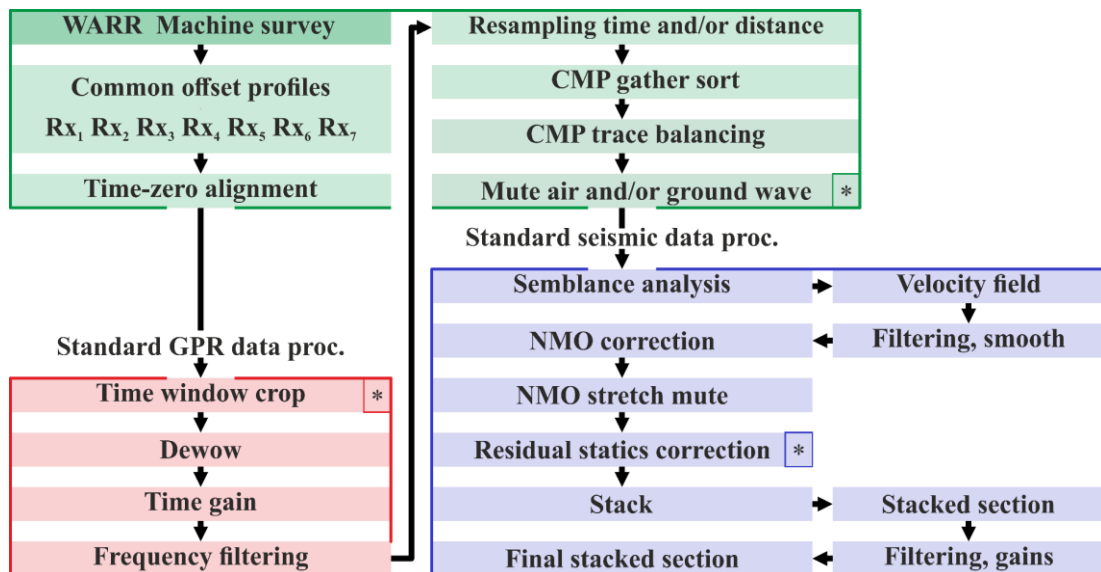


Figure 6.1: Proposed processing workflow for multi-concurrent receiver GPR data. Highlighted in red is a section that includes standard GPR data processing steps. Marked in blue is a section that incorporates standard seismic reflection data processing steps, adapted for GPR. Highlighted in green is a section that contains steps used to address multi-concurrent receiver GPR data challenges as well as to improve the efficiency of other processing steps. The “\*” symbol denotes the optional processing steps of the workflow.

## 6.2 Synthetic data case study 1

### 6.2.1 Model and data description

For the first synthetic data case study, a simple layered cake modelling scenario was considered. The model used, which is also shown in Figure 6.2a, is a complex 2D four-layered model in which the electrical permittivity increases from the top to the bottom layer, and hence velocity decreases with depth. Each one of the layers is made up of heterogeneous soil consisting of 50 different dispersive materials, with a bulk density of  $2 \text{ g/cm}^3$ , sand particle density of  $2.66 \text{ g/cm}^3$ , and a stochastic distribution of sand fraction (e.g., layer 1 sand fraction = 0.5), clay fraction (e.g., layer 1 clay fraction = 0.5), and volumetric water fraction (e.g., layer 1 water fraction range = 0.065 – 0.088), that was formed using the soil mixing methodology proposed by Peplinski et al. (1995). Therefore, it also provides additional lateral velocity variations. The model domain is equal to  $22 \times 2.2 \text{ m}$  (x, and z axes), with a spatial discretisation of  $\Delta x = \Delta z = 0.005 \text{ m}$ , and as a result, a time step of  $\Delta t = \sim 11.79 \text{ ps}$  as calculated by the CLF condition (4.6), as well as 20 PML layers on each side.

A single Hertzian dipole source, fed with a waveform shaped as the first derivative of a Gaussian with a 500 MHz centre frequency and an amplitude equal to 1, was used to represent the transmitter antenna, and seven receiver points to represent the receiver antennas. The source and the receiver points were all separated by 0.25 m, i.e., considering a transducer geometry similar to the 500 MHz centre frequency “WARR Machine” GPR (see Figure 4.5b), and moved along the surface of the model with a spatial trace step of 0.025 m (i.e.,  $T_x - R_{x1} / 10$ ) using the WARR mode of operation. The analysis steps were set to 771 to allow the creation of 801 CMP gathers after CMP sorting, and therefore of a final stacked section 20 m long. As for the time window, that was set to 60 ns resulting in a total of 5089 time steps.

The quality of the generated synthetic data is shown in Figure 6.2b, which illustrates the CO profile of the first, fourth, and seventh receiver after the application of time-zero alignment, time window crop, and SEC gain. In order to evaluate the proposed processing methods/processing workflow in a bad scenario with a very low and rapidly

declining SNR with receiver offset, random white Gaussian noise proportional to the offset and in a high percentage was added to the data. This was also done to represent more closely the real data, which can be noisier with increasing offset (see also Ch. 4.2.1 – Figure 4.7). Moreover, because it is quite difficult to directly reproduce strong AVO attenuation phenomena, such as those seen in real field data, especially when utilising 2D FDTD modelling without physical sub-models of the actual antennas, an additional artificial AVO reduction was applied to the synthetic data, as shown in Figure 6.2c. The contaminated synthetic CO data were then sorted into CMP gathers and subjected to further processing including velocity spectrum semblance analysis and horizontal stacking (see processing steps in Figure 6.1).

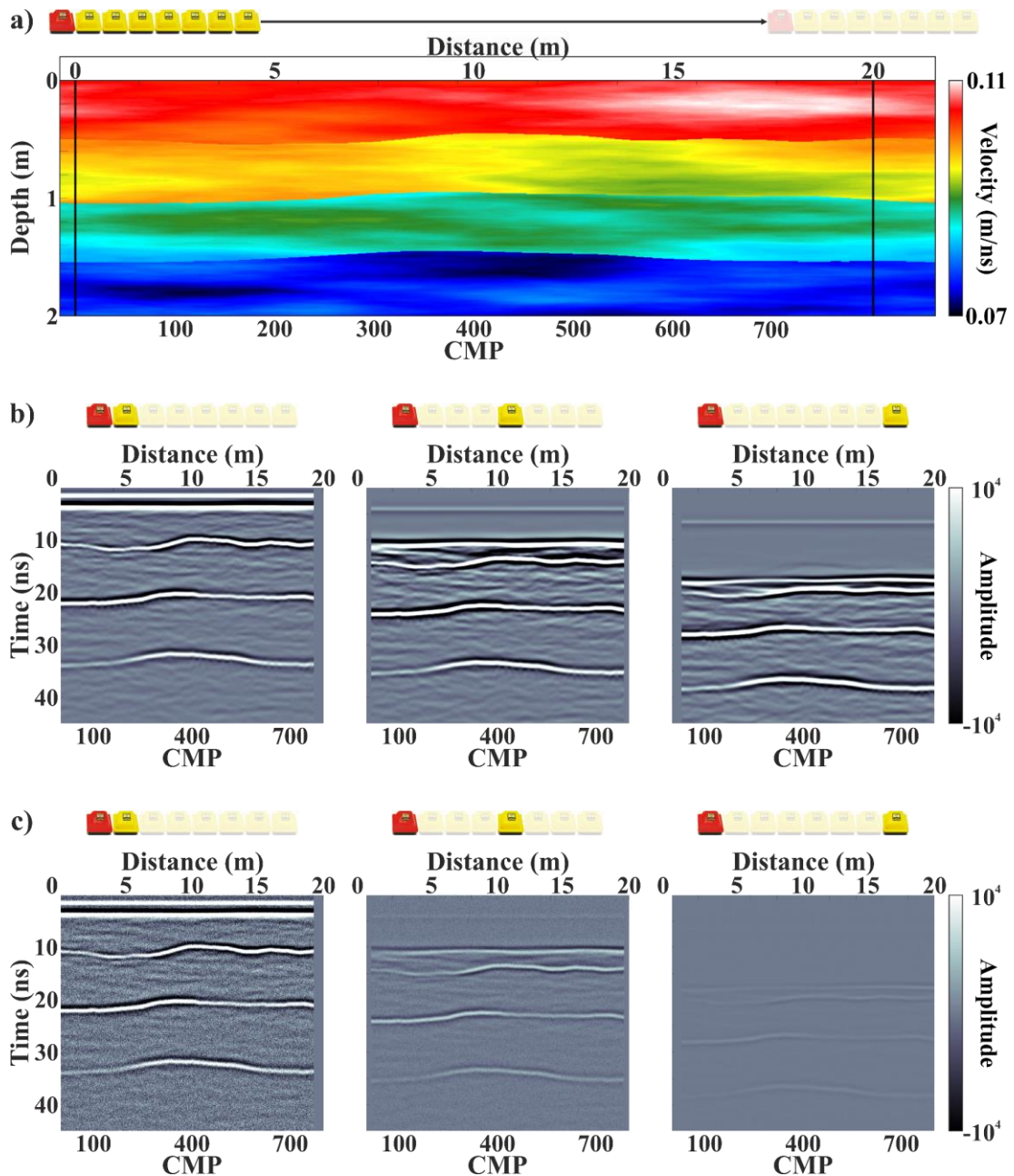


Figure 6.2: a) 2D four-layered model with both vertical and lateral velocity variations developed to generate the synthetic data to test and demonstrate the proposed processing methods/processing workflow. b) Processed CO profile of the first ( $Tx - Rx_1 = 0.25$  m), fourth ( $Tx - Rx_4 = 1.0$  m), and seventh receiver ( $Tx - Rx_7 = 1.75$  m). c) Processed CO profile of the first, fourth, and seventh receiver, after the application of white Gaussian noise and artificial AVO attenuation. The transducer configuration is shown at the top of each sub-figure, with the Tx in red and the Rxs in yellow.

## 6.2.2 Stacking velocity field and stacked section

To investigate whether it is feasible to automatically extract a detailed stacking velocity field, which could then be used to produce an enhanced zero-offset stacked section, from synthetic data developed to closely resemble real field multi-concurrent receiver GPR data, an automated combined LMO NMO semblance analysis was performed. Although according to the literature, velocity analysis is typically executed on selected high-SNR CMP gathers, it was, in this case, performed on all of the high-fold gathers to produce the most detailed velocity field possible. In addition to the automated analysis, a dense manual hand-picked velocity analysis every 0.5 m, i.e., every 20 CMP gathers, was also performed on the data, for both verification and comparison. Figure 6.3a shows the resultant stacking velocity cross-section derived via manual hand-picked semblance analysis. Since the analysis was conducted every 0.5 m, spatial interpolation was necessary to create the velocity field. Figure 6.3c depicts the resultant stacking velocity cross-section obtained through the automated semblance analysis. For this velocity field, no interpolation was required, only an extrapolation for the edges i.e., the low-fold areas, as in contrast to the previous one it was created by analysing all the high-fold gathers.

To remove possible velocity outliers, and thus create much more accurate and suitable velocity fields for the horizontal CMP stacking process that follows, the high volume of velocity data, i.e., the large number of available 1D velocity functions, was exploited. More specifically, in the first velocity field (Figure 6.3a) 2D Gaussian smoothing was applied using a rectangular kernel with a standard deviation (STD) equal to [2, 4], whilst in the second one (Figure 6.3c) both alpha-trimmed mean filtering every  $\sim 0.5$  m (i.e., every nineteenth 1D velocity function) and 2D Gaussian smoothing using the same rectangular kernel as in the previous field. Although both velocity fields could have been further smoothed and/or filtered, this was not done, as the objective of this process was to remove the extreme velocity outliers, whilst preserving as many of the general and consistent local velocity variations as possible, as these could potentially be associated with true local changes in material properties. The two resultant smoothed/filtered velocity cross-sections are shown in Figure 6.3b and Figure 6.3d, respectively.

Looking at the two figures (Figure 6.3b and Figure 6.3d), it is immediately observed that both fields are in very good agreement, as all the low-velocity and high-velocity areas coincide very well, a fact which in turn validates the resultant automated velocity field, and therefore the efficacy of the proposed automatic method. Nevertheless, it is also observed that the automated velocity field (Figure 6.3d) is, as expected due to the higher number of analyses, more detailed, with a higher spatial velocity resolution, and as a result more accurate, which is also evidenced by the fact that it captured better the boundaries of the layers (white arrows in Figure 6.3). The latter also demonstrates the superiority of the proposed automatic velocity analysis method over manual hand-picked velocity analysis, as not only allows for detailed and accurate fields to be obtained, but it does so in a much easier and faster manner, e.g., ~ 3.5 minutes for the automated combined LMO NMO velocity analysis of 740 seven-fold CMP gathers versus ~ 19 minutes for the respective manual analysis of 38 seven-fold CMP gathers – Intel® Core™ i7-10875H.

Subsequently, the two smoothed/filtered velocity fields were used to NMO correct the CMP gathers which were then stacked to create two different zero-offset stacked cross-sections. Both of these sections are shown in Figure 6.4, along with the CO section of the first receiver before and after the application of random white Gaussian noise, for comparison. In addition, each trace in each of the sections was normalised with its corresponding RMS value. While this normalisation process alters the amplitude of the data and essentially eliminates the relative amplitude differences in a section, it allows on the other hand for a better trace-by-trace comparison between all sections (i.e., all traces of all sections have an RMS value equal to 1).

By looking at the two stacked sections, shown in Figure 6.4c and Figure 6.4d, three observations can be made:

- The first observation is that in both stacked sections (Figure 6.4c and Figure 6.4d) compared to the contaminated with noise CO section of the first receiver (Figure 6.4b), there is a slight but noticeable change in the frequency content. In particular, there is a shift toward lower frequencies as well as a slight reduction of vertical resolution. This is a well-known and expected side effect of horizontal stacking of NMO corrected CMP gathers (Forte & Pipan, 2017; Yilmaz, 2001). A reminder

that the NMO correction is a dynamic correction that stretches the data resulting in a frequency distortion (see NMO stretch – Ch. 3.2) and that a CMP gather never has perfectly constant and flat events even after being corrected with the optimal stacking velocity.

- The second observation is that when comparing the stacked sections (Figure 6.4c and Figure 6.4d) to the contaminated with noise CO section of the first receiver (Figure 6.4b), all the expected benefits from the horizontal stacking procedure can be seen. More specifically, there is improved reflector continuity, as seen for instance in the area/reflector marked with a green arrow, as well as a significant reduction in high-frequency noise. The latter is also supported by the fact that details inside the layers, such as micro-reflections due to velocity variations, are more visible and have been significantly enhanced, as seen for example in the area/reflector highlighted with a blue arrow.
- The third and final observation, which is actually the more interesting one, is that both stacked sections (Figure 6.4c and Figure 6.4d) are almost identical despite being obtained using slightly different stacking velocity fields (Figure 6.3b and Figure 6.3d). Possibly the only, but not that evident, difference is that the stacked section obtained using the automated velocity field shows slightly less NMO stretching, as the reflectors in some areas, such as the one marked with a white arrow, appear slightly narrower. This is probably to the higher smoothness and accuracy of the automatic 1D velocity functions, as demonstrated in the previous chapter (see Ch. 5.3 – Figure 5.12), as well as due to the higher velocity resolution of the automated field compared to that of the manual one.

The above findings not only validate the obtained automated velocity field and corresponding stacked section but also demonstrate the overall value of the proposed processing methods/processing workflow. In addition, they reveal that in the case of a layered cake scenario, velocity analyses on every 0.5 m and 0.025 m could potentially result in nearly identical stacked sections.

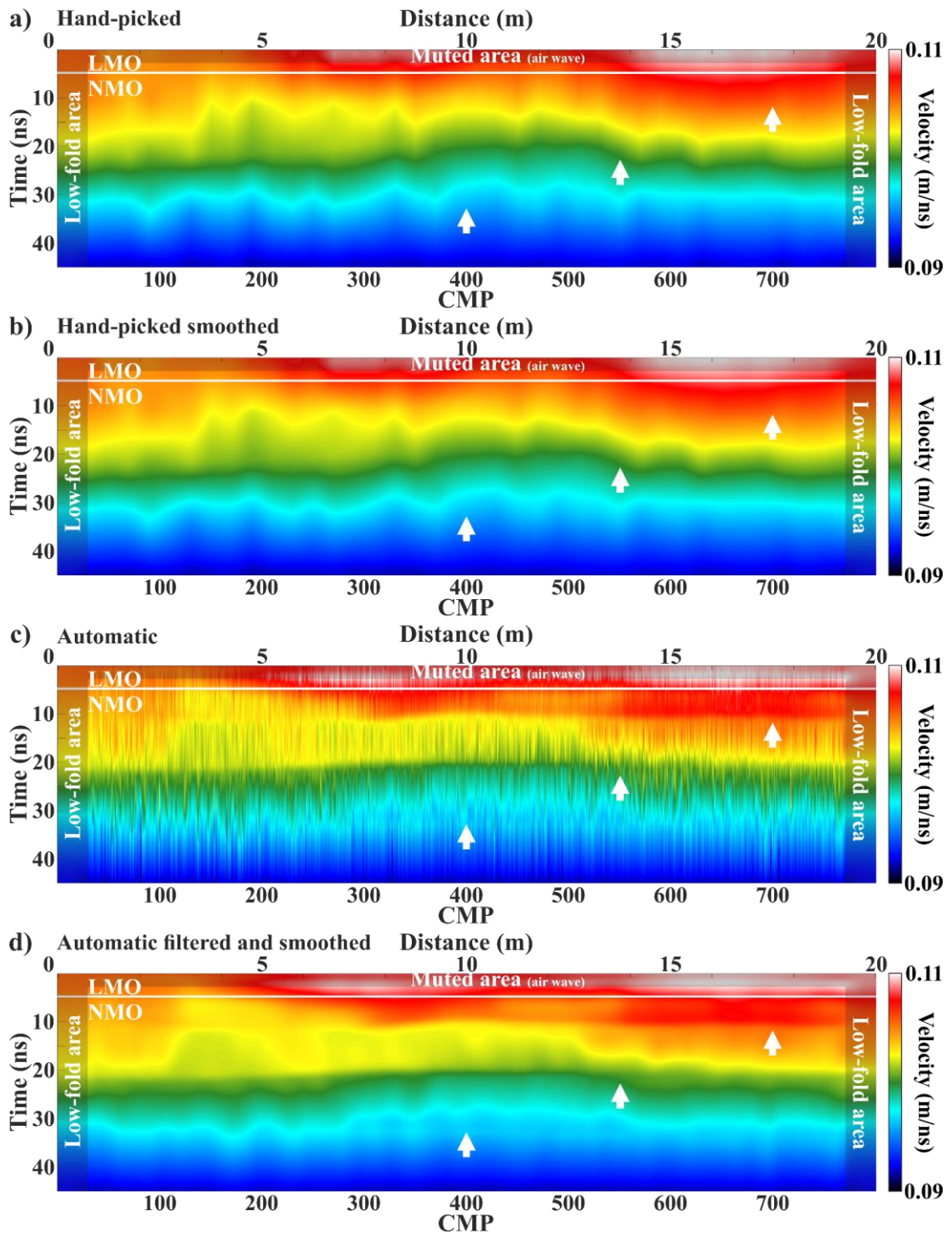


Figure 6.3: 2D four-layered model synthetic data set. a) Interpolated stacking velocity field derived from manual hand-picked combined LMO NMO velocity analysis on every 20 CMP gathers, i.e., every 0.5 m. b) Smoothed stacking velocity field of (a). c) Stacking velocity field derived from automated combined LMO NMO velocity analysis on all high-fold CMP gathers. d) Filtered and smoothed stacking velocity field of (c). The white arrows indicate some of the areas in which the automated velocity field outperforms the manual hand-picked one and captures much better the layer boundaries. The low-fold areas, as well as the muted area of the direct air wave, are also highlighted in the sub-figures.

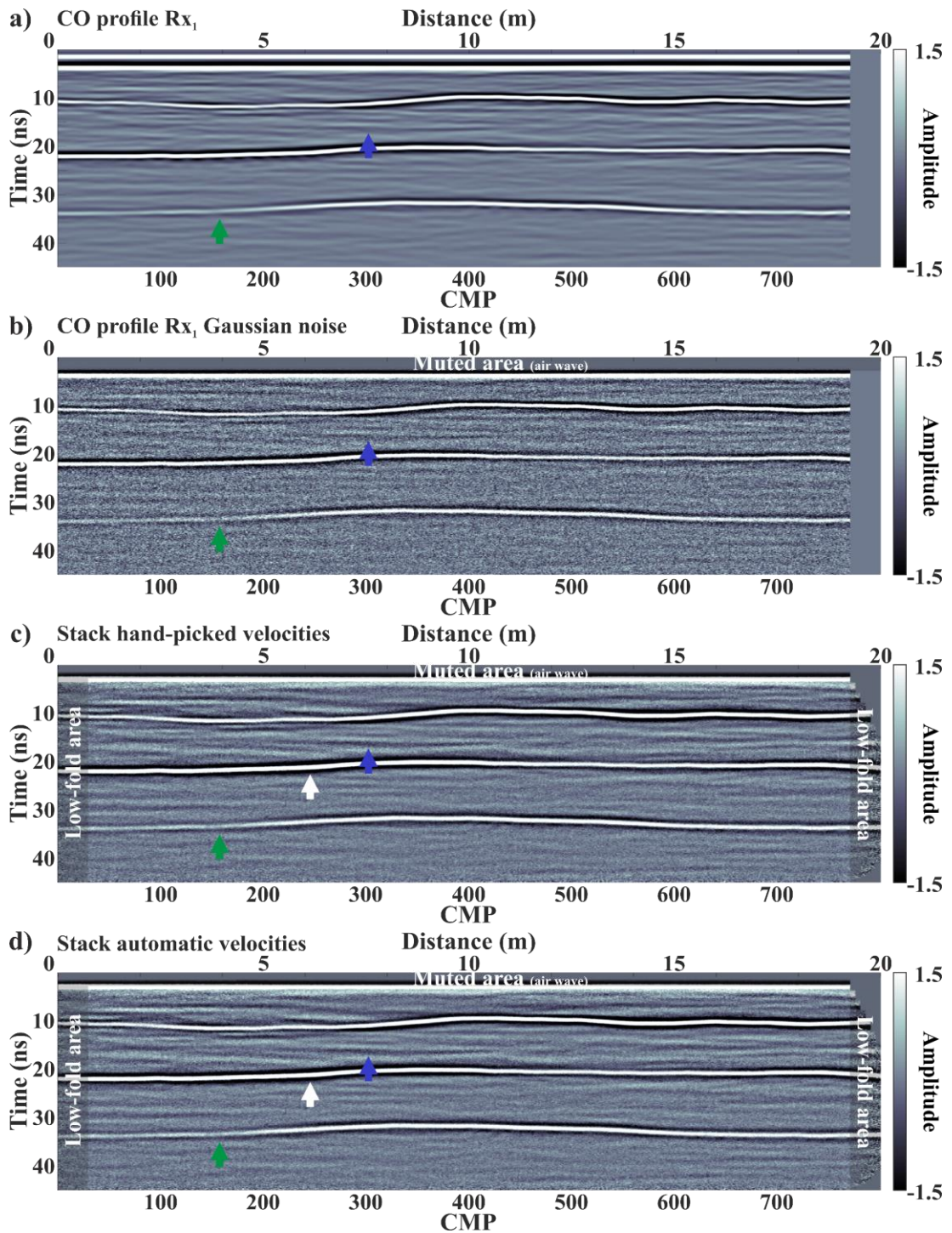


Figure 6.4: 2D four-layered model synthetic data set. a) Processed CO profile of the first receiver ( $Tx - Rx_1 = 0.25$  m). b) Processed and contaminated with white Gaussian noise CO profile of (a). c) Stacked section, derived using the smoothed velocity field obtained via manual hand-picked velocity analysis shown in Figure 6.3b. d) Stacked section, derived using the filtered/smoothed velocity field obtained via automated velocity analysis shown in Figure 6.3d. In (a) – (d) the blue arrow highlights an area of reduced high-frequency noise and an enhanced micro-reflector, and the green arrow marks a reflector with improved continuity. In (c), and (d), the white arrow shows a reflector with a slight difference in vertical width indicating an NMO stretch difference. The low-fold areas, as well as the muted area of the direct air wave, are also highlighted in the sub-figures.

## 6.3 Synthetic data case study 2

### 6.3.1 Model and data description

For the second synthetic data case study, a modelling scenario with dipping layers as well as simple and complex objects/targets was considered. The model, which is also depicted in Figure 6.5a, is a complex 2D three-layered model where the velocity decreases with depth. Each layer of the model is inhomogeneous, thus providing additional lateral velocity variations, and composed of heterogeneous soil consisting of several dispersive materials all mixed stochastically using the approach proposed by Peplinski et al. (1995), as in Ch. 6.2.1. Moreover, there are three different targets in the model, two of which were created using the voxel editor (see Ch. 4.1.3), a triangular-like complex target, a metal pipe, and an air-filled crack/cavity (white arrows in Figure 6.5a). The model has a size of 22 x 2.2 m (x, and z axes, respectively), 20 PML cells on each of its sides, and a spatial and temporal discretisation step equal to  $\Delta x = \Delta z = 0.005$  m and  $\Delta t = \sim 11.79$  ps (CLF condition (4.6)), respectively.

A single Hertzian dipole source, fed with a 500 MHz centre frequency waveform shaped as the first derivative of a Gaussian and an amplitude of 1 was used as the transmitter antenna, as were seven receiver points as the receiver antennas. Both the source and receivers points were all separated by 0.25 m, i.e., considering a transducer geometry similar to that of the “WARR Machine” GPR (500 MHz transducers – Figure 4.5), and moved using the WARR mode of operation along the surface of the model using a spatial trace step of 0.025 m (i.e.,  $T_x - R_{x1} / 10$ ). The analysis steps were set to 771 to create 801 CMP gathers, and thus a final stacked section 20 m long. Regarding the time window, it was set to 60 ns, yielding a total of 5089 time samples.

To show the quality of the generated synthetic data, Figure 6.5b illustrates the CO profile of the first, fourth, and seventh receiver after the application of time-zero alignment, time window crop, and SEC gain. Similarly to the previous synthetic data case study (see Ch. 6.2.1), to properly evaluate the proposed processing methods/processing workflow in bad a scenario with strong SNR versus receiver offset reduction and strong AVO variations, both random white Gaussian noise and artificial AVO

reduction were added/applied to the synthetic data, as shown in Figure 6.5c. Subsequently, the contaminated synthetic CO data were sorted into CMP gathers and subjected to further processing (see Figure 6.1 for processing steps).

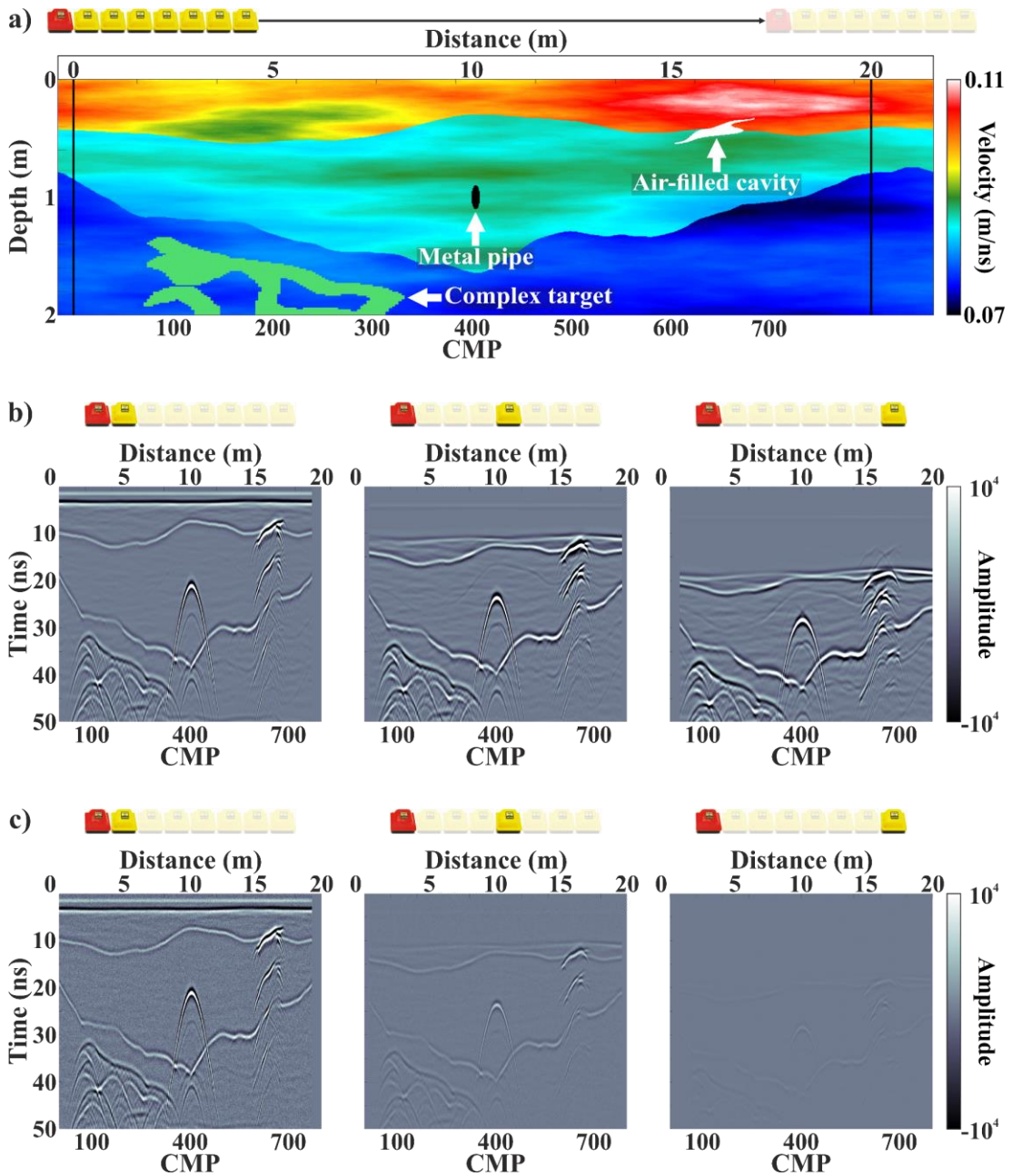


Figure 6.5: a) 2D three-layered model with both vertical and lateral velocity variations developed to generate the synthetic data to test and demonstrate the proposed processing methods/processing workflow. The white arrows highlight three different targets also contained in this model. b) Processed CO profile of the first ( $Tx - Rx_1 = 0.25$  m), fourth ( $Tx - Rx_4 = 1.0$  m), and seventh receiver ( $Tx - Rx_7 = 1.75$  m). c) Processed CO profile of the first, fourth, and seventh receiver, after the application of white Gaussian noise and artificial AVO attenuation. The transducer configuration is shown at the top of each sub-figure, with the Tx in red and the Rx's in yellow.

### 6.3.2 Stacking velocity field and stacked section

To investigate once more the feasibility of automatically extracting a detailed stacking velocity field capable of producing an enhanced zero-offset stacked section, from synthetic data that closely resemble real field multi-concurrent receiver GPR data, a combined LMO NMO semblance analysis was carried out. As in Ch. 6.2.2, an automated analysis was conducted on all high-fold CMP gathers as well as a dense manual hand-picked velocity analysis every 0.5 m (i.e., every 20 CMP gathers) for verification and comparison purposes. Figure 6.6a depicts the resultant interpolated stacking velocity cross-section obtained through manual hand-picked semblance analysis and Figure 6.6c shows the resultant stacking velocity cross-section derived via automated semblance analysis.

The large volume of available velocity data (i.e., the large number of available 1D velocity functions) was used, as in the previous case study (see Ch. 6.2.2), to remove potential velocity outliers, and hence to create more accurate and suitable velocity fields for the subsequent horizontal CMP stacking process. In particular, both velocity fields were smoothed and/or filtered. The first field (Figure 6.6a) was smoothed using a 2D Gaussian smoothing rectangular kernel with an STD equal to [2, 4], whereas the second one (Figure 6.6c) was both filtered, using alpha-trimmed mean filtering every  $\sim 0.5$  m, and smoothed with the same 2D Gaussian smoothing rectangular kernel. Figure 6.6b and Figure 6.6d show the resultant smoothed/filtered velocity cross-sections of the manual and automated analysis, respectively.

Comparing the two figures (Figure 6.6b and Figure 6.6d), it is clear that both velocity fields are generally very well correlated, which in turn, validates the obtained automated field. However, it is also clear that the velocity field derived via the automated analysis (Figure 6.6d) is, as expected, more detailed, and consequently more accurate. This is also corroborated by the fact that it captured better the velocity variations, such as the boundaries of the layers and the diffraction tails of the hyperbola (white arrows in Figure 6.6).

Next, the two smoothed/filtered velocity fields were used for the NMO correction of the CMP gathers, which were then stacked to produce two zero-offset stacked cross-

sections. The stacked sections are depicted together with the CO section of the first receiver before and after the application of random white Gaussian noise in Figure 6.7. Furthermore, to allow for a better comparison between all sections each trace in each section has been normalised with the corresponding RMS value.

By comparing the two stacked sections, illustrated in Figure 6.7c and Figure 6.7d, similar observations to those in the previous synthetic data case study (see Ch. 6.2.2) can be made:

- The first observation is that the stacked sections (Figure 6.7c and Figure 6.7d) have a slight shift in their frequency content along with a slight decrease in vertical resolution, which is the unavoidable side effect of horizontal stacking of NMO corrected CMP gathers.
- The second observation is that both stacked sections (Figure 6.7c and Figure 6.7d) show all the expected benefits of horizontal stacking. In particular, there is improved reflector continuity, as shown in the area/reflector marked with a green arrow, as well as a general and significant reduction in high-frequency noise. The latter is also corroborated by the fact that micro-reflectors, caused by velocity variations inside the layers, which were previously not visible have now been significantly enhanced, as shown in the area/reflector highlighted with a blue arrow. Finally, there is also a significant decrease in ringing noise, as can be seen in the area indicated by a red arrow. It should be noted, however, that for this specific area, velocity analysis was performed with extra care in order to avoid picking the semblance peaks corresponding to multiple reflections. For the automated analysis, this was achieved by simply tweaking the thresholds of the algorithm as well as muting parts of the semblance panel.
- The third and final observation is that both stacked sections (Figure 6.7c and Figure 6.7d) are generally very similar with slight differences. The only notable difference is that the stacked section of Figure 6.7d, i.e., the one produced using the automated velocity field of Figure 6.6d, exhibits slightly less NMO stretching and improved stacking, particularly in the areas of the diffraction tails of the hyperbola, which are marked with white arrows. This is due to the higher velocity resolution, both temporal and spatial, of the automated field, which can be essential, particularly for high-angle reflection events.

These findings validate the resultant automated velocity field and corresponding stacked section. In addition, when interpreted in conjunction with those of Ch. 6.2.2 they demonstrate once more the value of the proposed processing methods/processing workflow, and show that an extremely dense (e.g., every 2.5 cm) and a dense velocity analysis (e.g., 0.5 m) could result in quite similar stacked sections.

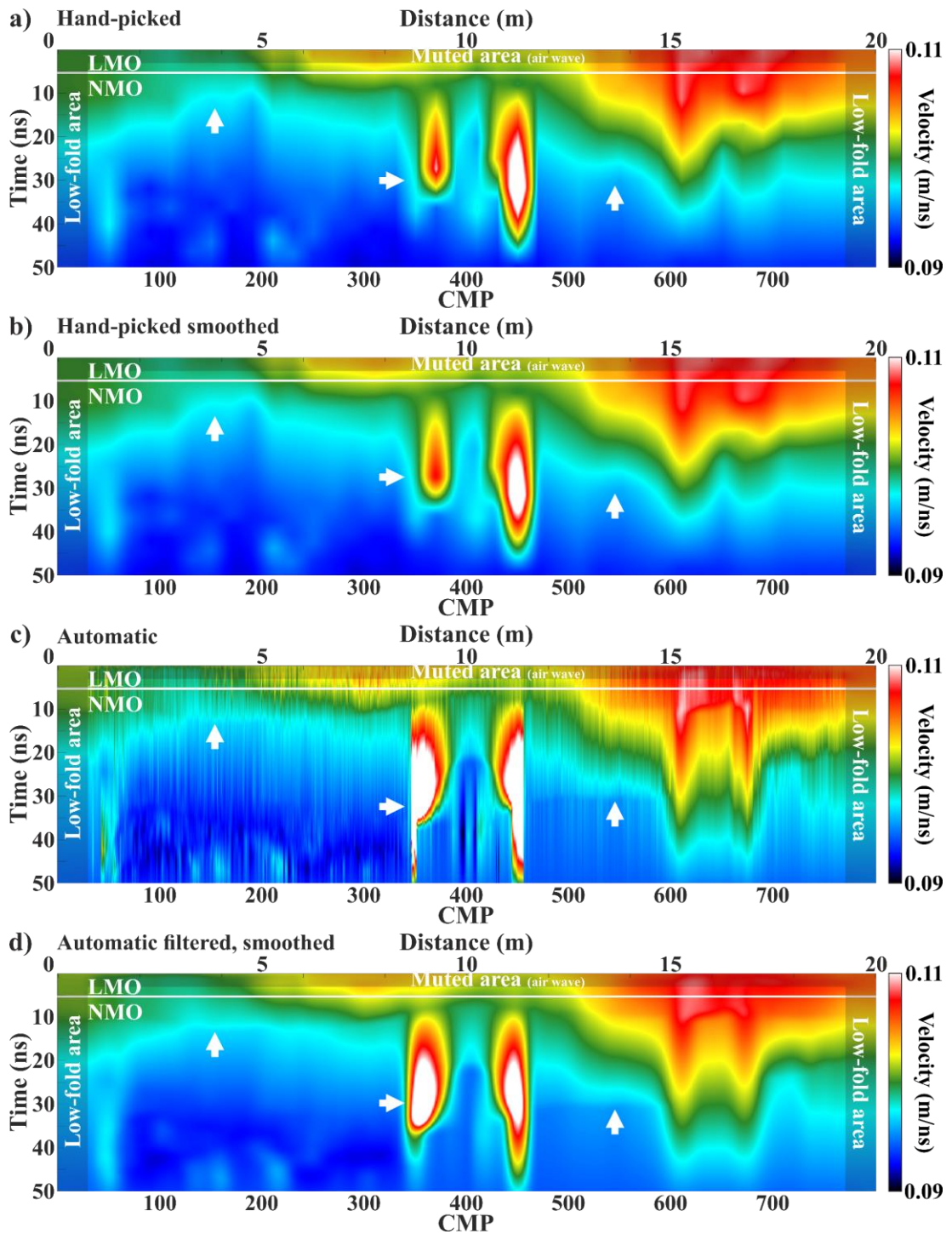


Figure 6.6: 2D three-layered model synthetic data set. a) Interpolated stacking velocity field derived from manual hand-picked combined LMO NMO velocity analysis on every 20 CMP gathers, i.e., every 0.5 m. b) Smoothed stacking velocity field of (a). c) Stacking velocity field derived from automated combined LMO NMO velocity analysis on all high-fold CMP gathers. d) Filtered and smoothed stacking velocity field of (c). The white arrows indicate some of the areas in which the automated velocity field outperforms the manual hand-picked one and captures much better the layer boundaries and the left-hand side of the hyperbola. The low-fold areas, as well as the muted area of the direct air wave, are also highlighted in the sub-figures.

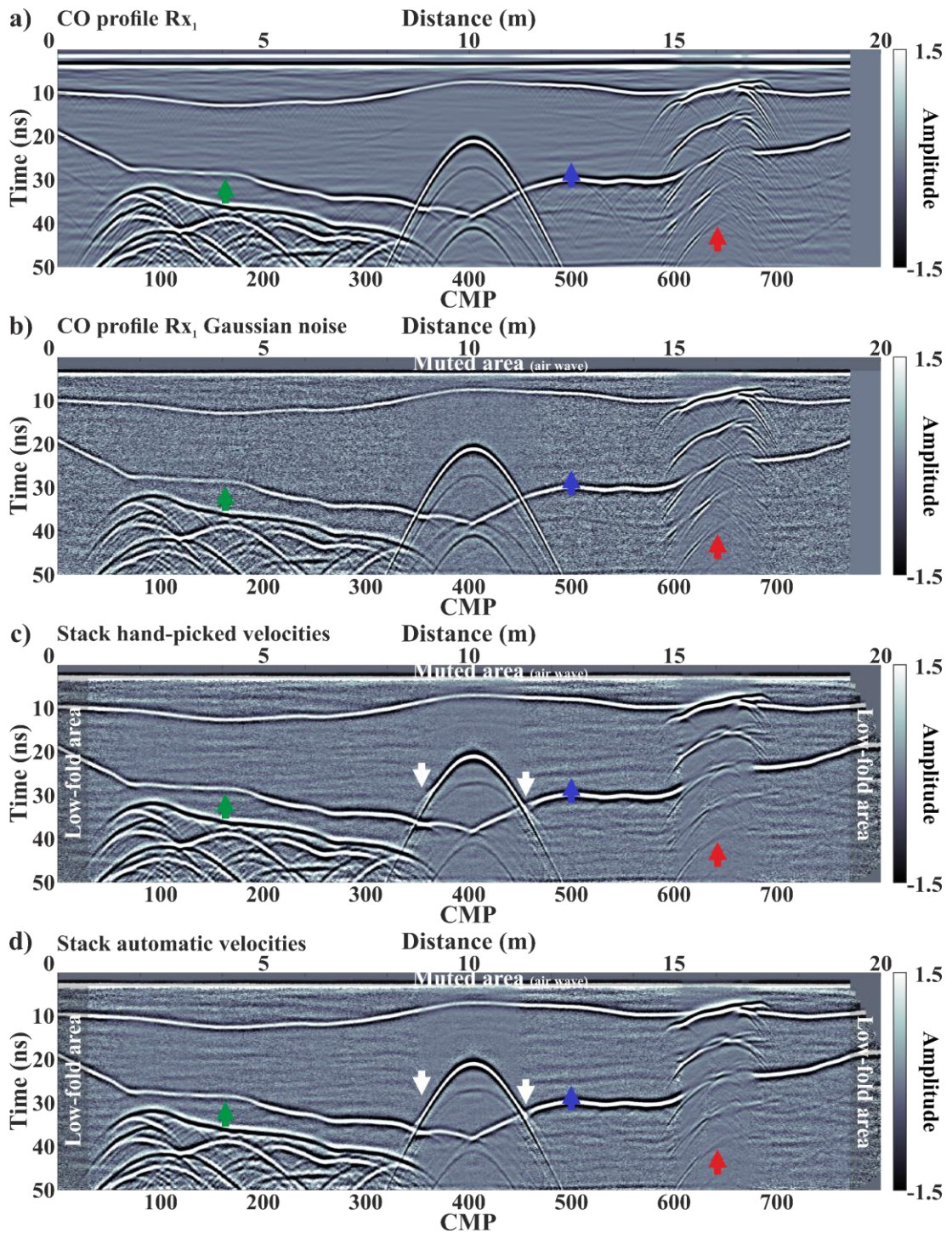


Figure 6.7: 2D three-layered model synthetic data set. a) Processed CO profile of the first receiver ( $Tx - Rx_1 = 0.25$  m). b) Processed and contaminated with white Gaussian noise CO profile of (a). c) Stacked section, derived using the smoothed velocity field obtained via manual hand-picked velocity analysis shown in Figure 6.6b. d) Stacked section, derived using the filtered/smoothed velocity field obtained via automated velocity analysis shown in Figure 6.6d. In (a) – (d) the red arrow highlights an area with a reduced ringing noise, the green arrow marks a reflector with improved continuity, and the blue arrow indicates an area of reduced high-frequency noise and an enhanced micro-reflector. In (c), and (d), the white arrows show two areas with slightly different stacking results. The low-fold areas, as well as the muted area of the direct air wave, are also highlighted in the sub-figures.

## 6.4 Field data case study 1

### 6.4.1 Data description

The field data for this case study were acquired from an asphalt-covered parking lot, with the target of interest being a linear pipe that crossed the parking lot. Data were collected with the “WARR Machine” GPR using the so-called SmartTow transducer configuration, i.e., the configuration in which the receivers trail the moving transmitter, with 500 MHz centre frequency transducers all separated by 0.25 m (see Figure 4.5a). Measurements were performed at a normal walking speed exactly above the long axis of the pipe while maintaining as much as possible the orientation of the antennas in relation to the direction of the pipe to avoid extreme amplitude and phase changes in the data. 16 vertical stacks per trace per receiver were used, as well as a spatial trace step of 0.0625 m (i.e.,  $Tx - Rx_1 / 4$ ) in order to enable direct CMP sorting without the need for spatial resampling. Finally, the time window was set to 40 ns and the sampling interval to 0.2 ns, hence resulting in a total of 200 time samples. Using these system/survey parameters, for a ~ 28 m long transect, seven CO profiles, equivalent to 461 WARRs and/or 473 CMPs, were acquired simultaneously.

The quality of the collected data is shown in Figure 6.8a to Figure 6.8d, which illustrates one of the WARR gathers (WARR 45), and the CO profile of the first, fourth, and seventh receiver, respectively. In order to aid visualisation, i.e., to highlight the different subsurface features, dc shift removal has been applied to the WARR gather, and both dc shift removal and IAD gain to the CO profiles. The colour scale/greyscale of the CO profiles has also been adjusted accordingly. Notice the character of the collected data, and in particular, the time misalignments, strong AVO, and SNR versus receiver offset reduction.

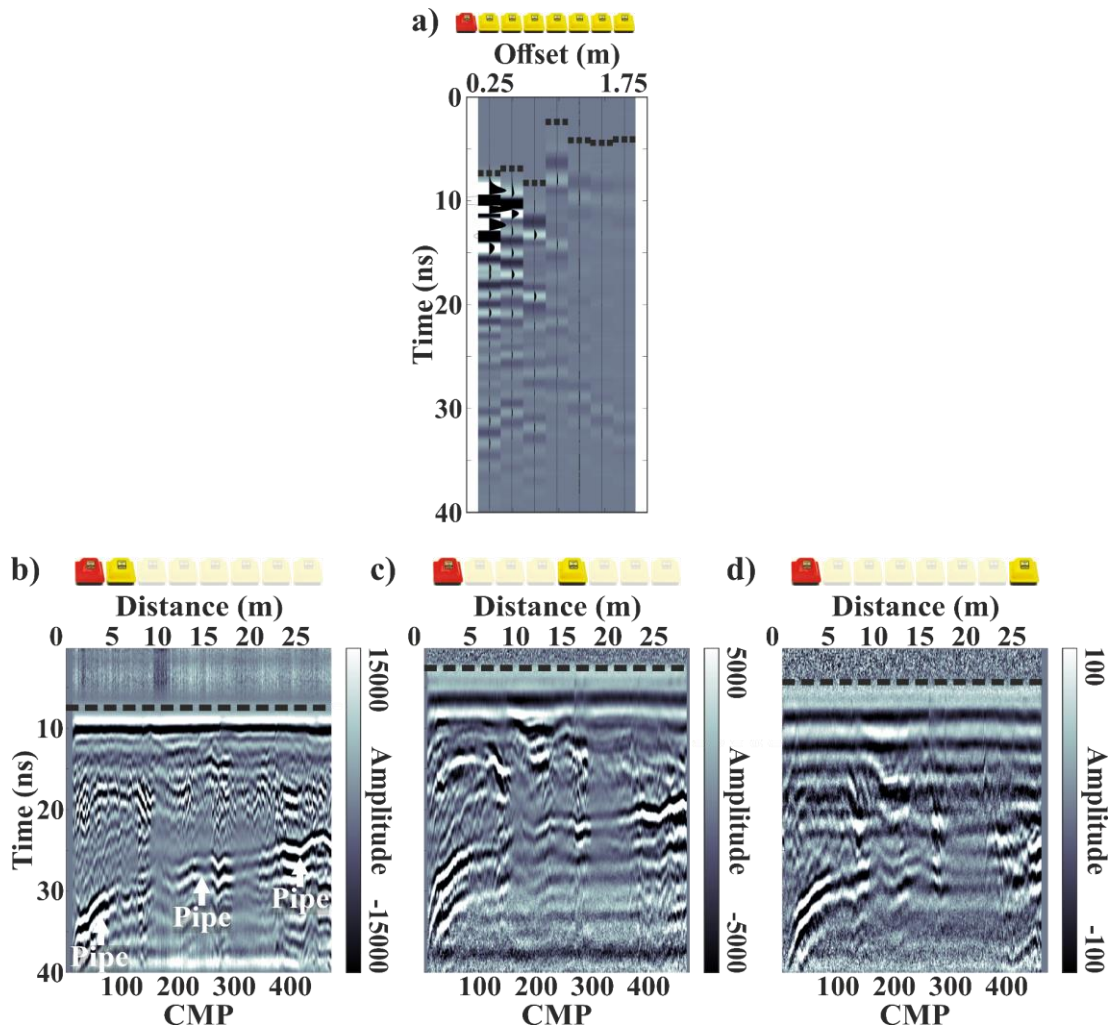


Figure 6.8: 500 MHz centre frequency field data set used to demonstrate the proposed processing methods/processing workflow. a) Field data WARR gather (WARR 45) after the application of dc shift removal. b) CO profile of the first receiver,  $T_x - R_{x_1} = 0.25$  m. c) CO profile of the fourth receiver,  $T_x - R_{x_4} = 1.0$  m. d) CO profile of the seventh receiver,  $T_x - R_{x_7} = 1.75$  m. DC shift removal and IAD gain have been applied to the CO profiles. The black dotted lines highlight the direct air wave responses and the white arrows the linear pipe response. The transducer configuration is shown at the top of each sub-figure, with the Tx in red and the Rx's in yellow.

## 6.4.2 Stacking velocity field and stacked section

To validate the results of the previous synthetic data case studies (see Ch. 6.2.2 and Ch. 6.3.2) a semblance analysis was performed on the processed field data (see processing steps in Figure 6.1). It should be noted that instead of a combined LMO NMO approach, a typical NMO approach was followed with this data set, as the direct ground wave was not coherent in the CMP gathers. The semblance analysis was carried out not only automatically but also manually, by hand-picking, for both verification and comparison. The automated analysis was performed on all high-fold CMP gathers, whilst the manual analysis in every 8 gathers, i.e., every 0.5 m. The resultant velocity cross-sections derived via manual hand-picked and automated semblance analyses are shown in Figure 6.9a and Figure 6.9c, respectively

As in Ch. 6.2.2 and Ch. 6.3.2, both velocity fields were processed to eliminate possible velocity outliers. Specifically, in the first velocity field, shown in Figure 6.9a, 2D Gaussian smoothing was applied using a square kernel with an STD equal [2, 2], while in the second field, depicted in Figure 6.9c, both alpha-trimmed mean filtering, every  $\sim 0.45$  m (i.e., every seventh 1D velocity function) and 2D Gaussian smoothing using the exact same square kernel were applied. The processed resultant velocity fields are shown in Figure 6.9b and Figure 6.9d, respectively.

Examining the two figures (Figure 6.9b and Figure 6.9d), it can be clearly seen that both fields are very well correlated, with almost all low- and high-velocity areas in the fields coinciding. This strong correlation between them validates the resultant automated velocity field. Nevertheless, it can be also seen that the automated velocity field is more detailed, owing, of course, to the larger number of analyses, and appears to better capture velocity variations caused by reflectors in some areas (e.g., white arrows in Figure 6.9).

Subsequently, the processed velocity fields were used to NMO correct the CMP gathers and these, in turn, created two different zero-offset stacked cross-sections. The resultant stacked sections are shown in Figure 6.10 along with the CO section of the first receiver for comparison. In addition, to facilitate comparison between the sections, each trace in each section was normalised with its corresponding RMS value.

By examining the stacked sections, depicted in Figure 6.10b and Figure 6.10c, similar observations to those in the previous synthetic data case studies can be made:

- The first observation is that there is a slight change in frequency content toward lower frequencies and a loss of vertical resolution in both stacked sections (Figure 6.10b and Figure 6.10c). This is to be expected, as it is the inevitable side effect of horizontal stacking of NMO corrected CMP gathers.
- The second observation is that comparing both stacked sections (Figure 6.10b and Figure 6.10c) to the CO section of the first receiver (Figure 6.10a) all the expected benefits of horizontal stacking can be seen. There is a general and noticeable decrease in high-frequency noise, and a slight reduction in ringing noise which is caused by the reverberation of EM waves in the pipe, as shown in the area indicated with a red arrow. Furthermore, there is also improved continuity, as seen in the area/reflector marked with a green arrow, and significant enhancement of reflectors, as seen in the area/reflector highlighted with a blue arrow.
- The third and final observation is that the stacked sections (Figure 6.10b and Figure 6.10c) are almost identical with no easily discernible differences to the naked eye, despite having been generated using slightly different velocity fields (Figure 6.9b and Figure 6.9d). It should be noted, however, that after a very careful examination, it can be seen that the events in the stacked section of Figure 6.10c, and in particular, the pipe response, are slightly narrower, indicating less NMO stretching, and therefore the use of a more suitable velocity field.

These findings validate the results of the previous synthetic data case studies, and therefore the efficacy of the proposed processing methods/processing workflow. In addition, they demonstrate for the first time that seven traces from seven multi-concurrent sampling receivers are sufficient to provide automatically detailed stacking velocity fields and enhanced zero-offset stacked reflection time sections.

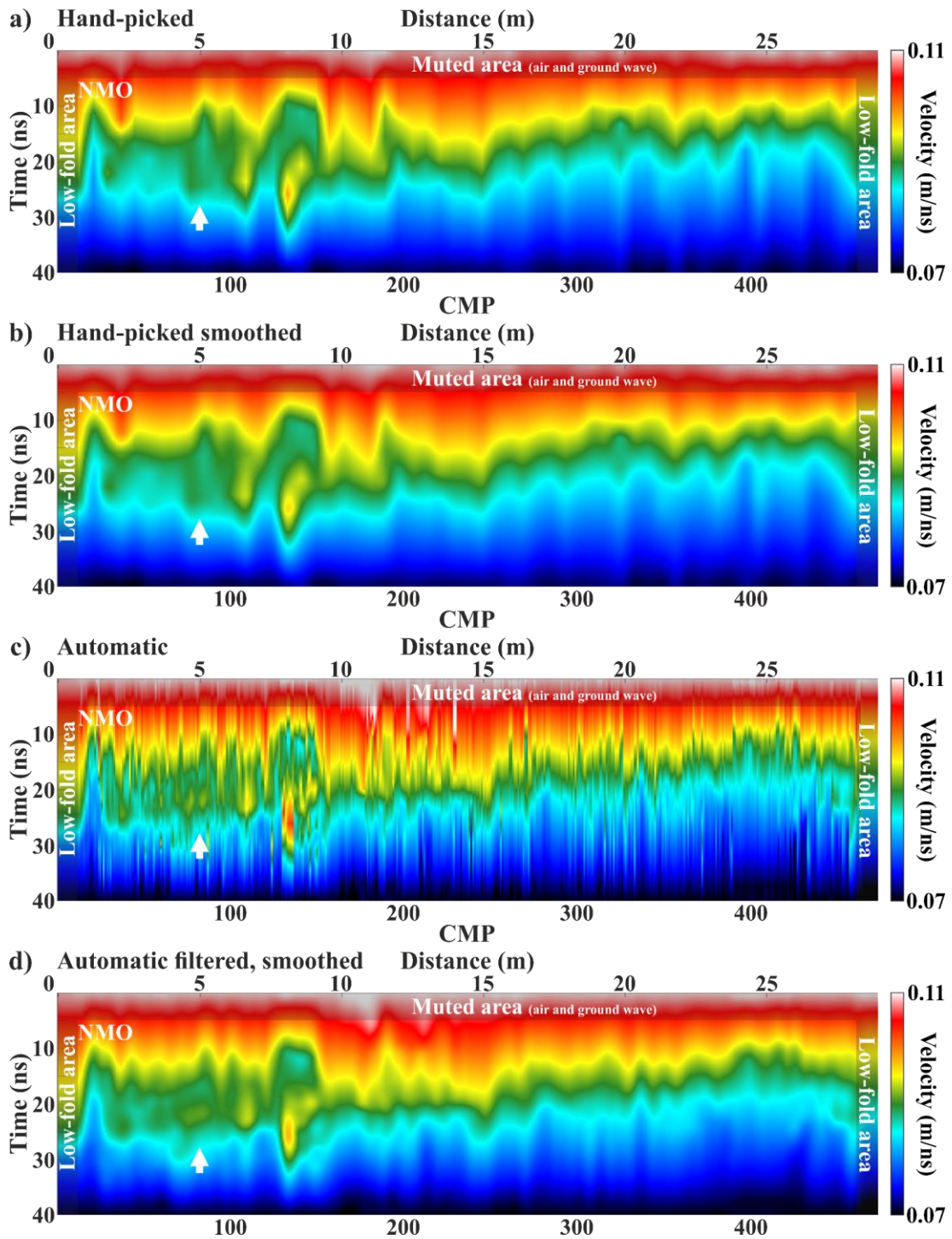


Figure 6.9: 500 MHz centre frequency field data set. a) Interpolated stacking velocity field derived from manual hand-picked NMO velocity analysis on every 8 CMP gathers, i.e., every 0.5 m. b) Smoothed stacking velocity field of (a). c) Stacking velocity field derived from automated NMO velocity analysis on all high-fold CMP gathers. d) Filtered and smoothed stacking velocity field of (c). The white arrows indicate an area (0 – 10 m and 10 – 30 ns) in which the automated velocity field outperforms the manual hand-picked one and captures much better the subsurface reflectors. The low-fold areas, as well as the muted area of the direct air wave and direct ground wave, are also highlighted in each sub-figure.

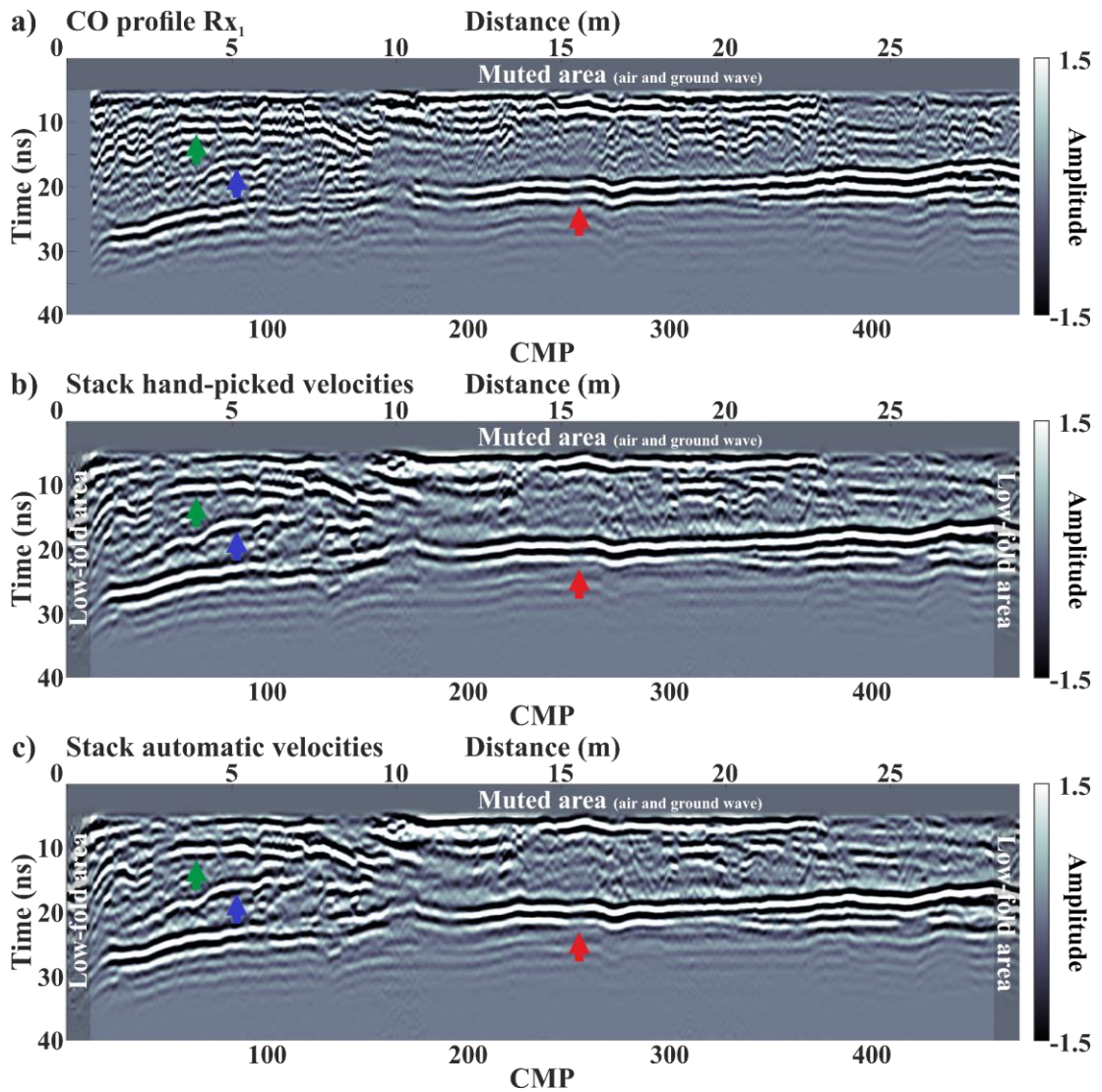


Figure 6.10: 500 MHz centre frequency field data set. a) Processed CO profile of the first receiver ( $Tx - Rx_1 = 0.25$  m). b) Stacked section, derived using the smoothed velocity field obtained via manual hand-picked velocity analysis shown in Figure 6.9b. c) Stacked section, derived using the filtered/smoothed velocity field obtained via automated velocity analysis shown in Figure 6.9d. In (a) – (c) the red arrow highlights an area with a reduced ringing noise, the green arrow marks a reflector with improved continuity, and the blue arrow indicates an enhanced reflector. The low-fold areas, as well as the muted area of the direct air wave and direct ground wave, are also highlighted in each sub-figure.

## 6.5 Field data case study 2

### 6.5.1 Data description

The field data for this case study were acquired from a shipping container storage yard that was recently paved with thick asphalt due to heavy/large equipment traffic. The site had just been re-paved with multiple lifts of asphalt in order to create a very thick asphalt to facilitate large heavily loaded trucks. The result was a site with several relatively flat-lying shallow layers, namely a site particularly interesting for a survey with a multi-concurrent sampling receiver GPR system. Data were collected with the “WARR Machine” GPR using the so-called SmartCart transducer configuration, i.e., the configuration in which the receivers precede the moving transmitter, with 1000 MHz centre frequency transducers all separated by 0.165 m (see Figure 4.6). Measurements were performed at normal walking speed using 16 vertical stacks per trace per receiver and a spatial trace step equal to 0.04125 m (i.e.,  $T_x - R_{x1} / 4$ ) to enable direct CMP sorting without the need for spatial resampling. Finally, the time window was set to 30 ns and the sampling interval to 0.05 ns, thus resulting in a total of 600 time samples. Using these system/survey parameters for a ~ 50 m long transect, seven CO profiles, equivalent to 1218 WARRs and/or 1230 CMPs, were acquired simultaneously.

To show the quality of the collected data, Figure 6.11a to Figure 6.11d illustrates one of the WARR gathers (WARR 500) and the CO profile of the first, fourth and seventh receiver, respectively. Only for visualisation purposes, i.e., to highlight the different subsurface features, dc shift removal has been applied to the WARR gather, and both dc shift removal and IAD gain to the CO profiles. The colour scale/greyscale of the CO profiles has also been adjusted accordingly. Notice once again, as in the previous field data case study (see also Ch. 6.4.1 – Figure 6.8), the character of the collected data, and in particular, the time misalignments, strong AVO, and SNR versus receiver offset reduction, despite the differences in environment, GPR system, transducers, centre frequency, etc.

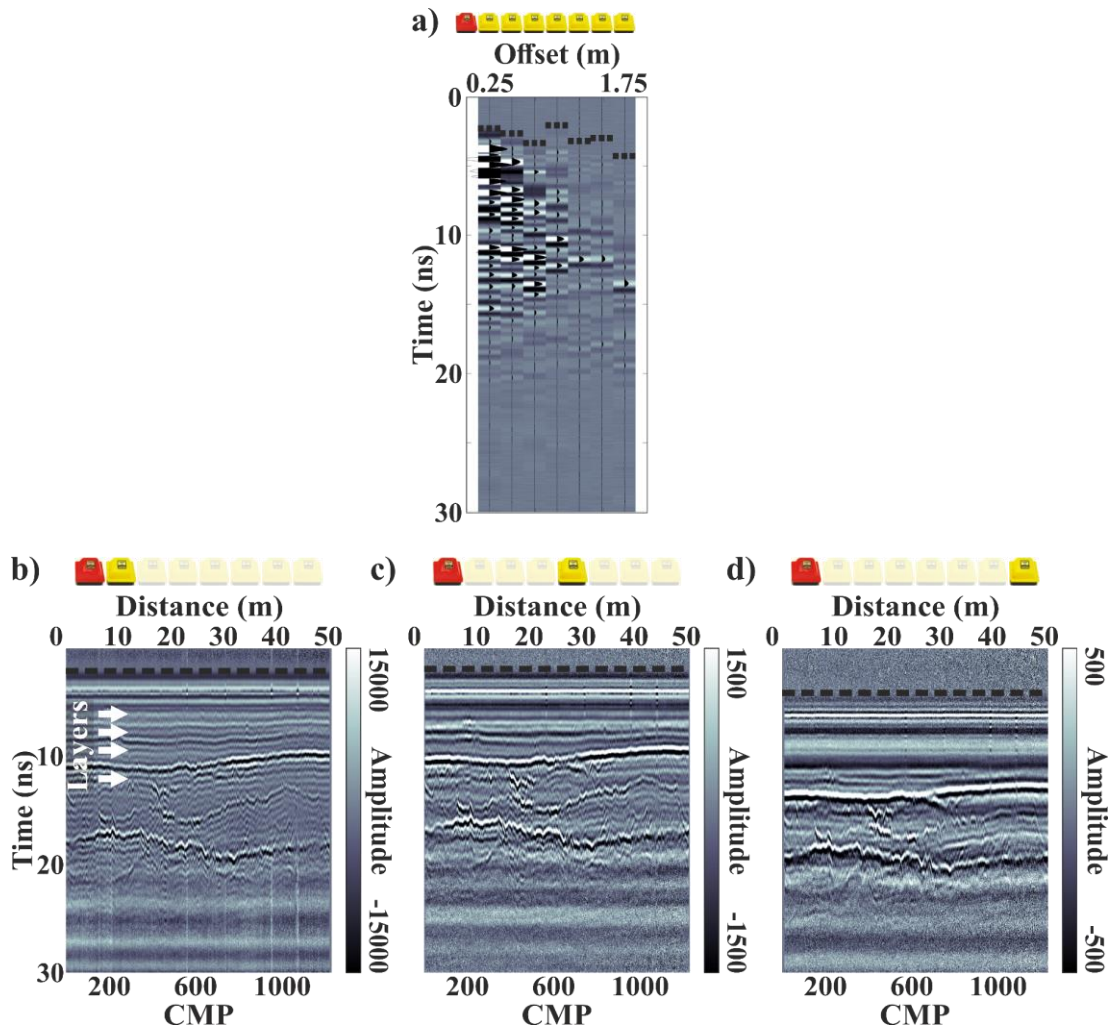


Figure 6.11: 1000 MHz centre frequency field data set used to demonstrate the proposed processing methods/processing workflow. a) Field data WARR gather (WARR 500) after the application of dc shift removal. b) CO profile of the first receiver,  $Tx - Rx_1 = 0.165$  m. c) CO profile of the fourth receiver,  $Tx - Rx_4 = 0.66$  m. d) CO profile of the seventh receiver,  $Tx - Rx_7 = 1.155$  m. DC shift removal and IAD gain have been applied to the CO profiles. The black dotted lines highlight the direct air wave responses and the white arrows the different layers. The transducer configuration is shown at the top of each sub-figure, with the Tx in red and the Rxs in yellow.

## 6.5.2 Stacking velocity field and stacked section

To validate the results of the previous case studies (see Ch. 6.2.2, Ch. 6.3.2, and Ch. 6.4.2) an automated combined LMO NMO semblance analysis was carried out on all of the processed high-fold CMP gathers (see Figure 6.1 for processing steps). In addition, to the automated analysis, a dense manual hand-picked velocity analysis every  $\sim 0.5$  m (i.e., every 12 CMP gathers), was also carried out, for verification and comparison purposes. Figure 6.12a shows the resultant interpolated stacking velocity cross-section derived via manual hand-picked semblance analysis and Figure 6.12c depicts the resultant stacking velocity cross-section obtained through automated semblance analysis.

To eliminate potential velocity outliers, both velocity fields were processed as the respective fields in Ch. 6.2.2, Ch. 6.3.2, and Ch. 6.4.2. More specifically, the first field, depicted in Figure 6.12a, was smoothed using a 2D Gaussian smoothing rectangular kernel with an STD equal to [3, 6], whilst the second field, shown in Figure 6.12c, was both filtered, with alpha-trimmed mean filtering every  $\sim 0.25$  m (i.e., every seventh 1D velocity function) and smoothed using the same 2D Gaussian kernel. Figure 6.12b and Figure 6.12d illustrate the resultant smoothed/filtered velocity cross-sections of the manual and automated analysis, respectively.

Looking at the two figures (Figure 6.12b and Figure 6.12d), it can be observed that both velocity fields are in very good agreement, with the majority of the low-velocity and high-velocity areas correlated. This high level of agreement validates the obtained automated velocity field. However, it is also observed that the velocity field obtained via the automated analysis is, as expected given the higher number of analyses, more detailed, and seems to capture much better velocity variations in some areas (white arrows in Figure 6.12).

Both processed velocity fields were then used to NMO correct the CMP gathers and subsequently to produce two zero-offset stacked cross-sections via horizontal stacking. The resultant two stacked sections are shown in Figure 6.13. For comparison, the CO section of the first receiver is also shown in the figure. Moreover, to aid comparison

between all the traces of all sections, each trace in each section was normalised with its corresponding RMS value.

By looking at the stacked sections, shown in Figure 6.13b and Figure 6.13c, exact similar observations to those shown in all previous case studies can be made:

- The first observation is that both stacked sections (Figure 6.13b and Figure 6.13c) exhibit the unavoidable side effect of NMO correction and horizontal stacking, i.e., a shift towards lower frequencies and a slight decrease in vertical resolution.
- The second observation is that both stacked sections (Figure 6.13b and Figure 6.13c) when compared to the CO section of the first receiver (Figure 6.13a) show all of the expected benefits of horizontal stacking. For example, there is a significant reduction in both high-frequency noise and ringing noise, as shown in the area which is indicated by a red arrow. In addition, there is also improved reflector continuity, as shown in the area/reflector marked with a green arrow, as well as a significant enhancement of reflectors that were previously not even fully visible, as shown in the areas highlighted with a blue arrow and blue boxes.
- The third and final observation is once again that the stacked sections (Figure 6.13b and Figure 6.13c) are very similar with the only notable difference being a difference in the NMO stretching, which is particularly noticeable for the horizontal reflector seen in  $\sim 9$  ns. The reduced stretching that is observed in the stacked section of Figure 6.13c compared to the one in Figure 6.13b indicates that a more appropriate velocity field was used for the NMO correction of the CMP gathers.

The above findings validate the results of all previous case studies and thus confirm the efficiency of the proposed processing methods/processing workflow. In addition, they clearly demonstrate the true potential of the multi-concurrent receiver GPR systems.

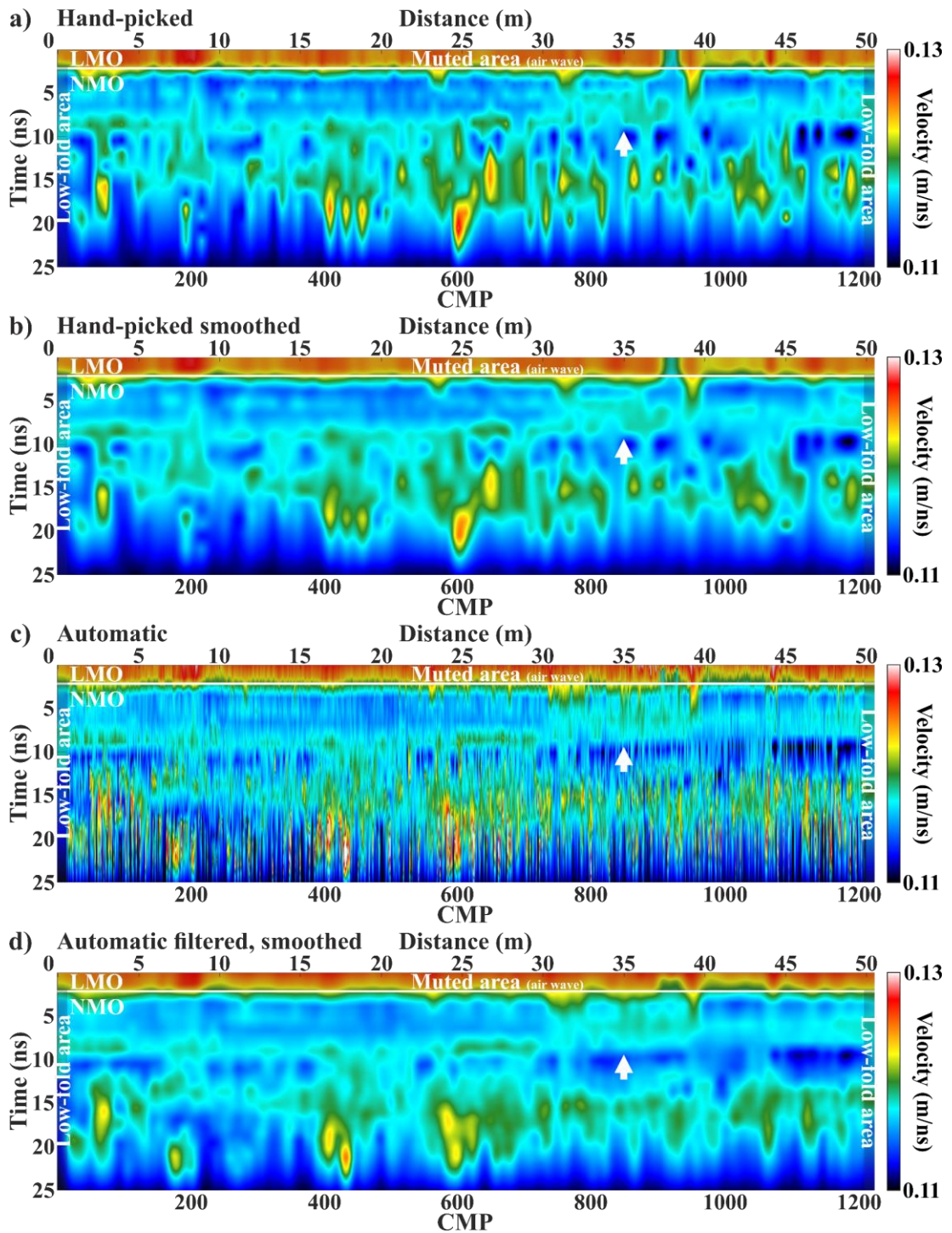


Figure 6.12: 1000 MHz centre frequency field data set. a) Interpolated stacking velocity field derived from manual hand-picked combined LMO NMO velocity analysis on every 12 CMP gathers, i.e., every 0.495 m. b) Smoothed stacking velocity field of (a). c) Stacking velocity field derived from automated combined LMO NMO velocity analysis on all high-fold CMP gathers. d) Filtered and smoothed stacking velocity field of (c). The white arrows indicate an area (35 – 50 m and 8 – 12 ns) in which the automated velocity field outperforms the manual hand-picked one and captures much better the layer boundary. The low-fold areas, as well as the muted area of the direct air wave, are also highlighted in each sub-figure.

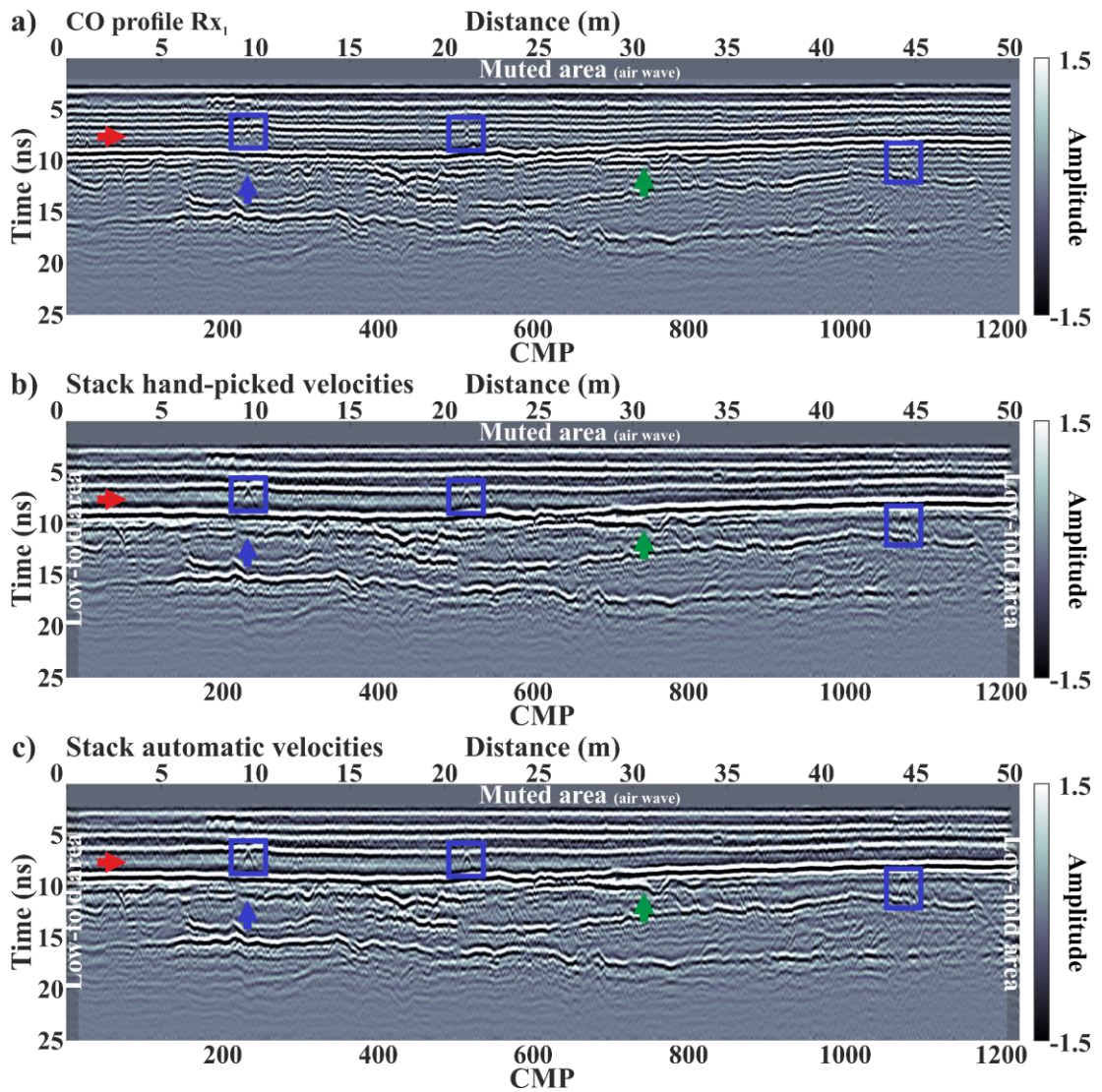


Figure 6.13: 1000 MHz centre frequency field data set. a) Processed CO profile of the first receiver ( $T_x - R_{x_1} = 0.165$  m). b) Stacked section, derived using the smoothed velocity field obtained via manual hand-picked velocity analysis shown in Figure 6.12b. c) Stacked section, derived using the filtered/smoothed velocity field obtained via automated velocity analysis shown in Figure 6.12d. In (a) – (c) the red arrow highlights an area with a reduced ringing noise, the green arrow marks a reflector with improved continuity, and the blue arrow and blue boxes indicate some enhanced reflectors. The low-fold areas, as well as the muted area of the direct air wave, are also highlighted in each sub-figure.

# 7

## **The effect of multi-concurrent receiver arrangement on velocity analysis**

This chapter focuses on the investigation of the effect of receiver arrangement of multi-concurrent receiver GPR systems on velocity spectrum analysis and is divided into two different sections. The first section examines the impact of reducing the number of receivers whilst the second section the impact of increasing the number of receivers.

Research in this chapter has been published in Angelis et al. (2022b).

## 7.1 Decrease in the number of receivers

Unlike traditional single-channel GPR systems that utilise two transducers, newly developed multi-channel GPR systems with multiple concurrent data acquisition receivers require a large number of transducers to operate. For instance, Sensors & Software Inc. “WARR Machine” GPR in its standard configuration uses eight transducers, namely one transmitter and seven multi-concurrent sampling receivers. Understandably, however, this large number of additional transducers significantly increases the overall size, weight, and power requirements of these systems, which, in turn, impacts their portability as well as manoeuvrability, and consequently the field environments and conditions under which they can be deployed. Obviously, it also affects their purchase and maintenance costs, which, as expected, can be much higher than those of a simple single-channel GPR.

Therefore, for the above reasons, the feasibility of reducing the number of receivers, whilst maintaining acceptable velocity spectra resolution, and thus, obtaining detailed stacking velocity fields and enhanced zero-offset stacked reflection time sections, was investigated. Due to COVID-19 restrictions, this research work was primarily focused on the investigation of Tx-Rx positions/spacings that were physically possible with the hardware/field data available (see Ch. 4.2). That is, the fixed positions available for the transducers on the cart/sledge of the “WARR Machine”, which were the multiples of the manufacturer's original spacing for one Tx and seven Rx's, as shown in Figure 7.1.

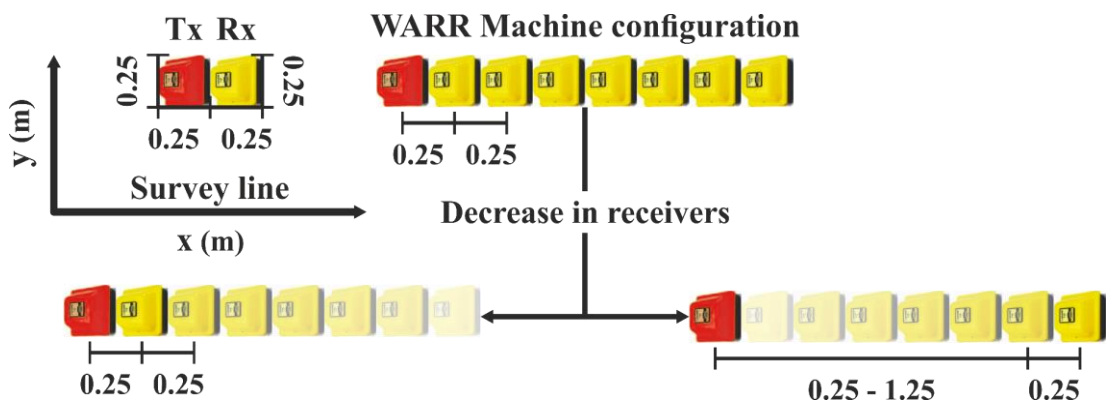


Figure 7.1: Initial plan for decreasing the number of receivers.

### 7.1.1 Synthetic data example

To adequately evaluate and compare different transducer configurations with reduced receivers via synthetic data, a layered cake modelling scenario was considered. This scenario was chosen primarily to visualise/illustrate the changes in velocity spectra peaks (i.e., changes in shape and/or strength) across different velocities and multiple time intervals (i.e., from shallow to deep events of varying velocities). The model used, which is also shown in Figure 7.2a, is a 3D six-layered model in which the velocity decreases with depth whilst also varying laterally. Each layer is inhomogeneous and composed of heterogeneous soil consisting of 50 different dispersive materials all stochastically mixed together using the soil mixing approach proposed by Peplinski et al. (1995), thus providing the aforementioned lateral velocity variations. The model has a size equal to 5 x 1 x 2.2 m (x, y, and z axes, respectively), a spatial discretisation of  $\Delta x = \Delta y = \Delta z = 0.005$  m, and therefore a time step of  $\Delta t = \sim 9.63$  ps (CLF condition (4.5)), as well as 20 PML cells on each of its sides.

A single Hertzian dipole source fed with a 500 MHz centre frequency waveform shaped as the first derivative of a Gaussian and an amplitude of 1 was used to represent the transmitter antenna, along with seven receiver points to represent the receiver antennas. The source and receiver points were all positioned according to the geometry of the 500 MHz centre frequency “WARR Machine” GPR, i.e., placed sequentially and separated by 0.25 m (see Figure 4.5b), and were all moved simultaneously using the WARR mode of operation along the surface of the model with a spatial trace step equal to 0.025 m (i.e.,  $Tx - Rx_1 / 10$ ). Finally, the analysis steps were set to  $\geq 31$  to allow the creation of maximum-fold, i.e., seven-fold, CMP gathers, whilst the time window was set to 60 ns, yielding a total of 5089 time samples. The synthetic data produced were then processed (see processing steps in Figure 6.1) and contaminated in post-processing with random white Gaussian noise proportional to the receiver offset. The latter was done to represent real data more closely, which can have noisy far-offset traces (see also Ch. 4.2.1 – Figure 4.7), and to simulate a strong SNR versus receiver offset reduction. Consequently, this would allow visualising the changes in semblance for the different transducer configurations, particularly in scenarios with noisy and/or corrupted far-offset traces.

Figure 7.2b shows a synthetic CMP gather consisting of seven traces each generated by one of the seven receiver points used in the simulation, with five clear hyperbolic events corresponding, of course, to the boundaries of the six layers of the model. The resultant semblance plot of the gather is also shown in the same figure. This is the baseline/reference model which was created to represent the Tx – Rx transducer geometry of the real seven-receiver multi-concurrent receiver GPR system. There are five distinct and sharp peaks of medium to high strength (i.e., orange to red coloured peaks – Figure 7.2b) in the semblance plot that correspond to the five different hyperbolic events of the gather. Subsequently, the traces of the CMP gather were gradually, one by one, removed, to simulate reducing the number of receivers, and the corresponding semblance plots were computed in order to compare with the aforementioned baseline model. At first, the far-offset traces were removed (Figure 7.3) and then the near-offset traces (Figure 7.4).

Figure 7.3 demonstrate the near-offset receiver configuration scenarios, i.e., the removal of the far-offset receivers/traces, and depicts the computed semblance plots from all seven traces (baseline model – Figure 7.3a) to the three near-offset traces (Figure 7.3e). By examining the figure(s), three observations can be made:

- The first observation is that as the number of far-offset traces decreases, the semblance plot becomes slightly noisier, as fewer traces are used for its computation.
- The second observation is that as the far-offset traces are removed the semblance peaks increase significantly in strength (i.e., red to white coloured peaks – Figure 7.3b to Figure 7.3e), as the higher-SNR near-offset traces are used for the computation.
- The third and final observation is that as the far-offset traces are removed, the sharpness of the semblance peaks decreases noticeably, as the spread length is reduced, and therefore some of the moveout information is lost. This loss of sharpness, which is essentially a loss of velocity resolution, could, in general, affect the ability to differentiate different peaks but, most importantly, could lead to inaccurate velocity estimates during the picking process, especially if done manually.

Figure 7.4 demonstrate the far-offset receiver configuration scenarios, i.e., the removal of the near-offset receivers/traces, and depicts the calculated semblance plots from all

seven traces (baseline model – Figure 7.4a) to the three far-offset traces (Figure 7.4e). As in the previous case, three observations can be made by examining the figure(s):

- The first observation is that as the number of near-offset traces decreases, the semblance plot becomes noisier because fewer traces are involved in its computation. Notice, however, that the semblance plots in Figure 7.4 are noisier than the respective ones in Figure 7.3 since they are computed from the far-offset and hence low-SNR traces instead of the near-offset high-SNR traces.
- The second observation is that as the near-offset traces are removed the semblance peaks reduce in strength (i.e., yellow to orange coloured peaks – Figure 7.4b to Figure 7.4e), as the lower-SNR far-offset traces are used for the computation.
- The third and final observation is that the sharpness of the semblance peaks decreases as the near-offset traces are removed. This is due to the loss of some moveout information, as well as the far-offset traces generally having higher percentages of NMO stretch (see NMO stretch – Ch. 3.2). Notice, however, that the loss in sharpness seen in the semblance peaks in Figure 7.4 is not so severe as the one seen in the respective semblance plots in Figure 7.3. This is mainly because most of the moveout information is retrieved from the far-offset traces.

The above findings highlight the significance of both near-offset and far-offset traces for computing velocity spectrum semblance panels for low-fold GPR data, which is similar to the one for seismic reflection data, as described by Yilmaz (2001):

“Adequate resolution in the velocity spectrum can only be obtained with a sufficiently large spread that spans both near and far offsets.”

Therefore, since the objective was to reduce the number of traces from the CMP gather, i.e., essentially the number of receivers from the GPR system, whilst preserving as much as possible velocity resolution of semblance, i.e., the sharpness as well as strength of the peaks, a sparse receiver configuration was considered.

Figure 7.5 demonstrate the sparse receiver configuration scenarios, i.e., the removal of the intermediate receivers/traces and depicts the computed semblance plots from all seven traces (baseline model – Figure 7.5a), the four intermediate traces (Figure 7.5b),

and the three intermediate traces (Figure 7.5c). By examining the figure(s), yet again three observations can be made:

- The first observation is that as the number of intermediate traces decreases, the semblance plot becomes noisier since fewer traces are used for its computation. Notice, however, that the semblance plots in Figure 7.5 are noisier than those in Figure 7.3 but also slightly less noisy than those in Figure 7.4. This is because they are computed using both high-SNR and low-SNR traces rather than just only high-SNR or low-SNR traces.
- The second observation is that despite the removal of the intermediate traces the strength of the semblance peaks remains almost the same (i.e., orange to red coloured peaks – Figure 7.5a to Figure 7.5c).
- The third and final observation, which is actually the most important one, is that the sharpness of the semblance peaks is maintained very well despite the removal of the intermediate traces. This essentially means that velocity resolution, and hence velocity information is well preserved.

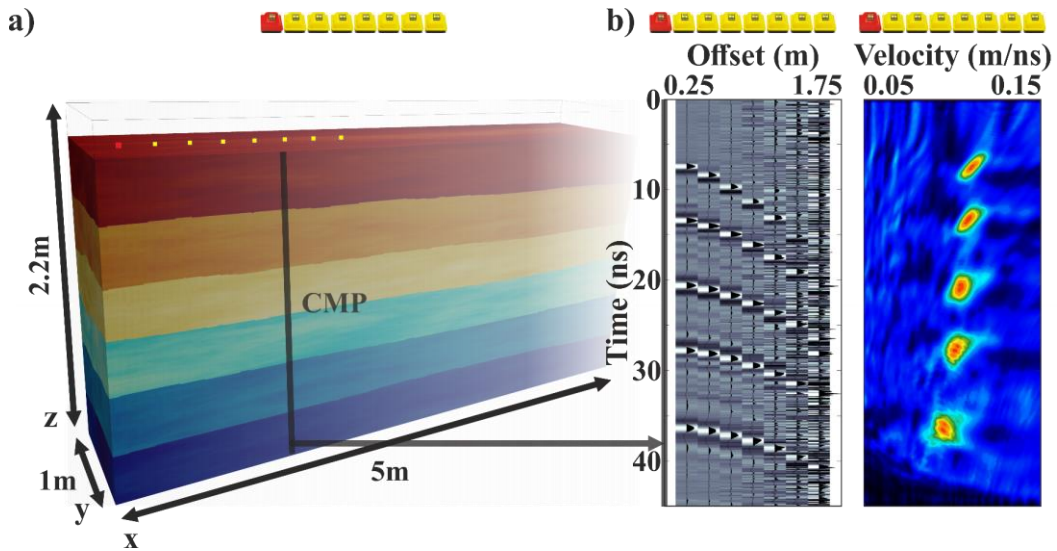


Figure 7.2: a) 3D six-layered model, with both vertical and lateral velocity variations, developed to generate synthetic data for demonstrating the effect of reducing the number of receivers on velocity spectrum semblance analysis. b) 7Rx synthetic data CMP gather contaminated with white Gaussian noise and resultant semblance plot of the CMP gather. The transducer configuration is shown at the top of each sub-figure, with the Tx in red and the Rx's in yellow.

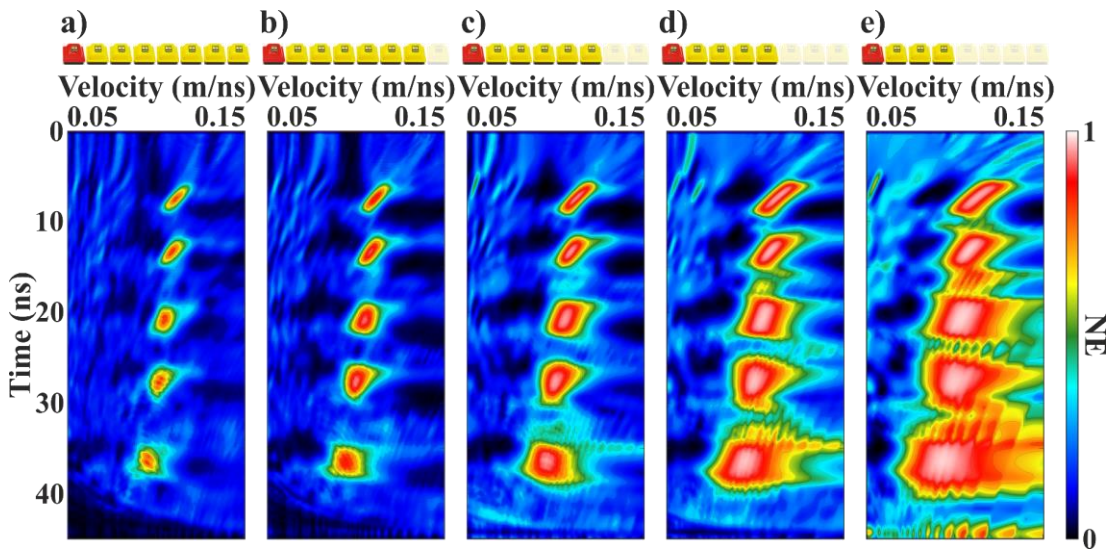


Figure 7.3: Near-offset receiver configuration scenarios/lack of far-offset receivers scenarios, using synthetic data CMP gather of Figure 7.2b. a) 7Rx semblance plot,  $Tx - Rx_1 = 0.25$  m,  $Tx - Rx_7 = 1.75$  m, Rx separation = 0.25 m. b) 6Rx semblance plot,  $Tx - Rx_1 = 0.25$  m,  $Tx - Rx_6 = 1.50$  m, Rx separation = 0.25 m. c) 5Rx semblance plot,  $Tx - Rx_1 = 0.25$  m,  $Tx - Rx_5 = 1.25$  m, Rx separation = 0.25 m. d) 4Rx semblance plot,  $Tx - Rx_1 = 0.25$  m,  $Tx - Rx_4 = 1.00$  m, Rx separation = 0.25 m. e) 3Rx semblance plot,  $Tx - Rx_1 = 0.25$  m,  $Tx - Rx_3 = 0.75$  m, Rx separation = 0.25 m. The transducer configuration is shown at the top of each sub-figure, with the Tx in red and the Rx's in yellow.

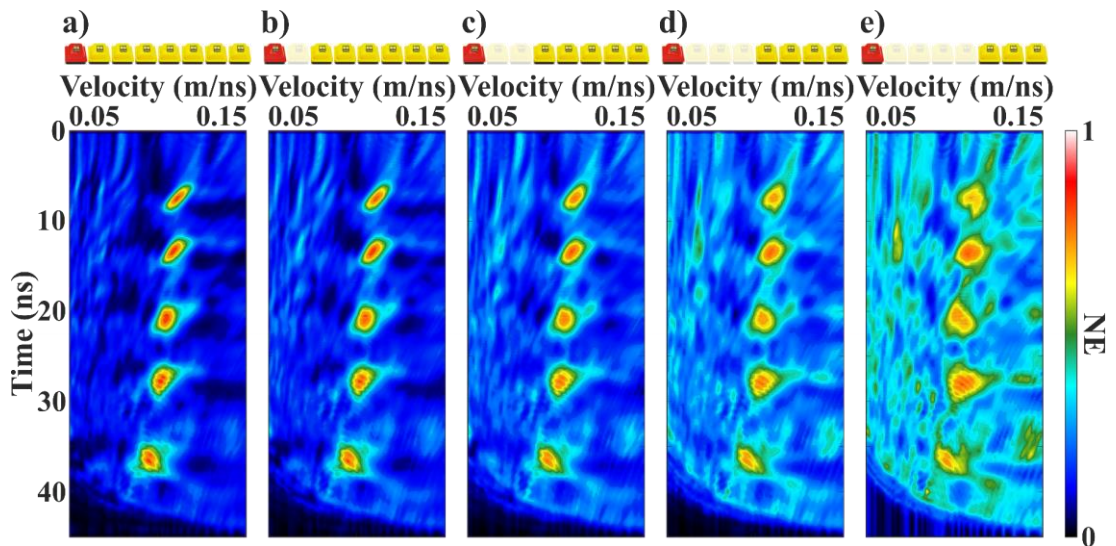


Figure 7.4: Far-offset receiver configuration scenarios/lack of near-offset receivers scenarios, using synthetic data CMP gather of Figure 7.2b. a) 7Rx semblance plot, Tx - Rx<sub>1</sub> = 0.25 m, Tx - Rx<sub>7</sub> = 1.75 m, Rx separation = 0.25 m. b) 6Rx semblance plot, Tx - Rx<sub>1</sub> = 0.50 m, Tx - Rx<sub>6</sub> = 1.75 m, Rx separation = 0.25 m. c) 5Rx semblance plot, Tx - Rx<sub>1</sub> = 0.75 m, Tx - Rx<sub>5</sub> = 1.75 m, Rx separation = 0.25 m. d) 4Rx semblance plot, Tx - Rx<sub>1</sub> = 1.00 m, Tx - Rx<sub>4</sub> = 1.75 m, Rx separation = 0.25 m. e) 3Rx semblance plot, Tx - Rx<sub>1</sub> = 1.25 m, Tx - Rx<sub>3</sub> = 1.75 m, Rx separation = 0.25 m. The transducer configuration is shown at the top of each sub-figure, with the Tx in red and the Rx's in yellow.

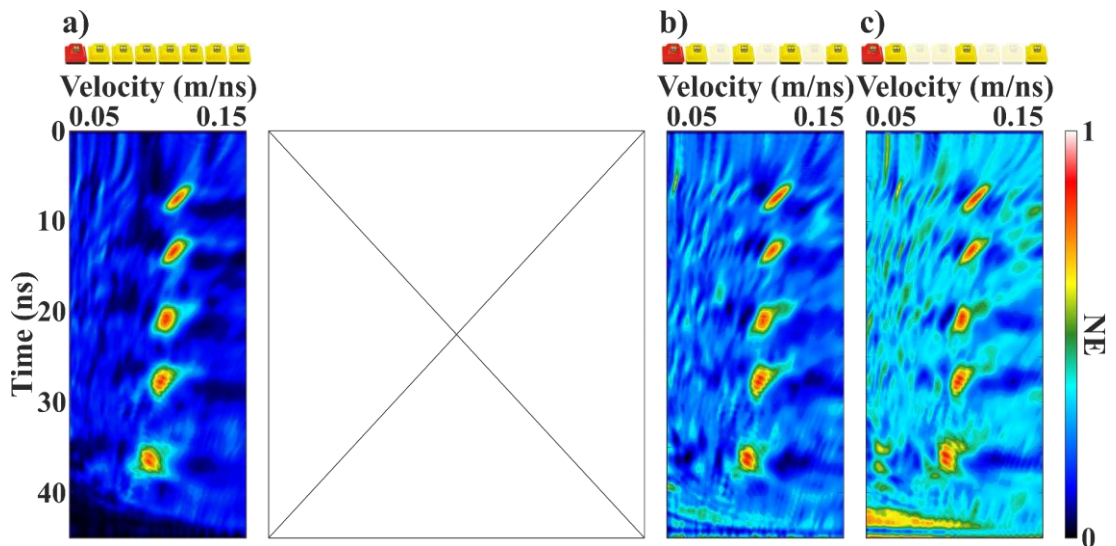


Figure 7.5: Sparse receiver configuration scenarios/lack of intermediate receivers scenarios, using synthetic data CMP gather of Figure 7.2b. a) 7Rx semblance plot, Tx - Rx<sub>1</sub> = 0.25 m, Tx - Rx<sub>7</sub> = 1.75 m, Rx separation = 0.25 m. b) 4Rx semblance plot, Tx - Rx<sub>1</sub> = 0.25 m, Tx - Rx<sub>4</sub> = 1.75 m, Rx separation = 0.5 m. c) 3Rx semblance plot, Tx - Rx<sub>1</sub> = 0.25 m, Tx - Rx<sub>3</sub> = 1.75 m, Rx separation = 1.00 m. The transducer configuration is shown at the top of each sub-figure, with the Tx in red and the Rx's in yellow.

## 7.1.2 Field data example

### Velocity spectra

The exact same analysis was carried out using a real field multi-concurrent receiver GPR data set, which was acquired by Sensors & Software Inc. from one of their test lines. The line passes through an asphalt-covered parking lot, a 1.3 m wide concrete sidewalk, a 5 m asphalt driveway, and a concrete curb, and terminates after crossing a city street (Diamanti et al., 2018). Data were collected with the “WARR Machine” GPR using the so-called SmartCart transducer configuration with 500 MHz centre frequency transducers all placed sequentially and separated by 0.25 m (see Figure 4.5b). Measurements were performed at a normal walking speed using 16 vertical stacks per trace per receiver and with a spatial trace step equal to 0.125 m (i.e.,  $T_x - R_{x_1} / 2$ ) to allow direct CMP sorting without the need for spatial resampling. Finally, the time window was set to 80 ns, whereas the sampling interval to 0.2 ns, thus resulting in a total of 400 time samples. Using the aforementioned system/survey parameters, for a ~ 40 m long transect, seven CO profiles, equivalent to 331 WARRs and/or 337 CMPs, were acquired simultaneously in less than two minutes (Diamanti et al., 2018).

This data set was selected for this analysis mainly for the following reasons:

- It has been collected from a standard test line of Sensors & Software Inc., and consequently, there is a large amount of representative reference data.
- It features a variety of complex as well as shallow reflections, thus making it very interesting for velocity analysis and potentially for horizontal stacking.
- It has previously been used unsuccessfully in the studies of Annan & Jackson (2017) and Diamanti et al. (2018) (see also Ch. 3.3.1) to demonstrate velocity analysis and horizontal stacking, therefore making it particularly interesting for demonstrating/testing the aforementioned utilising the processing tools and processing methods presented in this thesis.

The quality of the field data can be seen in Figure 7.6a which illustrates the processed (see Figure 6.1 for processing steps) CO profile of the first receiver accompanied by different annotations for the various subsurface features (white arrows in Figure 7.6a).

Figure 7.6b shows CMP gather 272 of the processed field data, which consists of seven traces, each collected by one of the seven receivers of the “WARR Machine”, and contains three primary hyperbolic events that correspond to the three events also seen in the CO profile (see black line in Figure 7.6a). This gather was chosen, as it is generally complex and has particularly shallow reflections. The resultant semblance plot of the gather is also shown in Figure 7.6b. This is the baseline model that represents the standard Tx – Rx transducer geometry (i.e., seven-receiver geometry) of the “WARR Machine”. There are three distinct and relatively sharp peaks of high strength (i.e., red coloured peaks – Figure 7.6b) in the semblance plot that correspond to the three different hyperbolic events shown in the gather.

Similarly, to the synthetic data example(s) above (see Ch. 7.1.1), the traces of the CMP gather were gradually one by one removed, thus simulating reducing the number of receivers, and the corresponding semblance plots were computed. Figure 7.7 demonstrate the near-offset receiver configuration scenarios, Figure 7.8 the far-offset receiver configuration scenarios, and finally Figure 7.9 the sparse receiver configuration scenarios. By examining these figures as well as comparing them with the respective ones produced by the synthetic data above (i.e., Figure 7.3, Figure 7.4, and Figure 7.5), the following observations can be made:

- The first observation is that in addition to the three distinct peaks shown in the seven-traces baseline semblance plot, there are also multiple spurious peaks of medium to high strength in all the other semblance plots of Figure 7.7, Figure 7.8, and Figure 7.9 (some of these additional peaks are marked with white arrows). This is because in real field data not all noise and/or clutter is random, such as the Gaussian noise added to the synthetic data above, and therefore becomes more easily consistent in the gather as the number of traces decreases, generating spurious peaks. Whilst such peaks are generally easily identified and bypassed by an interpreter during manual hand-picked velocity analysis, they will most certainly become detrimental during an automated analysis process, especially if there are many. The latter however also raises the question as to whether an automated velocity analysis from data acquired from a reduced receiver configuration is even possible, and if so, at what cost.

- The second and most important observation is that the sharpness and the strength of the three semblance peaks are very well maintained in the sparse receiver configurations, (i.e., the same behaviour is observed as in the synthetic data example), whereas this is not the case in the near-offset and far-offset receiver configurations. Note, however, that when comparing the resultant semblance plot of the four-receiver sparse configuration with that of the three-receiver sparse configuration, a significant increase in spurious semblance peaks is observed in the latter. This increase in spurious peaks, which as previously mentioned can be particularly detrimental during automated analysis, was observed in hundreds of semblance plots from a range of different data sets that were investigated in this thesis. This indicates that the four-receiver sparse configuration is potentially the minimum acceptable limit for most environments.

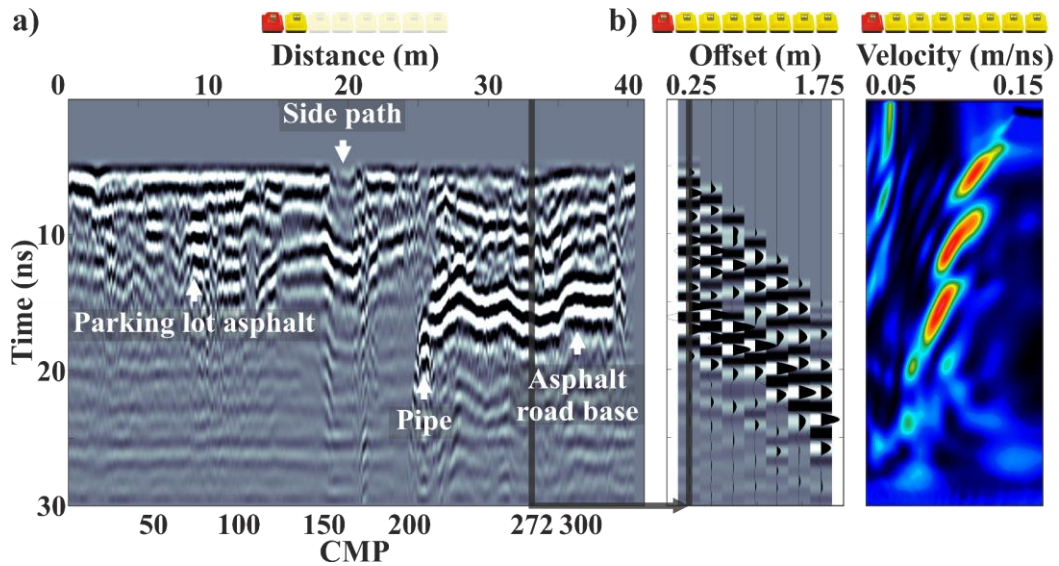


Figure 7.6: a) Processed CO profile of the first/near-offset receiver ( $Tx - Rx_1 = 0.25$  m). The white arrows indicate some of the subsurface features, and the black line indicates the location of the investigated CMP gather (CMP 272). b) 7Rx field data CMP gather 272 and resultant semblance plot of the CMP gather. The transducer configuration is shown at the top of each sub-figure, with the Tx in red and the Rx's in yellow.

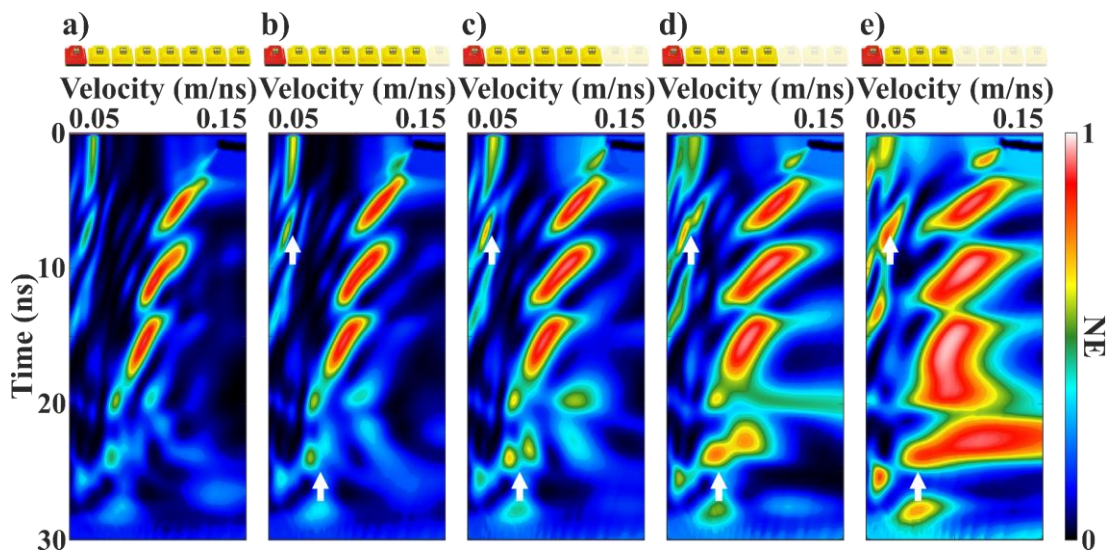


Figure 7.7: Near-offset receiver configuration scenarios/lack of far-offset receivers scenarios, using field data CMP gather 272 of Figure 7.6b. a) 7Rx semblance plot,  $Tx - Rx_1 = 0.25$  m,  $Tx - Rx_7 = 1.75$  m, Rx separation = 0.25 m. b) 6Rx semblance plot,  $Tx - Rx_1 = 0.25$  m,  $Tx - Rx_6 = 1.50$  m, Rx separation = 0.25 m. c) 5Rx semblance plot,  $Tx - Rx_1 = 0.25$  m,  $Tx - Rx_5 = 1.25$  m, Rx separation = 0.25 m. d) 4Rx semblance plot,  $Tx - Rx_1 = 0.25$  m,  $Tx - Rx_4 = 1.00$  m, Rx separation = 0.25 m. e) 3Rx semblance plot,  $Tx - Rx_1 = 0.25$  m,  $Tx - Rx_3 = 0.75$  m, Rx separation = 0.25 m. The white arrows mark some of the spurious semblance peaks. The transducer configuration is shown at the top of each sub-figure, with the Tx in red and the Rx's in yellow.

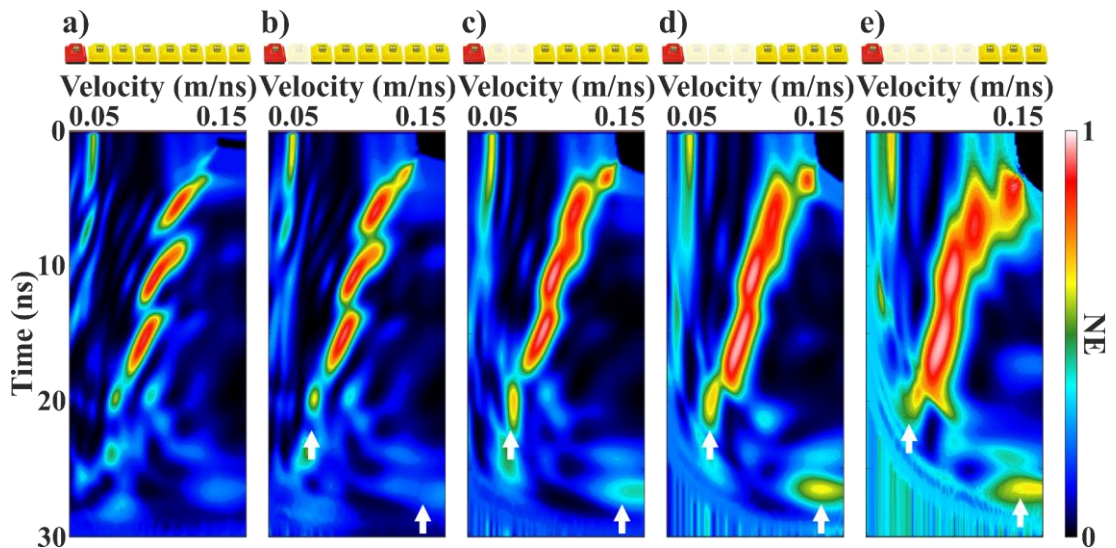


Figure 7.8: Far-offset receiver configuration scenarios/lack of near-offset receivers scenarios, using synthetic data CMP gather 272 of Figure 7.6b. a) 7Rx semblance plot,  $T_x - R_{x_1} = 0.25$  m,  $T_x - R_{x_7} = 1.75$  m, Rx separation = 0.25 m. b) 6Rx semblance plot,  $T_x - R_{x_1} = 0.50$  m,  $T_x - R_{x_6} = 1.75$  m, Rx separation = 0.25 m. c) 5Rx semblance plot,  $T_x - R_{x_1} = 0.75$  m,  $T_x - R_{x_5} = 1.75$  m, Rx separation = 0.25 m. d) 4Rx semblance plot,  $T_x - R_{x_1} = 1.00$  m,  $T_x - R_{x_4} = 1.75$  m, Rx separation = 0.25 m. e) 3Rx semblance plot,  $T_x - R_{x_1} = 1.25$  m,  $T_x - R_{x_3} = 1.75$  m, Rx separation = 0.25 m. The white arrows mark some of the spurious semblance peaks. The transducer configuration is shown at the top of each sub-figure, with the Tx in red and the Rx's in yellow.

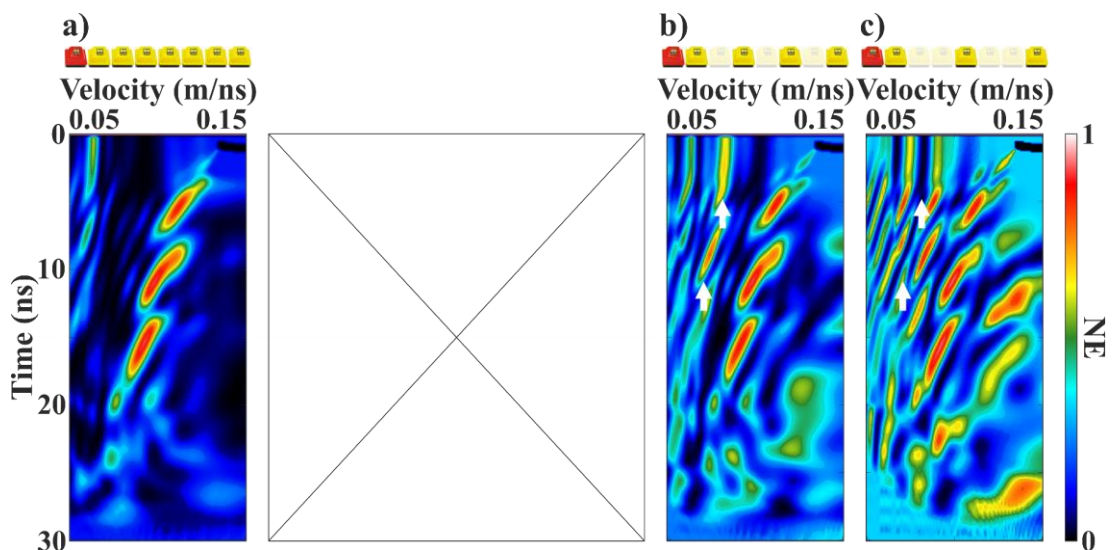


Figure 7.9: Sparse receiver configuration scenarios/lack of intermediate receivers scenarios, using synthetic data CMP gather 272 of Figure 7.6b. a) 7Rx semblance plot,  $T_x - R_{x_1} = 0.25$  m,  $T_x - R_{x_7} = 1.75$  m, Rx separation = 0.25 m. b) 4Rx semblance plot,  $T_x - R_{x_1} = 0.25$  m,  $T_x - R_{x_4} = 1.75$  m, Rx separation = 0.5 m. c) 3Rx semblance plot,  $T_x - R_{x_1} = 0.25$  m,  $T_x - R_{x_3} = 1.75$  m, Rx separation = 1.00 m. The white arrows mark some of the spurious semblance peaks. The transducer configuration is shown at the top of each sub-figure, with the Tx in red and the Rx's in yellow.

### Velocity field and stacked section

To answer the question of whether it is possible to automatically obtain a detailed stacking velocity field from a sparse four-receiver configuration, the corresponding data were subjected to automated semblance analysis. In addition, the respective data from the standard seven-receiver configuration were also analysed in the same way to provide a reference point, and therefore to enable a clear comparison between the two different transducer configurations. Although velocity analysis is generally performed on selected CMP gathers typically of high-SNR, it was conducted on all high-fold gathers in this case (i.e., four-fold and seven-fold gathers, respectively). This decision was made mainly because this data set contains multiple events, many of which are almost horizontal, across the entire survey line, as shown in the CO section of the first receiver (Figure 7.10a). Hence, making it a particularly interesting data set for comparing the results of the two configurations in as many different locations/CMP gathers/semblance plots as possible.

Figure 7.10b and Figure 7.10c illustrate the resultant stacking velocity fields of the standard seven-receiver configuration and the sparse four-receiver configuration, respectively. Both fields have been processed with light alpha-trimmed mean filtering, every 0.625 m (i.e., every fifth 1D velocity function) as well as 2D Gaussian smoothing using a square kernel with an STD equal [2, 2]. The processing was performed in order to eliminate potential velocity outliers and thus create more accurate velocity fields that could also be used for horizontal stacking if desired.

By comparing the two figures (Figure 7.10b and Figure 7.10c), it is clear that both velocity fields are in good agreement, as, with only a few exceptions, almost all the areas of low- and high-velocity are well correlated. One such exception is a small area located at ~ 25 m along the distance axis and ~18 ns along the time axis, which is highlighted in the figures with white arrows. The medium stacking velocities that are observed only in the resultant velocity field of the seven-receiver configuration (green to yellow colours – white arrow in Figure 7.10b) come from the left-hand side diffraction tail of the hyperbola (white arrow in Figure 7.10a) which is generated by a subsurface pipe located in the area. Although the same velocities are not observed in the resultant velocity field of the sparse four-receiver configuration, it should be noted

that both of these fields were derived from automated velocity analysis. This means that errors like this one could potentially be corrected afterwards via a manual re-picking, which is generally standard practice anyway.

To validate the above velocity fields (Figure 7.10b and Figure 7.10c), each one was used to NMO correct the CMP gathers of the corresponding transducer configurations, which were then stacked to create two zero-offset stacked cross-sections. Figure 7.10d and Figure 7.10e show the resultant stacked sections of the standard seven-receiver configuration and the sparse four-receiver configuration, respectively. The CO section of the first receiver is also shown in Figure 7.10a for comparison. Moreover, each trace of each section has been normalised with its corresponding RMS value in order to facilitate comparison between all the traces of all the aforementioned sections.

Unsurprisingly, since it has been also demonstrated with both synthetic and field data examples in chapter 6, when comparing the resultant stacked section of the standard seven-receiver configuration (Figure 7.10d) with the CO section of the first receiver (Figure 7.10a) all the expected benefits of the horizontal stacking procedure are observed. For instance, there is a decrease in both high-frequency noise and horizontal ringing noise. The latter is shown very well in the area indicated with a red arrow. There is also better reflector continuity, as shown in the area/reflector marked with a green arrow, as well as a major improvement of other reflectors, as seen in the area/reflector highlighted with a blue arrow.

Interestingly though, when comparing the resultant stacked section of the sparse four-receiver configuration (Figure 7.10e) with the CO section of the first receiver (Figure 7.10a) similar improvements are observed. Nevertheless, it should be noted that these improvements are obviously not as significant as in the case of the seven-receiver configuration, which is something expected, since, as the number of receivers is reduced so does the stacking fold (i.e., from seven to four).

These findings validate both stacking velocity fields and as a result, demonstrate for the first time that even four traces collected from four multi-concurrent sampling receivers in a sparse configuration are sufficient to provide not only detailed stacking velocity fields but also enhanced zero-offset reflection time sections.

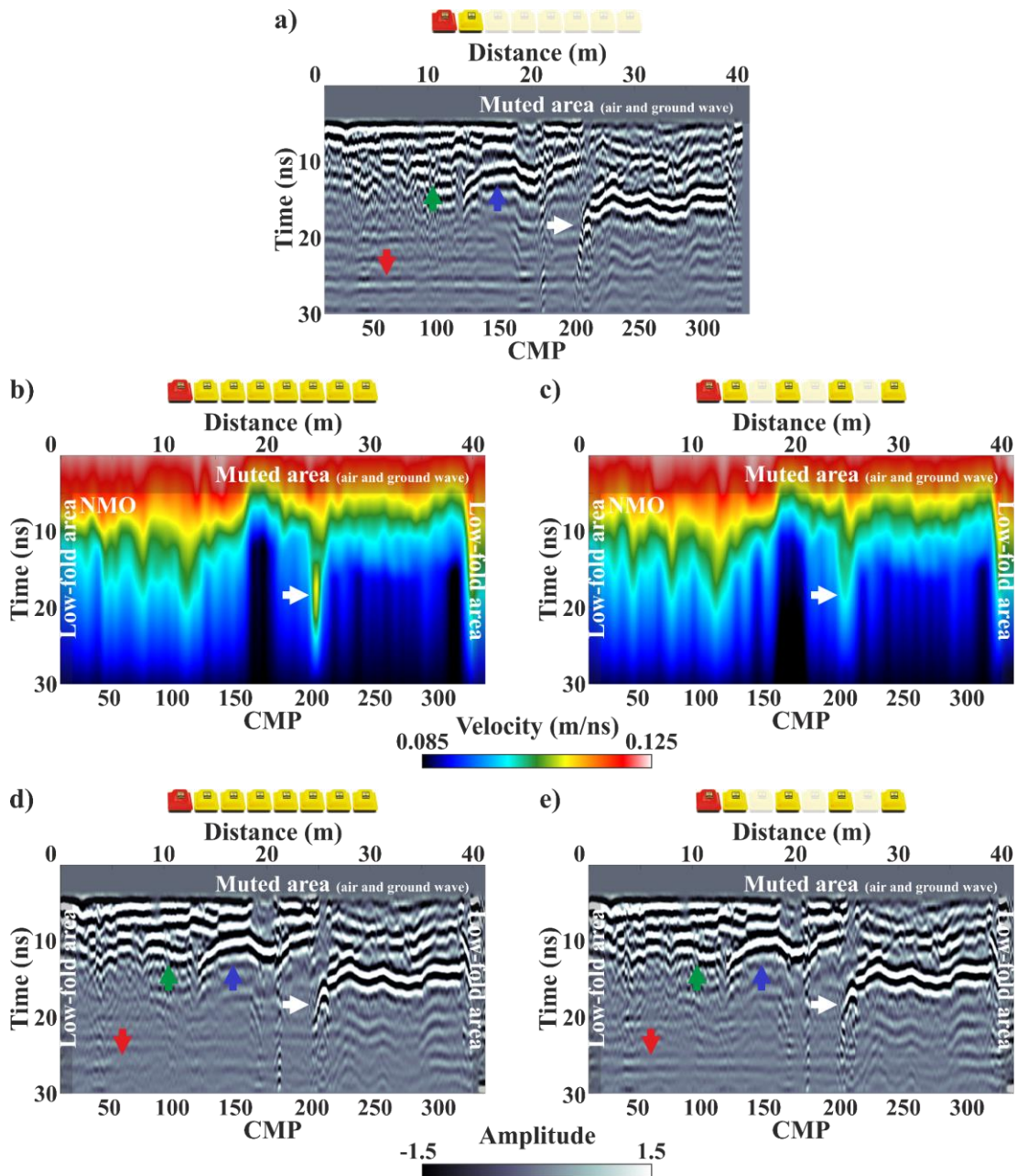


Figure 7.10: 500 MHz centre frequency field data set. a) Processed CO profile of the first receiver ( $Tx - Rx_1 = 0.25$  m). b) Filtered/smoothed stacking velocity field of the seven-receiver configuration derived from automated NMO velocity analysis on all high-fold/seven-fold CMP gathers. c) Filtered/smoothed stacking velocity field of the four-receiver sparse configuration derived from automated NMO velocity analysis on all high-fold/four-fold CMP gathers. d) Seven-fold stacked section obtained using the respective velocity field of (b). e) Four-fold stacked section obtained using the corresponding velocity field of (c). In (a), (d), and (e) the red arrow highlights an area with reduced horizontal ringing noise, the green arrow marks a reflector with improved continuity, and the blue arrow indicates an enhanced reflector. In (b) and (c) the white arrow indicates an area with different stacking velocities, whilst in (a), (d), and (e) the left-hand side of the hyperbola/pipe response. The transducer configuration is shown at the top of each sub-figure, with the Tx in red and the Rx's in yellow. The low-fold areas, as well as the muted area of the direct air wave and direct ground wave, are also highlighted in each sub-figure.

To further validate the above findings, the same analysis was also performed with additional data sets collected from different environments and with different multi-concurrent sampling receiver GPR systems. Figure 7.11 and Figure 7.12 depict two of these extra data sets and their corresponding results, i.e., stacking velocity fields and stacked zero-offset sections, for each transducer configuration (i.e., standard seven-receiver configuration and sparse four-receiver configuration). These data sets have been also presented in the previous chapter of this thesis and more information about them, such as area and target description, system and acquisition parameters used, can be found in Ch. 6.4.1 and Ch. 6.5.1. As observed, despite the differences in environment, GPR system, transducer separation, and operating centre frequency, the results from both data sets confirm that a multi-concurrent sampling receiver GPR system with a four-receiver sparse configuration is capable of providing not only acceptable stacking velocity fields but also enhanced zero-offset reflection time sections.

Nonetheless, obtaining such results from the four-receiver sparse configuration may come, depending on the data set (i.e., depending on the environment from which it was acquired and/or its quality of course), at the cost of an increased processing/analysis time compared to the standard seven-receiver configuration. Therefore, the following should also be stressed:

- Minor time misalignments of a few samples owing to an incorrect time-zero alignment do not have a significant impact on the semblance analysis and horizontal stacking of a seven-fold CMP gather (i.e., seven-receiver configuration), however, they can become harmful with the reduction of the fold in the gather (e.g., four-receiver configuration). Therefore, additional manual first break corrections could also be required.
- As the number of traces decreases in the CMP gather (e.g., four-receiver configuration), the primary hyperbolic events may mix with other non-primary events (e.g., noise and/or clutter responses). Hence, implementing a sliding window type CMP trace balancing method will be more difficult, and thus more experimentation with different lengths of sliding windows could also be required.
- With the reduction of traces in the CMP gather (e.g., four-receiver configuration), there will be multiple spurious semblance peaks as shown in the examples above. Many of these peaks, which are usually of medium to high strength, can be simply

avoided by either tweaking/increasing the threshold (see  $th_s - (5.3)$ ) of the proposed automatic velocity picking algorithm and/or even by muting parts of the velocity spectrum semblance plot. Doing so however means that other, potentially primary, peaks of medium to high strength could also be skipped, as the automated velocity analysis will be based solely on the high strength peaks (e.g., white arrows in Figure 7.10b and Figure 7.10c). Therefore, adjusting the threshold(s) and/or other parameters of the automatic velocity picking algorithm several times in the same data set and/or even performing additional manual velocity re-picking could also be required.

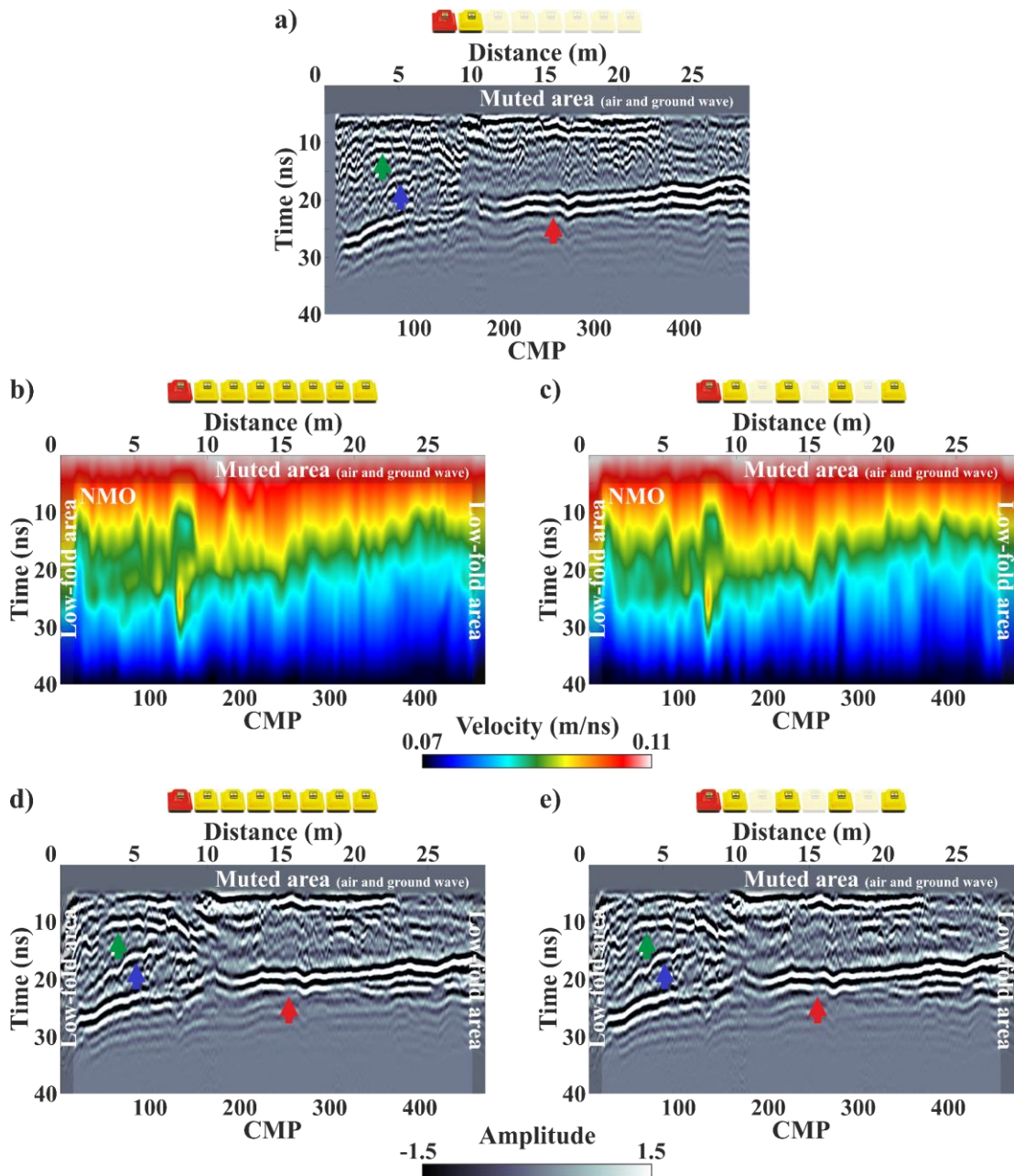


Figure 7.11: 500 MHz centre frequency field data set also previously presented in Ch. 6.4. a) Processed CO profile of the first receiver ( $T_x - R_{x1} = 0.25$  m). b) Filtered/smoothed stacking velocity field of the seven-receiver configuration derived from automated NMO velocity analysis on all high-fold/seven-fold CMP gathers. c) Filtered/smoothed stacking velocity field of the four-receiver sparse configuration derived from automated NMO velocity analysis on all high-fold/four-fold CMP gathers. d) Seven-fold stacked section obtained using the respective velocity field of (b). e) Four-fold stacked section obtained using the corresponding velocity field of (c). In (a), (d), and (e) the red arrow highlights an area with reduced ringing noise, the green arrow marks a reflector with improved continuity, and the blue arrow indicates an enhanced reflector. The transducer configuration is shown at the top of each sub-figure, with the  $T_x$  in red and the  $R_x$ s in yellow. The low-fold areas, as well as the muted area of the direct air wave and direct ground wave, are also highlighted in each sub-figure.

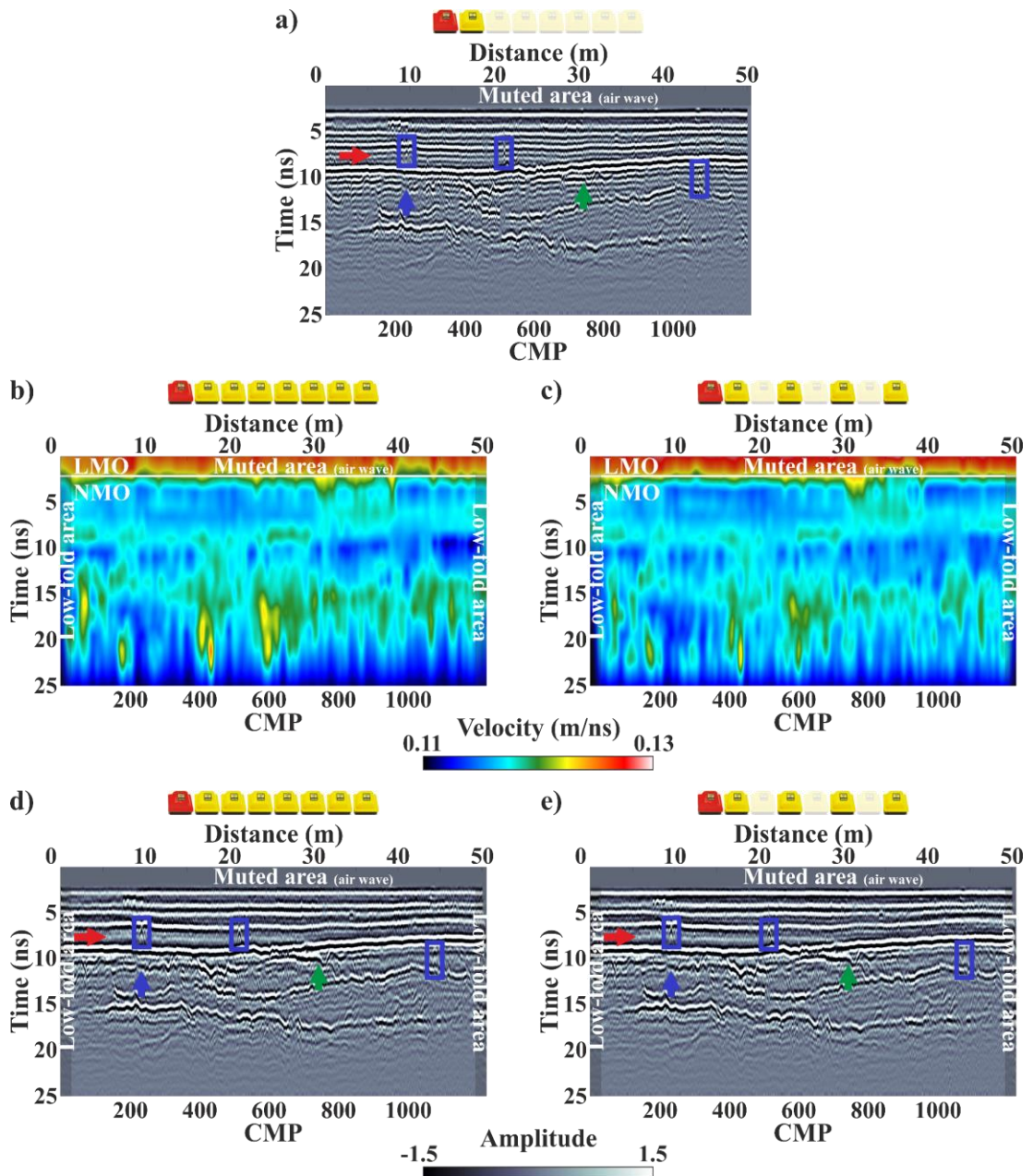


Figure 7.12: 1000 MHz centre frequency field data set also previously presented in Ch. 6.5. a) Processed CO profile of the first receiver ( $Tx - Rx_1 = 0.165$  m). b) Filtered/smoothed stacking velocity field of the seven-receiver configuration derived from automated combined LMO NMO velocity analysis on all high-fold/seven-fold CMP gathers. c) Filtered/smoothed stacking velocity field of the four-receiver sparse configuration derived from automated combined LMO NMO velocity analysis on all high-fold/four-fold CMP gathers. d) Seven-fold stacked section obtained using the respective velocity field of (b). e) Four-fold stacked section obtained using the corresponding velocity field of (c). In (a), (d), and (e) the red arrow highlights an area with reduced ringing noise, the green arrow marks a reflector with improved continuity, and the blue arrow and blue boxes indicate some enhanced reflectors. The transducer configuration is shown at the top of each sub-figure, with the Tx in red and the Rx's in yellow. The low-fold areas, as well as the muted area of the direct air wave, are also highlighted in each sub-figure.

## 7.2 Increase in the number of receivers

Newly developed multi-channel GPR systems with multi-concurrent sampling receivers enable a practically effortless and unprecedented rapid acquisition of multi-offset GPR data. However, the maximum stacking fold that these systems can achieve, which is an important factor since directly affects velocity spectra quality and stacking results, is actually quite small; especially, when compared with the one that can be achieved with a single-channel GPR, albeit much slower and with much more effort, or the one that is typically achieved in seismic utilising dozens or even hundreds of geophones. This is because for these systems the maximum stacking fold is practically dictated by the total number of receivers that they utilise, as they are placed exclusively at fixed positions in the cart or sledge.

Although it is possible to obtain automated stacking velocity fields and enhanced zero-offset stacked sections from a seven-receiver or even a four-receiver GPR system (see Ch. 7.1.2), and although an increase in the number of receivers would further shoot up the cost, size, weight, etc. of the system, which are already high, it was decided to investigate the feasibility of increasing the number of receivers. This decision was made primarily for research purposes since doing so can in theory improve velocity spectra quality and stacking results.

As described in the literature (e.g., Annan & Jackson, 2017; Diamanti et al., 2018) as well as shown in previous chapters (e.g., Ch. 4.2.1 – Figure 4.7), the maximum separation distance is generally very limited in GPR due to the strong AVO attenuation of the signal(s). Consequently, increasing the number of the receivers by simply adding more of them sequentially one after the other would not be particularly beneficial, as the signals reaching the far-offset receivers would likely be attenuated below the noise level. It is reminded that multi-concurrent receiver GPR systems utilise shielded transducers mounted on a cart or sledge, both of which factors obviously affect signal attenuation. Therefore, to increase the number of receivers while maintaining the same WARR mode of operation and maximum offset as that of the standard seven-receiver configuration, and thus acceptable SNRs for the far-offset receivers/traces, a rather unusual out-of-the-box configuration had to be considered.

The considered configuration, which for convenience will hereinafter be referred to as diagonal configuration, is depicted in Figure 7.13. As can be seen, it features fourteen transducers, namely one transmitter and thirteen receivers, all placed diagonally one after the other, as this is the only way to decrease the distance between them. The separation distances, along the survey line axis, between the transmitter and the first receiver as well as between the receivers, are equal to 0.25 m and 0.125 m, respectively, meaning that only spatial trace steps of  $Tx - Rx_1 /$  (multipliers of four) can be used to obtain maximum-fold CMP gathers (i.e., thirteen-fold CMP gathers). These transducer separation distances are used to sort the collected data into CMP gathers (blue coloured lines in Figure 7.13), whilst the actual true separation distances, which are calculated using the Pythagorean theorem, are used for the NMO-based processing steps (red coloured lines in Figure 7.13).

In the following section, the diagonal thirteen-receiver configuration is evaluated and compared with the standard seven-receiver configuration of the “WARR Machine”. The comparison is being done solely with synthetic data due to the various COVID-19 restrictions, and thus, the lack of hardware/field data.

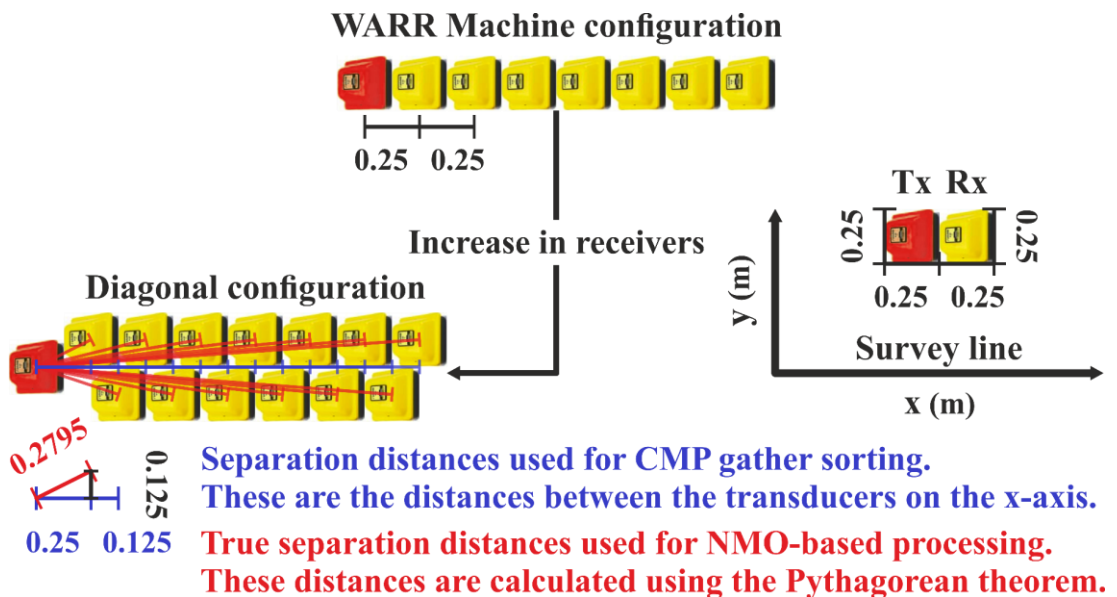


Figure 7.13: Plan for increasing the number of receivers.

### 7.2.1 Synthetic data example

To adequately evaluate and compare the two different transducer configurations, three different modelling scenarios were considered. More specifically, three 3D two-layered models were developed and used, with the second layer being flat in the first model (Figure 7.14a), dipping parallel to the survey line at an angle of 45 degrees in the second model (Figure 7.15a), and dipping perpendicular to the survey line at an angle of 45 degrees in the third model (Figure 7.16a). All of the models have homogeneous layers and the same specifications, i.e., a size equal to 4 x 2 x 2.2 m, a spatial discretisation of  $\Delta x = \Delta y = \Delta z = 0.005$  m, and thus a time step of  $\Delta t = \sim 9.63$  ps (CLF condition (4.5)), as well as 50 PML layers on each side to reduce boundary reflections as much as possible.

For all models, a single Hertzian dipole source, fed with a 500 MHz centre frequency waveform shaped as the first derivative of a Gaussian with an amplitude equal to 1, was used as the transmitter antenna, as were 20 receiver points, as the receiver antennas, i.e., seven receiver points plus another thirteen receiver points, for the two different configurations. The source and the receivers were all separated according to the geometry of the two configurations (see Figure 7.13) and all moved simultaneously using the WARR mode operation along the surface of each model with a spatial trace step of 0.025 m (i.e.,  $T_x - R_{x1} / 10$ ). Finally, the analysis steps were set to  $\geq 31$  to enable the creation of maximum-fold, i.e., seven-fold and thirteen-fold, CMP gathers, whereas the time window was set to 60 ns, resulting in a total of 5089 time samples.

The synthetic data produced were subsequently processed (see processing steps in Figure 6.1) and contaminated in post-processing with random white Gaussian noise to mimic the effects, of low and decreasing SNR with receiver offset, which is commonly observed in real data (see also Ch. 4.2.1 – Figure 4.7). It is also worth noting that the respective generated data of the diagonal configuration were spatially resampled (i.e., trace resampling) to a new spatial trace step equal to 0.03125 m, i.e., equal to  $T_x - R_{x1} / 8$ , as it was necessary in order to achieve the maximum possible fold and therefore to create thirteen-fold CMP gathers.

Starting with the first model (Figure 7.14a), i.e., the flat reflector scenario, Figure 7.14b and Figure 7.14c depict the generated synthetic CMP gathers for each transducer configuration (i.e., the standard seven-receiver configuration and the diagonal thirteen-receiver configuration, respectively), both with a clear hyperbolic event corresponding, of course, to the boundary of the two layers of the model. The computed semblance plots of the gathers are also depicted in the same figures. By examining the figures, two observations can be made. The first observation is that, despite the unconventional diagonal placement of the transducers, nothing particularly unusual is observed in the thirteen-fold CMP gather of the diagonal configuration. The second observation is that the respective semblance plot of the diagonal configuration is of higher quality than the one of the standard configuration (see light blue colours in Figure 7.14b versus dark blue colours in Figure 7.14c around the peak), as more traces are involved in its computation (i.e., thirteen traces versus seven traces).

Moving on to the second model (Figure 7.15a), i.e., the scenario of the dipping reflector parallel to the survey line, Figure 7.15b and Figure 7.15c depict the synthetic CMP gathers of each configuration, both with a clear hyperbolic event that corresponds to the boundary of the two layers of the model. The semblance plots obtained from the gathers are also depicted in the same figures. By looking at the figures, the exact same two observations as in the previous scenario (i.e., flat reflector scenario) can be made.

Finally, moving on to the third model (Figure 7.16a), i.e., the scenario of the dipping reflector perpendicular to the survey line, Figure 7.16b and Figure 7.16c depict the generated synthetic CMP gathers from the two configurations along with their corresponding semblance plots. By examining these figures, the following critical observation can be made. While the boundary of the layers appears as a clear hyperbolic event in the CMP gather of the standard seven-receiver configuration, this is not the case in the gather of the diagonal thirteen-receiver configuration, where the single event appears more like two separate stair-cased events. This is because the traces that compose the gather suffer from time misalignments, as the reflector dips perpendicular to the transducer configuration, thus requiring more time for the reflected signals to reach the right-hand side receivers than the left-hand side ones. Consequently, despite the overall good quality of the semblance plot of the diagonal configuration due to the higher fold, the semblance peak corresponding to the event is very weak.

The above findings, although not validated with field data, highlight the potential drawbacks of a WARR diagonal-like transducer configuration for multi-concurrent receiver GPR systems, as not only can significantly increase, among others, the cost of the system but also it could be proven particularly troublesome in areas with dipping reflectors.

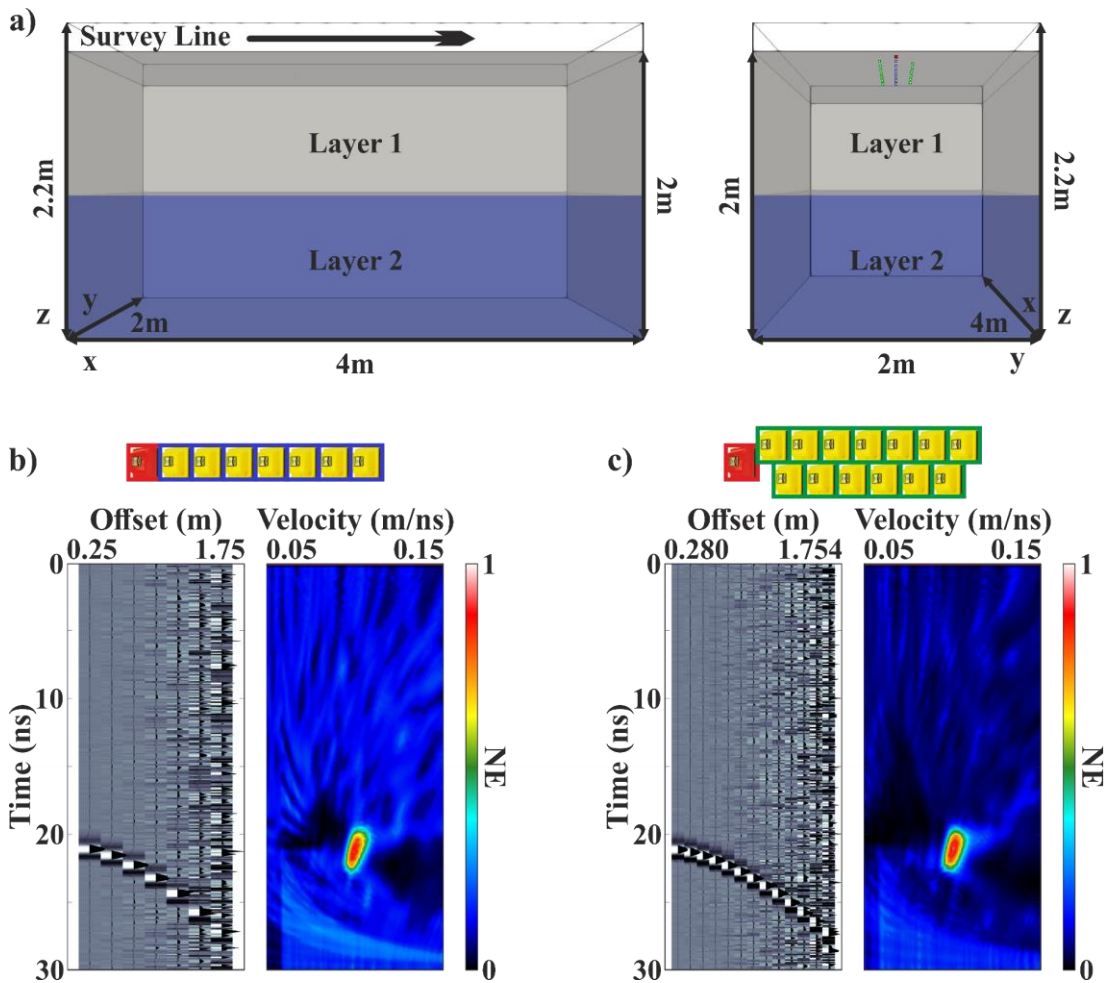


Figure 7.14: a) 3D model with two horizontal layers developed to generate synthetic data for demonstrating the effect of increasing the number of receivers on velocity spectrum semblance analysis. b) 7Rx synthetic data CMP gather, obtained from the standard seven-receiver configuration, contaminated with white Gaussian noise and resultant semblance plot of the CMP gather. c) 13Rx synthetic data CMP gather, obtained from the diagonal thirteen-receiver configuration, contaminated with white Gaussian noise and resultant semblance plot of the CMP gather. The transducer configuration is shown at the top of each sub-figure, with the Tx in red and the Rx's in yellow.

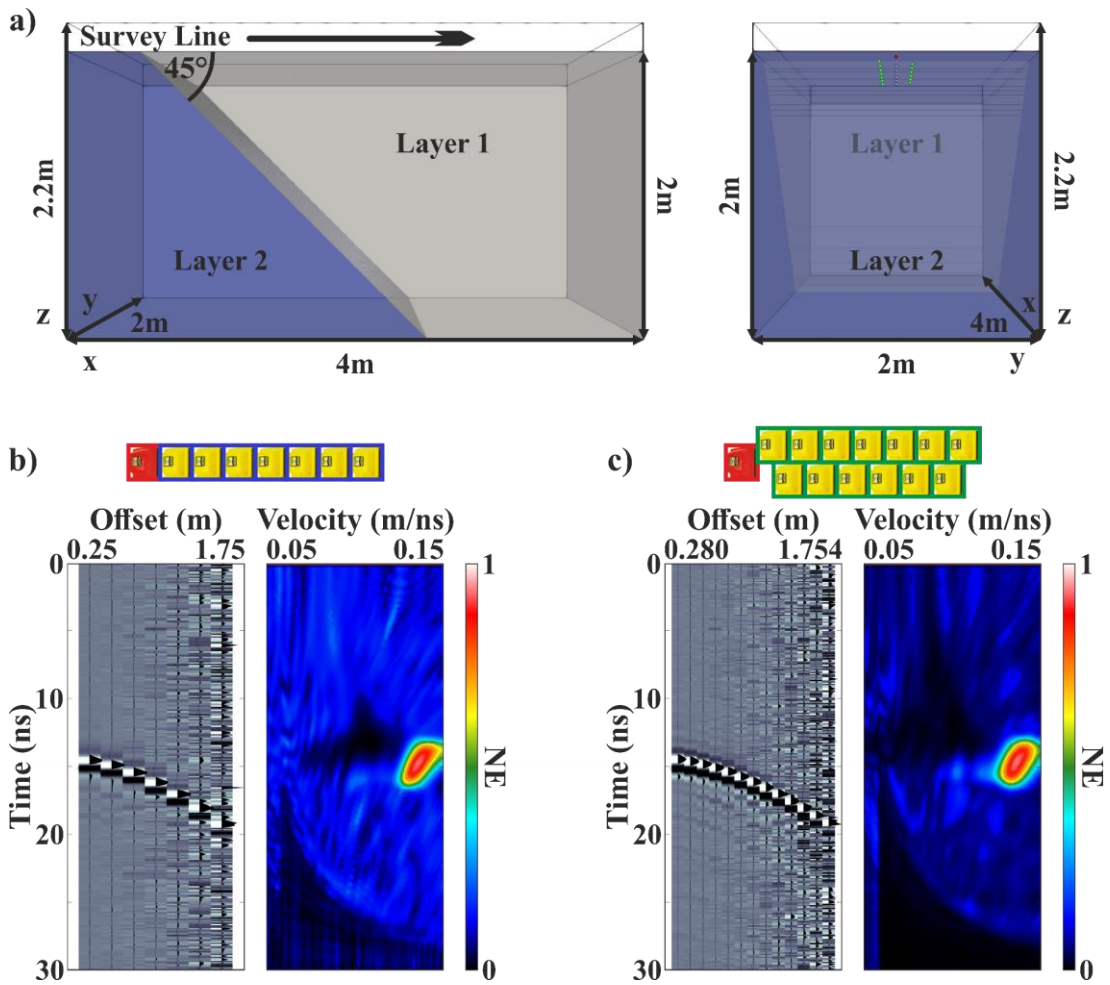


Figure 7.15: a) 3D two-layered model with the second layer dipping parallel to the survey line at a 45-degree angle developed to generate synthetic data for demonstrating the effect of increasing the number of receivers on velocity spectrum semblance analysis. b) 7Rx synthetic data CMP gather, obtained from the standard seven-receiver configuration, contaminated with white Gaussian noise and resultant semblance plot of the CMP gather. c) 13Rx synthetic data CMP gather, obtained from the diagonal thirteen-receiver configuration, contaminated with white Gaussian and resultant semblance plot of the CMP gather. The transducer configuration is shown at the top of each sub-figure, with the Tx in red and the Rxs in yellow.

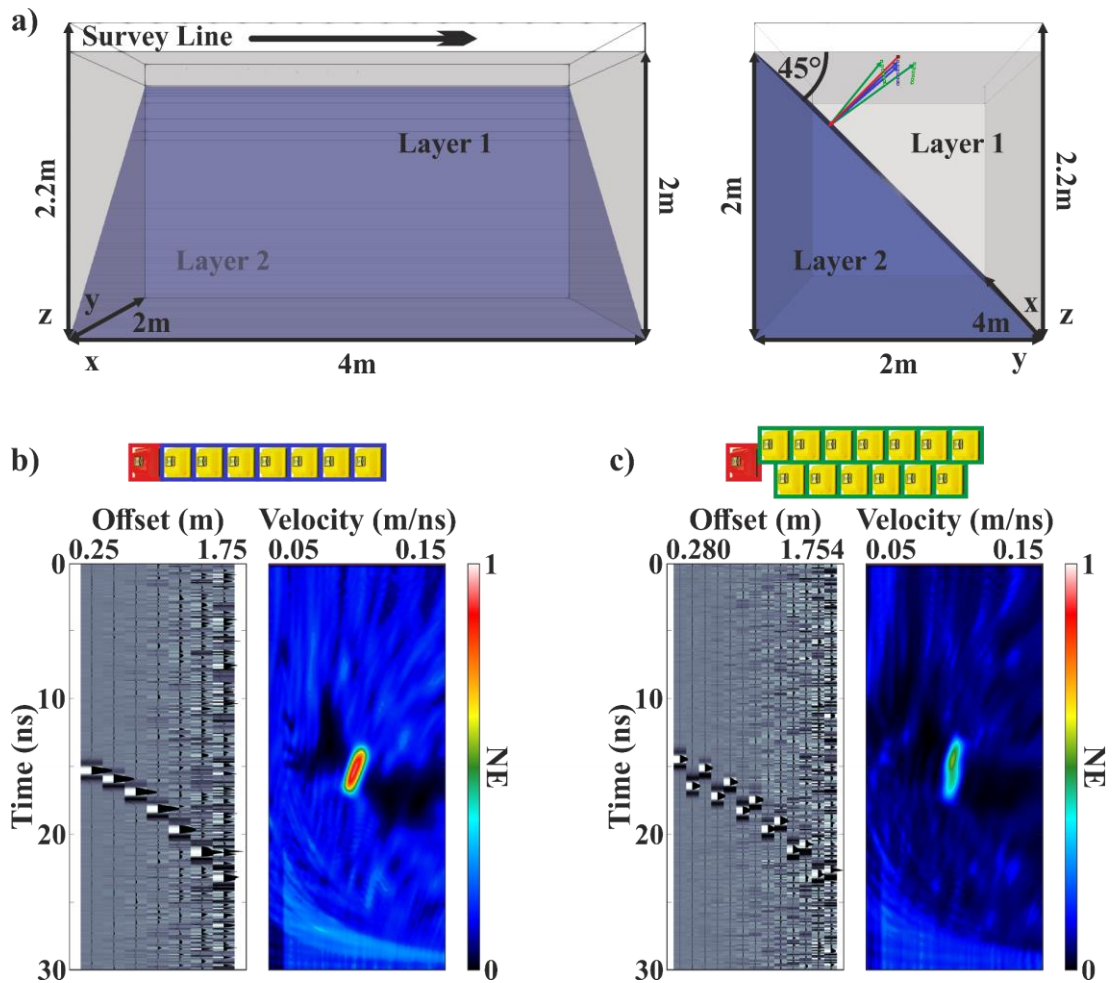


Figure 7.16: a) 3D two-layered model with the second layer dipping perpendicular to the survey line at a 45-degree angle developed to generate synthetic data for demonstrating the effect of increasing the number of receivers on velocity spectrum semblance analysis. b) 7Rx synthetic data CMP gather, obtained from the standard seven-receiver configuration, contaminated with white Gaussian noise and resultant semblance plot of the CMP gather. c) 13Rx synthetic data CMP gather, obtained from the diagonal thirteen-receiver configuration, contaminated with white Gaussian and resultant semblance plot of the CMP gather. The transducer configuration is shown at the top of each sub-figure, with the Tx in red and the Rx's in yellow.

# 8

## **Conclusions and recommendations**

This concluding chapter provides a summary of the main research findings and outputs of the preceding chapters as well as some recommendations for further future research.

## 8.1 Conclusions

The primary aim of this thesis was the investigation and development of new processing methods, workflows, as well as tools for GPR data acquired exclusively from the newly developed multi-channel GPR systems with multi-concurrent data acquisition receivers. The secondary aim was to investigate and evaluate different antenna configurations and survey parameters for these GPR systems. These aims sought to answer the key research question of whether highly accurate and detailed velocity models can be obtained as efficiently and economically as possible to boost the data quality and, as a result, GPR interpretations in a variety of geophysical problems, among others.

### 8.1.1 Development of processing tools

A novel MATLAB-based software with a user-friendly GUI was developed to enable large-volume multi-offset GPR data to be visualised and processed, as well as to test and evaluate new processing algorithms/methods and workflows for multi-concurrent receiver GPR data.

- The software supports file formats from a variety of GPR manufacturers, but most importantly, it supports the ability to handle both synthetic data generated by gprMax as well as multi-concurrent receiver GPR field data collected by the “WARR Machine” GPR.
- The software consists of three different interconnected modules, namely the 2D module, the CMP/WARR module, and the 3D module, each one developed with its own user-friendly GUI and data visualisation and processing functions, which can work either independently or together.
- The main 2D module can manage both single-offset and multi-offset GPR data and provides more than fifty different functions for visualising, analysing, editing, and processing GPR data, as well as novel functions developed exclusively for multi-concurrent receiver GPR data. In addition, the module allows for easy and fast control of the processing workflow as well as batch processing.

- The CMP/WARR module focuses on moveout-based processing and horizontal stacking but also provides functions for many other common as well as advanced multi-offset GPR data processing steps. The module also incorporates both an interactive GUI tool for manual hand-picked velocity spectrum analysis as well as an automatic velocity spectrum analysis tool which operates utilising a novel algorithm.
- The 3D module allows the creation, manipulation, and visualisation of 3D GPR data. The module offers most of the standard 3D data visualisation methods, as well as export in formats suitable for visualisation and processing with third-party software.

### **8.1.2 Development of processing methods**

Three novel processing algorithms/methods were developed to address specific challenges associated with processing multi-concurrent receiver GPR data such as time misalignments, signal versus offset attenuation, and large-volume data velocity analysis.

#### **Time-zero alignment**

- The importance of time-zero alignment for multi-concurrent receiver GPR data for moveout-based processing and horizontal stacking has been demonstrated. It has been shown that even small time errors/time misalignments in GPR signals from different receivers can result in misaligned linear and hyperbolic events in the WARR and CMP domains, and consequently lead to false stacking velocity estimates as well as poor stacking results.
- A novel time-zero alignment method to deal with the time misalignments of multi-concurrent receiver GPR data has been proposed. The proposed method has been validated with synthetic data generated by gprMax utilising a purpose-built 3D antenna model, as well as real field data collected with the “WARR Machine” GPR, demonstrating its effectiveness and performance.
- The proposed time-zero alignment method was also compared with the corresponding method proposed by Diamanti et al. (2018), but not with the method proposed by Kaufmann et al. (2020) owing to COVID-19 restrictions. The proposed method

has been shown to be superior to that of Diamanti et al. (2018), whilst it is also in practice easier and faster to implement than that of Kaufmann et al. (2020).

### **CMP trace balancing**

- The importance of CMP trace balancing for semblance analysis and horizontal stacking for multi-concurrent receiver GPR data has been demonstrated. It has been shown that a proper balancing of the CMP gather traces can improve not only velocity resolution in the resultant semblance plot (i.e., the sharpness and strength of semblance peaks), and hence the velocity information that could be obtained, but also stacking results.
- A novel sliding window CMP trace balancing method to compensate for the large AVO differences in multi-concurrent receiver GPR data has been proposed. The proposed method has been validated with both synthetic data generated from 3D numerical simulations performed in gprMax as well as real field data acquired with the “WARR Machine” GPR, demonstrating its efficacy and utility.
- The CMP gather and semblance results of the proposed sliding window trace balancing method were also compared with the corresponding results of the single-window trace balancing method as well as with the AB semblance results, showing the clear superiority of the proposed method.

### **Automated velocity spectra picking**

- The importance of automating velocity analysis for large-volume multi-concurrent receiver GPR data, as well as the necessity of developing new and not overly computationally intensive algorithms capable of overcoming the irregularities of velocity spectra semblance panels of such data, has been highlighted.
- A novel method for rapid automatic velocity spectra picking able to avoid, to some extent, spurious peaks present in multi-concurrent receiver GPR velocity spectra semblance panels, has been proposed. The proposed method has been validated directly with synthetic data generated in MATLAB as well as indirectly with real field data collected with the “WARR Machine” GPR, demonstrating both its effectiveness and accuracy.

- The proposed automatic velocity analysis method was also compared with manual hand-picked velocity analysis, generally showing an excellent agreement as well as a very slight superiority.

### **8.1.3 Development of a processing workflow**

A robust and complete processing workflow for multi-concurrent receiver GPR data was developed to create detailed velocity models capable of further improving the quality of the data, and as a result, qualitative and quantitative GPR interpretations.

- The processing workflow proposed for producing detailed stacking velocity fields and enhanced zero-offset stacked time sections consists of both standard GPR data and seismic reflection data processing methods as well as methods, such as the above-mentioned, developed for processing multi-concurrent receiver GPR data.
- The proposed processing methods/processing workflow have/has been validated with synthetic data sets generated by complex 2D models using gprMax, as well as real field data sets collected from different environments using two different “WARR Machine” GPRs with different types of transducers (i.e., centre frequency) and configurations (i.e., transducer separation distances), demonstrating their/its efficacy and, as a result, the true potential of the multi-concurrent receiver GPR systems.

#### **Velocity analysis and velocity fields**

In validating the proposed processing methods/workflow, for each data set, velocity analysis was performed automatically on all high-fold CMP gathers to investigate if it is feasible to automatically extract detailed stacking velocity fields suitable to produce enhanced zero-offset stacked sections. In addition to the automated analysis, a dense manual hand-picked velocity analysis was also performed, for verification and comparison purposes.

- The velocity fields obtained from the manual and automated analyses, were generally in very good agreement, demonstrating that seven traces from seven multi-concurrent sampling receivers are sufficient not only for manual hand-picked

velocity analysis, but also for automated velocity analysis, and therefore for providing automatically detailed stacking velocity fields.

- A thorough comparison between the manual and the corresponding automated velocity fields, as well as the time required to extract them by each method, revealed that the automated velocity fields were not only more detailed and accurate, as expected given the higher number of analyses, but were also much easier and faster to extract, thus demonstrating the clear superiority of the automated over the manual hand-picked velocity spectrum analysis.
- The resultant manual and automated velocity fields were smoothed and/or spatially filtered to remove potential velocity outliers, and hence to create more accurate and suitable velocity fields for horizontal stacking, showing both the importance and potential of large volumes of multi-concurrent receiver GPR data (in this particular case, of a large number of available 1D velocity functions) and how they can be exploited.

### **Stacking and stacked sections**

In validating the proposed processing methods/workflow, for each data set, both the manual and the automated filtered/smoothed velocity fields were used to create zero-offset stacked sections, for comparison purposes.

- The resultant stacked sections showed significant improvements compared to the corresponding CO profiles of the first receiver, such as high-frequency and/or ringing noise reduction, improved reflector continuity, and reflector enhancements, demonstrating that seven traces from seven multi-concurrent sampling receivers are sufficient not only to provide detailed stacking velocity fields but also enhanced zero-offset stacked time sections.
- A detailed comparison between the stacked sections obtained from the manual velocity fields with those obtained from the automated velocity fields revealed that they were, in general, very similar. Nonetheless, those obtained from the automated fields showed slightly less NMO stretching, and therefore improved narrower reflectors, as well as improved stacking, particularly in areas with high-angle reflection events; thus demonstrating the superiority of the automated over the

manual hand-picked velocity spectrum analysis, as well as the importance of a dense velocity analysis in areas with dipping reflectors.

### **8.1.4 System/survey design investigation**

An investigation of system/survey design has been carried out to make multi-concurrent receiver GPR systems more practicable and cost-effective as well as to further improve, if possible, the data quality.

#### **Decrease in the number of receivers**

The feasibility of reducing the number of receivers, while maintaining acceptable velocity spectra resolution, and hence, obtaining detailed stacking velocity fields and enhanced zero-offset stacked sections, was investigated.

- Several transducer configurations, which were physically possible with the hardware/field data available due to COVID-19 restrictions, with a reduced number of receivers also placed in different positions, were investigated. The investigated transducer configurations have been evaluated and compared with both synthetic data generated by 3D numerical simulations using gprMax as well as multiple real field data sets acquired from different environments with two different “WARR Machine” GPRs using different types of transducers and configurations.
- The importance of the total number of receivers/CMP gather traces (i.e., of the stacking fold) as well as of both the near-offset and the far-offset receivers/CMP gather traces (i.e., of the spread length), in the computation of velocity spectra panels for multi-concurrent receiver GPR data, has been demonstrated. It has been shown that reducing the number of receivers in a multi-concurrent receiver GPR system, and consequently the number of traces in the resultant CMP gathers, reduces velocity spectra quality and introduces spurious peaks, which can be particularly detrimental during an automated velocity analysis process. In addition, it has been also shown that reducing either the near-offset or the far-offset receivers/traces significantly reduces velocity spectra resolution, which can affect the ability to differentiate different peaks but, more importantly, can lead to inaccurate velocity estimates during the picking process, especially if this is done manually.

- Since it has been demonstrated that both near-offset and far-offset receivers/traces are required for obtaining adequate velocity spectra resolution, a four-receiver sparse configuration was proposed to reduce the number of receivers. The proposed four-receiver sparse configuration velocity spectra results were compared with corresponding results from the standard seven-receiver configuration of the “WARR Machine”, showing an increase in spurious peaks but a very good agreement between primary peaks; thus, demonstrating that the four-receiver sparse configuration can successfully maintain velocity resolution in the resultant velocity spectra panels, and hence, velocity information.

To investigate the feasibility of automatically obtaining detailed stacking velocity fields suitable for producing enhanced zero-offset stacked sections from a four-receiver sparse configuration, an automated velocity analysis was performed on the corresponding four-fold data. In addition, the corresponding seven-fold data from the standard seven-receiver configuration were also analysed in the same way for verification and comparison purposes.

- The velocity fields obtained from the four-receiver sparse configuration and the standard seven-receiver configuration, were generally in good agreement with only a few exceptions, demonstrating that generally not only seven traces are sufficient for automated velocity analysis but also four traces from four sparse receivers.

Both velocity fields obtained from the four-receiver sparse configuration and the standard seven-receiver configuration were smoothed and/or filtered and used to create zero-offset stacked sections.

- The resultant stacked sections showed significant improvements compared to the corresponding CO profile of the first receiver (i.e., high-frequency and/or ringing noise reduction, improved reflector continuity, and reflector enhancements), demonstrating that even four traces from four multi-concurrent sampling receivers placed in a sparse configuration are able not only to provide detailed stacking velocity fields but also enhanced zero-offset stacked time sections. Nevertheless, it should be noted that, as expected, the improvements shown in the stacked sections of the seven-receiver configuration were greater than in those shown in stacked

sections of the four-receiver configuration due to the increased number of receivers, and therefore the stacking fold.

### **Increase in the number of receivers**

The feasibility of increasing the number of receivers to further improve velocity spectra quality and horizontal stacking results was investigated.

- To successfully increase the number of receivers whilst maintaining acceptable SNRs for the far-offset receivers/traces, a configuration with thirteen receivers all placed diagonally one after the other was proposed. The proposed so-called diagonal configuration has been evaluated and compared with the standard seven-receiver configuration using only synthetic data generated by 3D numerical simulations with gprMax, owing to COVID-19 restrictions and, as a result, the lack of hardware/field data.
- A comparison between the synthetic CMP gather and semblance results of the two configurations revealed the potential disadvantages of a WARR diagonal-like transducer configuration for multi-concurrent receiver GPR systems. More specifically, a such configuration not only can substantially increase, the total cost of the system among other things, but it could also be problematic for surveying areas with dipping reflectors.

## **8.2 Recommendations for future research**

Although the aims of this thesis have been largely met, there are still several topics for further research. Below are some suggestions for additional future research:

- The GPR data visualisation and processing software presented in this work is still in development and it is intended to become open source in the future. Other researchers can then improve and/or expand the software over time, given, of course, that they have MATLAB programming skills, by adding new data visualisation and processing functions and/or even new entire data visualisation and processing modules.

- The velocity spectra analysis results could be further improved by exploiting the large volume of data that can be generated by the new multi-concurrent receiver GPR systems. In this work, for example, the large volume of data, and in particular, the large number of available 1D velocity functions, was used to filter velocity outliers from the stacking velocity fields. Other techniques commonly used in seismic such as spatial velocity spectra averaging, CMP gather averaging, and super CMP gathers could be used to suppress spurious peaks and improve velocity spectra analysis, and thus the final results.
- Although as demonstrated the automatic velocity spectra picking method proposed in this work is efficient and accurate, it requires the use of several user-defined thresholds and/or parameters. A new automated machine learning-based velocity analysis method could be developed by taking advantage of the hundreds of thousands of velocity spectra panels that can be generated by the new multi-concurrent receiver GPR systems as well as the current proposed velocity analysis method in order to create and provide the necessary training data sets.
- This work was primarily focused on the development of a workflow to produce detailed stacking velocity fields and enhanced zero-offset stacked reflection time sections. The next logical step in this workflow is the addition of depth imaging and migration. Furthermore, apart from NMO-based velocity spectra analysis, other more advanced velocity analysis methods such as prestack depth migration velocity analysis or reflection tomography could also be explored and/or integrated into this workflow.
- Finally, as mentioned above, only transducer configurations with Tx-Rx positions spacings that were physically possible with the available hardware/field data were investigated in this work. Other transducer configurations with, for example, two transmitters or different positions for the receivers can be also explored and tested.



**MATLAB scripts for converting Vox  
format to HDF5 format**

```

% vox2hdf5_converter
%
%
% This script converts MagicaVoxel output files (.vox) (https://ephtracy.github.io/)
% to gprMax HDF5 geometry files (.h5) (https://www.gprmax.com/) that can be
% used to import a model geometry in gprMax using the #geometry_objects_read
% command.
%
%
% Author: Dimitrios Angelis
% Last Modified: 20/12/2021

% Additional information =====
%
% * For the script to work properly and produce the exact representation of
% MagicaVoxel model in gprMax, the Z-axis must be selected as depth axis in the
% gprMax input file/model.
% i.e., #domain: x y z
%           ^
%           depth axis
%
% * Each voxel in MagicaVoxel will correspond to a cell in the gprMax model. Due
% to the canvas size limitations of MagicaVoxel (i.e., 256x256x256 (xyz)) the
% maximum domain size that can be used for the gprMax model is
% x = dx*256, y = dy*256, z = dz*256.
% Where dx dy dz are the values used for the discretisation of space in the gprMax
% input file/model.
%
% * If a larger domain size for the gprMax model is desired and given to the script
% (i.e., larger than x = dx*256, y = dy*256, z = dz*256) then the voxel model will
% be resized to fit in the desired gprMax domain. However, in this case, as it is
% understandable, each voxel will no longer correspond to a single gprMax cell.
%

```

```
% * Each colour in MagicaVoxel will correspond to a different material in gprMax.
% Only the 1st 15 colours of the 1st column of palette 0 of MagicaVoxel can be
% used. The 1st colour which is the light grey one will correspond to the first
% material of the materials (.txt) gprMax file.

clc;
clear;
close all;

% gprMax model info =====
while 1
    prompt = {'x (m)', 'y (m)', 'z (m)', 'dxdydz (m)'};
    dlg_title = 'gprMax model info';
    answer = inputdlg(prompt, dlg_title, [1 50]);
    answer = str2double(answer);
    if isempty(answer)
        return
    elseif isnan(answer(1)) || isnan(answer(2))...
        || isnan(answer(3)) || isnan(answer(4))...
        || answer(1) <= 0 || answer(2) <= 0 ...
        || answer(3) <= 0 || answer(4) <= 0
        continue
    else
        break
    end
end

x = answer(1);
y = answer(2);
z = answer(3);

dx = answer(4);
```

```

dy = answer(4);
dz = answer(4);

% Select MagicaVoxel file =====
[infile, path] = uigetfile('*.vox', 'Select MagicaVoxel file', ...
    'Multiselect', 'Off');
if isequal(infile, 0)
    return
end

fname = strrep(lower(infile), '.vox', '');
pname = path;

% Read MagicaVoxel file =====
infile = [pname infile];

fid = fopen(infile, 'r');
file_id = char(fread(fid, 4, 'char'));
version_num = fread(fid, 1, 'int');

skip1 = char(fread(fid, 4, 'char'));

bytes_chunk_content = fread(fid, 1, 'int');
bytes_childer_chunk = fread(fid, 1, 'int');

skip2 = char(fread(fid, 12, 'char'));

% MagicaVoxel model size in number of voxels =====
xdom = fread(fid, 1, 'int');
ydom = fread(fid, 1, 'int');
zdom = fread(fid, 1, 'int');

```

```

skip3 = char(fread(fid, 12, 'char'));

% MagicaVoxel voxel matrix X Y Z ID =====
info = 4;
voxel_num = fread(fid, 1, 'int');           % Total number of voxels

voxel = zeros(voxel_num, info);
for i = 1 : voxel_num
    voxel(i, :) = fread(fid, 4, 'int8');
end
fclose(fid);

xyz = [voxel(:, 1), voxel(:, 2), voxel(:, 3)];
ids = voxel(:, 4);

% XYZ voxel coordinates start from 0, 0, 0. Matlab does not support zero indexing =
xyz = xyz + 1;

% The 1st 15 colors/ids of the 1st column of palette 0 of MagicaVoxel are the
% following. Change them to 0 1 2 3 4 ... 14 =====
palet = -7 : -8 : -119;

for i = 1 : length(palet)
    ids(ids == palet(i)) = i - 1;
end

% Data matrix =====
data = -ones(zdom, ydom, xdom);           % -1 = free_space in gprMax
for i = 1 : voxel_num

```

```

    data(xyz(i, 3), xyz(i, 2), xyz(i, 1)) = ids(i);
end

% Resize data matrix if necessary. Also change data to int16 =====
if xdom == x/dx & ydom == y/dy & zdom == z/dz
    data = int16(data);
else
    warn = warndlg('Voxel Model will be resized!', 'Warning!');
    but = findobj(warn, 'Style', 'Pushbutton');
    delete(but);
    pause(2);
    close(warn);
    data = int16(imresize3(data, [z/dz y/dy x/dx], 'nearest'));
end

% Write to HDF5 geometry gprMax file =====
fid = H5F.create([fname '.h5'], ...
    'H5F_ACC_TRUNC', 'H5P_DEFAULT', 'H5P_DEFAULT');
h5writeatt([fname '.h5'], '/', 'dx_dy_dz', [dx dy dz]);
h5create([fname '.h5'], '/data', [z/dz y/dy x/dx]);
h5write([fname '.h5'], '/data', data);
H5F.close(fid);
h5disp([fname '.h5']);

```

```

% vox2hdf5_converter_combine
%
%
% This script combines multiple MagicaVoxel output files (.vox)
% (https://ephtracy.github.io/) and converts them to a single gprMax HDF5 geometry
% file (.h5) (https://www.gprmax.com/) that can be used to import a model geometry
% in gprMax using the #geometry_objects_read command.

```

```
%  
%  
% Author: Dimitrios Angelis  
% Last Modified: 20/12/2021  
  
clc;  
clear;  
close all;  
  
% gprMax model info =====  
while 1  
    prompt = {'x (m)', 'y (m)', 'z (m)', 'dxdydz (m)'};  
    dlg_title = 'gprMax Model Info';  
    answer = inputdlg(prompt, dlg_title, [1 50]);  
    answer = str2double(answer);  
    if isempty(answer)  
        return  
    elseif isnan(answer(1)) || isnan(answer(2))...  
        || isnan(answer(3)) || isnan(answer(4))...  
        || answer(1) <= 0 || answer(2) <= 0 ...  
        || answer(3) <= 0 || answer(4) <= 0  
        continue  
    else  
        break  
    end  
end  
  
x = answer(1);  
y = answer(2);  
z = answer(3);  
  
dx = answer(4);
```

```
dy = answer(4);
dz = answer(4);

% Size of each voxel model =====
each_voxel_x = 85;
each_voxel_y = 108;
each_voxel_z = 47;

% The number of voxel models that correspond to the gprMax domain chosen =====
x_vox_models = round(x / (each_voxel_x * dx));
y_vox_models = round(y / (each_voxel_y * dy));
z_vox_models = round(z / (each_voxel_z * dz));

% The coordinates of each voxel model will start from the 0, 0, 0 position. It is
% necessary to create a combined coordinate system. This is done here. =====
i = 1; p = 0;
for k = 1 : z_vox_models
    o = 0;
    for l = 1 : y_vox_models
        n = 0;
        for m = 1 : x_vox_models
            add(i, :) = [n, o, p];
            i = i + 1;
            n = n + each_voxel_x;
        end
        o = o + each_voxel_y;
    end
    p = p + each_voxel_z;
end
```

```

% In addition, since there is no zero indexing in matlab add 1 =====
add = add + 1;

% Select Magicalvoxel files =====
[infile, path] = uigetfile('*.vox', 'Select MagicaVoxel File(s)', ...
    'Multiselect', 'On');
if isequal(infile, 0)
    return
elseif ~iscell(infile)
    infile = mat2cell(infile, 1);
    num_files = 1;
elseif iscell(infile)
    num_files = length(infile);
end

fname = strtok(infile{1}, '-');
pname = path;

% Preallocate gprMax model geometry as a 3D matrix. Each element corresponds to
% a cell =====

% -1 = free_space in gprMax
data = -ones(round(z / dz), round(y / dy), round(x / dx));

% Read each file and place each voxel model to the correct coordinates
% using the matrix 'add' (see above). =====
for i = 1 : num_files
    infile{i} = [pname infile{i}];

    fid = fopen(infile{i}, 'r');
    file_id = char(fread(fid, 4, 'char'));

```

```

version_num = fread(fid, 1, 'int');

skip1 = char(fread(fid, 4, 'char'));

bytes_chunk_content = fread(fid, 1, 'int');
bytes_childer_chunk = fread(fid, 1, 'int');

skip2 = char(fread(fid, 12, 'char'));

% MagicaVoxel model size in number of voxels =====
xdom = fread(fid, 1, 'int');
ydom = fread(fid, 1, 'int');
zdom = fread(fid, 1, 'int');

skip3 = char(fread(fid, 12, 'char'));

% MagicaVoxel voxel matrix X Y Z ID =====
info = 4;
voxel_num = fread(fid, 1, 'int');           % Total number of voxels

voxel = zeros(voxel_num, info);
for k = 1 : voxel_num
    voxel(k, :) = fread(fid, 4, 'int8');
end
fclose(fid);

xyz = [voxel(:, 1), voxel(:, 2), voxel(:, 3)];

xyz = xyz + add(i, :);

% Ids =====

```

```

ids = voxel(:, 4);

for k = 1 : voxel_num
    data(xyz(k, 3), xyz(k, 2), xyz(k, 1)) = ids(k);
end
end

% The 1st 15 colors/ids of the 1st column of palette 0 of MagicaVoxel are the
% following =====
palet = -7 : -8: -119;

% Change them to 0 1 2 3 4 ... 14 =====
for i = 1 : length(palet)
    data(data == palet(i)) = i - 1;
end

% Change data to int16 =====
data = int16(data);

% Write to HDF5 file =====
fid = H5F.create([fname '.h5'], ...
    'H5F_ACC_TRUNC', 'H5P_DEFAULT', 'H5P_DEFAULT');
h5writeatt([fname '.h5'], '/', 'dx_dy_dz', [dx dy dz]);
h5create([fname '.h5'], '/data', ...
    [z_vox_models * each_voxel_z ...
    y_vox_models * each_voxel_y ...
    x_vox_models * each_voxel_x]);
h5write([fname '.h5'], '/data', data);
H5F.close(fid);
h5disp([fame '.h5']);

```

# References

- Ahrens, J., Geveci, B., & Law, C. (2005). ParaView: An End-User Tool for Large-Data Visualization. In *Visualization Handbook* (pp. 717–731). Elsevier. <https://doi.org/10.1016/B978-012387582-2/50038-1>
- Angelis, D., Tsourlos, P., Tsokas, G., Vargemezis, G., Zacharopoulou, G., & Power, C. (2018). Combined application of GPR and ERT for the assessment of a wall structure at the Heptapyrgion fortress (Thessaloniki, Greece). *Journal of Applied Geophysics*, *152*, 208–220. <https://doi.org/10.1016/j.jappgeo.2018.04.003>
- Angelis, D., Warren, C., & Diamanti, N. (2020). A software toolset for processing and visualization of single and multi-offset GPR data. *18th International Conference on Ground Penetrating Radar, Golden, Colorado, 14–19 June 2020*, 320–323. <https://doi.org/10.1190/gpr2020-084.1>
- Angelis, D., Warren, C., & Diamanti, N. (2019). Preliminary development of a workflow for processing multi-concurrent receiver GPR data. *10th International Workshop on Advanced Ground Penetrating Radar*, *1*, 1–7. <https://doi.org/10.3997/2214-4609.201902572>
- Angelis, D., Warren, C., Diamanti, N., James, M., & Annan, A. P. (2021). Challenges and opportunities from large volume, multi-offset Ground Penetrating Radar data. *EGU General Assembly 2021, Online, 19–30 Apr 2021*, EGU21-13138. <https://doi.org/https://doi.org/10.5194/egusphere-egu21-13138>
- Angelis, D., Warren, C., Diamanti, N., Martin, J., & Annan, A. P. (2022a). Development of a workflow for processing ground-penetrating radar data from multiconcurrent receivers. *Geophysics*, *87*(4), WB9–WB18. <https://doi.org/10.1190/geo2021-0376.1>
- Angelis, D., Warren, C., Diamanti, N., Martin, J., & Annan, A. P. (2022b). The effects of receiver arrangement on velocity analysis with multi-concurrent receiver GPR data. *Near Surface Geophysics*, *20*(5), 519–530. <https://doi.org/10.1002/nsg.12235>
- Annan, A. P. (1973). Radio Interferometry Depth Sounding: Part I—Theoretical Discussion. *Geophysics*, *38*(3), 557–580. <https://doi.org/10.1190/1.1440360>
- Annan, A. P. (2002). GPR—History, Trends, and Future Developments. *Subsurface Sensing Technologies and Applications*, *3*(4), 253–270.

- <https://doi.org/10.1023/A:1020657129590>
- Annan, A. P. (2003). *Ground Penetrating Radar: Principles, Procedures & Applications*. Sensors & Software Incorporated.
- Annan, A. P. (2005). 11. Ground-Penetrating Radar. In *Near-Surface Geophysics* (pp. 357–438). Society of Exploration Geophysicists. <https://doi.org/doi:10.1190/1.9781560801719.ch11>
- Annan, A. P. (2009). Electromagnetic principles of ground penetrating radar. In H. M. Jol (Ed.), *Ground Penetrating Radar* (pp. 1–40). Elsevier. <https://doi.org/10.1016/B978-0-444-53348-7.00001-6>
- Annan, A. P., & Cosway, S. W. (1992). Ground Penetrating Radar Survey Design. In *Symposium on the Application of Geophysics to Engineering and Environmental Problems 1992* (pp. 329–351). Environment and Engineering Geophysical Society. <https://doi.org/10.4133/1.2921946>
- Annan, A. P., & Davis, J. L. (1976). Impulse radar sounding in permafrost. *Radio Science*, *11*(4), 383–394. <https://doi.org/10.1029/RS011i004p00383>
- Annan, A. P., & Jackson, S. R. (2017). The WARR Machine. *2017 9th International Workshop on Advanced Ground Penetrating Radar, IWAGPR 2017 - Proceedings*, 1–4. <https://doi.org/10.1109/IWAGPR.2017.7996106>
- Arcone, S. A. (1984). Field observations of electromagnetic pulse propagation in dielectric slabs. *Geophysics*, *49*(10), 1763–1773. <https://doi.org/10.1190/1.1441584>
- Arcone, S. A., Lawson, D. E., Delaney, A. J., Strasser, J. C., & Strasser, J. D. (1998). Ground-penetrating radar reflection profiling of groundwater and bedrock in an area of discontinuous permafrost. *Geophysics*, *63*(5), 1573–1584. <https://doi.org/10.1190/1.1444454>
- Babcock, E. L., Annan, A. P., & Bradford, J. H. (2016). Cable Effects in Ground-Penetrating Radar Data and Implications for Quantitative Amplitude Measurements. *Journal of Environmental and Engineering Geophysics*, *21*(3), 99–104. <https://doi.org/10.2113/JEEG21.3.99>
- Bailey, J. T., Evans, S., & Robin, G. D. Q. (1964). Radio echo sounding of polar ice sheets. *Nature*, *204*(4957), 420–421. <https://doi.org/10.1038/204420a0>
- Balanis, C. A. (2012). *Advanced engineering electromagnetics* (2nd ed.). John Wiley & Sons.
- Balanis, C. A. (2016). *Antenna Theory: Analysis and Design* (4th ed.). John Wiley & Sons.

- Bangbing, W., Gang, T., Bo, S., Jinxue, G., & Xiangpei, Z. (2006). An analysis of the multi-fold method for GPR exploration. *Applied Geophysics*, 3(3), 187–191. <https://doi.org/10.1007/s11770-006-0028-x>
- Baysal, E., Kosloff, D. D., & Sherwood, J. W. C. (1983). Reverse time migration. *Geophysics*, 48(11), 1514–1524. <https://doi.org/10.1190/1.1441434>
- Becht, A., Appel, E., & Dietrich, P. (2006). Analysis of multi-offset GPR data: A case study in a coarse-grained gravel aquifer. *Near Surface Geophysics*, 4(4), 227–240. <https://doi.org/10.3997/1873-0604.2005047>
- Benedetto, A., Manacorda, G., Simi, A., & Tosti, F. (2012). Novel perspectives in bridges inspection using GPR. *Nondestructive Testing and Evaluation*, 27(3), 239–251. <https://doi.org/10.1080/10589759.2012.694883>
- Benedetto, A., Tosti, F., Bianchini Ciampoli, L., & D’Amico, F. (2017). An overview of ground-penetrating radar signal processing techniques for road inspections. *Signal Processing*, 132, 201–209. <https://doi.org/10.1016/j.sigpro.2016.05.016>
- Berard, B. A., & Maillol, J. M. (2007). Multi-offset ground penetrating radar data for improved imaging in areas of lateral complexity - Application at a Native American site. *Journal of Applied Geophysics*, 62(2), 167–177. <https://doi.org/10.1016/j.jappgeo.2006.10.002>
- Berenger, J.-P. (1994). A perfectly matched layer for the absorption of electromagnetic waves. *Journal of Computational Physics*, 114(2), 185–200. <https://doi.org/10.1006/jcph.1994.1159>
- Bérenger, J.-P. (2007). Perfectly Matched Layer (PML) for Computational Electromagnetics. *Synthesis Lectures on Computational Electromagnetics*, 2(1), 1–117. <https://doi.org/10.2200/S00030ED1V01Y200605CEM008>
- Bernard, É., Friedt, J. M., Saintenoy, A., Tolle, F., Griselin, M., & Marlin, C. (2014). Where does a glacier end? GPR measurements to identify the limits between valley slopes and actual glacier body. Application to the Austre Lovénbreen, Spitsbergen. *International Journal of Applied Earth Observation and Geoinformation*, 27, 100–108. <https://doi.org/https://doi.org/10.1016/j.jag.2013.07.006>
- Bohidar, R. N., & Hermance, J. F. (2002). The GPR refraction method. *Geophysics*, 67(5), 1474–1485. <https://doi.org/10.1190/1.1512792>
- Booth, A. D., Clark, R. A., Hamilton, K., & Murray, T. (2010). Multi-offset ground penetrating radar methods to image buried foundations of a Medieval Town Wall, Great Yarmouth, UK. *Archaeological Prospection*, 17(2), 103–116.

- <https://doi.org/10.1002/arp.377>
- Booth, A. D., Clark, R. A., & Murray, T. (2010). Semblance response to a ground-penetrating radar wavelet and resulting errors in velocity analysis. *Near Surface Geophysics*, 8(3), 235–246. <https://doi.org/10.3997/1873-0604.2010008>
- Booth, A. D., Linford, N. T., Clark, R. A., & Murray, T. (2008). Three-dimensional, multi-offset ground-penetrating radar imaging of archaeological targets. *Archaeological Prospection*, 15(2), 93–112. <https://doi.org/10.1002/arp.327>
- Bradford, J. H. (2003). GPR Offset Dependent Reflectivity Analysis for Characterization of a High-Conductivity LNAPL Plume. In *Symposium on the Application of Geophysics to Engineering and Environmental Problems 2003* (pp. 238–252). Environment and Engineering Geophysical Society. <https://doi.org/10.4133/1.2923166>
- Bradford, J. H. (2004). 3D Multi-Offset, Multi-Polarization Acquisition and Processing of GPR Data: A Controlled DNAPL Spill Experiment. In *Symposium on the Application of Geophysics to Engineering and Environmental Problems 2004* (pp. 514–527). Environment and Engineering Geophysical Society. <https://doi.org/10.4133/1.2923365>
- Bradford, J. H. (2006). Applying reflection tomography in the postmigration domain to multifold ground-penetrating radar data. *Geophysics*, 71(1), K1–K8. <https://doi.org/10.1190/1.2159051>
- Bradford, J. H. (2008). Measuring Water Content Heterogeneity Using Multifold GPR with Reflection Tomography. *Vadose Zone Journal*, 7(1), 184–193. <https://doi.org/10.2136/vzj2006.0160>
- Bradford, J. H., Clement, W. P., & Barrash, W. (2009). Estimating porosity with ground-penetrating radar reflection tomography: A controlled 3-D experiment at the Boise Hydrogeophysical Research Site. *Water Resources Research*, 45(4). <https://doi.org/10.1029/2008WR006960>
- Bradford, J. H., & Deeds, J. C. (2006). Ground-penetrating radar theory and application of thin-bed offset-dependent reflectivity. *Geophysics*, 71(3), K47–K57. <https://doi.org/10.1190/1.2194524>
- Bradford, J. H., Nichols, J., Mikesell, T. D., & Harper, J. T. (2009). Continuous profiles of electromagnetic wave velocity and water content in glaciers: An example from Bench Glacier, Alaska, USA. *Annals of Glaciology*, 50(51), 1–9. <https://doi.org/10.3189/172756409789097540>

- Bristow, C. S., & Jol, H. M. (2003). *Ground Penetrating Radar in Sediments*. Geological Society of London. <https://doi.org/10.1144/GSL.SP.2003.211>
- Carcione, J. M. (2015). Wave Fields in Real Media. In *Wave Fields in Real Media: Wave Propagation in Anisotropic, Anelastic, Porous and Electromagnetic Media: Third Edition*. Elsevier. <https://doi.org/10.1016/C2013-0-18893-9>
- Carcione, J. M., & Cavallini, F. (1995). On the acoustic-electromagnetic analogy. *Wave Motion*, 21(2), 149–162. [https://doi.org/10.1016/0165-2125\(94\)00047-9](https://doi.org/10.1016/0165-2125(94)00047-9)
- Cassidy, N. (2008a). Introduction to gpr. In *Workshop at the 12th International Conference on Ground Penetrating Radar*.
- Cassidy, N. (2008b). Frequency-dependent attenuation and velocity characteristics of nano-to-micro scale, lossy, magnetite-rich materials. *Near Surface Geophysics*, 6(6), 341–354. <https://doi.org/10.3997/1873-0604.2008023>
- Cassidy, N. (2009a). Electrical and magnetic properties of rocks, soils and fluids. In H. M. Jol (Ed.), *Ground Penetrating Radar* (pp. 41–72). Elsevier. <https://doi.org/10.1016/B978-0-444-53348-7.00002-8>
- Cassidy, N. (2009b). Ground penetrating radar data processing, modelling and analysis. In H. M. Jol (Ed.), *Ground Penetrating Radar* (pp. 141–176). Elsevier. <https://doi.org/10.1016/B978-0-444-53348-7.00005-3>
- Cassidy, N., & Millington, T. M. (2009). The application of finite-difference time-domain modelling for the assessment of GPR in magnetically lossy materials. *Journal of Applied Geophysics*, 67(4), 296–308. <https://doi.org/10.1016/j.jappgeo.2008.09.009>
- Causse, E., & Sénéchal, P. (2006). Model-based automatic dense velocity analysis of GPR field data for the estimation of soil properties. *Journal of Geophysics and Engineering*, 3(2), 169–176. <https://doi.org/10.1088/1742-2132/3/2/008>
- Chamberlain, A. T., Sellers, W., Proctor, C., & Coard, R. (2000). Cave Detection in Limestone using Ground Penetrating Radar. *Journal of Archaeological Science*, 27(10), 957–964. <https://doi.org/10.1006/jasc.1999.0525>
- Church, G., Grab, M., Schmelzbach, C., Bauder, A., & Maurer, H. (2020). Monitoring the seasonal changes of an englacial conduit network using repeated ground-penetrating radar measurements. *Cryosphere*, 14(10), 3269–3286. <https://doi.org/10.5194/tc-14-3269-2020>
- Ciampoli, L. B., Tosti, F., Economou, N., & Benedetto, F. (2019). Signal processing of GPR data for road surveys. In *Geosciences (Switzerland)* (Vol. 9, Issue 2).

- <https://doi.org/10.3390/geosciences9020096>
- Clarke, G. K. C. (1987). A short history of scientific investigations on glaciers. *Journal of Glaciology*, 33(S1), 4–24. <https://doi.org/10.3189/s0022143000215785>
- Clough, J. W. (1976). Electromagnetic Lateral Waves Observed By Earth-Sounding Radars. *Geophysics*, 41(6 A), 1126–1132. <https://doi.org/10.1190/1.2035908>
- Conyers, L., Ernenwein, E., & Bedal, L.-A. (2002). Ground-Penetrating Radar (GPR) Mapping as a Method for Planning Excavation Strategies, Petra, Jordan. *E-Tiq-uity*, 1.
- Dal Bo, I., Klotzsche, A., Schaller, M., Ehlers, T. A., Kaufmann, M. S., Fuentes Espoz, J. P., Vereecken, H., & van der Kruk, J. (2019). Geophysical imaging of regolith in landscapes along a climate and vegetation gradient in the Chilean coastal cordillera. *Catena*, 180, 146–159. <https://doi.org/10.1016/j.catena.2019.04.023>
- Daniels, D. J. (2004). *Ground Penetrating Radar* (2nd ed.). The Institution of Electrical Engineers.
- Daniels, J. J., Roberts, R., & Vendl, M. (1995). Ground penetrating radar for the detection of liquid contaminants. *Journal of Applied Geophysics*, 33(1–3), 195–207. [https://doi.org/10.1016/0926-9851\(95\)90041-1](https://doi.org/10.1016/0926-9851(95)90041-1)
- Davis, J. L., & Annan, A. P. (1989). Ground-Penetrating Radar for High-Resolution Mapping of Soil and Rock Stratigraphy. *Geophysical Prospecting*, 37(5), 531–551. <https://doi.org/10.1111/j.1365-2478.1989.tb02221.x>
- De Domenico, D., Teramo, A., & Campo, D. (2013). GPR surveys for the characterization of foundation plinths within a seismic vulnerability analysis. *Journal of Geophysics and Engineering*, 10(3). <https://doi.org/10.1088/1742-2132/10/3/034007>
- Deeds, J. C., & Bradford, J. H. (2002). Characterization of an aquitard and direct detection of LNAPL at Hill Air Force Base using GPR AVO and migration velocity analyses. In S. Koppenjan & H. Lee (Eds.), *Ninth International Conference on Ground Penetrating Radar* (Vol. 4758, pp. 323–329). <https://doi.org/10.1117/12.462236>
- Delaney, A. J., Arcone, S. A., & Chacho, E. F. (1990). Winter short-pulse radar studies on the Tanana River, Alaska. *Arctic*, 43(3), 244–250. <https://doi.org/10.14430/arctic1618>
- Diamanti, N. (2008). *An efficient ground penetrating radar finite-difference time-domain subgridding scheme and its application to the non-destructive testing of*

- masonry arch bridges*. The University of Edinburgh.
- Diamanti, N., & Annan, A. P. (2013). Characterizing the energy distribution around GPR antennas. *Journal of Applied Geophysics*, 99, 83–90. <https://doi.org/10.1016/j.jappgeo.2013.08.001>
- Diamanti, N., & Annan, A. P. (2019). Understanding the use of ground-penetrating radar for assessing clandestine tunnel detection. *The Leading Edge*, 38(6), 453–459. <https://doi.org/10.1190/tle38060453.1>
- Diamanti, N., & Annan, A. P. (2017). Air-launched and ground-coupled GPR data. *2017 11th European Conference on Antennas and Propagation (EUCAP)*, 1694–1698. <https://doi.org/10.23919/EuCAP.2017.7928409>
- Diamanti, N., & Giannopoulos, A. (2011). Employing ADI-FDTD subgrids for GPR numerical modelling and their application to study ring separation in brick masonry arch bridges. *Near Surface Geophysics*, 9(3), 245–256. <https://doi.org/10.3997/1873-0604.2010065>
- Diamanti, N., Judith Elliott, E., Jackson, S. R., & Peter Annan, A. (2018). The WARR Machine: System Design, Implementation and Data. *Journal of Environmental and Engineering Geophysics*, 23(4), 469–487. <https://doi.org/10.2113/JEEG23.4.469>
- Dix, C. H. (1955). Seismic Velocities From Surface Measurements. *Geophysics*, 20(1), 68–86. <https://doi.org/10.1190/1.1438126>
- Dojack, L. (2012). Ground Penetrating Radar Theory, Data Collection, Processing, and Interpretation: A Guide for Archaeologists. In *Project Report, University of British Columbia* (Issue April). <https://doi.org/http://dx.doi.org/10.14288/1.0086065>
- Dougherty, M. E., Michaels, P., Pelton, J. R., & Liberty, L. M. (1994). Enhancement of Ground Penetrating Radar Data through Signal Processing. In *Symposium on the Application of Geophysics to Engineering and Environmental Problems 1994* (pp. 1021–1028). Environment and Engineering Geophysical Society. <https://doi.org/10.4133/1.2922053>
- Ebihara, S., Sato, M., & Niitsuma, H. (1998). Analysis of a guided wave along a conducting structure in a borehole. *Geophysical Prospecting*, 46(5), 489–505. <https://doi.org/10.1046/j.1365-2478.1998.00103.x>
- Ebrahimi, S., Kahoo, A. R., Chen, Y., & Porsani, M. (2017). A high-resolution weighted AB semblance for dealing with amplitude-variation-with-offset

- phenomenon. *Geophysics*, 82(2), V85–V93. <https://doi.org/10.1190/GEO2016-0047.1>
- Ebrahimi, S., Kahoo, A. R., Porsani, M. J., & Kalateh, A. N. (2017). Obtaining high-resolution velocity spectra using weighted semblance. *Exploration Geophysics*, 48(3), 210–218. <https://doi.org/10.1071/EG15100>
- El-Said, M. A. H. (1956). Geophysical Prospection of Underground Water in the Desert by Means of Electromagnetic Interference Fringes. *Proceedings of the IRE*, 44(1), 24–30. <https://doi.org/10.1109/JRPROC.1956.274846>
- Endres, A. L., Clement, W. P., & Rudolph, D. L. (2000). Ground penetrating radar imaging of an aquifer during a pumping test. *Ground Water*, 38(4), 566–576. <https://doi.org/10.1111/j.1745-6584.2000.tb00249.x>
- Endres, A. L., Murray, T., Booth, A. D., & West, L. J. (2009). A new framework for estimating englacial water content and pore geometry using combined radar and seismic wave velocities. *Geophysical Research Letters*, 36(4). <https://doi.org/10.1029/2008GL036876>
- Feng, X., & Sato, M. (2004). Pre-stack migration applied to GPR for landmine detection. *Inverse Problems*, 20(6). <https://doi.org/10.1088/0266-5611/20/6/S07>
- Feng, X., Sato, M., Zhang, Y., Liu, C., Shi, F., & Zhao, Y. (2009). CMP antenna array GPR and signal-to-clutter ratio improvement. *IEEE Geoscience and Remote Sensing Letters*, 6(1), 23–27. <https://doi.org/10.1109/LGRS.2008.2006634>
- Fisher, E., McMechan, G. A., & Annan, A. P. (1992). Acquisition and processing of wide-aperture ground-penetrating radar data. *Geophysics*, 57(3), 495–504. <https://doi.org/10.1190/1.1443265>
- Fomel, S. (2003). Time-migration velocity analysis by velocity continuation. *Geophysics*, 68(5), 1662–1672. <https://doi.org/10.1190/1.1620640>
- Fomel, S. (2009). Velocity analysis using AB semblance. *Geophysical Prospecting*, 57(3), 311–321. <https://doi.org/10.1111/j.1365-2478.2008.00741.x>
- Forte, E., Dossi, M., Pipan, M., & Colucci, R. R. (2014). Velocity analysis from common offset GPR data inversion: theory and application to synthetic and real data. *Geophysical Journal International*, 197(3), 1471–1483. <https://doi.org/10.1093/gji/ggu103>
- Forte, E., & Pipan, M. (2017). Review of multi-offset GPR applications: Data acquisition, processing and analysis. *Signal Processing*, 132, 210–220. <https://doi.org/10.1016/j.sigpro.2016.04.011>

- Galagedara, L. W., Redman, J. D., Parkin, G. W., Annan, A. P., & Endres, A. L. (2005). Numerical Modeling of GPR to Determine the Direct Ground Wave Sampling Depth. *Vadose Zone Journal*, 4(4), 1096–1106. <https://doi.org/10.2136/vzj2004.0143>
- Gedney, S. D. (2011). Introduction to the Finite-Difference Time-Domain (FDTD) Method for Electromagnetics. *Synthesis Lectures on Computational Electromagnetics*, 6(1), 1–250. <https://doi.org/10.2200/S00316ED1V01Y201012CEM027>
- Gehrig, M., Morris, D., & Bryant, J. (2004). Ground Penetrating Radar for Concrete Evaluation Studies. *Technical Presentation Paper for Performance Foundation Association*.
- Geolitix Technologies Inc. (2021). *Geolitix*. <https://geolitix.com/>
- Giannakis, I. (2016). *Realistic numerical modelling of Ground Penetrating Radar for landmine detection*. The University of Edinburgh.
- Giannakis, I., & Giannopoulos, A. (2014). A Novel Piecewise Linear Recursive Convolution Approach for Dispersive Media Using the Finite-Difference Time-Domain Method. *IEEE Transactions on Antennas and Propagation*, 62(5), 2669–2678. <https://doi.org/10.1109/TAP.2014.2308549>
- Giannakis, I., Giannopoulos, A., & Warren, C. (2016). A Realistic FDTD Numerical Modeling Framework of Ground Penetrating Radar for Landmine Detection. *IEEE Journal of Selected Topics in Applied Earth Observations and Remote Sensing*, 9(1), 37–51. <https://doi.org/10.1109/JSTARS.2015.2468597>
- Giannakis, I., Giannopoulos, A., & Warren, C. (2019). Realistic FDTD GPR Antenna Models Optimized Using a Novel Linear/Nonlinear Full-Waveform Inversion. *IEEE Transactions on Geoscience and Remote Sensing*, 57(3), 1768–1778. <https://doi.org/10.1109/TGRS.2018.2869027>
- Giannakis, I., Giannopoulos, A., & Warren, C. (2021). A Machine Learning Scheme for Estimating the Diameter of Reinforcing Bars Using Ground Penetrating Radar. *IEEE Geoscience and Remote Sensing Letters*, 18(3), 461–465. <https://doi.org/10.1109/LGRS.2020.2977505>
- Giannakis, I., Giannopoulos, A., & Yarovoy, A. (2016). Model-Based Evaluation of Signal-to-Clutter Ratio for Landmine Detection Using Ground-Penetrating Radar. *IEEE Transactions on Geoscience and Remote Sensing*, 54(6), 3564–3573. <https://doi.org/10.1109/TGRS.2016.2520298>
- Giannopoulos, A. (2005). Modelling ground penetrating radar by GprMax.

- Construction and Building Materials*, 19(10), 755–762.  
<https://doi.org/10.1016/j.conbuildmat.2005.06.007>
- Giannopoulos, A. (2012). Unsplit Implementation of Higher Order PMLs. *IEEE Transactions on Antennas and Propagation*, 60(3), 1479–1485.  
<https://doi.org/10.1109/TAP.2011.2180344>
- Giannopoulos, A. (2018). Multipole Perfectly Matched Layer for Finite-Difference Time-Domain Electromagnetic Modeling. *IEEE Transactions on Antennas and Propagation*, 66(6), 2987–2995. <https://doi.org/10.1109/TAP.2018.2823864>
- Golden Software LLC. (2021). *Products*. <https://www.goldensoftware.com/products>
- Goodman, D., & Piro, S. (2013). *GPR Remote Sensing in Archaeology*. Springer Berlin Heidelberg. <https://doi.org/10.1007/978-3-642-31857-3>
- Goodman, D., Piro, S., Nishimura, Y., Schneider, K., Hongo, H., Higashi, N., Steinberg, J., & Damiata, B. (2009). GPR archaeometry. In H. M. Jol (Ed.), *Ground Penetrating Radar* (pp. 479–508). Elsevier. <https://doi.org/10.1016/B978-0-444-53348-7.00015-6>
- GPR-SLICE. (2021). *GPR-Slice*©. <https://www.gpr-survey.com/>
- Greaves, R. J., Lesmes, D. P., Lee, J. M., & Toksöz, M. N. (1996). Velocity variations and water content estimated from multi-offset, ground-penetrating radar. *Geophysics*, 61(3), 683–695. <https://doi.org/10.1190/1.1443996>
- GSSI. (2021). *RADAN*®. <https://www.geophysical.com/software>
- Guy, E. D., Daniels, J. J., Radzevicius, S. J., & Vendl, M. A. (1999). Demonstration of using crossed dipole GPR antennae for site characterization. *Geophysical Research Letters*, 26(22), 3421–3424. <https://doi.org/10.1029/1999GL008365>
- Guy, E., & Radzevicius, S. (2001). Recognition of Borehole Radar Cable-Related Effects Using Variable Offset Sounding. *Subsurface Sensing Technologies and Applications*, 2, 127–139. <https://doi.org/10.1023/A:1011574820079>
- Hamann, G., Tronicke, J., Steelman, C. M., & Endres, A. L. (2013). Spectral velocity analysis for the determination of ground-wave velocities and their uncertainties in multi-offset GPR data. *Near Surface Geophysics*, 11(2), 167–176. <https://doi.org/10.3997/1873-0604.2012038>
- Hamran, S. E., Paige, D. A., Amundsen, H. E. F., Berger, T., Brovoll, S., Carter, L., Damsgård, L., Dypvik, H., Eide, J., Eide, S., Ghent, R., Hellenen, Ø., Kohler, J., Mellon, M., Nunes, D. C., Plettemeier, D., Rowe, K., Russell, P., & Øyan, M. J. (2020). Radar Imager for Mars' Subsurface Experiment—RIMFAX. *Space*

- Science Reviews*, 216(8), 128. <https://doi.org/10.1007/s11214-020-00740-4>
- Hatton, L., Worthington, M. H., & Makin, J. (1986). *Seismic Data Processing. Theory and practice*.
- He, X., Zhu, Z., Lu, G., & Lu, Q. (2009). The FDTD Modeling of GPR for Tunnel Inspection. *2009 International Conference on Information Engineering and Computer Science*, 1–4. <https://doi.org/10.1109/ICIECS.2009.5366793>
- Huber, E., & Hans, G. (2018). RGPR — An open-source package to process and visualize GPR data. *2018 17th International Conference on Ground Penetrating Radar (GPR)*, 1–4. <https://doi.org/10.1109/ICGPR.2018.8441658>
- Hugenschmidt, J. (2000). Railway track inspection using GPR. *Journal of Applied Geophysics*, 43(2–4), 147–155. [https://doi.org/10.1016/S0926-9851\(99\)00054-3](https://doi.org/10.1016/S0926-9851(99)00054-3)
- Huisman, J. A., Hubbard, S. S., Redman, J. D., & Annan, A. P. (2003). Measuring Soil Water Content with Ground Penetrating Radar: A Review. *Vadose Zone Journal*, 2(4), 476–491. <https://doi.org/10.2113/2.4.476>
- Hülßenbeck, R., & Co. (1926). *Verfahren zur elektrischen Bodenforschung* (Patent No. 489434).
- Hülsmeier, C. (1904). *Verfahren, um metallische Gegenstände mittels elektrischer Wellen einem Beobachter zu melden* (Patent No. 165546).
- Igel, J., Günther, T., & Kuntzer, M. (2013). Ground-penetrating radar insight into a coastal aquifer: The freshwater lens of Borkum Island. *Hydrology and Earth System Sciences*, 17(2), 519–531. <https://doi.org/10.5194/hess-17-519-2013>
- Inan, U. S., & Marshall, R. A. (2011). Introduction. In *Numerical Electromagnetics* (pp. 1–7). Cambridge University Press. <https://doi.org/10.1017/CBO9780511921353.002>
- Instanes, A., Lønne, I., & Sandaker, K. (2004). Location of avalanche victims with ground-penetrating radar. *Cold Regions Science and Technology*, 38(1), 55–61. <https://doi.org/10.1016/j.coldregions.2003.08.002>
- Jacob, R. W., & Urban, T. M. (2016). Ground-Penetrating Radar Velocity Determination and Precision Estimates Using Common-Midpoint (CMP) Collection with Hand-Picking, Semblance Analysis and Cross-Correlation Analysis: A Case Study and Tutorial for Archaeologists. *Archaeometry*, 58(6), 987–1002. <https://doi.org/10.1111/arcm.12214>
- Johnsson, T., & Björklund, N. (2005). *Real-time sampling of ground penetrating radar and related processing*.

- Jol, H. M. (2009). Ground Penetrating Radar Theory and Applications. In D. J. Daniels (Ed.), *Ground Penetrating Radar* (2nd ed.). Elsevier. <https://doi.org/10.1016/B978-0-444-53348-7.X0001-4>
- Kämäri, M., Alho, P., Colpaert, A., & Lotsari, E. (2017). Spatial variation of river-ice thickness in a meandering river. *Cold Regions Science and Technology*, *137*, 17–29. <https://doi.org/10.1016/j.coldregions.2017.01.009>
- Kaufmann, M. S., Klotzsche, A., Vereecken, H., & van der Kruk, J. (2020). Simultaneous multichannel multi-offset ground-penetrating radar measurements for soil characterization. *Vadose Zone Journal*, *19*(1), e20017. <https://doi.org/10.1002/vzj2.20017>
- Kim, J. H., Cho, S. J., & Yi, M. J. (2007). Removal of ringing noise in GPR data by signal processing. *Geosciences Journal*, *11*(1), 75–81. <https://doi.org/10.1007/BF02910382>
- King, F. W. (Ed.). (2009a). Introduction. In *Hilbert Transforms* (Vol. 1, pp. 1–10). Cambridge University Press. <https://doi.org/DOI:10.1017/CBO9780511721458.002>
- King, F. W. (2009b). The Hilbert transform of waveforms and signal processing. In *Hilbert Transforms* (Vol. 2, pp. 119–181). Cambridge University Press. <https://doi.org/10.1017/CBO9780511735271.005>
- Klotzsche, A., Jonard, F., Looms, M. C., van der Kruk, J., & Huisman, J. A. (2018). Measuring Soil Water Content with Ground Penetrating Radar: A Decade of Progress. *Vadose Zone Journal*, *17*(1), 180052. <https://doi.org/10.2136/vzj2018.03.0052>
- Koppenjan, S. (2009). Ground penetrating radar systems and design. In H. M. Jol (Ed.), *Ground Penetrating Radar* (pp. 73–97). Elsevier. <https://doi.org/10.1016/B978-0-444-53348-7.00003-X>
- Lambot, S., André, F., Slob, E., & Vereecken, H. (2012). Effect of antenna-medium coupling in the analysis of ground-penetrating radar data. *Near Surface Geophysics*, *10*(6), 631–639. <https://doi.org/10.3997/1873-0604.2012005>
- Leimbach, G., & Löwy, H. (1910a). *Verfahren zum Nachweis unterirdischer Erzlager oder von Grundwasser mittels elektrischer Wellen* (Patent No. 246836).
- Leimbach, G., & Löwy, H. (1910b). *Verfahren zur systematischen Erforschung des Erdinnern größerer Gebiete mittels elektrischer Wellen* (Patent No. 237944).
- Liu, H., & Sato, M. (2012). Dynamic groundwater level estimation by the velocity

- spectrum analysis of GPR. *2012 14th International Conference on Ground Penetrating Radar, GPR 2012*, 413–418. <https://doi.org/10.1109/icgpr.2012.6254901>
- Liu, S., Lu, Q., Li, H., & Wang, Y. (2020). Estimation of moisture content in railway subgrade by ground penetrating radar. In *Remote Sensing* (Vol. 12, Issue 18). <https://doi.org/10.3390/RS12182912>
- Liu, S., Wu, J., Zhou, J., & Zeng, Z. (2011). Numerical Simulations of Borehole Radar Detection for Metal Ore. *IEEE Geoscience and Remote Sensing Letters*, 8(2), 308–312. <https://doi.org/10.1109/LGRS.2010.2066545>
- Looyenga, H. (1965). Dielectric constants of heterogeneous mixtures. *Physica*, 31(3), 401–406. [https://doi.org/10.1016/0031-8914\(65\)90045-5](https://doi.org/10.1016/0031-8914(65)90045-5)
- Lopera, O., & Milisavljevic, N. (2007). Prediction of the effects of soil and target properties on the antipersonnel landmine detection performance of ground-penetrating radar: A Colombian case study. *Journal of Applied Geophysics*, 63(1), 13–23. <https://doi.org/10.1016/j.jappgeo.2007.02.002>
- Lualdi, M., & Lombardi, F. (2014). Significance of GPR polarisation for improving target detection and characterisation. *Nondestructive Testing and Evaluation*, 29(4), 345–356. <https://doi.org/10.1080/10589759.2014.949708>
- Lutz, P., Garambois, S., & Perroud, H. (2003). Influence of antenna configurations for GPR survey: information from polarization and amplitude versus offset measurements. *Geological Society, London, Special Publications*, 211(1), 299–313. <https://doi.org/10.1144/GSL.SP.2001.211.01.24>
- Macheret, Y. Y., Moskalevsky, M. Y., & Vasilenko, E. V. (1993). Velocity of radio waves in glaciers as an indicator of their hydrothermal state, structure and regime. *Journal of Glaciology*, 39(132), 373–384. <https://doi.org/10.3189/s0022143000016038>
- Maxwell, J. C. (1865). VIII. A dynamical theory of the electromagnetic field. *Philosophical Transactions of the Royal Society of London*, 155, 459–512. <https://doi.org/10.1098/rstl.1865.0008>
- Mayne, W. H. (1962). Common reflection point horizontal data stacking techniques. *Geophysics*, 27(6), 927–938. <https://doi.org/10.1190/1.1439118>
- Metwaly, M. (2007). Detection of metallic and plastic landmines using the GPR and 2-D resistivity techniques. *Natural Hazards and Earth System Science*, 7(6), 755–763. <https://doi.org/10.5194/nhess-7-755-2007>

- Miorali, M., Zhou, F., Slob, E., & Arts, R. (2011). Coupling ground penetrating radar and fluid flow modeling for oilfield monitoring applications. *GEOPHYSICS*, 76(3), A21–A25. <https://doi.org/10.1190/1.3569580>
- Mousa, W. A., & Al-Shuhail, A. A. (2011). Processing of seismic reflection data using MATLAB™. *Synthesis Lectures on Signal Processing*, 5(1), 1–97. <https://doi.org/10.2200/S00384ED1V01Y201109SPR010>
- Murray, T., Booth, A. D., & Rippin, D. M. (2007). Water-content of Glacier-ice: Limitations on estimates from velocity analysis of surface ground-penetrating radar surveys. *Journal of Environmental and Engineering Geophysics*, 12(1), 87–99. <https://doi.org/10.2113/JEEG12.1.87>
- Murray, T., Stuart, G. W., Fry, M., Gamble, N. H., & Crabtree, M. D. (2000). Englacial water distribution in a temperate glacier from surface and borehole radar velocity analysis. *Journal of Glaciology*, 46(154), 389–398. <https://doi.org/10.3189/172756500781833188>
- Nakashima, Y., Zhou, H., & Sato, M. (2001). Estimation of groundwater level by GPR in an area with multiple ambiguous reflections. *Journal of Applied Geophysics*, 47(3–4), 241–249. [https://doi.org/10.1016/S0926-9851\(01\)00068-4](https://doi.org/10.1016/S0926-9851(01)00068-4)
- Neal, A. (2004). Ground-penetrating radar and its use in sedimentology: Principles, problems and progress. *Earth-Science Reviews*, 66(3–4), 261–330. <https://doi.org/10.1016/j.earscirev.2004.01.004>
- Neidell, N. S., & Taner, M. T. (1971). Semblance and Other Coherency Measures for Multichannel Data. *Geophysics*, 36(3), 482–497. <https://doi.org/10.1190/1.1440186>
- Olhoeft, G. (1998). Electrical, magnetic, and geometric properties that determine ground penetrating radar performance. In *Proceedings of the Seventh International Conference on Ground Penetrating Radar*.
- Olhoeft, G., & Capron, D. E. (1993). Laboratory measurements of the radiofrequency electrical and magnetic properties of soils from near Yuma, Arizona. In *Open-File Report*. <https://doi.org/10.3133/ofr93701>
- Onajite, E. (2014). Understanding NMO, Velocity Analysis DMO, and Stacking. In E. Onajite (Ed.), *Seismic Data Analysis Techniques in Hydrocarbon Exploration* (pp. 117–137). Elsevier. <https://doi.org/10.1016/B978-0-12-420023-4.00009-5>
- Özdemir, C., Demirci, Ş., Yiğit, E., & Yilmaz, B. (2014). A Review on Migration Methods in B-Scan Ground Penetrating Radar Imaging. *Mathematical Problems*

- in Engineering*, 2014, 1–16. <https://doi.org/10.1155/2014/280738>
- Paren, J. (1970). *Dielectric Properties of Ice*. <https://doi.org/https://doi.org/10.17863/CAM.27518>
- Peacock, K. L., & Treitel, S. (1969). PREDICTIVE DECONVOLUTION: THEORY AND PRACTICE. *Geophysics*, 34(2), 155–169. <https://doi.org/10.1190/1.1440003>
- Pelgrom, M. J. M. (2013). *Analog-to-Digital Conversion*. Springer New York. <https://doi.org/10.1007/978-1-4614-1371-4>
- Peplinski, N. R., Ulaby, F. T., & Dobson, M. C. (1995). Dielectric Properties of Soils in the 0.3–1.3-GHz Range. *IEEE Transactions on Geoscience and Remote Sensing*, 33(3), 803–807. <https://doi.org/10.1109/36.387598>
- Peters, L. P., Daniels, J. J., & Young, J. D. (1994). Ground penetrating radar as a subsurface environmental sensing tool. *Proceedings of the IEEE*, 82(12), 1802–1822. <https://doi.org/10.1109/5.338072>
- Pipan, M., Baradello, L., Forte, E., Prizzon, A., & Finetti, I. (1999). 2-D and 3-D processing and interpretation of multi-fold ground penetrating radar data: A case history from an archaeological site. *Journal of Applied Geophysics*, 41(2–3), 271–292. [https://doi.org/10.1016/S0926-9851\(98\)00047-0](https://doi.org/10.1016/S0926-9851(98)00047-0)
- Pipan, M., Forte, E., Dal Moro, G., Sukan, M., & Finetti, I. (2003). Multifold ground-penetrating radar and resistivity to study the stratigraphy of shallow unconsolidated sediments. *The Leading Edge*, 22(9), 876–881. <https://doi.org/10.1190/1.1614161>
- Plattner, A. M. (2020). GPRPy: Open-source ground-penetrating radar processing and visualization software. *The Leading Edge*, 39(5), 332–337. <https://doi.org/10.1190/tle39050332.1>
- Porcello, L. J., Jordan, R. L., Zelenka, J. S., Adams, G. F., Phillips, R. J., Brown, W. E., Ward, S. H., & Jackson, P. L. (1974). The Apollo Lunar Sounder Radar System. *Proceedings of the IEEE*, 62(6), 769–783. <https://doi.org/10.1109/PROC.1974.9517>
- Porsani, J. L., Ruy, Y. B., Ramos, F. P., & Yamanouth, G. R. B. (2012). GPR applied to mapping utilities along the route of the Line 4 (yellow) subway tunnel construction in São Paulo City, Brazil. *Journal of Applied Geophysics*, 80, 25–31. <https://doi.org/10.1016/j.jappgeo.2012.01.001>
- Porsani, J. L., Slob, E., Lima, R. S., & Leite, D. N. (2010). Comparing detection and

- location performance of perpendicular and parallel broadside GPR antenna orientations. *Journal of Applied Geophysics*, 70(1), 1–8. <https://doi.org/10.1016/j.jappgeo.2009.12.002>
- Radzevicius, S. J., & Daniels, J. J. (2000). Ground penetrating radar polarization and scattering from cylinders. *Journal of Applied Geophysics*, 45(2), 111–125. [https://doi.org/10.1016/S0926-9851\(00\)00023-9](https://doi.org/10.1016/S0926-9851(00)00023-9)
- Rao Hu, Lixun Lu, & Shuiqiang Wang. (2012). The numerical simulation study on ground penetrating radar detection of the typical adverse geological structure. *2012 14th International Conference on Ground Penetrating Radar (GPR)*, 243–247. <https://doi.org/10.1109/ICGPR.2012.6254868>
- Rashed, M. (2008). Smart stacking: A new CMP stacking technique for seismic data. *The Leading Edge*, 27(4), 462–467. <https://doi.org/10.1190/1.2907176>
- Rashed, M. (2014). Fifty years of stacking. *Acta Geophysica*, 62(3), 505–528. <https://doi.org/10.2478/s11600-013-0191-4>
- Rashed, M., Kawamura, D., Nemoto, H., Miyata, T., & Nakagawa, K. (2003). Ground penetrating radar investigations across the Uemachi fault, Osaka, Japan. *Journal of Applied Geophysics*, 53(2–3), 63–75. [https://doi.org/10.1016/S0926-9851\(03\)00028-4](https://doi.org/10.1016/S0926-9851(03)00028-4)
- Reynolds, J. M. (2011). An introduction to applied and environmental geophysics. In *An introduction to applied and environmental geophysics* (2nd ed.). Chichester, West Sussex. <https://doi.org/10.1071/pvv2011n155other>
- Sarkar, D., Baumel, R. T., & Lerner, K. L. (2002). Velocity analysis in the presence of amplitude variation. *Geophysics*, 67(5), 1664–1672. <https://doi.org/10.1190/1.1512814>
- Sarkar, D., Castagna, J. P., & Lamb, W. J. (2001). AVO and velocity analysis. *Geophysics*, 66(4), 1284–1293. <https://doi.org/10.1190/1.1487076>
- Sassen, D. S., & Everett, M. E. (2005). Multi-component ground penetrating radar for improved imaging and target discrimination. In *Proceedings of the Symposium on the Application of Geophysics to Engineering and Environmental Problems, SAGEEP* (Vol. 1, pp. 11–20). Environment and Engineering Geophysical Society. <https://doi.org/10.4133/1.2923436>
- Sassen, D. S., & Everett, M. E. (2009). 3D polarimetric GPR coherency attributes and full-waveform inversion of transmission data for characterizing fractured rock. *Geophysics*, 74(3), J23–J34. <https://doi.org/10.1190/1.3103253>

- Sato, M., Iguchi, M., & Sato, R. (1984). Transient response of coupled linear dipole antennas. *IEEE Transactions on Antennas and Propagation*, 32(2), 133–140. <https://doi.org/10.1109/TAP.1984.1143277>
- Sato, M., & Thierbach, R. (1991). Analysis of a borehole radar in cross-hole mode. *IEEE Transactions on Geoscience and Remote Sensing*, 29(6), 899–904. <https://doi.org/10.1109/36.101368>
- Scheers, B. (2001). *Ultra-wideband ground penetrating radar with application to the detection of anti personnel landmines*. Université catholique de Louvain.
- Schneider, W. A. (1978). Integral formulation for migration in two and three dimensions. *Geophysics*, 43(1), 49–76. <https://doi.org/10.1190/1.1440828>
- Schroeder, W., Martin, K., & Lorensen, B. (2006). *The visualization toolkit : an object-oriented approach to 3D graphics ; [visualize data in 3D-medical, engineering or scientific ; build your own applications with C++, Tcl, Java ord Python/ Will Schroeder ; Ken Martin ; Bill Lorensen*. Kitware.
- Schubert, G. (2015). *Treatise on geophysics*. Elsevier.
- Sensors & Software Inc. (2001). *Technical Manual 30: Ekko-for-DVL pulseEKKO 100. User's Guide v1.0*. Sensors & Software Inc.
- Sensors & Software Inc. (2021a). *EKKO\_Project<sup>TM</sup>*. <https://www.sensoft.ca/products/ekko-project/overview/>
- Sensors & Software Inc. (2021b). *pulseEKKO® For The GPR Professional*. <https://www.sensoft.ca/products/pulseekkopro/overview-pulseekko/>
- Skolnik, M. I. (2001). *Introduction to radar systems* (3rd ed.). McGraw Hill.
- Stern, W. (1929). Versuch einer elektrodynamischen Dickenmessung von Gletschereis. *Gerlands Beitrage Zur Geophysik*, 23, 292–333.
- Stern, W. (1930). Über Grundlagen, Methodik und bisherige Ergebnisse elektrodynamischer Dickenmessung von Gletschereis. *Zeitschrift Für Gletscherkunde*, 15, 24–42.
- Stolt, R. H. (1978). Migration By Fourier Transform. *Geophysics*, 43(1), 23–48. <https://doi.org/10.1190/1.1440826>
- Szymczyk, M., & Szymczyk, P. (2013). Preprocessing of GPR data. *Image Processing & Communications*, 18(2–3), 83–90. <https://doi.org/doi:10.2478/v10248-012-0082-3>
- Taflove, A., & Hagness, S. C. (2005). *Computational Electrodynamics: The Finite-difference Time-domain Method* (3rd ed.). Artech House.

- <https://us.artechhouse.com/Computational-Electrodynamics-Third-Edition-P1929.aspx>
- Taner, M. T., & Koehler, F. (1969). Velocity Spectra. Digital Computer Derivation and Applications of Velocity Functions. *Geophysics*, 34(6), 859–881. <https://doi.org/10.1190/1.1440058>
- Taner, M. T., Koehler, F., & Sheriff, R. E. (1979). Complex Seismic Trace Analysis. *Geophysics*, 44(6), 1041–1063. <https://doi.org/10.1190/1.1440994>
- Telford, W. M., Geldart, L. P., & Sheriff, R. E. (1990). Applied Geophysics. In *Applied Geophysics*. Cambridge University Press. <https://doi.org/10.1017/cbo9781139167932>
- The MathWorks Inc. (2021). *MATLAB*®. <https://uk.mathworks.com/>
- Topp, G. C., Davis, J. L., & Annan, A. P. (1980). Electromagnetic determination of soil water content: Measurements in coaxial transmission lines. *Water Resources Research*, 16(3), 574–582. <https://doi.org/10.1029/WR016i003p00574>
- Tsoflias, G. P., Perll, C., Baker, M., & Becker, M. W. (2015). Cross-polarized GPR imaging of fracture flow channeling. *Journal of Earth Science*, 26(6), 776–784. <https://doi.org/10.1007/s12583-015-0612-1>
- Turesson, A. (2006). Water content and porosity estimated from ground-penetrating radar and resistivity. *Journal of Applied Geophysics*, 58(2), 99–111. <https://doi.org/10.1016/j.jappgeo.2005.04.004>
- Tzanis, A. (2010). MATGPR Release 2: A freeware MATLAB package for the analysis & interpretation of common & single offset GPR data. *FastTimes*, 15(1), 17–43. <http://scholar.google.com/scholar?hl=en&btnG=Search&q=intitle:MATGPR+Release+2:+A+freeware+MATLAB+package+for+the+analysis+&+interpretation+of+common+&+single+offset+GPR+data#0>
- Uieda, L. (2017). Step-by-step NMO correction. *The Leading Edge*, 36(2), 179–180. <https://doi.org/10.1190/tle36020179.1>
- Ursin, B. (1983). Review of Elastic and Electromagnetic Wave Propagation in Horizontally Layered Media. *Geophysics*, 48(8), 1063–1081. <https://doi.org/10.1190/1.1441529>
- van der Kruk, J. (2001). *Reflection seismic 1*. ETH Zürich, Institut für Geophysik. <https://doi.org/10.3929/ethz-a-010025751>
- van der Kruk, J., Wapenaar, C. P. A., Fokkema, J. T., & van den Berg, P. M. (2003). Three-dimensional imaging of multicomponent ground-penetrating radar data.

- Geophysics*, 68(4), 1241–1254. <https://doi.org/10.1190/1.1598116>
- Van Overmeeren, R. A., Sariowan, S. V., & Gehrels, J. C. (1997). Ground penetrating radar for determining volumetric soil water content; results of comparative measurements at two test sites. *Journal of Hydrology*, 197(1–4), 316–338. [https://doi.org/10.1016/S0022-1694\(96\)03244-1](https://doi.org/10.1016/S0022-1694(96)03244-1)
- Wai-Lok Lai, W., Dérobert, X., & Annan, A. P. (2018). A review of Ground Penetrating Radar application in civil engineering: A 30-year journey from Locating and Testing to Imaging and Diagnosis. *NDT and E International*, 96, 58–78. <https://doi.org/10.1016/j.ndteint.2017.04.002>
- Waite, A. H., & Schmidt, S. J. (1962). Gross Errors in Height Indication from Pulsed Radar Altimeters Operating over Thick Ice or Snow. *Proceedings of the IRE*, 50(6), 1515–1520. <https://doi.org/10.1109/JRPROC.1962.288195>
- Warren, C. (2009). *Numerical modelling of high-frequency ground-penetrating radar antennas*. The University of Edinburgh.
- Warren, C., & Giannopoulos, A. (2011). Creating finite-difference time-domain models of commercial ground-penetrating radar antennas using Taguchi's optimization method. *Geophysics*, 76(2), G37–G47. <https://doi.org/10.1190/1.3548506>
- Warren, C., & Giannopoulos, A. (2017). Characterisation of a ground penetrating radar antenna in lossless homogeneous and lossy heterogeneous environments. *Signal Processing*, 132, 221–226. <https://doi.org/10.1016/j.sigpro.2016.04.010>
- Warren, C., Giannopoulos, A., & Giannakis, I. (2016). gprMax: Open source software to simulate electromagnetic wave propagation for Ground Penetrating Radar. *Computer Physics Communications*, 209, 163–170. <https://doi.org/10.1016/j.cpc.2016.08.020>
- Warren, C., Giannopoulos, A., Gray, A., Giannakis, I., Patterson, A., Wetter, L., & Hamrah, A. (2019). A CUDA-based GPU engine for gprMax: Open source FDTD electromagnetic simulation software. *Computer Physics Communications*, 237, 208–218. <https://doi.org/10.1016/j.cpc.2018.11.007>
- Wharton, R. P., Rau, R. N., & Best, D. L. (1980, September 21). Electromagnetic Propagation Logging: Advances In Technique And Interpretation. *All Days*. <https://doi.org/10.2118/9267-MS>
- Wilson, V., Power, C., Giannopoulos, A., Gerhard, J., & Grant, G. (2009). DNAPL mapping by ground penetrating radar examined via numerical simulation.

- 
- Journal of Applied Geophysics*, 69(3–4), 140–149.  
<https://doi.org/10.1016/j.jappgeo.2009.08.006>
- Wright, D. L., Watts, R. D., & Bramsoe, E. (1984). A short-pulse electromagnetic transponder for hole-to-hole use. *IEEE Transactions on Geoscience and Remote Sensing*, GE-22(6), 720–725. <https://doi.org/10.1109/TGRS.1984.6499195>
- Xie, F., Wu, C. G. W., Lai, W. W. L., & Sham, J. F. C. (2018). Correction of multi-frequency GPR wave velocity with distorted hyperbolic reflections from GPR surveys of underground utilities. *Tunnelling and Underground Space Technology*, 76, 76–91. <https://doi.org/10.1016/j.tust.2018.02.005>
- Yalçiner, C. Ç., Bano, M., Kadioglu, M., Karabacak, V., Meghraoui, M., & Altunel, E. (2009). New temple discovery at the archaeological site of Nysa (western Turkey) using GPR method. *Journal of Archaeological Science*, 36(8), 1680–1689. <https://doi.org/10.1016/j.jas.2008.12.016>
- Yee, K. (1966). Numerical solution of initial boundary value problems involving maxwell's equations in isotropic media. *IEEE Transactions on Antennas and Propagation*, 14(3), 302–307. <https://doi.org/10.1109/TAP.1966.1138693>
- Yelf, R. (2004). Where is true time zero? *Proceedings of the Tenth International Conference Ground Penetrating Radar, GPR 2004*, 1, 279–282.
- Yilmaz, Ö. (2001). Seismic Data Analysis. In *Seismic Data Analysis*. Society of Exploration Geophysicists. <https://doi.org/10.1190/1.9781560801580>
- Zhou, H.-W. (2014). Practical Seismic Data Analysis. In *Practical Seismic Data Analysis*. Cambridge University Press. <https://doi.org/10.1017/cbo9781139027090>